STRONG DYNAMICS AT THE LHC

By

Pawin Ittisamai

A DISSERTATION

Submitted to
Michigan State University
in partial fulfillment of the requirements
for the degree of

Physics-Doctor of Philosophy

2014

ABSTRACT

STRONG DYNAMICS AT THE LHC

By

Pawin Ittisamai

The limitations of the Standard Model of particle physics, despite its being a well-established theory, have prompted various proposals for new physics capable of addressing its shortcomings. The particular issue to be explored here is the mechanism of electroweak symmetry breaking, the probing of which lies within the TeV-scale physics accessible to the Large Hadron Collider (LHC). This thesis focuses on the phenomenology of a class of models featuring a dynamical breaking of the electroweak symmetry via strong dynamics. Consequences of recent experiments and aspects of near-future experiments are presented.

We study the implications of the LHC Higgs searches available at the time the related journal article was written for technicolor models that feature colored technifermions. Then we discuss the properties of a technicolor model featuring strong-top dynamics that is viable for explaining the recently discovered boson of mass 126 GeV. We introduce a novel method of characterizing the color structure of a new massive vector boson, often predicted in various new physics models, using information that will be promptly available if it is discovered in the near-future experiments at the LHC. We generalize the idea for more realistic models where a vector boson has flavor non-universal couplings to quarks. Finally, we discuss the possibilities of probing the chiral structure of a new color-octet vector boson.

ACKNOWLEDGMENTS

The road to the end of the first step of a long adventure in high-energy physics has been positively challenging and my journey has been full of pleasure and joy. While only my name appears on the end product, this thesis, it is actually a result of contributions from a great many people. Without influences and supports from others, either directly or indirectly, this would not have been possible. So I would like to mention some of them here.

A journey is a journey only if one could start. For this, I am greatly thankful to my dear parents, *Wasin* and *Passanee*, for their devotions and supports to make sure that I could follow the path of my interests.

Without the following medical doctors, several physical challenges might have derailed me along the way during the last decade. I am able to live upright thanks to *Prof. Wicharn Yingsakmongkol* who replaced a broken part of my spine. I am able to hear stereo thanks to *Doctor Andrea Palmieri* who helped me recover from not-so-partial hearing loss. I am able to use my right arm again thanks to *Doctor Andrew Schorfhaar* who repaired my torn shoulder tendon.

Now, in terms of education, past scientific advisors greatly contributed to many pivotal points. My deep gratitude goes to *Prof. Ahpisit Ungkitchanukit* and *Prof. Goran Senjanović*.

I also thank all the professors who helped me appreciate different layers of beauty in physics. At Michigan State University (MSU), I am particularly thankful to *Prof. Mark I. Dykman*, *Prof. Carl R. Schmidt*, and *Prof. Vladimir G. Zelevinsky*, with whom I have multiple wonderful experience in their classes. I also would like thank the first two professors, along with *Prof. Reinhard H. Schwienhorst*, for serving as committee members of the thesis.

A great amount of physics appreciations happened outside classrooms. I will not forget a series of "dinner discussions" back there in Thailand led by *Prof. Rujikorn Dhanawittayapol* and "lunch discussions" at MSU led by *Prof. Chien-Peng "C.-P." Yuan*.

I would like to extend my gratitude to past and current members of the theory group for interesting and friendly discussions: *Dr. Arsham Farzinnia*, *Dr. Chiu Man Ho*, *Joshua Isaacson*, *Dr. Vikram Rentala*, *Dr. Natascia Vignaroli*, *Dr. Devin Walker*, *Dr. Jiang-Hao Yu*. Many thanks also go to Josh for his feedbacks on the introduction of the thesis.

This thesis is based on a set of collaborative works. For that, I am deeply grateful to all my collaborators, particularly *Dr. Anupama Atre* and *Dr. Jing Ren* for their significant contributions to both the works and my education.

Financial support played an important role during decisive moments. I was fully supported during the first five years at MSU from a government-funded program called *the Development and Promotion of Science and Technology talents project (DPST)*, Thailand. Thus, I am deeply grateful to the people of Thailand for giving me this rare opportunity.

My life in the Department of Physics has been good. I am grateful to *Brenda Wenzlick*, *Debby Barratt* and *Kim Crossland* for their kind assistances throughout the years.

My life outside the Department has also been good. I am indebted to a great atmosphere my friends in the *Thai community* have created.

My life everywhere inside this planet has always been wonderful once it is shared extensively with *Jaruswan Warakanont* years ago.

Above all, I very deeply appreciate a complete package of opportunity, support, and care that I have been receiving from my advisors, *Prof. R. Sekhar Chivukula* and *Prof. Elizabeth H. Simmons*, who have also taught me well what "infinity" meant through their patience. It has been a great privilege working with both of you.

TABLE OF CONTENTS

LIST OF TABLES

LIST OF FIGURES

Chapter 1

Introduction

The Standard Model (SM) is a well-established theory describing particle physics. Simple and beautiful as it is, the model is considered phenomenologically incomplete and theoretically unsatisfactory. Various types of "new physics" beyond the Standard Model have been proposed. This thesis was written during the time when the Large Hadron Collider (LHC), hosting experiments that could potentially confirm or exclude various new physics models, had finished its first phase of operation. It focuses on two phenomenological aspects of new physics: implications of the data from the LHC on models explaining the electroweak symmetry breaking via strong dynamics, and the future-LHC prospects for characterizing a new massive vector boson which is a common prediction of new physics models.

In section 1.1, I give an overview of the Standard Model and its problems, focusing on the aspects related to electroweak symmetry breaking. Then, in Section 1.2, I present an overview of the theories based on strong dynamics that are relevant to this thesis. I briefly discuss the issues these theories address and the features they add. Finally, Section 1.3 illustrates where the works [1, 3, 4, 6, 7] to which my collaborators and I contributed stand in the field.

1.1 Particle Physics and the Standard Model

The ultimate goal of particle physics is to understand, at the most fundamental level, particles and their interactions describing the observed picture of the universe with a set of, hopefully, simple laws. The modern picture of the subject has been developed immensely during the past century, thanks to the healthy interplays between advances in various aspects of theoretical ideas and experiments. Let us begin this section with the theoretical idea that has become established as a well-tested theory.

Successful theoretical development has been achieved via a prescription of quantum field theory, where an elementary particle is regarded as an excited state of a quantum field. This follows the pioneering interacting theory of this sort: Quantum Electrodynamics (QED) [8, 9, 10, 11, 12], where the electromagnetic interaction between charged particles is explained by the quantum version of the so-called gauge theory. In a gauge theory, one requires that physical phenomena are equally well described by any member of a class of matter fields that are related by a continuous group of spacetime-dependent (*i.e.*, local) transformations called a gauge transformation. Doing so not only implies the existence of a gauge field, but also constrains its interactions to be determined by the Lie group describing the symmetry transformations. The gauge field's quanta are called gauge bosons. A quantum gauge theory (in four dimensions) possesses a feature of making consistent predictions to arbitrarily small length scales in terms of a finite number of parameters as long as the theory remains perturbative. In other words, a finite number of measurements of its parameters at a particular length scale uniquely determines its predictions at any other scale. This property, called "renormalizability", while not being an absolute necessity, is a much-desired feature in a model attempting to be the ultimate theory.

The current experimentally-accepted theory of particle physics that has been developed along these lines is referred to as the "Standard Model"[1] [13, 14, 15]. It is a renormalizable gauge theory [16] describing physical processes, governed by all known fundamental interactions (except gravity) relevant below subatomic length scales. In the Standard Model, matter particles — the quarks and the leptons — are grouped according to their interactions into three generations that are identical in most aspects apart from their masses. The matter contents are illustrated in Table 1.1. The interactions between the particles are classified into two sectors: strong and electroweak.

The strong sector utilizes a non-Abelian gauge invariance under an $SU(3)$ group [18] to describe the strong nuclear interaction. The underlying theory is known as quantum chromodynamics (QCD) [19, 20]. A striking feature that sets it apart from QED[2] is that the non-Abelian nature of QCD implies that the charge of the interaction, called color, is carried by both the matter particles (the quarks) and the gauge mediators, called gluons. Its properties are shown in Table 1.2. Therefore, unlike the photon, the gluons also interact directly among themselves. This leads to several interesting phenomena. First, in contrast to what happens in QED, the gluon-gluon interactions turn out to cause the coupling strength to be *smaller* when probing to smaller length scales. This feature, known as *asymptotic freedom* [21, 22], allows the theory to sensibly describe strong interactions at small distances as a perturbation theory. Second, this means at a certain finite length scale — around $\mathcal{O}(10^{-15}\,\mathrm{m})$ or equivalently the energy scale $\Lambda_{\mathrm{QCD}} \sim \mathcal{O}(200\,\mathrm{MeV})$ — the coupling becomes so large that the perturbative method completely stops making sense. In other words, QCD has a dimensional scale built in [23]! Third, this leads to an experimentally verified

[1] A partial review of the Standard Model is presented in Appendix A.

[2] In QED, photons do not interact among themselves. This leads to the phenomenon that strength of QED interaction increases with decreasing distance.

Table 1.1: Fermions of the Standard Model are categorized into two classes: quarks and leptons (top and bottom entries, respectively). Both classes are subdivided into 3 generations (columns labeled I, II, and III) which are identical apart from the different masses of the members of each generation. Properties of the particles are taken from [17].

		I	II	III
Quarks	name symbol charge mass	**up** u $+2/3$ 2.3 MeV	**charm** c $+2/3$ 1.28 GeV	**top** t $+2/3$ 173 GeV
		down d $-1/3$ 4.8 MeV	**strange** s $-1/3$ 95 MeV	**bottom** b $-1/3$ 4.18 GeV
Leptons		**electron** e -1 0.511 MeV	**muon** μ -1 105.7 MeV	**tau** τ -1 1.77 GeV
		electron neutrino ν_e 0 $\mathcal{O}$(eV)	**muon neutrino** ν_μ 0 $\mathcal{O}$(eV)	**tau neutrino** ν_τ 0 $\mathcal{O}$(eV)

Table 1.2: Bosons of the Standard Model: the gauge bosons (top panel) and the Higgs (bottom panel). Properties of the particles are taken from [17].

		photon (γ)	gluon	Z boson	W boson
Gauge Bosons	symbol	γ	g	Z^0	$W^{\pm}$
	charge	$< 10^{-35}$	0	0	± 1
	mass	$< 10^{-18}$eV	0	91.19 GeV	80.4 GeV

Higgs Boson
h or H
0
126 GeV

conjecture that at length scales greater than Λ_{QCD}, only a "colorless" object is observed. This phenomenon is called *confinement*. These phenomena of QCD serve as principal ideas underpinning models considered in this thesis.

The electroweak sector uses a product gauge group $SU(2) \times U(1)$ to describe processes involving the electromagnetic and the weak nuclear interactions, with the typical length scale around $\mathcal{O}(10^{-18}\, m)$, the electroweak scale. Under the weak interaction, the two states describing fermions, the left- and right-handed chirality Dirac fermions, interact in a different fashion. Only a left-handed fermion carries the weak charge and can transform into another fermion belonging to the same representation of the $SU(2)$ symmetry group (*i.e.*, the same "generation", as shown in Table 1.1). This so-called charged current interaction is explained by the charged gauge bosons $W^{\pm}$. Together with the Z boson and the photon that govern neutral current phenomena, these four gauge bosons constitute the gauge mediators of the $SU(2) \times U(1)$ gauge theory.

The weak interaction exhibits several interesting phenomena. First, unlike the electromagnetic interaction whose range spans infinitely, its subatomically short range means that the gauge bosons are massive. However, a prescription for describing a massive vector boson is not manifestly gauge invariant. Second, only the symmetry of electrodynamics remains exact at large length scales. The electroweak symmetry $SU(2) \times U(1)$ corresponding to the unified interaction has to be hidden or broken. A spontaneously hidden symmetry would have implied an unobserved massless scalar particle called a Nambu-Goldstone boson (NGB) remaining in the physical spectrum if the symmetry were global [24, 25, 26]. Third, non-zero mass of fermions also implies that the electroweak symmetry is hidden at length scales above the electroweak scale. This is because the mass of a fermion field is explained by a coupling between the left- and right-handed chirality fields, which carry different gauge charges; hence violating the gauge invariance.

The massiveness of a gauge field and the spontaneous hidden of a local symmetry turn out to be related to each other under a prescription known as the "BEH mechanism" — for Brout, Englert, and Higgs (the firsts, among many, of its pioneers) [27, 28, 29, 30, 31]. This can be understood as follows. When the hidden symmetry is local, the NGBs are no longer physical and can be gauge transformed away from the spectrum: becoming the longitudinal degrees of freedom of the gauge field and making the gauge field massive. Roughly speaking, the vacuum of quantum field theory is not empty, but is filled with an agent that has a non-zero averaged field structure preserving only a subset of the full symmetry group describing the interaction. Particles interacting with this field then have "effective mass". This agent can be either an additional elementary scalar field or a composite object consisting of other elementary particles that interact strongly at smaller length scales. The Standard Model is constructed using the fundamental scalar field option. This has an additional benefit of explaining the fermion masses via an interaction between the fermion bilinear and the scalar field with the right quantum number. I will focus on reviewing the Standard Model for now and will discuss the latter approach in Section 1.2.

In the SM, electroweak symmetry breaking is realized via the BEH mechanism featuring additional fundamental scalar fields in a doublet representation of $SU(2)$ [14]. This doublet is usually referred to as the Higgs field. It is *assumed* that the field develops a non-zero vacuum expectation value that respects only the electromagnetic gauge group. As mentioned above, the doublet structure of the Higgs is also convenient for the fermion sector. The mass of a fermion can be introduced into the Lagrangian via the Yukawa interaction of the left- and right-handed chiralities of the fermion with the Higgs doublet. Constructed in this manner, the Standard Model is renormalizable [16].

The implementation of the fundamental scalar doublet also predicts an additional elementary scalar particle, a particle whose existence has no previous example in nature, as an excitation of the Higgs field. This particle is known as the Higgs boson. It leads to unique experimental features of the Standard Model. First, while the Higgs is produced from and decays to various states, the characteristics of its production and decay (production cross section, and decay branching ratios) depend only on the mass of the Higgs! Second, the doublet structure of the Higgs field implies a particular ratio between the masses of W and Z [32] (or the ratio between isospin-triplet charged and neutral current interactions at zero momentum). This ratio is generally not guaranteed in other models but the one predicted by the Standard Model agrees well with experiments [17]. It is explained by an accidental global $SU(2)$ symmetry, called the custodial symmetry, respected by the interaction of the Higgs doublet. The custodial symmetry is broken by unequal electromagnetic charges and the unequal masses of the fermions within an $SU(2)$ doublet. This leads to small deviations of the ratio from the predicted value at leading order. These unique features, along with others, provide definite experimental tests of the model.

Experiments have been playing vital roles in developing and verifying the Standard Model, particularly to see the origin of electroweak symmetry breaking (or at least where to look further). Of particular importance are particle accelerators that collide well-controlled beams with one another; they are called colliders. Unlike accelerators that direct a beam into a fixed target, colliders allow all of the beam energy to be used for production of elementary particles. Various kinds of colliding beams have been used: from the electron-positron collider at the "Organisation européenne pour la recherche nucléaire"[3] (CERN) known as "Large Electron-Positron collider" (LEP), to the Fermi National Laboratory (Fermilab) proton-antiproton collider named the Tevatron, to the current CERN's proton-proton collider called the "Large Hadron Collider" (LHC). The latter started its operation in 2009, achieved the goal for the first run of center-of-mass energy of 7 TeV in 2011, and 8 TeV in 2012, and eventually finished the run in 2012. It will resume operation at 13 TeV in 2015 and will eventually be operating at its designed center-of-mass energy of 14 TeV. Analyses of existing data have been taken care of by various collaborations including the ATLAS (A Toroidal LHC Apparatus) [33, 34] and CMS (Compact Muon Solenoid) [35, 36].

These accelerators and the collaborations working with them have contributed to notable recent discoveries in particle physics. They include the weak gauge bosons in 1983 [37, 38, 39], the unusually heavy top quark in 1995 [40, 41], and eventually the the τ neutrino in 2000 [42]. The latter completely established the physical existence of the Standard Model's fermion and gauge contents. In addition to making the discoveries, some of these experiments also contributed to measuring certain observables to unprecedented precision to uncover any deviations from the Standard Model's predictions. They are referred to as "precision electroweak tests" (See, for example, [43]). While the Standard Model has been surviving

[3] Previously, "Conseil Européen pour la Recherche Nucléaire".

well enough under these tests, there have also been some indications of room for small deviations.

Along with the aforementioned discoveries and measurements, one of the primary goals for pushing towards “the next accelerator” during the past three decades had been to look for the Higgs boson. The Higgs hunting lasted until the 4^{th} of July 2012, the day the ATLAS and CMS collaborations announced the observation of a particle having properties that are consistent with the Higgs boson of the Standard Model [44, 45]. Following the discovery, a natural next step is to inspect the new state in detail. Is it actually a scalar or a pseudoscalar? Are the couplings (hence branching fraction of its decays to various channels) in agreement with the Standard Model predictions? Does it have any partner states not predicted by the Standard Model such as a charged one? So far, to the present precision, it appears to be “the Higgs” of the SM [46, 47, 48, 49, 50, 51, 52, 53]. However, there are reasons suggesting that this does not need to be the case when the Higgs is probed to better precision.

The question whether the recently discovered particle actually is the Higgs boson of the Standard Model stems from the reason that the Standard Model itself is regarded as incomplete. The needs for a new physics model can be illustrated from both phenomenological and theoretical points of view.

Phenomenologically, the need for a new physics model is clear. The Standard Model is unable to cope with several experimentally established facts. As the ideas and the evidence of massive neutrinos [54, 55, 56] were not established when the Standard Model was proposed, neutrinos were assumed to be massless — we know this assumption is no longer valid. The Standard Model does not account for the existence of the enigmatic constituents inferred from cosmology known as Dark Matter and Dark Energy (see, for example, [57, 58, 59, 60, 61]) — these two are not unsubstantial!. In addition, while matter and anti-matter feature in the SM, the model does not explain why the majority of the observable universe consists of matter. Last but not least, what about gravity?

Theoretically, the Standard Model accounts for several descriptions in an unsatisfying manner. For example, electroweak symmetry breaking is assumed without any explanation of underlying dynamics. In addition, the renormalizability of the model itself could cause an issue. It allows one to extrapolate the model to arbitrary smaller length scales inaccessible by current experiments; *i.e.*, going across the "desert" between the electroweak symmetry breaking scale $\mathcal{O}(10^{-18}\,m)$ down to the Planck scale $\mathcal{O}(10^{-35}\,m)$, for gravity, if one assumes no new physics showing up in between. This poses a problem, known as "naturalness" problem, for a theory with an elementary scalar.

A theory is considered natural if macroscopic phenomena are not explained by a set of excessively carefully adjusted parameters of microscopic physics working at a much smaller length scale. In particle physics, the consensus is that the smallness of a parameter at a certain scale is acceptable only if its smallness is viewed as a result of an enhanced exact symmetry had the parameter vanished[4]. For example, fermion masses of $\mathcal{O}(\text{eV} - \text{GeV})$ or gauge boson masses of $\mathcal{O}(\text{GeV})$ can be naturally small (compared to the Planck scale) because their disappearances would have led to a chiral symmetry and a gauge symmetry, respectively. These symmetries also do protect the masses from being large in the calculations including quantum effects. A theory with a fundamental scalar field, however, does not typically have this feature of "naturalness" [62].

There is no symmetry restored upon having a scalar's mass set to zero. Then quantum corrections in that particular theory would drive its mass to the largest mass scale of the

[4] Note that this naturalness argument is for a model construction point of view. On a physical point of view, one does not say that the mass of a fermion is small because of chiral symmetry. But one rather says, the smallness mass of a fermion implies that chiral symmetry is only approximate.

theory unless unnaturally fine cancellations between the theory's parameters occurred. For the Standard Model [63], that mass scale is the Planck scale and the cancellations would have to be of $\mathcal{O}(10^{-32})$ if the particle at 126 GeV is the fundamental scalar predicted by the model. In other words, according to this naturalness guideline, the Standard Model is not a natural theory describing the recently-discovered scalar particle with mass 126 GeV [64, 65]. If the argument is taken seriously, although it is important to stress that this need not be so, models addressing the naturalness issue usually predict new physics appearing around a TeV energy scale. Coincidentally, there is another clue leading to the TeV scale as the arena one expects to learn more about the electroweak symmetry breaking or new physics model.

The TeV energy scale is actually a "built-in" feature of the SM. In a standard-model-like theory without a scalar field that couples like the Higgs, the tree-level amplitudes for longitudinal W^+W^- scattering ($WW \to WW$) violate unitarity around ~ 1 TeV [66]. This means either the W and Z interactions become strongly coupled or a sub-TeV particle capable of canceling out the dangerous effect shows up — or both. Now the sub-TeV particle has recently been discovered. In the case that the particle is actually the Standard Model Higgs boson, new physics at the TeV scale is no longer guaranteed unless one takes the naturalness argument seriously.

So far, apart from having discovered a particle that might behave like the Higgs of the Standard Model, the LHC has not yet found a clue to what kind of new physics is preferred by nature. But after all, we expect that a new physics model is out there somewhere. So while we wait (and hope) for the near-future experiments to shed light on what the model viable for explaining new physics looks like, it is worthwhile to see what the current data "tell" us about some of those models, and what we could do if something is found from the near-future data.

1.2 Going Dynamically Beyond the Standard Model

From the aspect of the agent of electroweak symmetry breaking and the naturalness issue, one can classify the paths beyond the Standard Model to two major directions: more fundamental scalars and no fundamental scalar. Each has its own merits. The "more fundamental scalars" path includes Supersymmetry (SUSY), where an additional mechanism is introduced to stabilize the hierarchy. Among many benefits, it could provide a unified picture of strong and electroweak interactions [67, 68, 69] and stands as an essential part of other branches of new physics such as string theory (see, for example, [70, 71, 72, 73]). The "no fundamental scalars" path is based on theories with symmetries broken dynamically, where a composite particle plays the role of the Higgs boson. This picture is motivated by the superconductor theory in condensed matter physics — by Bardeen, Coopers, and Schrieffer (BCS) [74, 75] — and has been brought to particle physics by Nambu and Jona-Lasinio [76, 77]. In the BCS theory, a symmetry is broken dynamically by the formation of a condensate due to interactions among electrons, making the photon massive. In this thesis, we focus on models transplanting this idea into the beyond-the-Standard-Model physics. To introduce the idea, let us begin by considering a well-studied example of dynamical symmetry breaking in the regime of low-energy phenomena of QCD. This will illustrate how the electroweak gauge bosons could become massive without the existence of a fundamental scalar in the theory.

Dynamical symmetry breaking is implemented to QCD under the context of chiral symmetry breaking in the presence of electroweak interaction. Without the electroweak interaction, the chiral symmetry breaking works as follows. The intrinsic energy scale of QCD, $\Lambda_{\text{QCD}} \sim \mathcal{O}(200\,\text{MeV})$ [23], is large enough to consider the up and down quarks as approximately massless. This means their left- and right-handed degrees of freedom transform independently under unitary transformations. In the exact massless limit, this exhibits an $SU(2)_L \times SU(2)_R$ global chiral symmetry. Interestingly, this symmetry is hidden even in this massless quark limit. At energy scales lower (or length scales larger) than the confinement scale Λ_{QCD}, the attractive interaction for color singlet states leads to a Lorentz-invariant bound state $\bar{u}_L u_R$ of a quark and an antiquark with opposite chiralities. It has non-zero vacuum expectation value of this bound state $\langle 0|\bar{u}_L u_R|0\rangle = \langle 0|\bar{d}_L d_R|0\rangle \sim \Lambda^3_{\text{QCD}}$ (where $|0\rangle$ is a hadronless ground state), called a *condensate*. The condensate is no longer invariant under the chiral transformation, while still it respects the vectorial symmetry $SU(2)_{L+R}$ (where both left- and right-handed fields transform in the same way). So there exists an $SU(2)$-triplet of massless Nambu-Goldstone bosons of the chiral symmetry breaking and these are interpreted as the pions of QCD[5].

What is interesting for our purposes is that the left- and right-handed chirality quarks that form the condensate carry different charges under the electroweak group. The left-handed ones "feel" the $SU(2)_L$ (now the weak gauge group), while the right-handed "feel" the $U(1)_Y$ hypercharge subgroup of the $SU(2)_R$. So the condensate's formation breaks the electroweak symmetry, and the pattern of electroweak symmetry breaking is indeed $SU(2)_L \times U(1)_Y \to U(1)_{\text{em}}$. The Nambu-Goldstone bosons interact with the gauge currents of electroweak interactions and become the longitudinal degrees of freedom of the W and Z, making them massive. Electroweak symmetry breaking by condensates provides additional benefits. The ratio of the W and Z masses also turns out to be correct thanks to the $SU(2)_{L+R}$ global symmetry which is still respected by the condensates. The unitarity behavior at energy large (energy) scales of the model (for processes such as the WW scattering) is taken care

[5]Pions are not exactly massless, but have small masses compared to the hadronic scale. This means that the chiral symmetry is only approximate. They are referred to as Pseudo-Nambu-Goldstone Bosons (PNGB).

of by composite resonances. Perhaps most interestingly, the intrinsic energy scale of QCD, which could be far below from the scale above which new physics appear, means there is no naturalness problem.

QCD, nevertheless, is not a suitable candidate for fully explaining electroweak symmetry breaking as it accounts for only a small fraction of the mass of the gauge bosons; *i.e.*, $\mathcal{O}(\Lambda_{\text{QCD}}) \sim 200\,\text{MeV}$ — many orders of magnitude too small! This is expected, as QCD becomes strong at energy scales much lower than the electroweak symmetry breaking scale. A new source of strong interaction with much higher intrinsic energy scale is needed.

A model describing electroweak symmetry breaking via strong dynamics utilizes new QCD-like interactions to explain the $\mathcal{O}(100\,\text{GeV})$ masses of the electroweak gauge bosons. This class of models is known as Technicolor (TC) [78, 79, 80]. Its earlier versions are essentially a scaled-up version of QCD where the new strong interaction governed by a $SU(N_{\text{TC}})$ gauge theory are experienced by a set of N_{Tf} flavors of new massless fermions called technifermions, $T = \{U, D, \ldots\}$. Similar to what happened in QCD, the simplest realization requires a doublet of technifermions so the $SU(2)$ chiral symmetry is exhibited, and then hidden spontaneously by the presence of a condensate $\langle 0|\bar{U}_L U_R|0\rangle$ (and similarly for other technifermions). The resulting Nambu-Goldstone bosons are called the technipions. Once coupled with the electroweak interaction, they will be the main source[6] of the W and Z masses provided that the energy scale of technicolor Λ_{TC} is large enough. The structure of a model determines how large this scale has to be. A larger number of technifermion doublets, say N_D, leads to a greater contribution to the gauge bosons' masses (by a factor of $\sqrt{N_D}$). A larger gauge group for Technicolor interaction (larger N_{TC}) also means an enhancement to the gauge bosons' masses (also by a factor of $\sqrt{N_{\text{TC}}}$). This means the scale of Technicolor

[6]The quark condensate of QCD still provides masses of the gauge boson, but to a much less extent.

could be $\sim \mathcal{O}(\mathrm{TeV})$. As simple and elegant as it may appear, this basic Technicolor scenario does not explain the origins of the masses of the fermions.

The masses and the mixings of quarks and leptons require an additional mechanism to transfer the effect of the technifermion condensate to the Standard Model fermion fields. At energies far below the scale above which new physics responsible for the interaction takes over, the non-renormalizable effective interaction appears as an apparent "four-fermion" interaction (suppressed by the mass scale of that interaction). A class of models that handles this by coupling these fields to the Technicolor currents via an additional interaction at higher energies is called *Extended Technicolor* (ETC) [81, 82].

ETC is a gauge theory having a gauge group G_{ETC} that contains technicolor and flavor as sub-groups. The Standard Model fermions and technifermions are in the same irreducible representation of this group so they interact via an ETC gauge-boson exchange. The group G_{ETC} is assumed to be spontaneously hidden at high energies, the size of the mass M_{ETC} of the ETC-gauge bosons. At energies low compared to M_{ETC}, this interaction manifests as a "four-fermion" interaction $(\bar{q}T)(\bar{T}q)/M^2_{\mathrm{ETC}}$. A technifermion condensate formed via technicolor interactions then induces the operator $\bar{q}q\langle\bar{T}T\rangle_{\mathrm{ETC}}/M^2_{\mathrm{ETC}}$. Masses of the fermions (and other observables) at low energies are obtained by renormalization group running of the interaction down from M_{ETC}, where the value of the condensate is evaluated. Given that Technicolor behaves as a scaled-up version of QCD where the coupling decreases very quickly as energy increases, there is approximately no enhancement of the value of the condensate when running from Λ_{TC} to M_{ETC}. This means $\langle\bar{T}T\rangle_{\mathrm{ETC}} \sim \langle\bar{T}T\rangle_{\mathrm{TC}} \sim \Lambda^3_{\mathrm{TC}}$; hence, $m_f \sim \Lambda^3_{\mathrm{TC}}/M^2_{\mathrm{ETC}}$. In addition, each fermion requires its own ETC scale. Heavy fermions such as the tau, charm, bottom, and especially the top demands low scale M_{ETC} — the top with $m_t = 175\,\mathrm{GeV}$ implies a very small $M_{\mathrm{ETC}} \sim m_t$ as $\Lambda_{\mathrm{TC}} \sim v \sim m_t$. This is a defining feature of the model: unlike the Standard Model where flavors are treated as free parameters, ETC models deal with flavor physics dynamically.

There is a cost for a model attempting to explain both mass generation and flavor physics. The fermion-technifermion interaction that is introduced to give mass to the Standard Model fermions must also allow a generation-changing interaction between fermions. In ETC models, various scales of the M_{ETC} are required for the theory to account for the wide range of fermion masses. This is problematic as an interaction such as $(\bar{d}s)(\bar{d}s)/M_{\mathrm{ETC}}^2$ which leads to the highly constrained flavor-changing neutral current (FCNC) phenomena is also present in ETC models [83]. The values of M_{ETC} that account for the correct fermion masses could give rise to FCNC effects larger than what have been observed in experiments. Current bounds from FCNC observables such as those from neutral kaons $(K_L - K_S)$ mass difference are very stringent [17] and require that $M_{\mathrm{ETC}} > \mathcal{O}(10 - 100\,\mathrm{TeV})$, a range of values much larger than what is required to generate even the mass of the strange and charm quarks!

The flavor problem of ETC models arises because the theory becomes asymptotically free with increasing energy above TC scale quickly the way QCD does. The evolution of couplings eventually affects how the fermion condensate changes via what is called the anomalous dimension for the technifermion mass operator. To deal with this problem, a class of models where the coupling decreases very slowly with increasing energy called Walking Technicolor (WTC) have been proposed [84, 85, 86, 87, 88, 89]. The slow evolution of the coupling is achieved by having more technifermions to enhance the "screening effect". This in turn enhances the value of the technifermion condensate evaluated at the M_{ETC} scale. A larger fermion mass is then possible before the flavor problem re-emerges. In short, viable extended Technicolor models cannot be a scaled-up version of QCD and have to have structure leading to walking. Unfortunately, the idea of walking is still not sufficient to deal with the third generation [90].

The third generation is special. On the one hand, it contains the fermion that couples to the electroweak symmetry breaking much more strongly than the others: the top quark. It requires an (walking) ETC scale so low that it is even too close to the TC scale for comfort. This would invalidate the picture of "low-energy" contact interaction that is used to explain the mass of the other fermions. On the other hand, as the bottom quark's mass is $\sim 4\,\mathrm{GeV}$, the mechanism explaining the mass of the top must also exhibits larger weak isospin violation compared to the other generations [91]. As the violation of weak isospin is constrained by precision electroweak experiments, the isospin violating effect must be suppressed by a high ETC scale. But then that scale is too high to produces the top quark mass. So, should the top quark be treated in the same manner as other quarks after all?

The intimate relationship between the top quark and electroweak symmetry breaking suggests that perhaps the top plays a special role [92, 93, 94, 95, 96, 97]. In other words, the top, rather than the technifermions, could form a condensate itself via a new strong isospin-symmetric interaction in an extended strong sector. To prevent the bottom from also forming a condensate, another isospin-violation interaction is introduced, which could be either weak or strong. The new symmetries corresponding to both the extended strong sector and the isospin-violation sector do not manifest at low energies, implying the existence of new massive gauge bosons. A class of models describing the mechanism for this condensate to form is known as "Topcolor".

In the minimal topcolor model [98], one introduces two isospin-symmetric strong interaction groups and two "hypercharge" groups. The third-generation quarks are charged under one $SU(3)$ group where the rest are charged under the other $SU(3)$ group. Similar assignments apply for the two $U(1)$ groups with specific conditions ensuring the bottoms do not form a condensate. The pattern of symmetry breaking $SU(3)_1 \times SU(3)_2 \times U(1)_1 \times U(1)_2 \to SU(3)_C \times U(1)_Y$ means there will be nine new massive gauge bosons. One set is color octet, which is referred to collectively as colorons (or topgluons in some of the literature). The other is a color singlet to which we refer generically as a Z'. Still, Topcolor is not a viable model by itself. It was found that Topcolor implemented this way either requires a mass for the top quark $\sim \mathcal{O}(500 - 1000\,\text{GeV})$, or requires a significant amount of fine tuning $\Lambda_t/m_t \gg 1$, which could also mean it provides a weak scale (hence masses of the weak gauge bosons) that is slightly too low [99]. These issues can be addressed in two ways. One is incorporating Extended Technicolor to supply the missing part of the weak scale. Another is introducing an electroweak iso-singlet quark to help the top "supply" the EWSB and still have the observed mass, so that we might not need technicolor at all.

Topcolor-assisted Technicolor (TC^2 or TC2) is a model proposed to utilize the good parts of both technicolor and topcolor [99, 100, 101, 102, 103, 104]. Electroweak symmetry is hidden mainly by the technifermion condensate while the third generation is mainly taken care of by Topcolor in the ways introduced in the previous paragraph. TC2 is rich in phenomenology without being too complicated at low energies. Having two sources of dynamical electroweak symmetry breaking means there are two sets of iso-triplet Nambu-Goldstone Bosons. One set of the triplets becomes the longitudinal parts of the W and Z while the orthogonal set survives in the spectrum. The members of the latter, known as the top-pions, couple only (*i.e.*, at leading order) to the quarks in the third generation. There could also be a composite scalar degree of freedom orthogonal to the neutral top-pion state, known as the top-Higgs.

The alternative top-condensate model does not need Technicolor. Top-Seesaw [105, 106, 107] is a model where the electroweak symmetry is broken by a top condensate, formed via

Topcolor interaction, in the presence of an electroweak isosinglet vectorlike quark (usually denoted as χ) that mixes with the top. The mixing is arranged in such a way that the heaviness of this extra quark results in a mass for the top that agrees with experiment. Being an isospin singlet, the χ can generally be introduced in a manner that does not spoil various aspects of results from precision electroweak experiments. In this case, the top-Higgs is a bound state of the top and the even heavier χ.

In the next section of this chapter, I will discuss the task of realizing the neutral top-pion or the top-Higgs in either of the top-condensate models as the recently-discovered 126 GeV particle, which is a chapter in this thesis on its own. Until then, I present an overview of how quantitative predictions from models with strong dynamics are carried out.

The models introduced so far present qualitative pictures of strong dynamics while actual calculations (and predictions!) could be anything but trivial. Knowledge of the non-perturbative dynamics required for doing such calculations is gradually being established through lattice gauge theory calculations. Nevertheless, quantitative predictions can be achieved in approximate models with sensible assumptions motivated by QCD and experiments. Typically, these models are constructed as a low-energy effective theory, which captures mainly the low-energy degrees of freedom of interest at energy scales accessible to experiment while systematically including only the leading indirect impacts of the majority of the degrees of freedom that are too massive to actually be produced at those energy scales. In the context of dynamical symmetry breaking, one uses an effective theory that focuses on the scalar sector of the model. It is characterized mainly by parameters relevant to the strong-top sector; namely, the masses of the top-pions and top-Higgs, and the fraction of the contribution of the strong-top dynamics to the mechanism of electroweak symmetry breaking. The rest of this section discusses an approximate model for describing the generation of the condensate dynamically.

The low-energy effective model describing the top quark sector in the presence of a separate mechanism responsible for generating electroweak symmetry breaking is constructed based on a minimal model called the Higgsless model [108, 109, 110, 111, 112, 113, 114, 115, 116]. The Higgsless model utilizes the AdS-CFT correspondence [73, 72, 117] between a strongly-interacting four-dimensional theory (parts of which we do not know how to calculate perturbatively) to a weakly-interacting five-dimensional gauge theory (where calculations can be done). The presence of the extra dimension is suppressed as it decouples from low-energy physics via compactification. While the details on extra-dimension inspired theories are beyond the scope of this thesis, here are some typical features of this type of extra dimension models as follow: First, electroweak symmetry is broken by boundary conditions in the extra-dimension. Second, the onset of unitarity violation within W and Z scattering is delayed by contributions arising from exchange of tower of Kaluza-Klein (KK) gauge bosons. Third, electroweak precision constraints can be satisfied by feeding the fermions their electroweak properties through multiple gauge groups located at different "sites" in the extra dimension. Chivukula *et al.* [118] found that the minimal model featuring these properties combines an extended electroweak gauge group $SU(2) \times SU(2) \times U(1)$ with the Standard Model color group. The symmetry breaking of the extended electroweak group to $U(1)_{\mathrm{EM}}$ is governed by two non-linear sigma model fields $\frac{SU(2)\times SU(2)}{SU(2)}$; each connects the gauge group at the "middle site" to one at an "outer site"[7] on the boundary of the extra dimension. The dual picture of this "three-site" Higgsless model is a model describing dynamical symmetry breaking.

Based on the three-site model, a model called the "top-triangle moose" (TTM) was intro-

[7] So the non-linear sigma model is $SU(2) \times SU(2) \times SU(2)$.

duced by Chivukula *et al.* [119] to consistently focus on the low-energy behavior of models featuring separate sectors for top mass generation and electroweak symmetry breaking (*i.e.*, mass generation of other particles). The low-energy phenomenology is still captured by a three-site gauge group conventionally arranged as $SU(2)_0 \times SU(2)_1 \times U(1)_2$. The symmetry breaking patterns $SU(2)_0 \times SU(2)_1 \to SU(2)$ and $SU(2)_1 \times U(1)_2 \to U(1)$ are governed by the non-linear sigma fields presented in the three-site model. The TTM extends the scope of the three-site model to incorporate strong top dynamics by introducing a top-Higgs field connecting the "outer sites" $SU(2)_0$ and $U(1)_2$. This top-Higgs field is an $SU(2)$ doublet field corresponding to the low-energy picture of the bound-states of t and b. The electroweak symmetry is broken by both the non-linear sigma model and the top-Higgs fields. The top-pions arise as a triplet orthogonal to the would-be Nambu-Goldstone bosons "eaten" by the Standard Model W and Z, while the top-Higgs state remains in the spectrum.

The most interesting feature of the top-triangle moose model is the observation that different points in its parameter space correspond to different strong-top dynamics models. It serves as a low-energy effective theory for a TC2 model in the region where the contribution from strong-top dynamics to electroweak symmetry breaking and the mass of the top-Higgs are both relatively small. It also serves as a low-energy effective theory for top-seesaw assisted technicolor when the top-dynamics contribution to electroweak symmetry breaking is relatively large (due to the seesaw partner of top) and the top-Higgs are massive, $\mathcal{O}(2m_t)$ as seen in the previous paragraphs. This property makes the top-triangle moose model versatile in describing the scalar sector of low-energy strong-dynamics models where only the top-pions and the top-Higgs are present. An overview of the implications of LHC constraints on models with strong-top dynamics obtained by studying this model will be discussed in the next section.

1.3 Phenomenology, the LHC, and this Thesis

The LHC has done much more than discovering the 126 GeV-particle having properties resemble the "standard Higgs". Higgs boson property measurements that have been carried out by the collaborations at the LHC [46, 47, 48, 49, 50, 51, 52, 53, 120] can be used as a guide to directly and indirectly probe for viable new physics models. After all, the experiments at the LHC can be considered just started, with the 8 TeV program ended in 2012. The physics program resumes at 13 TeV in 2015. Then, the LHC will eventually go through a long-run period of high luminosity at 14 TeV. That is the period one can safely expect a large abundance of TeV-scale related events and sees whether they are pointing to any new physics.

This thesis is organized into two parts which are roughly summarized as follow:

- What are the implications from the data available at the time of writing on theories with strong dynamics?
- What can one do if a new vector resonance, one of the key predictions of these kinds of model or others, is discovered in the near future?

In short, Part I of this thesis is dedicated to phenomenological implications from the LHC for both technicolor models and models with strong top dynamics. Part II provides the possibilities of characterizing color and chiral properties of a new massive vector resonances, which will typically appear in most new physics models, if they are discovered during the future run of the LHC at 14 TeV. The rest of this chapter provides an introduction to each part.

1.3.1 Part I: Phenomenology of Strong Dynamics

Technicolor models feature technipions as a result of global chiral symmetry breaking. While three of them are engineered to become the longitudinal degrees of freedom of the W and Z bosons through the BEH mechanism, models constructed with more than one technifermion doublets will result in a number of technipions' remaining in the spectrum. Various phenomenological reasons could lead to a model's having color-singlet, colored, or electroweak charged technipions. The electrically neutral technipion behaves like the Higgs in many ways. So analyses from the Higgs searches at colliders could be used to provide constraints on corresponding strong dynamics models.

The general strategy is that the current lack of evidence for the Higgs boson (or similar) of a particular mass in a particular decay channel will place an upper bound on the cross section for that mass and channel [121, 122, 123]. The bound can be translated directly for constraining the neutral technipion which shares the same kinematical properties as it is also a spin-0 particle. A variant of model that predicts much greater rates than the Standard Model Higgs will be greatly constrained. While analyses in this fashion have been carried out since the time of the LEP e^+e^- collider, the LHC has great advantages over LEP for studying several Technicolor models.

The LHC, being a hadron collider, could produce a copious amount of particles that have strong interactions; *i.e.*, carry color charges. This means that if there exists a technipion in a Technicolor model featuring colored technifermions, it will be produced in abundance, particularly by a gluon fusion via a colored-technifermion loop. As noted in a previous study on extracting the information from searches for a Higgs decaying to $\tau^+\tau^-$ and $\gamma\gamma$ by Alexander Belyaev, Alexander Blum, R. Sekhar Chivukula, and Elizabeth H. Simmons in [124] in 2005, the signal rates for these channels are expected to be enhanced in models featuring colored technifermions.

In 2011, about a year after the LHC began its Higgs hunting operation, R. Sekhar Chivukula, Elizabeth H. Simmons, Jing Ren, and I used data from ATLAS and CMS available at the time to provide a follow-up to that strategy in [1]. We found that the constraints on a large class of Technicolor predicting light technipions, in the mass range of $110-350\,\mathrm{GeV}$, are rather tight if the model has at least one of the following properties: (a) includes colored technifermions (b) s significant contributions from topcolor dynamics and (c) has Technicolor groups with three or more Technicolors ($N_{TC} \geq 3$). Thus, the work provides a set of guidelines for building a viable Technicolor model with colored technifermions that are not affected significantly by these constraints. Chapter 2 of Part I is based on this work.

Now, let us turn the attention to models featuring strong top dynamics in general — ones that might or might not involve colored technifermions. This is where the low-energy effective theory that captures all the essential properties of strong top dynamics — the top-triangle moose — could play a role. Recall that the scalar particles in this theory include both the scalar top-Higgs and the pseudoscalar top-pions. Key phenomena in the scalar sector are determined by masses of the top-Higgs and the top-pions, and the fraction of the contribution of top-color dynamics (along with technicolor) to the electroweak symmetry breaking. That fraction is usually denoted as the "mixing" $\sin\omega$. On the one hand, this fraction enhances the top-Higgs and top quark coupling; *i.e.*, by $1/\sin\omega$ (hence the production from gluon-fusion and the decays to gluon pairs by $1/\sin^2\omega$). On the other hand, it suppresses the production of top-Higgs and the Standard Model vector-boson pairs, WW and ZZ; *i.e.*, by $\sin\omega$ (hence the production from vector boson fusion and the decays to vector boson pairs by $\sin^2\omega$). The neutral top-pion, being a pseudoscalar, does not even have tree-level couplings to the

WW and the ZZ states. The couplings are possible only at the quantum level; *e.g.*, via a top quark loop.

The properties and the LHC search strategies of the scalar sector of various models with strong top dynamics via the top-triangle moose model was discussed by R. Sekhar Chivukula, Elizabeth H. Simmons, Baradhwaj Coleppa, Heather E. Logan, and Adam Martin in [125]. The authors also presented the implications of data from the Higgs searches, in the WW and ZZ decay channels, for the top-Higgs in [126]. It was found that the searches in these final states could pose a stringent bound on the top-Higgs, particularly when the top-pion is heavier than the top quark or when the strong top dynamics contributes substantially to EWSB. Specifically, a 150 GeV-top-pion would imply the exclusion of a top-Higgs with mass below 300 GeV. The top-pions themselves cannot be too light, particularly if they are degenerate, or the charged top-pions would have been the final states of the top quarks decays — and those processes are also well-constrained [127, 128]. In short, the date from 2011 already showed that it would be very challenging to explain a light Higgs-like particle with the top-Higgs state. The remaining candidate was then the neutral top-pion.

Near the mid-2012, there was an indication of a “Higgs-like” signature with mass 126 GeV observed at the LHC by the ATLAS and CMS collaborations. At the time, the evidence for the new state was larger than what to be expected from the Standard Model Higgs in the di-photon and ZZ^* (to four charged leptons) channels, and moderate for the WW^* channel. The data for the di-tau and bottom-pair final states were inconclusive. My colleagues — Sekhar Chivukula, Baradhwaj Coleppa, Heather Logan, Adam Martin, Jing Ren, Elizabeth Simmons — and I used the top-triangle moose model to find the range of model parameters such that the Higgs-like state could be explained by the neutral top-pion [3]. We found that the top-pion, lacking tree-level couplings to the ZZ and WW, could not explain the excess in the data for those corresponding final states. In addition, while it is possible to explain the 126 GeV data in the di-photon final state with the neutral top-pion, this requires large mass splitting from the charged top-pions which are constrained by the top quark decays. This splitting requires larger isospin violation than exists in TC2 models. Further details on this study and its results can be found in Chapter 3, which is based on this work.

Now we have seen the implications from the recent experiments at the LHC for the two classes of model built on strong dynamics: technicolor and strong top dynamics. The LHC still has a long-term high-luminosity plan to follow at 14 TeV. That will open windows to both new physics at high-energy scales or physics leaving traces that can be uncovered by having large number of events. So we will now focus on a class of particles that features in most new physics models, not just those with strong dynamics: new massive vector bosons. We would like to know what one can do *shortly* after the particle has been discovered. This is the main focus of the Part II of the thesis.

1.3.2 Part II: Coloron Phenomenology

New massive vector bosons are often predicted in theories of physics beyond the standard model, particularly if they contain an extra local symmetry group that is hidden spontaneously. Those bosons having couplings with the Standard Model's fermions will have a chance to be produced directly at a collider that has a sufficiently high beam energy. The new vector bosons can be either colored or color-singlet. The colored particles that transform as color octets naturally arise from models with extended color sectors including strong dynamics, as well as models built on extra dimensions. Color-octet bosons are the main focus in this thesis. Color-singlet vector bosons are a very common prediction of models having an extended electroweak gauge group (see, for example, [129] for a review of models).

We generically refer to the color-octet and the color-singlet vector bosons as a coloron and a Z', respectively.

The possibility of having the ''coloron and the Z' coupled to hadrons provides a two-fold advantage for searches at a hadron collider such as the LHC [121, 130]. First, those resonances within the reach of the LHC can be produced copiously. Second, both particles decay to so-called "di-jet" final states of simple topology consisting of two groups of hadrons called "jets", while the Z' can also decay to the two-lepton final state. The searches for new vector resonances have been ongoing from the 1980's (see, for example, [131] for a review) up to the current LHC era. While none of the new resonances have been discovered, the LHC still has years left in its program and the potential of future colliders has been under serious discussions [132, 133]. There is room for a new vector resonance to be discovered within the foreseeable future.

The question one might ask is then: suppose a vector resonance is discovered, how does one quickly characterize its properties? Some of the properties that could allow identification of the origin of the vector boson include the color structure and the chiral structure of its couplings to the Standard Model fermions. While there have been several proposals of ways to characterize the resonance (see, for example, [130, 134, 135, 136, 137, 138, 139]), several require detailed knowledge from observables that could take time to measure. It is then helpful to have some means to characterize a particle using the information after its discovery such as the cross section from the discovery channel, its mass, and its decay width together with as few complementary measurements of other observables as possible.

The knowledge of the color structure of the new gauge boson could allow identifications or exclusion of a number of new physics models. Both the colorons and Z' that could be produced copiously at the LHC are likely to have the dijet final state as the discovery channel.

The Z' can even have the dilepton final states. A "bump" in both di-jet and di-lepton final states having the same mass and the same total decay width would immediately imply that the resonance could not be a color-octet. However, a bump that is present in the dijet final state but not in the dilepton final state could come from either a color-octet vector resonance or a color-singlet one that does not have leptonic couplings. The latter is called a "leptophobic Z'". How can we then distinguish between the coloron and the leptophobic Z'?

In 2012, my colleagues — Anupama Atre, Sekhar Chivukula, Elizabeth Simmons — and I addressed this question of how one can still quickly tell a coloron apart from a *leptophobic* Z' [4, 5]. The goal is to construct a variable from observables that allows one to do so as model-independent a manner as possible; *i.e.*, without having to consider different points in a parameter space of the model's couplings. We found that their different color structures lead the coloron and Z' to lie in different ranges of value of a variable constructed from mass, width and dijet cross section corresponding to each resonance. The variable is referred to as a "color discriminant". We illustrated the use of this method in the scenarios where the resonance couples universally to all quarks, or have different couplings to quarks in the third family. The work is presented in Chapter 4.

The next step is to implement the method based on the color discriminant variable within a realistic scenario where the new vector boson couplings are not necessarily flavor-universal. More realistic models usually predict a Z' carrying $SU(2)_L$ charges which makes it couple differently to up- and down-type quarks. The right-handed couplings are typically not constrained from the theory point of view. At first sight, this would have suggested that a large number of complementary measurements are needed to identify the color structure of the resonance. However, in 2013, Sekhar Chivukula, Elizabeth Simmons and I found that this is not the case [7] for the following reasons. First, the differences in couplings to quarks in the first two generations, which are inaccessible in the dijet final state, were found to be practically irrelevant to our method in most reasonable cases. Second, the difference in chiral couplings would play no role as long as the variables considered are not sensitive to it (fermion-antifermion cross sections, mass, and width). Supplementary measurements on heavy-flavor decays will determine the top and bottom couplings. So we extended the scope of the method to a flavor non-universal scenario, where in most cases the measurements for the di-top and di-bottom final states could supplement to the information on the color structure. Chapter 5 is based on this work.

Another important aspect of the new vector boson's properties that could eventually lead to uncovering its origin is the chiral structure of its couplings to the Standard Model fermions. Measuring the cross-section for the boson's production followed by decay into di-fermion channels, either dijet or di-leptons, allow one to probe the magnitude of the gauge couplings but not the separate couplings to left- and right-handed fermions. However, the associated production of the new resonance with the Standard Model W bosons (sensitive only to left-handed couplings) and Z boson (sensitive asymmetrically to left- and right-handed couplings) can provide the additional information. In 1992, Cvetič and Langacker [140] discussed the associated productions for the new electroweak gauge bosons, the W' and Z', with the ordinary bosons: the W, Z and γ. The dijet cross section is to be supplemented by cross sections for the rare process $pp \to V' \to \bar{f} f' V$ where $V' = (W', Z')$ and $f,\ f' =$ SM fermions, and the observable proportional to the difference between the numbers of charged leptons that go into the forward and backward directions. The accuracy of this method relies on the assumption that the new gauge bosons have leptonic decay channels, which are considered "clean". The situation for probing the chiral structure of the gauge boson that do not couple to leptons will be substantially different, both in terms of the backgrounds (now the "dirty" QCD backgrounds) and the decay final states (such as the dijets).

Back in 2012, inspired by a question raised by Devin G. Walker[8], my colleagues — Anupama Atre, Sekhar Chivukula, Elizabeth Simmons, Jiang-Hao Yu — and I proposed a new channel, the associated production of W, Z gauge bosons and color octet resonances, to help determine the chiral structure of the couplings [4, 5]. This is a counting experiment where a combination between cross sections of the two modes of associated productions along with a dijet cross section allows one to determine the chiral structure of the vector boson with flavor-universal couplings to quarks. We found that the early run of the 14 TeV-LHC (*i.e.*, $10\,\text{fb}^{-1}$ to $100\,\text{fb}^{-1}$) can probe a large region of the parameter space down to very small couplings. This work is presented in Chapter 6 of this thesis.

A summary for each set of results is presented at the end of each chapter. In Chapter 7, I conclude the thesis, giving an overview summary and a discussion of the aspects one can explore in the future.

[8] Private communication.

Part I

Phenomenology of Strong Dynamics

Chapter 2

Technipion Limits from LHC Higgs Searches

— This chapter is based on a work in collaboration with R. Sekhar Chivukula, Elizabeth H. Simmons, and Jing Ren which has appeared in [1]. The contents also have appeared in parts in the conference proceeding [2].

2.1 Introduction

Before the Higgs-like signal was observed on July 4th 2012, experiments at the Large Hadron Collider were striving to discover the agent of electroweak symmetry breaking. The negative findings were generally phrased in terms of placing constraints on the properties of the fundamental scalar Higgs boson state (h_{SM}) predicted to exist in the standard model. In 2011, both the ATLAS and CMS collaborations at the CERN LHC reported the results from searches for the standard model Higgs in the two-photon [141, 142] and $\tau^+\tau^-$ [143, 144, 145] decay channels. They placed upper bounds on the cross-section times branching ratio ($\sigma \cdot B$) for each channel over the approximate mass range 110 GeV $\leq m_h \leq$ 145 GeV, finding that $\sigma \cdot B$ cannot exceed the standard model prediction by more than a factor of a few. In addition, ATLAS independently constrained the production of a heavy neutral scalar SM

Higgs boson with mass up to 600 GeV and decaying to $\tau^+\tau^-$.

This chapter presents the work [1] where we applied these limits to the neutral "technipion" (Π_T) states predicted to exist in technicolor models that include colored technifermions. Because both the technipion production rates and their branching fractions to $\gamma\gamma$ or $\tau\tau$ can greatly exceed the values for a standard model Higgs, the LHC results place strong constraints on technicolor models. This strategy was first suggested as a possible for hadron supercolliders over fifteen years ago in Refs. [121, 122, 123].

As we have introduced in Sec. 1.2, which will be reviewed below (see also [99]), many technicolor models, including those with walking and topcolor dynamics, feature technipion states, pseudo-scalar bosons that are remnants of electroweak symmetry breaking in models with more than one weak doublet of technifermions. Production of light technipion states at lepton colliders has been studied by a variety of authors [146, 147, 148, 149, 150, 151]; the most comprehensive analysis [151] used LEP I and LEP II data to constrain the anomalous couplings of technipions to neutral electroweak gauge bosons and derived limits on the size of the technicolor gauge group and the number of technifermion doublets in various representative technicolor models. Subsequently, the authors of [124] considered technipion phenomenology at hadron colliders; they demonstrated both that technipions can be produced at a greater rate than the standard model Higgs, because the technipion decay constant is smaller than the electroweak scale, and also that the technipions can also have higher branching fractions to $\gamma\gamma$ or $\tau\tau$ final states. As a result, the technipions are predicted to produce larger signals in these two channels at LHC than the h_{SM} would [124].

In [1], we showed that the ATLAS [141, 143, 144] and CMS [142, 145] searches for the standard model Higgs exclude, at 95% CL, technipions of masses from 110 GeV to nearly $2m_t$ in technicolor models that (a) include colored technifermions (b) feature topcolor dynamics and (c) have technicolor groups with three or more technicolors ($N_{TC} \geq 3$). For certain models of this kind, the limits also apply out to higher technipion masses or down to the minimum number of technicolors ($N_{TC} = 2$). We also showed how the limits may be modified in models in which extended technicolor plays a significant role in producing the mass of the top quark; in some cases, this makes little difference, while in other cases the limit is softened somewhat. Overall, we found that the ATLAS and CMS significantly constrain technicolor models. Moreover, as the LHC collaborations collect additional data on these di-tau and di-photon final states and extend the di-photon analyses to higher mass ranges, they should be able to quickly expand their reach in technicolor parameter space.

The rest of this chapter is organized as follows. In Sec. 2.2, we provide a brief review of Technicolor models and properties of a neutral technipion relevant to the Higgs production and decays to the final states of interest. Then, in Sec. 2.3, we show how the LHC data constraints technipions composed of colored technifermions and discuss the constraints on theories where mass of the top quark is mainly generated by topcolor dynamics. We then discuss the implications of the constraints in theories where the top quark's mass receives a substantial contribution from ETC in Sec. 2.4. Finally, the conclusions and discussions are presented in Sec. 2.5.

2.2 Technicolor and Technipions

Dynamical theories of electroweak symmetry breaking embody the possibility that the scalar states involved in electroweak symmetry breaking could be manifestly composite at scales not much above the weak scale $v \approx 246$ GeV. In technicolor theories [78, 79, 80], a new asymptotically free strong gauge interaction breaks the chiral symmetries of massless fermions T

at a scale $\Lambda \sim 1$ TeV. If the fermions carry appropriate electroweak quantum numbers (e.g. left-hand (LH) weak doublets and right-hand (RH) weak singlets), the resulting condensate $\langle \bar{T}_L T_R \rangle \neq 0$ breaks the electroweak symmetry correctly to its electromagnetic subgroup. Three of the Nambu-Goldstone Bosons of the chiral symmetry breaking become the longitudinal modes of the W and Z, making those gauge bosons massive. The hierarchy and triviality problems plaguing the standard model are absent: the logarithmic running of the strong gauge coupling renders the low value of the electroweak scale natural, while the absence of fundamental scalars obviates concerns about triviality.

In so-called minimal technicolor models, there are no composite scalars left in the spectrum. However, many dynamical symmetry-breaking models include more than the minimal two flavors of technifermions needed to break the electroweak symmetry. In that case, there will exist light pseudo Nambu-Goldstone bosons known as technipions, which could potentially be accessible to a standard Higgs search. Technipions that are bound states of colored technifermions can be produced through quark or gluon scattering at a hadron collider, like the LHC, through the diagrams in Fig. 2.1. In the models with topcolor dynamics, where ETC interactions (represented by the shaded circle) contribute no more than a few GeV to the mass of any quark, there is only a small ETC-mediated coupling between the technipion and ordinary quarks in diagrams 2.1(b) and 2.1(c). Combining that information with the large size of the gluon PDF at the LHC and the N_{TC} enhancement factor in the techniquark loop at left, we expect that the diagram in Fig. 2.1(a) will dominate technipion production in these theories, which we study here and in Section 2.3. Technipions in models without strong top dynamics could, in contrast, have a large top-technipion coupling, making diagram 1(c) potentially important; we will consider that scenario in Section 2.4. Technipions that are bound states of non-colored technifermions would be produced at hadron colliders only through diagrams 2.1(b) and 2.1(c), which would generally yield a significantly lower production rate; we comment on these models in the discussion (Section 2.5).

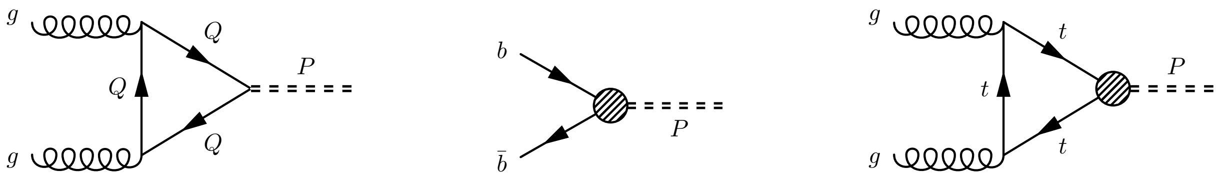

(a) gluon-gluon fusion through techniquark loop

(b) $b\bar{b}$ annihilation

(c) gluon-gluon fusion through top quark loop

Figure 2.1: Feynman diagrams for single technipion production at LHC. The shaded circle in diagrams (b) and (c) represents an ETC coupling between the ordinary quarks and techniquarks. *For interpretation of the references to color in this and all other figures, the reader is referred to the electronic version of this thesis.*

No single technicolor model has been singled out as a benchmark; rather, different classes of models have been proposed to address the challenges of dynamically generating mass while complying with precision electroweak and flavor constraints. We will study the general constraints that the current LHC data can place a variety of theories with colored technifermions and light technipions. Following [124, 151], the specific models we examine are: 1) the original one-family model of Farhi and Susskind [152] with a full family of techniquarks and technileptons, 2) a variant on the one-family model [150] in which the lightest technipion contains only down-type technifermions and is significantly lighter than the other pseudo Nambu-Goldstone bosons, 3) a multiscale walking technicolor model [153] designed to reduce flavor-changing neutral currents, 4) a low-scale technicolor model (the Technicolor Straw Man – TCSM – model) [154] with many weak doublets of technifermions and 5) a one-family models with weak-isotriplet technifermions [146]. Properties of the lightest electrically-neutral technipion in each model that couples to gluons (and can therefore be readily produced at LHC) are shown in Table 2.1. For completeness, we show the name and technifermion content of each state in the notation of the original paper proposing its existence; while each paper has its own conventions, all technifermion names including "Q" or "D" refer to color-triplets (a.k.a. techniquarks) while those including "L" or "E" refer to color-singlets (a.k.a. technileptons).[1] In the TCSM low-scale model, the second-lightest technipion is the state relevant for our study (the lightest, being composed of technileptons, lacks an anomalous coupling to gluons); in the other models the lightest technipion is the relevant one. For simplicity the lightest relevant neutral technipion of each model will be generically denoted P. Furthermore, we will assume that the lightest technipion state is significantly lighter than other neutral (pseudo)scalar technipions in the spectrum, in order to facilitate the comparison to the standard model Higgs boson.[2]

Single production of a technipion can occur through the axial-vector anomaly which couples the technipion to pairs of gauge bosons. For an $SU(N_{TC})$ technicolor group with technipion decay constant F_P, the anomalous coupling between the technipion and a pair of gauge bosons is given, in direct analogy with the coupling of a QCD pion to photons,[3] by [155, 156, 157]

$$N_{TC}\mathcal{A}_{V_1V_2}\frac{g_1g_2}{8\pi^2F_P}\epsilon_{\mu\nu\lambda\sigma}k_1^\mu k_2^\nu\epsilon_1^\lambda\epsilon_2^\sigma \tag{2.1}$$

where

$$\mathcal{A}_{V_1V_2} \equiv Tr\,[T^a(T_1T_2+T_2T_1)_L + T^a(T_1T_2+T_2T_1)_R] \tag{2.2}$$

is the anomaly factor, T^a is the generator of the axial vector current associated with the techipion, subscripts L and R denote the left- and right-handed technifermion components of

[1] Note that the LR multiscale model [153] incorporates six technileptons, which we denote L_ℓ.

[2] The detailed spectrum of any technicolor model depends on multiple factors, particularly the parameters describing the "extended technicolor" [81, 82] interaction that transmits electroweak symmetry breaking to the ordinary quarks and leptons. Models in which several light neutral PNGBs are nearly degenerate could produce even larger signals than those discussed here.

[3] Note that the normalization used here is identical to that in [124] and differs from that used in [151] by a factor of 4.

the technipion, the T_i and g_i are the generators and couplings associated with gauge bosons V_i, and the k_i and ϵ_i are the four-momenta and polarizations of the gauge bosons. The value of the anomaly factor $\mathcal{A}_{gg}$ for the lightest PNGB of each model that is capable of coupling to gluons appears in Table 2.1, along with the anomaly factor $\mathcal{A}_{\gamma\gamma}$ coupling the PNGB to photons. Also shown in the table is the value of the technipion decay constant, F_P for each model.[4]

Examining the technipion wave functions in Table 2.1 we note that the PNGB's do *not* decay to W boson pairs, since the W^+W^- analog of Fig. 2.1 vanishes due to a cancellation between techniquarks and technileptons. The corresponding ZZ diagrams will not vanish but, again due to a cancellation between techniquarks and technileptons, will instead yield small couplings for the technipion to ZZ (and $Z\gamma$) proportional to the technifermion hypercharge couplings [151]. The small coupling and phase space suppression yield much smaller branching ratios for the PNGB's to decay to ZZ or $Z\gamma$, and hence these modes are irrelevant to our limits.

The rate of single technipion production via glue-glue fusion and a techniquark loop (Fig.2.1(a)) is proportional to the technipion's decay width to gluons through that same techniquark loop

$$\Gamma(P \to gg) = \frac{m_P^3}{8\pi} \left(\frac{\alpha_s N_{TC} \mathcal{A}_{gg}}{2\pi F_P} \right)^2 . \tag{2.3}$$

In the SM, the equivalent expression (for Higgs decay through a top quark loop) looks like [158]

$$\Gamma(h_{SM} \to gg) = \frac{m_h^3}{8\pi} \left(\frac{\alpha_s}{3\pi v} \right)^2 \left[\frac{3\tau}{2} (1 + (1-\tau) f(\tau)) \right]^2 , \tag{2.4}$$

[4] In the multi-scale model [model 3], various technicondensates form at different scales; we set $F_P^{(3)} = \frac{v}{4}$ in keeping with [153] and to ensure that the technipion mass will be in the range to which the standard Higgs searches are sensitive.

Table 2.1: Properties of the lightest relevant PNGB (technipion) in representative technicolor models with colored technifermions. In each case, we show the name and technifermion content of the state (in the notation of the original paper), the ratio of the weak scale to the technipion decay constant, the anomaly factors for the two-gluon and two-photon couplings of the technipion, and the technipion's couplings to leptons and quarks. The symbols "Q" or "D" refer to color-triplets (a.k.a. techniquarks) while those including "L" or "E" refer to color-singlets (a.k.a. technileptons). The multiscale model incorporates six technileptons, which we denote by L_ℓ. For the TCSM low-scale model, N_D refers to the number of weak-doublet technifermions contributing to electroweak symmetry breaking; this varies with the size of the technicolor group. The parameter y in the isotriplet model is the hypercharge assigned to the technifermions.

TC models	PNGB and content		v/F_P	A_{gg}	$A_{\gamma\gamma}$	λ_l	λ_f
FS one family[152]	P^1	$\frac{1}{4\sqrt{3}}(3\bar{L}\gamma_5 L - \bar{Q}\gamma_5 Q)$	2	$-\frac{1}{\sqrt{3}}$	$\frac{4}{3\sqrt{3}}$	1	1
Variant one family[150]	P^0	$\frac{1}{2\sqrt{6}}(3\bar{E}\gamma_5 E - \bar{D}\gamma_5 D)$	1	$-\frac{1}{\sqrt{6}}$	$\frac{16}{3\sqrt{6}}$	$\sqrt{6}$	$\sqrt{\frac{2}{3}}$
LR multiscale[153]	P^0	$\frac{1}{6\sqrt{2}}(\bar{L}_\ell\gamma_5 L_\ell - 2\bar{Q}\gamma_5 Q)$	4	$-\frac{2\sqrt{2}}{3}$	$\frac{8\sqrt{2}}{9}$	1	1
TCSM low scale[154]	$\pi_T^{0\prime}$	$\frac{1}{4\sqrt{3}}(3\bar{L}\gamma_5 L - \bar{Q}\gamma_5 Q)$	$\sqrt{N_D}$	$-\frac{1}{\sqrt{3}}$	$\frac{100}{27\sqrt{3}}$	1	1
MR Isotriplet [146]	P^1	$\frac{1}{6\sqrt{2}}(3\bar{L}\gamma_5 L - \bar{Q}\gamma_5 Q)$	4	$-\frac{1}{\sqrt{2}}$	$24\sqrt{2}y^2$	1	1

where $\tau \equiv (4m_t^2/m_h^2)$ and

$$f(\tau) = \begin{cases} \left[\sin^{-1}(\tau^{-\frac{1}{2}})\right]^2 & \text{if } \tau \geq 1 \\ -\frac{1}{4}\left[\log\left(\frac{1+\sqrt{1-\tau}}{1-\sqrt{1-\tau}}\right) - i\pi\right]^2 & \text{if } \tau < 1. \end{cases} \tag{2.5}$$

so that the expression in square brackets in Eq. (2.4) approaches 1 in the limit where the top quark is heavy ($\tau >> 1$). Therefore, the rate at which P is produced from gg fusion exceeds that for a standard Higgs of the same mass by a factor

$$\kappa_{gg\ prod} = \frac{\Gamma(P \to gg)}{\Gamma(h_{SM} \to gg)} = \frac{9}{4} N_{TC}^2 \mathcal{A}_{gg}^2 \frac{v^2}{F_P^2} \left[\frac{3\tau}{2}(1 + (1-\tau)f(\tau))\right]^{-2} \tag{2.6}$$

where, again, the factor in square brackets is 1 for scalars much lighter than $2m_t$. A large technicolor group and a small technipion decay constant can produce a significant enhancement factor.

Technipions can also be produced at hadron colliders via $b\bar{b}$ annihilation (as in Fig. 2.1(b)), because the ETC interactions coupling quarks to techniquarks afford the technipion a decay mode into fermion/anti-fermion pairs. The rate is proportional to the technipion decay width into fermions:

$$\Gamma(P \to f\overline{f}) = \frac{N_C\, \lambda_f^2\, m_f^2\, m_P}{8\pi\, F_P^2} \left(1 - \frac{4m_f^2}{m_P^2}\right)^{\frac{s}{2}} \tag{2.7}$$

where N_C is 3 for quarks and 1 for leptons. The phase space exponent, s, is 3 for scalars and 1 for pseudoscalars; the lightest PNGB in our technicolor models is a pseudoscalar. For the technipion masses considered here, the value of the phase space factor in (2.7) is so close to one that the value of s makes no practical difference. The factors λ_f are non-standard Yukawa couplings distinguishing leptons from quarks. The variant one-family model has $\lambda_{quark} = \sqrt{\frac{2}{3}}$ and $\lambda_{lepton} = \sqrt{6}$; the multiscale model also includes a similar factor, but with average value 1; $\lambda_f = 1$ in the other models. For comparison, the decay width of the SM Higgs into b-quarks is:

$$\Gamma(h_{SM} \to b\overline{b}) = \frac{3\, m_b^2\, m_h}{8\pi\, v^2} \left(1 - \frac{4m_b^2}{m_h^2}\right)^{\frac{3}{2}} \tag{2.8}$$

Thus, the rate at which P is produced from $b\bar{b}$ annihilation exceeds that for a standard Higgs

Table 2.2: Branching ratios for phenomenologically important modes (in percent) for technipions of mass 130 GeV for $N_{TC} = 2, 4$ and for a standard model Higgs [159] of the same mass.

Decay Channel	One Family N_{TC} =2	One Family N_{TC} =4	Variant one family N_{TC} =2	Variant one family N_{TC} =4	Multiscale N_{TC} =2	Multiscale N_{TC} =4	TCSM low-scale N_{TC} =2	TCSM low-scale N_{TC} =4	Isotriplet N_{TC} =2	Isotriplet N_{TC} =4	SM Higgs
$b\bar{b}$	77	56	61	50	64	36	77	56	60	31	49
$c\bar{c}$	7	5.1	0	0	5.8	3.2	7	5.1	5.4	2.8	2.3
$\tau^+\tau^-$	4.5	3.3	32	26	3.8	2.1	4.5	3.3	3.5	1.8	5.5
gg	12	35	7	23	26	59	12	35	14	29	7.9
$\gamma\gamma$	0.011	0.033	0.11	0.35	0.025	0.056	0.088	0.26	17	36	0.23
W^+W^-	0	0	0	0	0	0	0	0	0	0	31

of the same mass by

$$\kappa_{bb\ prod} = \frac{\Gamma(P \to b\bar{b})}{\Gamma(h_{SM} \to b\bar{b})} = \frac{\lambda_b^2\, v^2}{F_P^2} \left(1 - \frac{4m_b^2}{m_h^2}\right)^{\frac{s-3}{2}} \tag{2.9}$$

The enhancement is smaller than that in Eq. (2.6) because there is no loop-derived factor of N_{TC}.

For completeness, we note that the branching fraction for a technipion into a photon pair via a techniquark loop is:

$$\Gamma(P \to \gamma\gamma) = \frac{m_P^3}{64\pi} \left(\frac{\alpha_s N_{TC} \mathcal{A}_{\gamma\gamma}}{2\pi F_P}\right)^2 . \tag{2.10}$$

as compared with the result for the standard model Higgs boson (through a top quark loop) [158]

$$\Gamma(h_{SM} \to \gamma\gamma) = \frac{m_h^3}{9\pi} \left(\frac{\alpha}{3\pi v}\right)^2 \left[\frac{3\tau}{2}(1 + (1-\tau) f(\tau))\right]^2 , \tag{2.11}$$

Table 2.3: Branching ratios for phenomenologically important modes (in percent) for technipions of mass 350 GeV for $N_{TC} = 2, 4$ and for a standard model Higgs [159] of the same mass.

Decay Channel	One Family N_{TC} =2	One Family N_{TC} =4	Variant one family N_{TC} =2	Variant one family N_{TC} =4	Multiscale N_{TC} =2	Multiscale N_{TC} =4	TCSM low-scale N_{TC} =2	TCSM low-scale N_{TC} =4	Isotriplet N_{TC} =2	Isotriplet N_{TC} =4	SM Higgs
$b\bar{b}$	44	18	42	20	24	7.7	44	18	20	6.2	0.036
$c\bar{c}$	4	1.6	0	0	2.2	0.69	4	1.6	1.8	0.56	0.0017
$\tau^+\tau^-$	2.6	1	22	11	1.4	0.45	2.6	1	1.2	0.36	0.0048
gg	49	79	35	68	72	91	49	79	34	41	0.085
$\gamma\gamma$	0.047	0.076	0.54	1	0.069	0.087	0.36	0.58	42	51	~ 0
W^+W^-	0	0	0	0	0	0	0	0	0	0	68

From these decay widths, we can now calculate the technipion branching ratios to all of the significant two-body final states, taking $N_{TC} = 2$ and $N_{TC} = 4$ by way of example. In the TCSM low-scale model we set $N_D = 5$ (10) for $N_{TC} = 2$ (4) to make the technicolor coupling walk; in the Isotriplet model, we set the technifermion hypercharge to the value $y = 1$. We find that the branching ratio values are nearly independent of the size of M_P within the range 110 GeV - 145 GeV and also show little variation once $M_P > 2m_t$; to give a sense of the patterns, the branching fractions for $M_P = 130$ GeV are shown in Table II and those for $M_P = 350$ GeV are shown in Table III. The branching ratios for the SM Higgs at NLO are given for comparison; these were obtained from the Handbook of LHC Higgs Cross Sections [159]. The primary differences are the absence of a WW decay for technipions and the enhancement of the two-gluon coupling (implying increased $gg \to P$ production); the di-photon and di-tau decay widths can also vary moderately from the standard model values.

Pulling this information together, and noting that the PNGBs are narrow resonances, we may define an enhancement factor for the full production-and-decay process $yy \to P \to xx$ as the ratio of the products of the width of the (exclusive) production mechanism and the branching ratio for the decay:

$$\kappa^P_{yy/xx} = \frac{\Gamma(P \to yy) \times BR(P \to xx)}{\Gamma(h_{SM} \to yy) \times BR(h_{SM} \to xx)} \equiv \kappa_{yy\ prod}\, \kappa_{xx\ decay}\ . \tag{2.12}$$

And to include both the gluon fusion and b-quark annihilation production channels when looking for a technipion in the specific decay channel $P \to xx$, we define a combined enhancement factor

$$\begin{aligned}
\kappa^P_{total/xx} &= \frac{\sigma(gg \to P \to xx) + \sigma(bb \to P \to xx)}{\sigma(gg \to h_{SM} \to xx) + \sigma(bb \to h_{SM} \to xx)} \\
&= \frac{\kappa^P_{gg/xx} + \sigma(bb \to P \to xx)/\sigma(gg \to h_{SM} \to xx)}{1 + \sigma(bb \to h_{SM} \to xx)/\sigma(gg \to h_{SM} \to xx)} \\
&= \frac{\kappa^P_{gg/xx} + \kappa^P_{bb/xx}\sigma(bb \to h_{SM} \to xx)/\sigma(gg \to h_{SM} \to xx)}{1 + \sigma(bb \to h_{SM} \to xx)/\sigma(gg \to h_{SM} \to xx)} \\
&\equiv [\kappa^P_{gg/xx} + \kappa^P_{bb/xx} R_{bb:gg}]/[1 + R_{bb:gg}].
\end{aligned} \tag{2.13}$$

Here $R_{bb:gg}$ is the ratio of $b\bar{b}$ and gg initiated Higgs boson production in the Standard Model, which can be calculated using the HDECAY program [160]. In practice, as noted in [124], the contribution from b-quark annihilation is far smaller than that from gluon fusion for colored technifermions.

2.3 Models with colored technifermions and a topcolor mechanism

We will now show how the LHC data constrains technipions composed of colored technifermions in theories where the top-quark's mass is generated by new strong "topcolor" dynamics [100] preferentially coupled to third-generation quarks. In such models, the ETC coupling between ordinary quarks and technifermions (or technipions) is very small, so that gluon fusion through a top-quark loop will be negligible by comparison with gluon fusion through a technifermion loop, as a source of technipion production.

2.3.1 LHC Limits on Models with Light Technipions

Here we report our results for technipions in the 110 - 145 GeV mass range where direct comparison with Higgs production is possible. We consider final states with pairs of photons or tau leptons, since the LHC experiments have reported limits on the standard model Higgs boson in both channels.

First, we show the limits derived from the CMS and ATLAS searches for a standard model Higgs boson decaying to $\gamma\gamma$ in Fig. 2.3.1. The multiscale [153], TCSM low-scale [154], and isotriplet [146] models predict rates of technipion production and decay to diphotons that exceed the experimental limits in this mass range even for the smallest possible size of the technicolor gauge group (larger N_{TC} produces a higher rate). Note that we took the value of the technifermion hypercharge parameter y in the isotriplet model to have the value $y = 1$ for purposes of illustration; choosing $y \sim 1/7$ could make this model consistent with the di-photon data for $N_{TC} = 2$, but that would not affect the limits from the di-tau channel discussed below. For the original [152] and variant [150] one-family models, the data still allow $N_{TC} = 2$ over the whole mass range, and $N_{TC} = 3$ is possible for 115 GeV $< M_P <$ 120 GeV; even $135 < M_P < 145$ GeV is marginally consistent with the data for $N_{TC} = 3$ in the original one-family model.

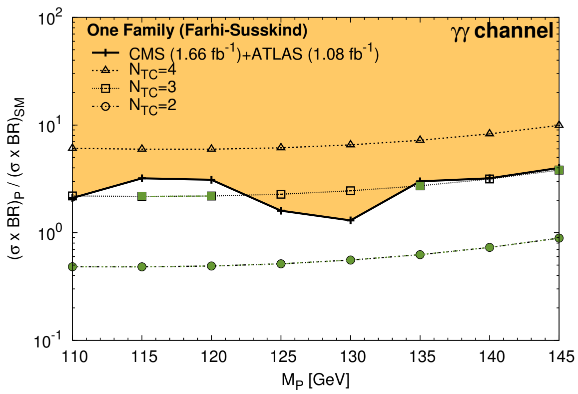

(a) Original one-family model [152].

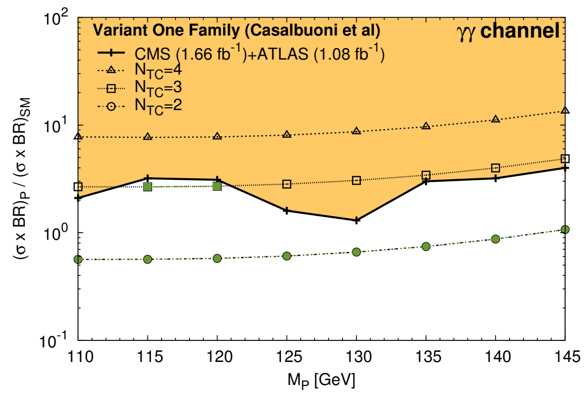

(b) Variant one-family model [150].

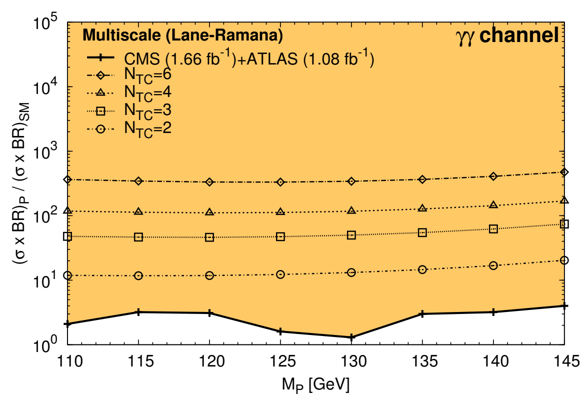

(c) Multiscale walking technicolor model [153].

Figure 2.2: Comparison of experimental limits and technicolor model predictions for production of a new scalar decaying to photon pairs. In each pane, the shaded region (above the solid line) is excluded by the combined 95% CL upper limits on $\sigma_h B_{\gamma\gamma}$ normalized to the SM expectation as observed by CMS [142] and ATLAS [141]. Each pane also displays (as open symbols) the theoretical prediction from one of our representative technicolor models with colored technifermions, as a function of technipion mass and for several values of N_{TC}. Values of mass and N_{TC} for a given model that are not excluded by the data are shown as solid (green) symbols. *Continued next page.*

The limits from the the CMS and ATLAS searches for a standard model Higgs boson decaying to $\tau^+\tau^-$ in the same mass range need extra considerations. The results from the

Figure 2.2 (cont'd)

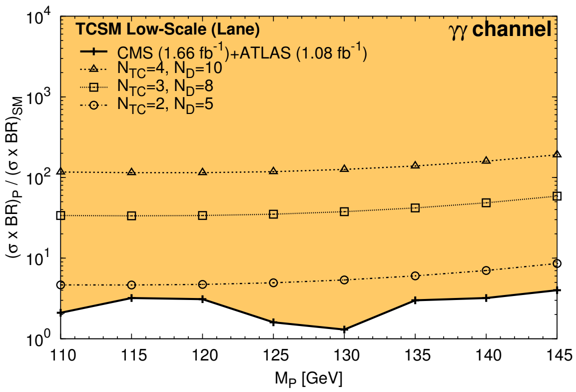

(d) TCSM Low-scale techncriolor model (the Technicolor Straw Man model) [154].

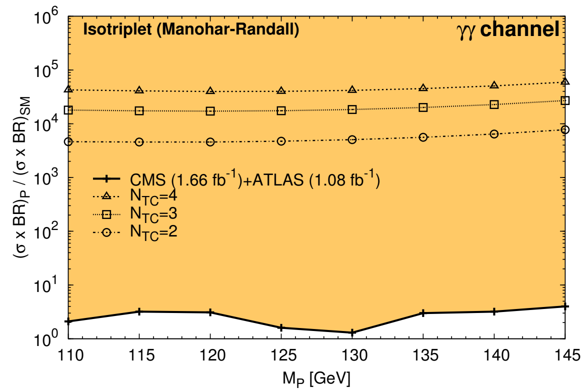

(e) Isotriplet model [146]. The magnitude of the technifermion hypercharge variable y has been set to 1 for illustration.

analyses [161, 144, 162], arose in large part from the production of a standard model Higgs boson through vector-boson fusion or in association with a W bosonproduction mechanisms that are absent for technipions. Thus, the updated results on searches for the Higgs in the $\tau\tau$ decay mode from the ATLAS experiment [163] are used instead.

The search for the standard model Higgs boson in the $\tau\tau$ decay mode reported in [163] is based on the combination of searches for three different decay channels of the final state τparticles: $\tau_{\text{had}}\tau_{\text{had}}\nu\nu$, $l\tau_{\text{had}}3\nu$, and $ll4\nu$. The results of the individual analysis in each channel I is expressed as a 95% C.L. upper limit on

$$\mu_I(m_H) = \frac{\sigma(pp \to H)\text{BR}(H \to \tau\tau \to I)}{\sigma_{\text{SM}}(pp \to H)\text{BR}_{\text{SM}}(H \to \tau\tau \to I)}\,, \tag{2.14}$$

as a function of the Higgs boson mass m_H. The individual channels are then combined

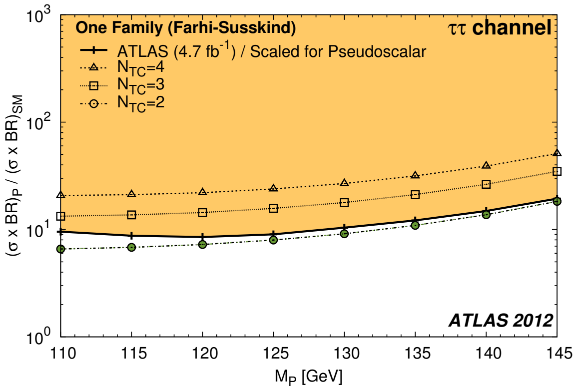

(a) Original one-family model [152].

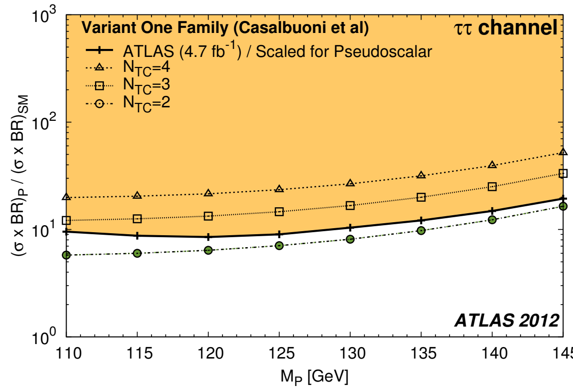

(b) Variant one-family model [150].

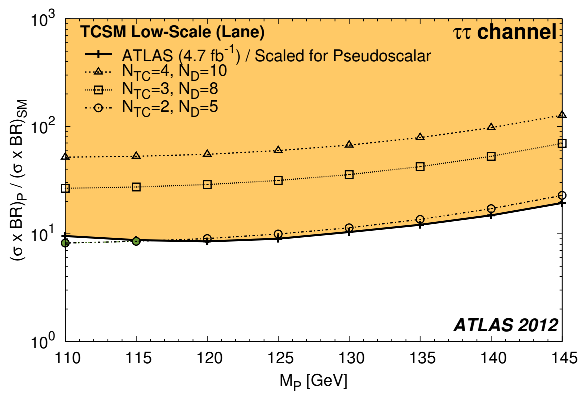

(c) TCSM Low-scale technciolor model (the Technicolor Straw Man model) [154].

Figure 2.3: Comparison of experimental limits and technicolor model predictions for production of a new scalar decaying to tau lepton pairs. In each pane, the shaded region (above the solid line) is excluded by the combined 95% CL upper limits on $\sigma_h B_{\tau^+\tau^-}$ normalized to the SM expectation as observed by CMS [145] and ATLAS [143]. Each pane also displays (as open symbols) the theoretical prediction from one of our representative technicolor models with colored technifermions, as a function of technipion mass and for several values of N_{TC}. Values of M_P and N_{TC} for a given model that are not excluded by the data are shown as solid (green) symbols.

using[5]

$$\mu(m_H) = \left(\sum_{l}^{N} \frac{1}{\mu_I^2(m_H)} \right)^{-(1/2)} . \tag{2.15}$$

to find an overall bound on the standard model Higgs boson in the $\tau\tau$ decay channel.

In the Higgs search, each $\tau\tau$ decay channel receives contributions from three different production modes for the Higgs boson: gluon fusion (gg), vector-boson fusion (VBF), and associated production (VH). In order to correctly scale these results to find limits on technipions, we need the limits on μ_I that would arise solely from gluon fusion. This can be done by scaling $\mu_I(m_H)$ by using the fraction of expected signal events (including both production cross section and detection efficiency) arising from gluon fusion, through

$$\tilde{\mu}_I(m_H) = \left(\frac{n^I_{\mathrm{gg}}(m_H)}{n^I_{\mathrm{gg}}(m_H) + n^I_{\mathrm{VBF}}(m_H) + n^I_{\mathrm{VH}}(m_H)} \right)^{-1} \mu_I \,, \tag{2.16}$$

where $n^I_P(m_H)$ is the number of signal events expected for a standard model Higgs boson produced via mechanism P and detected in $\tau\tau$ decay channel I. In [163] the expected number of signal events for each production mode and decay channel, including both cross section and detection efficiency, is listed for a 120 GeV standard model Higgs boson. Assuming that the detection efficiency is roughly constant over the mass range of interest ($100\,\mathrm{GeV} < m_H < 145\,\mathrm{GeV}$), we estimate the number of expected signal events by

$$n^I_P(m_H) = \frac{\sigma_P(m_H)}{\sigma_P(120\,\mathrm{GeV})} n^I_P(120\,\mathrm{GeV}) \equiv R_P(m_H) \cdot n^I_P(120\,\mathrm{GeV}) \,. \tag{2.17}$$

We take the ratio of production cross sections, $R_P(m_H)$, from [7].

[5]This equation is only approximately correct since the limit on each μ_I arises from a finite number of events in the data sample in channel I, and this formula does not account for fluctuations in the number of events observed. For a recent analysis of the validity of this approximation, see [164] — on the basis of which we expect this approximation to be good to 20%.

Using (2.17) and (2.16), we scale the data from [163] to obtain the upper bound $\tilde{\mu}(m_H)$ on $\sigma(pp \to H \to \tau\tau \to I)/\sigma_{\rm SM}(pp \to H \to \tau\tau \to I)$ arising solely from gluon fusion. We then combine these different $\tau\tau$ decay channels using (2.15). This result is then used to bound the production cross section for technipions in the three models in Refs. [152, 150, 154]. Our results are shown in Fig. 2.3.

The constraints are even more stringent, as shown in Fig, 2.3. Only the original [152], the variant [150] one-family model, and the TCSM low-scale [154] with $N_{TC} = 2$ is marginally consistent with data. Forthcoming LHC data on $\tau\tau$ final states should provide further insight on these two models for $N_{TC} = 2$.

2.3.2 LHC Limits on Heavier Technipions Decaying to Tau-Lepton Pairs

We now consider technipions that are too heavy to be directly compared with a Higgs in the LHC data, but which can be directly constrained by looking at data from final states with tau-lepton pairs. ATLAS has obtained [144] limits on the product of the production cross section with the branching ratio to tau pairs at 95% confidence level for a generic scalar boson in the mass range $100 - 600$ GeV. We use this limit to constrain technicolor models as follows. The production cross section $\sigma(gg \to P)$ for technicolor models can be estimated by scaling from the standard model[6] using the production enhancement factor calculated for each technicolor model [124]. And the branching fraction of the technipions into tau pairs

[6]The standard model production cross section $\sigma(gg \to h_{SM})$ at several values of the Higgs mass can be obtained from the Handbook [159].

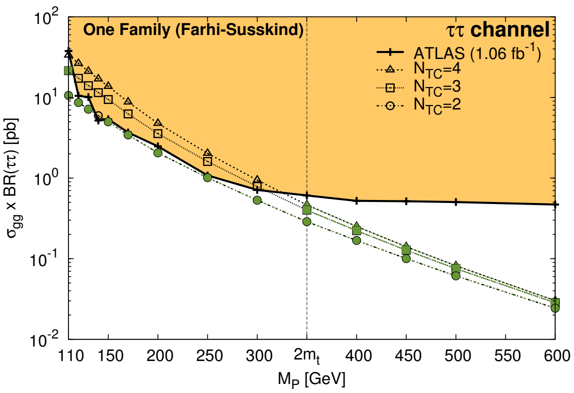

(a) Original one-family model [152].

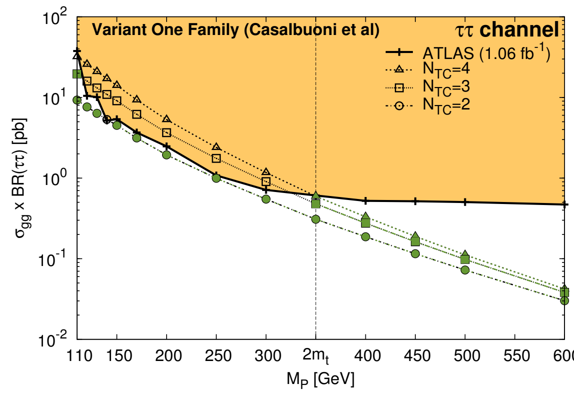

(b) Variant one-family model [150].

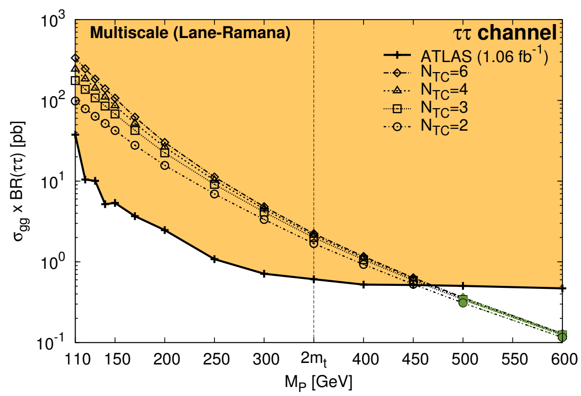

(c) Multiscale walking technicolor model [153].

Figure 2.4: Comparison of experimental limits and technicolor model predictions for production of a new scalar decaying to tau lepton pairs for scalar masses in the mass range 110 - 600 GeV . In each pane, the shaded region (above the solid line) is excluded by the 95% CL upper limits on $\sigma_h B_{\tau^+\tau^-}$ from ATLAS [144]. Each pane also displays (as open symbols) the theoretical prediction from one of our representative technicolor models with colored technifermions, as a function of technipion mass and for several values of N_{TC}. Values of M_P and N_{TC} for a given model that are not excluded by this data are shown as solid (green) symbols; nearly all such values at low technipion masses are excluded by the data shown in Fig. 2.3.1. As discussed in the text, limits to the right of the vertical bar at $M_P = 2m_t$ apply only when a topcolor sector, rather than extended technicolor, generates most of the top quark's mass. *Continued next page.*

Figure 2.4 (cont'd)

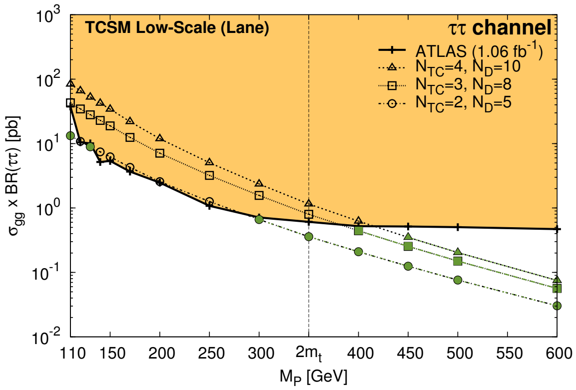

(d) TCSM Low-scale technicolor model (the Technicolor Straw Man model) [154].

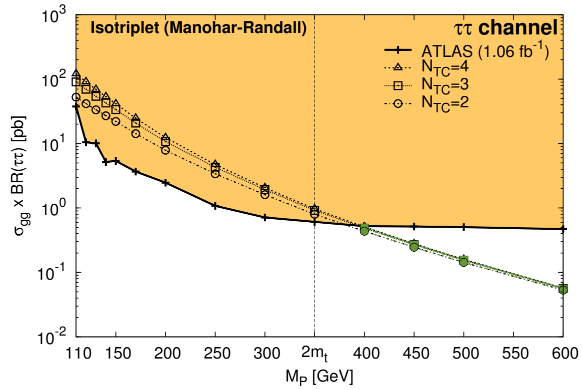

(e) Isotriplet model [146].The magnitude of the technifermion hypercharge variable y has been set to 1 for illustration

is shown in Table II, above. Therefore,

$$\sigma(gg \to P)BR(P \to \tau\tau) \;=\; \kappa_{gg\ prod}\sigma(gg \to h_{SM})BR(P \to \tau\tau)\,. \tag{2.18}$$

Our comparison of the experimental limits with the model predictions is shown in Fig. 2.4.

In the region of the figures to the left of the vertical bar, we see that the data excludes technipions in the mass range from 145 GeV up to nearly $2m_t$ in all models for $N_{TC} \geq 3$. For the multiscale and isotriplet models, $N_{TC} = 2$ is excluded as well in this mass range; for the TCSM low-scale model, $N_{TC} = 2$ is excluded up to nearly 300 GeV (the few points that are allowed at low mass on this plot are excluded by the data shown in Figs. 2.3.1 and 2.3; while for the original and variant one-family models, $N_{TC} = 2$ can be consistent with data at these higher masses. Again, further LHC data on di-tau final states will be valuable for discerning whether the models with only two technicolors remain viable. At present, technicolor models with colored technifermions are strongly constrained even if their lightest technipion is just below the threshold at which it can decay to top-quark pairs.

Moreover, as the region of the figures to the right of the vertical bar demonstrates, the data also impacts technipions in the mass range above $2m_t$ in some cases: $M_P \leq 450$ GeV (375 GeV) is excluded for any size technicolor group in the multiscale (isotriplet) model and $M_P \leq 375$ GeV is excluded for $N_{TC} \geq 3$ in the TCSM low-scale model. Note that these limits apply only in cases where the technipion has a very small branching fraction into top quarks, and the branching fraction to di-taus just varies smoothly with the increasing mass of the technipion. As we shall discuss shortly, such limits on technipions heavier than $2m_t$ would not hold in models where the extended technicolor dynamically generates the bulk of the top quark mass and the technipion has an appreciable top-quark branching fraction.

2.4 Models with colored technifermions and a top mass generated by ETC

We will now illustrate how the above constraints are modified in theories where the top-quark's mass includes a substantial contribution from extended technicolor. In such models, the ETC coupling between the top quark and technipion can be relatively large, which has several consequences.

First, it means that for technipions heavy enough to decay to top-quark pairs that channel will dominate, so that the branching fractions to $\tau^+\tau^-$ and $\gamma\gamma$ become negligible. So these models can be constrained by the LHC data discussed in this work only for $M_P < 2m_t$. Second, it implies that charged technipions P^+ that are lighter than the top quark can open a new top-quark decay path: $t \to P^+ b$. Existing bounds on this decay rate preclude charged technipions lighter than about 160 GeV; for simplicity, we will take this to be an effective lower bound on the mass of our neutral technipions in our discussion here – though, in

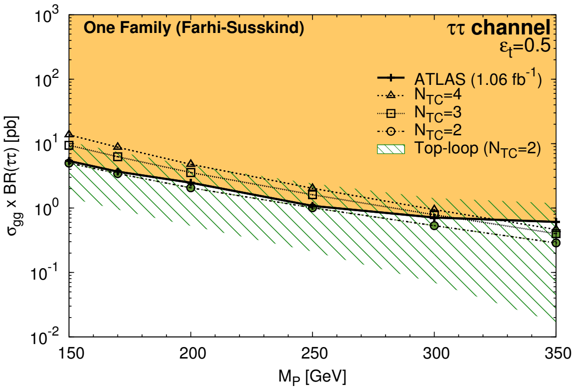

(a) Original one-family model [152].

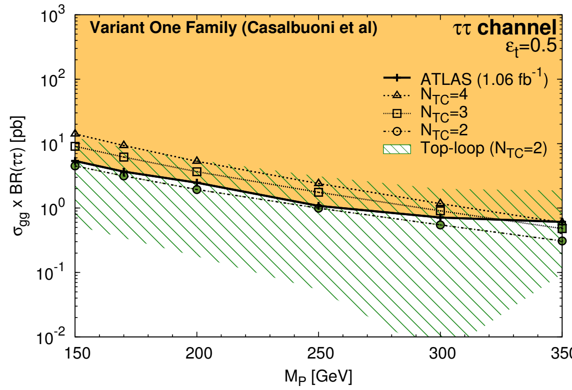

(b) Variant one-family model [150].

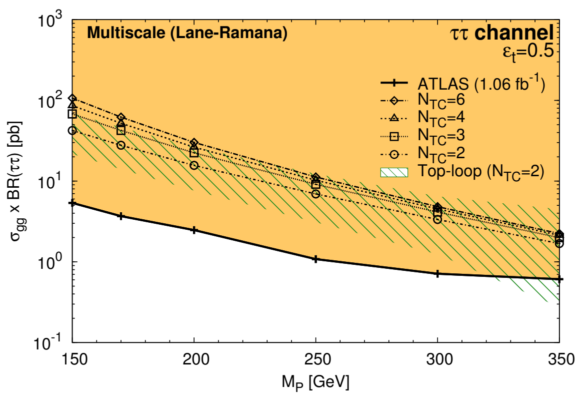

(c) Multiscale walking technicolor model [153].

Figure 2.5: Comparison of data and theory for production of a new scalar of mass 150 - 350 GeV that decays to tau lepton pairs; here, technipion production through techniquark loops is potentially modified by including production via top quark loops assuming extended technicolor generates most of the top quark's mass. In each pane, the shaded region (above the solid line) is excluded by the 95% CL upper limits on $\sigma_h B_{\tau^+\tau^-}$ from ATLAS [144]. As in Fig. 2.4, each pane displays the theoretical prediction (including techniquark loops only) from one technicolor model with colored technifermions, as a function of technipion mass and for several values of N_{TC}. Values of M_P and N_{TC} for a given model that are not excluded by this data are shown as solid (green) symbols. The hatched region indicates (for $N_{TC} = 2$) how including the contributions of top-quark loops could impact the model prediction, assuming $\epsilon_t = 0.5$. If the top and techniquark loop contributions interfere constructively, the model prediction moves to the top of the hatched region; if they interfere destructively, the model prediction moves to the bottom of the hatched region. *Continued next page.*

Figure 2.5 (cont'd)

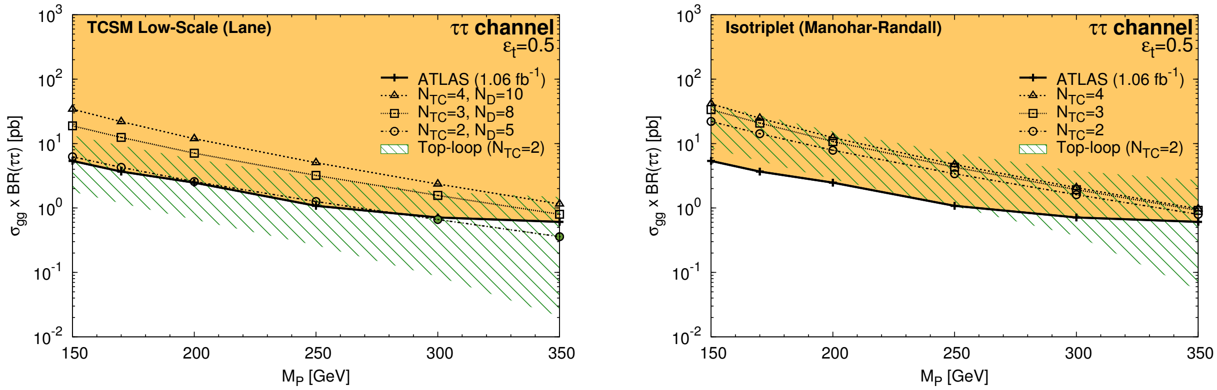

(d) TCSM Low-scale techncilor model (the Technicolor Straw Man model) [154].

(e) Isotriplet model [146].

principle, it is possible for the neutral technipion to be lighter than its charged counterpart. Based on these considerations, we will be considering possible LHC bounds on technipions with substantial coupling to top quarks and lying in the mass range 160 GeV $< m_P < 2m_t$; at present only data on di-tau final states exists for this mass range.

Within this mass range, the presence of a large top-technipion coupling allows gluon fusion through a top-quark loop (as in Fig.2.1(c)) to become a significant source of technipion production. Extrapolating from the expressions for decay of a pseudoscalar boson in [158], one finds that the decay of technipion P to gluons through a top-quark loop has the rate:

$$\Gamma^{top}(P \to gg) = \frac{m_P^3}{8\pi} \left(\frac{\alpha_s \epsilon_t}{2\pi F_P} \right)^2 [\tau f(\tau)]^2 \tag{2.19}$$

where ϵ_t is the ETC-mediated top-quark coupling to technipions, τ and $f(\tau)$ are as defined in Eqs. (2.4) and (2.5), and the expression $[\tau f(\tau)] \to 1$ in the limit of large top-quark mass. Comparing this with Eqn. (2.3), we see that the ratio

$$\frac{\Gamma^{top}(P \to gg)}{\Gamma(P \to gg)} = \left(\frac{\epsilon_t [\tau f(\tau)]}{N_{TC} \mathcal{A}_{gg}} \right)^2 \equiv \left(R^{loops} \right)^2 \tag{2.20}$$

can be substantial if $\epsilon_t \approx 1$ and N_{TC} is small.

The relative sign of the techniquark loop and top-quark loop contributions depends on the structure of the ETC sector of the theory. In models where this sign is positive, the top-quark and techniquark amplitudes will add constructively and the limits derived in the previous section will be strengthened. However, in models where the relative sign is negative, the diagrams in Fig. 2.1(a) and 2.1(c) will interfere destructively, reducing the rate of technipion production calculated in the previous section by a factor of

$$\left(1 - R^{loops}\right)^2 \tag{2.21}$$

That has the potential to weaken the bounds from the LHC data.

Moreover, in a technicolor model where both N_{TC} and $\mathcal{A}_{gg}$ are relatively small, for light technipion masses where $\tau f(\tau) \approx 1$, the ratio R^{loops} can be greater than one, meaning that the top-quark loop can contribute more to technipion production than the techniquark loop. For heavier technipion masses, the relative importance of the top-quark loop declines, and the two contributions interfere strongly, so that the production rate declines and the limits from LHC data become much weaker. For still heavier technipion masses, the techniquark loop begins to dominate again and the interference loses its impact on the strength of the bounds.

This behavior is visible in Fig. 2.5, which shows how the limits on the $N_{TC} = 2$ version of each model would be affected by the presence of top-quark loops with $\epsilon_t = 0.5$. The data, shaded region, and model prediction curve are as in Fig. 2.4, for the mass range 160 GeV $< M_P < 2m_t$. Also shown here is a hatched region that illustrates how the model curve would move upwards (downwards) in the presence of constructive (destructive) interference between the top and technifermion loops. The destructive interference would have little impact on the constraint the LHC data places upon the multiscale model, and progressively greater impact on the viability of the $N = 2$ versions of the isotriplet, TCSM low-scale, and original one-family models. In the variant one-family model, we see that the contribution from the top loop would, as discussed above, dominate at lower m_P, cancel the techniquark loop contribution at $m_P \approx 300$ GeV (so that the expected cross-section would vanish), and then diminish in size for larger m_P.

We have also explored the impact of top loop contributions with $\epsilon_t = 0.5$ on the $N_{TC} = 4$ versions of the models, where the value of R^{loops} would be smaller by a factor of two. We find that destructive interference from top loops would leave the LHC data's exclusion of technipions intact across the range 160 GeV $< m_P < 2m_t$ in the multiscale model, would bring the upper end of the excluded range down to 325 GeV (300 GeV, 250 GeV) in the isotriplet (TCSM low-scale, variant one-family) model from the value of $2m_t$ shown in Fig. 2.4, and bring the upper range of the excluded range down to about 250 GeV from the previous 325 GeV (per Fig. 2.4) in the original one-family model. The impact on models with even larger values of N_{TC} would be proportionately smaller.

Finally, we note that if data were available for di-photon final states in the applicable mass range, it would be possible to discern the impact of destructive interference between top and technifermion loops on the data's ability to constrain the models. In this case, one would need to include effects of top-quark loops both on technipion production from gluon fusion and also on technipion decay to two photons.

2.5 Discussion and Conclusions

In [1] we have used the LHC limits on the $\gamma\gamma$ [141, 142] and $\tau^+\tau^-$ [143, 144, 145] decay modes of a standard model Higgs boson to constrain the technipion states predicted in technicolor models with colored technifermions. As discussed in [124], the technipions tend to produce larger signals in both channels than h_{SM} would, so that this is an effective way of constraining such technicolor models. Because the technipions are spinless, just like the standard model Higgs boson, the di-photon and di-tau final states resulting from decay of the produced boson would have the same kinematic properties, so there should be no change in the efficiencies and acceptances. Hence, it is possible to adapt the limits quoted by the collaborations for the Higgs searches very directly to technicolor models with colored technifermions.

We have found that the combined limits on Higgs bosons decaying to di-photon or di-tau final states from the ATLAS and CMS collaborations exclude at 95% CL the presence of technipions in the mass range from 110 GeV nearly up to $2m_t$ for any of the representative models considered here for $N_{TC} \geq 3$. Even if one takes $N_{TC} = 2$ to make the production rate as small as possible, the multiscale [153] and isotriplet [146] models are excluded up to $2m_t$; the TCSM low-scale [154] is excluded for technipion masses up to nearly 300 GeV; and the original [152] and variant [150] one-family model are only marginally consistent with data. The implication for technicolor model building is clear: models with light technipions and colored technifermions are not allowed by the LHC data, except possibly in a few models with $N_{TC} = 2$. Model-builders will need to consider scenarios with heavier pseudo Nambu-Goldstone bosons or theories in which the technifermions are color-neutral.

Moreover, we have also seen that the ATLAS limits on a scalar decaying to $\tau^+\tau^-$ constrain the presence of technipions in the mass range $2m_t < M_P < 450$ GeV if the technipion decays only negligibly to top quarks – as in models where the top quark's mass is being generated by a topcolor [98] sector instead of by extended technicolor. The excluded mass range extends to 450 GeV (375 GeV) for a multi scale (isotriplet) technicolor sector for any value of N_{TC} and reaches 375 GeV for a TCSM low-scale technicolor sector with $N_{TC} \geq 3$. Hence, starting from these technicolor sectors, building a topcolor-assisted technicolor [100] model would now require ensuring that the technipions have masses above 375 - 450 GeV. This complements recent LHC searches for $H \to WW, ZZ$ that exclude the top-Higgs state of TC2 models for masses below 300 GeV if the associated top-pion has a mass of 150 GeV (the lower bound rises to 380 GeV if the top-pion mass is at least 400 GeV) [126].

In principle, there are several ways to construct technicolor models that could reduce the scope of these limits. As discussed earlier, one possibility is to arrange for the extended technicolor sector to provide a large fraction of the top quark's mass (though it would be necessary to find a new way to evade bounds on FCNC and weak isospin violation). In this case, gluon fusion through a top-quark loop (as in Fig. 2.1(c)) could provide an alternative production mechanism for the technipions. If the ETC structure of the model caused the top-quark and techniquark loop amplitudes to interfere constructively, our bounds would be strengthened; but, as illustrated in Fig. 2.5, in a model where the interference was destructive, our limits on the technipion mass could be weakened, at least for small values of N_{TC}.

Another possibility is to build a technicolor model that includes technipions but not colored technifermions[7]. In order for extended technicolor to provide mass to the quarks, color must then be embedded in the ETC group alongside technicolor, and some ETC gauge

[7] One example is the "minimal walking technicolor" model in [165] with technifermions in the symmetric tensor representation and $N_{TC} = 2$; various aspects of its collider phenomenology have been predicted, for instance, in [166, 167]

bosons will carry color charge. It would be more difficult to use the LHC data discussed here to set broadly-applicable limits on technipions appearing in such models. The production mechanism contributing most strongly to the rate for the states we studied would not be operative; that is, without colored technifermions, the process illustrated in Fig. 2.1(a) would be absent. The analogous process with top quarks instead of colored technifermions in the loop (as in Fig. 2.1(c)) could, in principle, contribute, but there will be no loop-derived enhancement by N_{TC} as in the diagram of Fig. 2.1(a). If the coupling of the top quarks to the technipion were large, that could provide an enhancement to replace the missing N_{TC} factor – but, as we have seen, the coupling is highly model-dependent. And, as mentioned earlier, building a model where ETC provides most of the top quark mass (and the top-technipion coupling is large) remains an open challenge, because it is hard to accomplish this without contravening experimental limits on flavor-changing neutral currents [81, 82] or isospin violation [91].

A third option would be to base a model around a technicolor sector devoid of technipions, such as the original one-doublet model of [78, 79, 80] or a modern "next-to-minimal" walking technicolor model with technifermions in the symmetric tensor representation of technicolor and $N_{TC} = 3$ [165]. Of course, these models come with their own complexities and challenges.

This first set of LHC data has excluded a large class of technicolor and topcolor-assisted technicolor models that include colored technifermions – unless the technipions states can be made relatively heavy or the extended technicolor sector can be arranged to cause interference between top-quark and techniquark loops. Model builders will need to either identify specific technicolor theories able to withstand the limits discussed here, while generating the top quark mass without excessive weak isospin violation or FCNC, or else seek new directions for a dynamical explanation of the origin of mass. Finally, we would like to stress that additional LHC data that gives greater sensitivity to new scalars decaying to $\tau^+\tau^-$ or that addresses scalars with masses over 145 GeV decaying to $\gamma\gamma$ could quickly probe models down to the minimum number of technicolors and up to higher technipion masses.

Chapter 3

Discovering Strong Top Dynamics at the LHC

— *This chapter is based on a work in collaboration with R. Sekhar Chivukula, Elizabeth H. Simmons, Baradhwaj Coleppa, Heather E. Logan, Adam Martin, and Jing Ren, which has appeared in [3].*

3.1 Introduction

In Chapter 2, we saw how the searches for the Higgs placed restrictions on new physics models describing the electroweak symmetry breaking via strong dynamics. The "4^{th} of July 2012 discovery" of the Higgs-like boson with mass of approximately 125 GeV was able to provide much stronger constraints on models of this kind. In this chapter, we focus on models where the top-quark plays a special role in electroweak symmetry breaking; *i.e.*, models with strong top dynamics.

As discussed in Section 1.2 of Chapter 1 phenomenology of the scalar sector of a model with separate sectors for mass generation of the top quark and of the electroweak bosons can be conveniently described by the Top Triangle Moose model [119]. In section, 1.3, we noted that a light top-Higgs has already been tightly constrained [125, 126] by negative findings from the Higgs searches. The work on which this chapter is based then presents an update of that result in light of new data from the LHC and considers bounds on the top-pions that are also present. In particular, it explores the possibility that the new boson with a mass of approximately 125 GeV [168, 45, 161, 44] observed at the LHC is consistent with a neutral pseudoscalar top-pion state.[1] We demonstrate that a neutral pseudoscalar top-pion can generate the diphoton signal at the observed rate. However, the region of model parameter space where this is the case does not correspond to classic topcolor-assisted technicolor scenarios with degenerate charged and neutral top-pions and a top-Higgs mass of order $2m_t$; rather, additional isospin violation would need to be present and the top dynamics would be more akin to that in top seesaw models [105, 106, 107]. Moreover, the interpretation of the new state as a top-pion can be sustained only if the ZZ (four-lepton) and WW (two-lepton plus missing energy) signatures initially observed at the 3σ level decline in significance as additional data is accrued.[2]

The LHC evidence for a new boson is composed of several components, based on separate event samples optimized to be sensitive to the production of the new boson via gluon-fusion, via vector-boson fusion, or in association with an electroweak boson or a top-quark pair, and the subsequent decay of the boson to two photons, two massive electroweak bosons, or pairs of tau-leptons or bottom-quarks [45, 44]. While the totality of evidence including all subchannels provides convincing evidence of a new bosonic state – one consistent with a Standard Model (SM) Higgs – the statistical significance of the different subchannels varies, and it is not yet certain that the object discovered is *the* Higgs boson. With the data

[1] The possibility that the boson observed at the LHC is a pseudo-scalar has been considered by a number of authors recently [169, 170, 171, 172, 173, 174, 175].

[2] Currently, the production and decay properties of the observed 126 GeV boson in the ZZ and WW final states are consistent with the expectations for the Higgs boson of the Standard Model [46, 52, 53, 120].

available at the time of the work the evidence for the new boson is strongest in the diphoton channel, with a local p-value showing that the "background-only" hypothesis is excluded at more than the 4σ level by both experiments (a level which is *larger* than would have been expected with the current data set for the SM Higgs). The evidence in the next most sensitive decay channel, ZZ^* subsequently decaying to four charged-leptons (e or μ), is also strong – with a local p-value rejecting the background-only hypothesis at the 3σ level. The search for the WW^* decay mode, in which the W-bosons subsequently decay to e or μ and corresponding neutrino, is less constraining since it is not possible to measure the diboson invariant mass – though the background only hypothesis is disfavored by 2-3 σ. Finally, the evidence for the decay of the new boson to fermions, either tau-leptons or bottom-quarks, is so far inconclusive.

Our goal in this work [3] is to further the phenomenological investigation of the top-pions and top-Higgs at the LHC that was started in [119, 125, 126]. We begin in Sec. 3.2 by setting out the relevant details of the Top Triangle Moose model. Sections 3.3 – 3.5 contain the bulk of our phenomenological results. In Sec. 3.3 we first consider the possibility that the diphoton signal observed at the LHC arises from the neutral pseudoscalar top-pion and find the range of model parameters consistent with these experimental results. Since this object is a psuedoscalar, it lacks tree-level couplings to ZZ and WW [173, 176, 177]. While the top-pion can decay to ZZ or WW through a top-quark loop, we show that these effects would be too small to be observable in the current data. In Sec. 3.4 we demonstrate that, for the value of model parameters such that the neutral top-pion can account for the observed LHC diphoton signal, the properties of top-quark decay imply that the corresponding charged top-pions would have to be heavier than 150 GeV. As reviewed in Appendix B.1, however, this implies that the model would need to include more isospin violation than is the minimum required to produce a heavy top-quark – i.e., more isospin violation than is usually assumed to exist in these models. In Sec. 3.5 we review and update the constraints previously derived in [126], in the case that the 125 GeV object is associated with the neutral top-pion. We summarize our findings and discuss their implications in Sec. 3.6.

3.2 The Scalar Spectrum and Properties

On one level, the Top Triangle Moose model is an example of a deconstructed Higgsless model of electroweak symmetry breaking. Inspired by the possibility of maintaining perturbative unitarity in extra-dimensional models through heavy vector resonance exchanges in lieu of a Higgs [108, 109, 110], Higgsless models were initially introduced in an extra-dimensional context as $SU(2) \times SU(2) \times U(1)$ gauge theories living in a slice of AdS_5, with symmetry breaking codified in the boundary condition of the gauge fields [111, 112, 113, 114, 115, 116]. The low energy dynamics of these extra-dimensional models can be understood in terms of a collection of 4-D theories, using the principle of "deconstruction" [178, 179]. Essentially, this involves latticizing the extra dimension, associating a 4-D gauge group with each lattice point and connecting them to one another by means of nonlinear sigma models; the picture that emerges is called a "Moose" diagram [180]. The five dimensional gauge field is now spread in this theory as four dimensional gauge fields residing at each lattice point, and the fifth scalar component residing as the eaten pion in the sigma fields.

The key features of these models [181, 182, 183, 184, 185, 186, 187, 188, 189, 190, 191, 192] that are relevant to our discussion are as follows: Spin-1 resonances created by the strong dynamics underlying the sigma fields are described as massive gauge bosons, following the Hidden-Local-Symmetry scenario originally used for QCD [193, 194, 195, 196, 197] and also the BESS [181, 182] models. The phenomenology of those resonances in the Top Triangle Moose have been discussed in Refs. [118, 119]. Standard model (SM) fermions reside primarily on the exterior sites – the sites approximately corresponding to $SU(2)_w$ and $U(1)_Y$ gauge groups; these fermions become massive through mixing with massive, vector-like fermions located on the interior, 'hidden' sites. The phenomenology of these fermions has previously been discussed in [119, 125]. Precision electroweak parameters [198], are accommodated by adjusting the SM fermion's distribution across sites [191] to match the gauge boson distribution, a process called "ideal delocalization" [184]. This is identical to the solution used in extra-dimensional Higgsless models, where the spreading of a fermion among sites becomes a continuous distribution, or profile, in the extra dimension [114].

The AdS/CFT correspondence suggests that these weakly-coupled Higgsless models can be understood to be dual to the strongly coupled models of electroweak symmetry breaking. Indeed the Top Triangle Moose is a deconstructed analog of topcolor-assisted technicolor (TC2) [98, 100, 101, 102, 103, 99, 104], a scenario of dynamical electroweak symmetry breaking in which the new strong dynamics is partitioned into two different sectors. The technicolor sector [79, 80] is responsible for the bulk of electroweak symmetry breaking, through condensation of a technifermion bilinear, and is therefore characterized by a scale $F \sim v$, where $v = 246$ GeV is the EWSB scale. Consequently, technicolor dynamics is responsible for the majority of the weak gauge boson masses and, more indirectly [82, 81], the masses of the light fermions. The second strong sector, the topcolor sector [98, 100], communicates directly with the top quark. Its purpose is to generate a large mass for the top quark through new strong dynamics that cause top quark condensation [92, 93, 94, 95, 96]. In generating a top-quark mass, this second sector also helps to break the electroweak symmetry. If the characteristic scale of the topcolor sector is low, $f \ll F$, it plays only a minor role in electroweak breaking, but can still generate a sufficiently large top-quark mass given a strong enough top-topcolor coupling. Because electroweak symmetry is effectively broken twice in this scenario, there are two sets of Goldstone bosons. One linear combination of the weak-triplet Goldstone bosons (the combination primarily composed of technifermions) is eaten to become the longitudinal modes of the $W^{\pm}/Z^{0}$, while the orthogonal triplet and accompanying weak singlet state remain in the spectrum. These remaining states, typically referred to as the top-pions and the top-Higgs, are the focus of this chapter.

Probing the dynamics of topcolor assisted technicolor will involve discovering the top-Higgs and top-pions which are associated with the generation of the large top-quark mass, and measuring their properties. In this section we describe briefly our expectations for the properties of these states, and summarize the model-dependence of their couplings.

3.2.1 The Triangle Moose Model

The Top Triangle Moose model [119] is shown in Moose notation in Fig. 3.1. The circles represent global SU(2) symmetry groups; the full SU(2) at sites 0 and 1 are gauged with gauge couplings g and $\tilde{g}$, respectively, while the τ^3 generator of the global SU(2) at site 2 is gauged with U(1) gauge coupling g'. The lines represent spin-zero link fields which transform as a fundamental (anti-fundamental) representation of the group at the tail (head) of the link. Σ_{01} and Σ_{12} are nonlinear sigma model fields, describing the technicolor/three-site [118] sector of the theory, while Φ (the top-Higgs doublet) is a linear sigma model field arising from top-color [98, 100].

The kinetic energy terms of the link fields corresponding to these charge assignments are:

$$\mathcal{L}_{gauge} = \frac{F^2}{4}\mathrm{Tr}[(D_\mu\Sigma_{01})^\dagger D^\mu\Sigma_{01}] + \frac{F^2}{4}\mathrm{Tr}[(D_\mu\Sigma_{12})^\dagger D^\mu\Sigma_{12}] + (D_\mu\Phi)^\dagger D^\mu\Phi, \qquad (3.1)$$

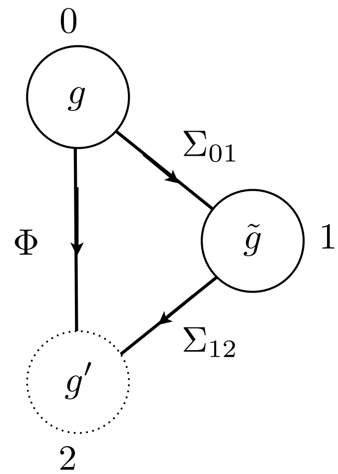

Figure 3.1: The gauge structure of the model in Moose notation. g and g' are approximately the Standard Model $SU(2)$ and hypercharge gauge couplings while $\tilde{g}$ represents the 'bulk' gauge coupling. The left (right) handed light fermions are mostly localized at site 0 (2) while their heavy counterparts are mostly at site 1. The links connecting sites 0 and 1 and sites 1 and 2 are nonlinear sigma model fields while the one connecting sites 0 and 2 is a linear sigma field. Site 2 is dotted to indicate that only the τ_3 component is gauged.

where the covariant derivatives are:

$$
\begin{aligned}
D_\mu \Sigma_{01} &= \partial_\mu \Sigma_{01} + igW_{0\mu}\Sigma_{01} - i\tilde{g}\Sigma_{01}W_{1\mu}, \\
D_\mu \Sigma_{12} &= \partial_\mu \Sigma_{12} + i\tilde{g}W_{1\mu}\Sigma_{12} - ig'\Sigma_{12}\tau^3 B_\mu, \\
D_\mu \Phi &= \partial_\mu \Phi + igW_{0\mu}\Phi - \frac{ig'}{2}B_\mu \Phi.
\end{aligned}
\tag{3.2}
$$

Here the gauge fields are represented[3] by the matrices $W_{0\mu} = W^a_{0\mu}\tau^a$ and $W_{1\mu} = W^a_{1\mu}\tau^a$, where $\tau^a = \sigma^a/2$ are the generators of SU(2). The nonlinear sigma model fields Σ_{01} and Σ_{12} are 2×2 special unitary matrix fields. To mimic the symmetry breaking caused by underlying technicolor and topcolor dynamics, we assume all link fields develop vacuum

[3]Here the subscripts appearing in the fields will refer to the "site" numbers and the superscripts will be reserved for $SU(2)$ indices.

expectation values (vevs):

$$\langle \Sigma_{01} \rangle = \langle \Sigma_{12} \rangle = \mathbf{1}_{2\times 2}, \qquad \langle \Phi \rangle = \begin{pmatrix} f/\sqrt{2} \\ 0 \end{pmatrix}. \tag{3.3}$$

In order to obtain the correct amplitude for muon decay, we parameterize the vevs in terms of a new parameter ω,

$$F = \sqrt{2}\, v \, \cos \omega, \qquad f = v \, \sin \omega, \tag{3.4}$$

where $v = 246$ GeV is the weak scale. We will explore the parameter range[4] $0.2 \leq \sin\omega \leq 0.8$, in which the Top Triangle Moose acts as a low-energy effective theory for a variety of models with strong top dynamics [126]. As a consequence of the vacuum expectation values, the gauge symmetry is broken all the way down to electromagnetism and we are left with massive gauge bosons (analogous to techni-resonances), top-pions and a top-Higgs. To keep track of how the degrees of freedom are partitioned after we impose the symmetry breaking, we expand Σ_{01}, Σ_{12} and Φ around their vevs. The coset degrees of freedom in the bi-fundamental link fields Σ_{01} and Σ_{12} can be described by nonlinear sigma fields:

$$\Sigma_{01} = \exp\left(\frac{2i\pi_0^a \tau^a}{F}\right), \qquad \Sigma_{12} = \exp\left(\frac{2i\pi_1^a \tau^a}{F}\right), \tag{3.5}$$

[4]The extreme case in which $\sin\omega \to 1$ would have a rather different phenomenology, as the properties of the top-Higgs boson would approach those of the Standard Model Higgs boson, the top-Higgs could potentially be light, and the top-pions would become heavier.

while the degrees of freedom in Φ fill out a linear representation,

$$\Phi = \begin{pmatrix} (f + H_t + i\pi_t^0)/\sqrt{2} \\ \\ i\pi_t^- \end{pmatrix}. \tag{3.6}$$

The gauge-kinetic terms in Eq. (3.1) yield mass matrices for the charged and neutral gauge bosons. The photon remains massless and is given by the exact expression

$$A_\mu = \frac{e}{g} W_{0\mu}^3 + \frac{e}{\tilde{g}} W_{1\mu}^3 + \frac{e}{g'} B_\mu, \tag{3.7}$$

where e is the electromagnetic coupling. Normalizing the photon eigenvector, we get the relation between the coupling constants:

$$\frac{1}{e^2} = \frac{1}{g^2} + \frac{1}{\tilde{g}^2} + \frac{1}{g'^2}. \tag{3.8}$$

This invites us to conveniently parametrize the gauge couplings in terms of e by

$$g = \frac{e}{\sin\theta\cos\phi} = \frac{g_0}{\cos\phi}, \qquad \tilde{g} = \frac{e}{\sin\theta\sin\phi} = \frac{g_0}{\sin\phi}, \qquad g' = \frac{e}{\cos\theta}. \tag{3.9}$$

We will take $\tilde{g} \gg g$, which implies that $\tan\phi \equiv x$ is a small parameter.

3.2.2 The Triangle Moose Potential: Scalar Spectrum and Isospin Violation

Counting the number of degrees of freedom, we see that there are six scalar degrees of freedom on the technicolor side $(\Sigma_{01}, \Sigma_{12})$ and four on the topcolor side (Φ). Six of these will be eaten to form the longitudinal components of the $W^{\pm}$, Z^0, $W'^{\pm}$, and Z'^0. This leaves one isospin triplet of scalars, the top-pions Π_t^a, and the top-Higgs H_t as physical states in the spectrum. While the interactions in Eq. (3.1) are sufficient to give mass to the gauge bosons, the top-pions and top-Higgs remain massless at tree level. Quantum corrections will give the top-pions a mass, however this loop-level mass is far too small to be consistent with experimental constraints. To generate phenomenologically acceptable masses for the top-pions and top-Higgs, we add three[5] additional interactions:

$$\begin{aligned}\mathcal{L}_M &= -\lambda\,\mathrm{Tr}\left(M^\dagger M - \frac{f^2}{2}\right)^2 - \kappa f^2\,\mathrm{Tr}\left|M - \frac{f}{\sqrt{2}}\Sigma_{01}\Sigma_{12}\right|^2 \\ &\quad + \left\{\epsilon f^2\left(\mathrm{Tr}\left[M^\dagger\Sigma_{01}\Sigma_{12}\tau^3\right]\right)^2 + \text{h.c.}\right\}\ , \end{aligned} \tag{3.10}$$

where the first of these interactions arises from topcolor interactions, the second from ETC-like interactions [82, 81], and the third is an example of possible isospin-violating interactions in the top-color sector. Here λ, κ, and ϵ are three new dimensionless parameters that depend on the details of the top-color dynamics, f is the same vacuum expectation value appearing in Eq. (3.4), and M is the Φ field expressed as a matrix[6], schematically given by $M = (\Phi, \tilde{\Phi})$

[5] In [119] the possibility of isospin violation, and hence the last term in Eq. (3.10), was neglected. As we show in Appendix B.1, isospin violation in the top color sector is usually assumed to be small, and hence the size of the dimensionless parameter ϵ, is *small*. We introduce it here to explore the phenomenology that would arise from non-degenerate top-pions.

[6] This corrects the expression in [119].

with $\tilde{\Phi} = -i\sigma_2 \Phi^*$:

$$M = \begin{pmatrix} (f + H_t + i\pi_t^0)/\sqrt{2} & i\pi_t^+ \\ i\pi_t^- & (f + H_t - i\pi_t^0)/\sqrt{2} \end{pmatrix}, \tag{3.11}$$

where $\pi_t^+ = (\pi_t^-)^*$. The first term in Eq. (3.10) depends only on the modulus of M, and therefore contributes only to the mass of the top-Higgs. The second and third terms give mass to both the top-Higgs and the physical (uneaten) combination of pion fields, as we will show shortly. Because these masses depend on three parameters, λ, κ, and ϵ, we can treat the mass of the top-Higgs and the masses of the uneaten charged and neutral top-pions as three independent parameters. In addition to generating masses, the potential in Eq. (3.10) also induces interactions between the top-Higgs and top-pions which are important in our analysis.

The next step towards understanding top-pion phenomenology is to identify the combination of degrees of freedom which make up the physical (uneaten) top-pions. While the top-Higgs H_t remains a mass eigenstate, the pions π_0^a, π_1^a and π_t^a mix. We can identify the physical top-pions as the linear combination of states that cannot be gauged away. We do this by isolating the Goldstone boson states that participate in interactions of the form $V_\mu \partial^\mu \pi$ in the Lagrangian. We start by expanding the nonlinear sigma fields to first order in π/F,

$$\Sigma_{01} = 1 + \frac{2i\pi_0^a \tau^a}{F} + \mathcal{O}\left(\frac{\pi^2}{F^2}\right), \tag{3.12}$$

$$\Sigma_{12} = 1 + \frac{2i\pi_1^a \tau^a}{F} + \mathcal{O}\left(\frac{\pi^2}{F^2}\right). \tag{3.13}$$

Plugging this in Eq. (3.1), we can read off the various interaction terms. The gauge-Goldstone mixing terms are of the form:

$$\mathcal{L}_{\text{mixing}} = \frac{g}{2} W_0^{a\mu} \partial_\mu \left[F\pi_0^a + f\pi_t^a\right] + \frac{\tilde{g}}{2} W_1^{a\mu} \partial_\mu \left[F\pi_1^a - F\pi_0^a\right] - \frac{g'}{2} B_2^\mu \partial_\mu \left[F\pi_1^3 + f\pi_t^3\right]. \quad (3.14)$$

Note that the pion combination in the third term can be written as a linear combination of those appearing in the first two terms:

$$F\pi_1^3 + f\pi_t^3 = [F\pi_0^3 + f\pi_t^3] + [F\pi_1^3 - F\pi_0^3]. \quad (3.15)$$

The two eaten triplets of pions span the linear combinations that appear in the first two terms of Eq. (3.14), leaving the third linear combination as the remaining physical top-pions, which we will denote Π_t^a:

$$\Pi_t^a = -\sin\omega \left(\frac{\pi_0^a + \pi_1^a}{\sqrt{2}}\right) + \cos\omega\, \pi_t^a, \quad (3.16)$$

where we have normalized the state properly using the definitions of F and f in Eq. (3.4).

The physical top-pions can also be identified by expanding the top-Higgs potential given in Eq. (3.10) and collecting the mass terms. The physical masses of the top-Higgs and top-pions are

$$\begin{aligned} M^2_{\Pi_t^\pm} &= 2\kappa v^2 \tan^2\omega \\ M^2_{\Pi_t^0} &= 2(\kappa - \epsilon) v^2 \tan^2\omega \\ M^2_{H_t} &= 2(4\lambda + \kappa) v^2 \sin^2\omega = 8\lambda v^2 \sin^2\omega + M^2_{\Pi_t^+} \cos^2\omega. \end{aligned} \quad (3.17)$$

while the other two linear combinations of pions are massless, as true Goldstone bosons should be. Equation (3.10) also contains trilinear couplings between H_t and two top-pions; the Feynman rules for the $H_t\Pi_t^+\Pi_t^-$ and $H_t\Pi_t^0\Pi_t^0$ interactions are given by

$$
\begin{aligned}
H_t\Pi_t^+\Pi_t^- : \qquad & -2iv\sin\omega\left[4\lambda\cos^2\omega+\kappa\frac{\sin^4\omega}{\cos^2\omega}\right] \\
& = \frac{-i}{v\sin\omega}\left[M_{H_t}^2\cos^2\omega - M_{\Pi_t^+}^2 + 2M_{\Pi_t^+}^2\sin^2\omega\right] \\
H_t\Pi_t^0\Pi_t^0 : \qquad & -2iv\sin\omega\left[4\lambda\cos^2\omega+\kappa\frac{\sin^4\omega}{\cos^2\omega} - 2\epsilon\frac{\sin^2\omega}{\cos^2\omega}\right] \\
& = \frac{-i}{v\sin\omega}\left[M_{H_t}^2\cos^2\omega - M_{\Pi_t^+}^2 + 2M_{\Pi_t^0}^2\sin^2\omega\right] .
\end{aligned}
\tag{3.18}
$$

These couplings are important for top-Higgs decays when $M_{H_t} > 2M_{\Pi_t}$.

For the purposes of our phenomenological analysis we will take the masses of the top-Higgs, and of the charged and neutral top-pions as independent parameters. To give a sense of what might be expected from TC2 dynamics, we have looked at the expectations for these parameters in a Nambu– Jona-Lasinio (NJL) [76] approximation for the topcolor dynamics; our NJL calculation is summarized in Appendix B.1. From the NJL analysis we find:

- The top-Higgs mass satisfies $M_{H_t} = \mathcal{O}(2m_t)$ [76]. This result is known to change once subleading interactions are taken into account [96], and hence we take this result as only indicative that the top-Higgs should have a mass of order 200 - 700 GeV.

- The mass splitting between the charged and neutral top-pions is relatively small – with $\Delta M_\Pi/M_\Pi$ less than about 10%. We therefore conclude that the minimum amount of isospin violation required in topcolor (the amount necessary to yield the top-quark mass) need not produce a large mass splitting between the top-pions.

- The analysis also confirms that the form of the potential in Eq. (3.10), with $\epsilon \simeq 0$, correctly summarizes the non-derivative interactions yielding the top-pion and top-

Higgs masses and interactions. We therefore typically expect $M_{\Pi_t} \lesssim M_{H_t}$, *c.f.* Eq. (3.17) for small $\sin\omega$.

Based on these considerations, in what follows we explore the possibility that the new state at a mass of approximately 125 GeV observed at the LHC is consistent with a neutral pseudoscalar top-pion state. We consider two representative cases: (1) assuming degenerate charged and neutral top-pion masses, $M_{\Pi_t^\pm} = M_{\Pi_t^0}$, and (2) fixing $M_{\Pi_t^0} \approx 125$ GeV and allowing the charged top-pion mass to vary. As discussed above, the first case is that generically expected in top color models, and the second allows us to illustrate how these results would change if the top-color dynamics includes additional sources of isospin violation.

3.2.3 Scalar Couplings to Fermions

The couplings of the top-pion and top-Higgs to fermions are model dependent. Unlike in the standard model, the presence of two different sources for the quark masses (topcolor and technicolor) implies that the top-pion and top-Higgs couplings depend on the individual left-handed and right-handed rotations in the separate up- and down-quark sectors that relate the *topcolor* gauge eigenstates (in which the top-pion and top-Higgs couplings are simple) to the mass-eigenstates [100, 199, 200].

For our analysis, we make the following assumptions:

- Following [100, 199, 200], we assume that the top- and bottom-quarks both receive most of their mass as a result of topcolor (which would naturally explain why $V_{tb} \simeq 1$), while the other quarks and the leptons receive their masses from the (extended) technicolor sector. That is, if we were to "turn off" technicolor electroweak symmetry breaking ($F \to 0$ or $\cos\omega \to 0$) the top and bottom quarks would have masses close to their observed values, but all other quarks and the leptons would be massless.

- The usual CKM angles are related to the difference between the left-handed up- and down-quark rotations which are required. Since the observed CKM matrix is non-trivial, it is not possible that *both* of the left-handed up- and down-quark rotations are trivial. As we show in appendix B.2, however, if the observed CKM angles arise predominantly from rotations in the left-handed down-quark sector, charged top-pion exchange will lead to unacceptably large contributions to the process $b \to s\gamma$. We therefore assume that CKM mixing arises from the rotations in the left-handed up-quark sector.

- The rotations in the right-handed sector are, *a priori*, unconstrained. However, if present, they have the potential to lead to unacceptably large contributions to $B_d^0 - \bar{B}_d^0$ [199] and $D^0 - \bar{D}^0$ meson mixing. We therefore assume that there is no mixing in the right-handed sector.

With these assumptions, to leading order, the flavor-diagonal couplings of the neutral top-pions to the third generation fermions[7] are

$$\frac{i\,\Pi_t^0}{v}\left[m_t \cot\omega\, \bar{t}_L t_R + m_b \cot\omega\, \bar{b}_L b_R + m_\tau \tan\omega\, \bar{\tau}_L \tau_R\right] + h.c.\ . \tag{3.19}$$

The mixing in the left-handed up-quark sector will necessarily lead to flavor-changing decays of the neutral top-pion [201, 202] of the form

$$\frac{i\,\Pi_t^0}{v}\, m_t \cot\omega\, \left[V_{cb}^{CKM} \bar{c}_L t_R + V_{ub}^{CKM} \bar{u}_L t_R\right]\ . \tag{3.20}$$

[7] Couplings to the light quarks and leptons would follow the same pattern as for the τ lepton, but will not be needed in what follows.

The couplings of the top-Higgs to fermions are the scalar analogs of the pseudo-scalar couplings of the Π_t^0 listed in Eqs. (3.19) and (3.20) above.

Similarly, the corresponding charged-pion couplings are of the form[8]

$$\frac{i\sqrt{2}\Pi_t^+}{v}\left[m_t \cot\omega\, \bar{t}_R b_L + m_b \cot\omega\, \bar{t}_L b_R \right.$$
$$\left. + m_b \cot\omega\, V_{cb}^{CKM} \bar{c}_L b_R + m_\tau \tan\omega\, \bar{\nu}_{\tau L} \tau_R + m_c \tan\omega\, R_{cs} \bar{c}_R s_L \right] + h.c.\ , \tag{3.21}$$

where R_{cs} is an unknown mixing parameter which, for the purposes of illustration, we take equal to its maximum value $R_{cs} \simeq \cos\theta_C \simeq 1$.[9]

The relation between the assumptions made here and the simpler form of the fermion couplings used in [119] is presented in Appendix B.2.

3.3 Neutral top-pion phenomenology

In this section, we will discuss the phenomenology of the neutral top-pion assuming it has a mass of 125 GeV. We start by reviewing the couplings and decays, examine the production cross-section, and then discuss various decay modes in light of the LHC data. More details about the model can be found in Ref. [125].

3.3.1 Couplings and decays

The couplings of the neutral top-pion that are most relevant to our analysis are those to $gg, \gamma\gamma, b\bar{b}$, and $\tau\bar{\tau}$. The couplings to gluon pairs or photon pairs arise from top quark loops

[8]The coupling of Π_t^+ to $\bar{t}_R b_L$ gives a potentially large contribution to the process $Z \to b\bar{b}$ [203], which must be compensated for by adjusting the properties of the top-quark [125]. See the discussion in appendix B.2.

[9]If this coefficient were smaller, this would increase the branching ratio $BR(\Pi_t^+ \to \bar{\tau}\nu_\tau)$ which would strengthen the limits in section 3.4.

(contributions from loops containing heavy top-quark partners would be suppressed by powers of the heavy quark mass). Those to fermions arise from top color (for t and b) and/or extended technicolor dynamics (especially for lighter fermions). Being a pseudoscalar, the top-pion lacks tree-level couplings to WW and ZZ, and the loop induced couplings to these massive gauge bosons are small compared to the dominant ones listed above. These decays do occur through a top-quark loop, and are discussed separately.

We have calculated the branching ratios of Π_t^0 using the MSSM pseudoscalar decay routines in `HDECAY` version 3.531 [160], modified to take into account the different fermion coupling structure of Eqs. (3.19)–(3.20) and the absence of superpartners. The resulting branching ratios are illustrated in Fig. 3.2 for $\sin\omega = 0.3$, 0.5 and 0.7. Decays to $b\bar{b}$ dominate at low Π_t^0 mass, with the gg and tc channels becoming important only once $M_{\Pi_t^0} \gtrsim 200$ GeV. Decays to $t\bar{t}$ turn on at $M_{\Pi_t} \simeq 2m_t \simeq 350$ GeV and completely dominate above this mass. Note that our calculation using `HDECAY` includes decays to off-shell $t\bar{t}$ below threshold. As these plots indicate, for a 125 GeV top-pion, only the decay branching ratios to $gg, \gamma\gamma, b\bar{b}$ and $\tau\bar{\tau}$ are significant.

The total width of Π_t^0 is shown in the top panel of Fig. 3.3 as a function of $\sin\omega$, with $M_{\Pi_t^0} = 125$ GeV. Because its mass is well below the $t\bar{t}$ threshold, the Π_t^0 remains a narrow resonance with width below 1 GeV for all values of $\sin\omega \geq 0.2$.

In the bottom panel of Fig. 3.3 we display the branching ratio for $\Pi_t^0 \to \gamma\gamma$ as a function of $\sin\omega$ with $M_{\Pi_t^0} = 125$ GeV. This branching ratio reaches at most 0.5 parts per mil and is roughly five times smaller than the SM Higgs branching ratio into photons.

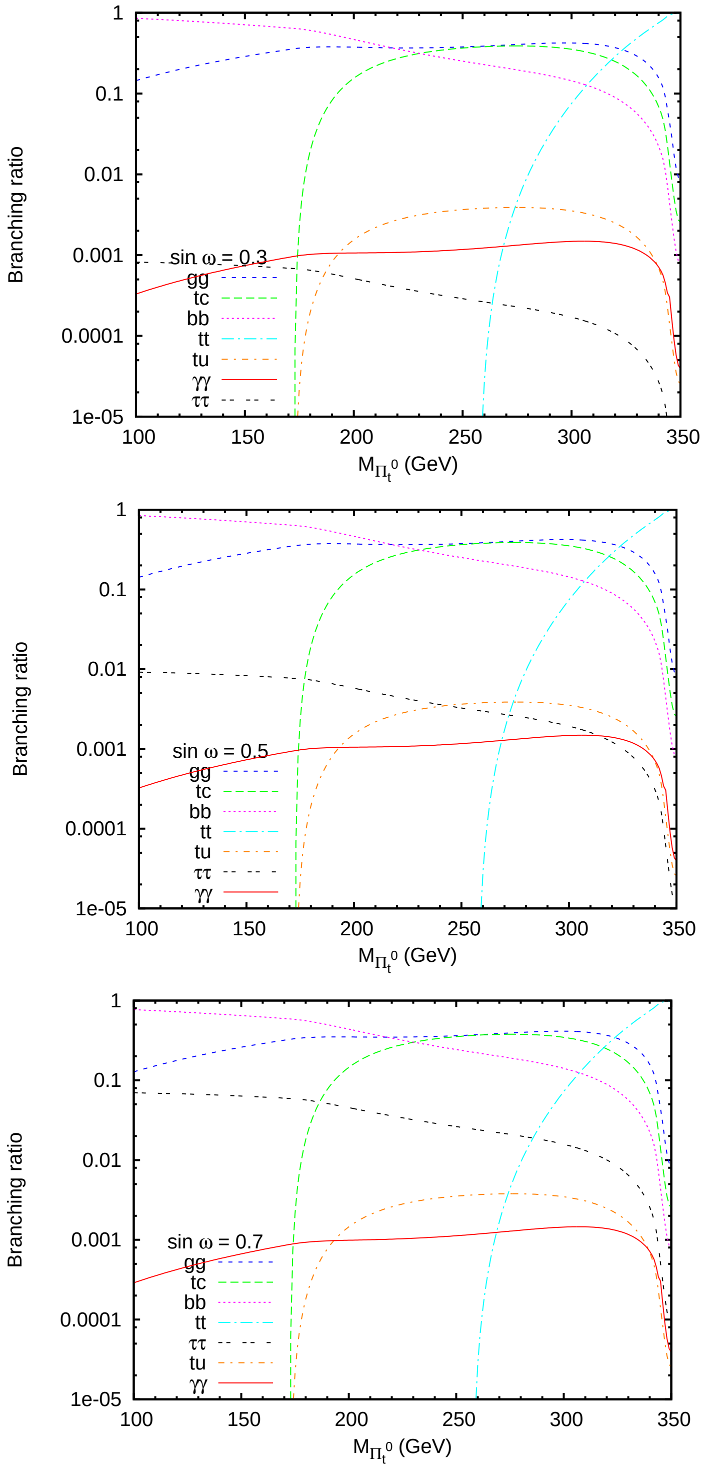

Figure 3.2: Branching ratios of the Π_t^0 into its dominant decay modes for $\sin\omega = 0.3$ (top), 0.5 (middle), and 0.7 (bottom). The order of the curves in the key (from top to bottom) reflects the order of the curves at $M_{\Pi_t^0} = 300$ GeV.

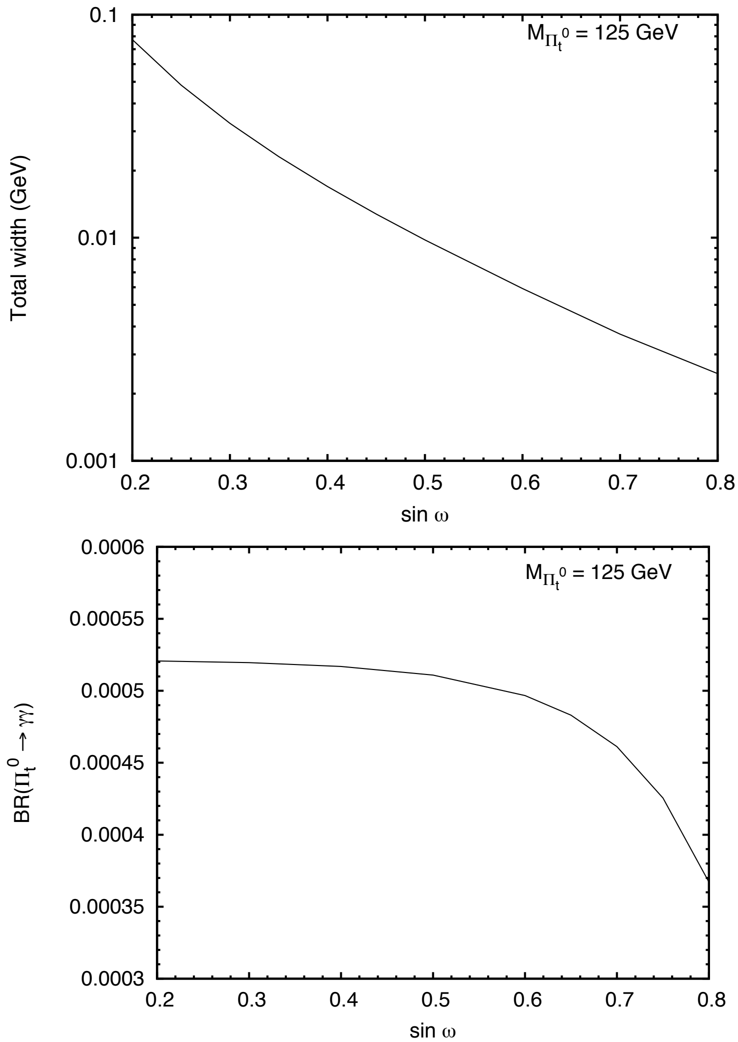

Figure 3.3: Total decay width (top) and branching ratio for $\Pi_t^0 \to \gamma\gamma$ (bottom) of a 125 GeV Π_t^0 as a function of $\sin\omega$.

3.3.2 Production cross-section

Here, we calculate the production cross-section of the neutral top-pion; in subsequent subsections we will compare this prediction to various ATLAS and CMS results to analyze the current and future LHC sensitivity to neutral top-pions.

The neutral top-pion is produced at the LHC almost exclusively via gluon fusion. We calculate the cross section for Π_t^0 production in gluon fusion according to

$$\sigma(gg \to \Pi_t^0) = \frac{\left|\sum_f \alpha_f F^A_{1/2}(\tau_f)\right|^2}{\left|\sum_f F^H_{1/2}(\tau_f)\right|^2} \times \sigma(gg \to H_{\rm SM}), \tag{3.22}$$

where in the sum over fermions we include[10] t, b and c; also $\alpha_t = \alpha_b = \cot\omega$ and $\alpha_c = \tan\omega$. Here the fermion loop functions $F^H_{1/2}(\tau)$ and $F^A_{1/2}(\tau)$, for scalars and pseudoscalars respectively, are given by [158]:

$$\begin{aligned} F^H_{1/2} &= -2\tau\left[1 + (1-\tau)f(\tau)\right], \\ F^A_{1/2} &= -2\tau f(\tau), \end{aligned} \tag{3.23}$$

where $\tau_f = 4m_f^2/M_\Pi^2$ and

$$f(\tau) = \begin{cases} \left[\sin^{-1}\left(\sqrt{1/\tau}\right)\right]^2 & \text{if } \tau \geq 1 \\ -\frac{1}{4}\left[\ln(\eta_+/\eta_-) - i\pi\right]^2 & \text{if } \tau < 1, \end{cases} \tag{3.24}$$

with $\eta_\pm = (1 \pm \sqrt{1-\tau})$. In the limit of a heavy fermion in the loop, $F^H_{1/2} \to -4/3$ and

[10] Technifermion loops do not contribute to top-pion production because the $SU(2)_{weak} \times [SU(3)]^2$ anomaly vanishes for any realistic technicolor theory.

$F^A_{1/2} \to -2$.

We take the SM gluon-fusion Higgs production cross section $\sigma(gg \to H_{\rm SM})$ from Ref. [204] for the 7 TeV LHC. This SM Higgs cross section includes the state-of-the-art radiative corrections, which boost the cross section by a substantial factor ~ 2. Our cross section in Eq. (3.22) relies on the equality of the k-factors for pseudoscalar production and scalar production. In fact, because most of the QCD k-factor comes from real radiation, this equality has been shown to hold to within 20%, as illustrated in [205].

3.3.3 Current and Prospective Limits from the Diphoton channel

The diphoton decay channel has played a leading role in LHC searches for the Standard Model Higgs boson. Although this is not the dominant decay mode for the neutral top-pion, it would certainly be highly visible in the LHC detectors. We have calculated $\sigma(gg \to \Pi_t^0) \times {\rm BR}(\Pi_t^0 \to \gamma\gamma)$ and our results are shown as a function of $\sin\omega$ (fixing $M_{\Pi_t^0} = 125$ GeV) in the top pane of Fig. 3.4. The signal rate is largest for small $\sin\omega$, due to the enhancement of both the Π_t^0 production cross section and the branching ratio to $\gamma\gamma$ at small $\sin\omega$.

The LHC SM Higgs searches in Refs. [206, 207] have exclusion sensitivity to $\gamma\gamma$ resonances with a cross section of order 50 fb for resonance masses between 110 and 150 GeV. We find that this excludes a neutral top-pion in this mass range with $\sin\omega \lesssim 0.4 - 0.5$. We show the excluded region in the right plot in Fig. 3.7, based on the 95% confidence level limit on $\sigma/\sigma_{\rm SM}$ in the $\gamma\gamma$ channel alone for the SM Higgs from Refs. [206, 207]; those limits are based on 4.9 fb^{-1} (ATLAS) and 4.8 fb^{-1} (CMS) at 7 TeV. We translated the LHC results into bounds on our model by comparing the CMS and ATLAS limits on $\sigma/\sigma_{\rm SM}$ with

$$\frac{\sigma}{\sigma_{\rm SM}} = \frac{\sigma(gg \to \Pi_t^0) \times {\rm BR}(\Pi_t^0 \to \gamma\gamma)}{[\sigma(gg \to H_{\rm SM}) + \sigma({\rm VBF} \to H_{\rm SM})] \times {\rm BR}(H_{\rm SM} \to \gamma\gamma)}, \tag{3.25}$$

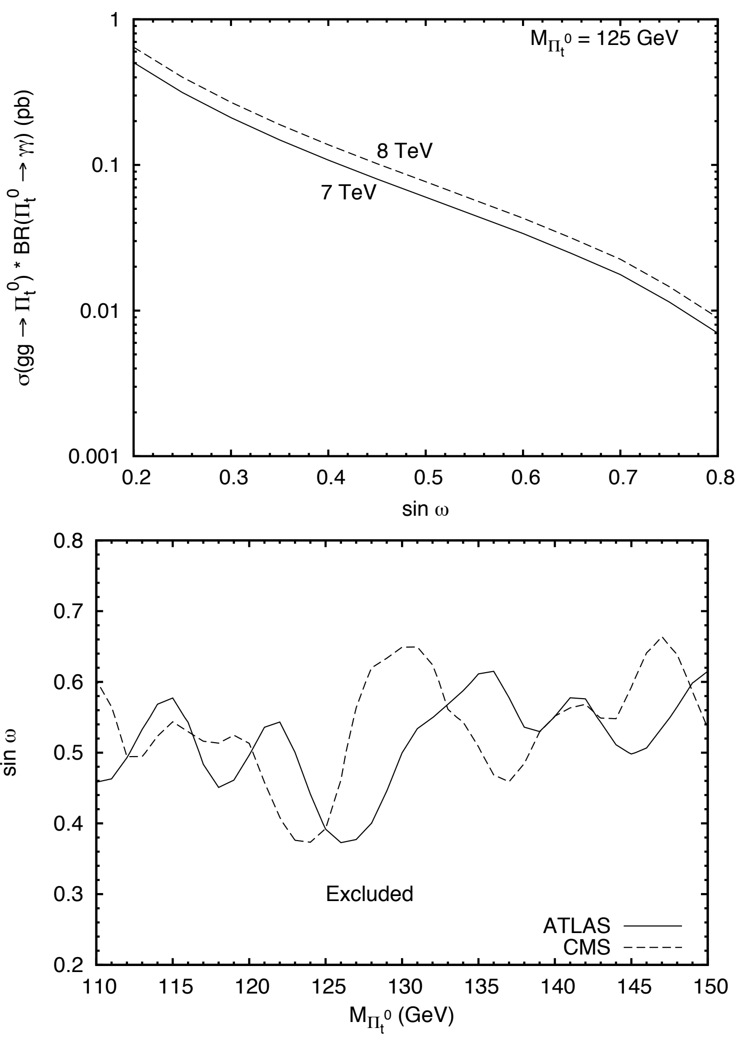

Figure 3.4: Top: Cross section times branching ratio for $gg \to \Pi_t^0 \to \gamma\gamma$ for a 125 GeV top-pion at the 7 and 8 TeV LHC. Bottom: 95% confidence level exclusion limits in the M_{Π^0} vs. $\sin\omega$ plane, extrapolated from the LHC SM Higgs search limits in the $\gamma\gamma$ channel with 4.8–4.9 fb^{-1} at 7 TeV from Refs. [206, 207].

where $\sigma(gg \to \Pi_t^0)$ is obtained from Eq. (3.22) and $\sigma(\text{VBF} \to H_{\text{SM}})$ is the SM Higgs production cross section via vector boson fusion (VBF). Note that the CMS analysis includes a contribution from a dedicated VBF search topology channel, which would not be present for the top-pion. The ATLAS analysis does not include a dedicated VBF channel and is thus more directly applicable to the top-pion. However, the inclusion of the dedicated VBF search channel by CMS does not appear to significantly affect our results: the limits are consistent with each other in excluding low values of $\sin\omega$.

Both CMS and ATLAS observe a new state with a mass of about 125 GeV decaying to diphotons whose properties appear to be consistent with those of a SM Higgs boson. However, the observed diphoton rate is nearly twice that expected for a SM Higgs [168, 161], which also makes the excess consistent with a neutral top-pion with $\sin\omega \simeq 0.5$, as shown in the bottom pane of Fig. 3.4.

3.3.4 Decays to ZZ, $Z\gamma$ and WW

It is interesting to consider how one would be able to distinguish a neutral top-pion from a SM Higgs boson once more data is in hand. The SM Higgs has tree-level couplings to W^+W^- and ZZ, while couplings to $\gamma\gamma$ arise only at one loop. In contrast, being a pseudoscalar, Π_t^0 does not have tree-level couplings to W^+W^- or ZZ [173, 176, 177]. It can, however, have couplings to W^+W^-, ZZ, and $Z\gamma$ at one loop. Ref. [177] considered the possibility that the loop-induced pseudoscalar coupling to the $SU(2)$ and hypercharge gauge bosons can account for the observed $\gamma\gamma$ and 4ℓ signal. Essentially, the strategy consisted in adjusting the relative value of the $SU(2)$ and hypercharge gauge couplings so that the equation

$$\frac{\Gamma^c(H \to ZZ^* \to 4e)}{\Gamma(H \to \gamma\gamma)} = \frac{\Gamma^c(\phi \to 4e)}{\Gamma(\phi \to \gamma\gamma)}. \tag{3.26}$$

is satisfied. Here, ϕ refers to the pseudoscalar and the superscript c means the quantities are computed with the experimental cuts imposed. It was shown that the $Z\gamma^*$ contribution to the 4ℓ signal completely dominates the ZZ^* contribution, in direct contrast to the SM case where the $Z\gamma^*$ contribution is negligible. Fixing the ratio of the coupling strengths this way leads to a well-defined prediction [177]:

$$R^{\phi}_{Z\gamma/\gamma\gamma} \equiv \frac{\Gamma(\phi \to Z\gamma)}{\Gamma(\phi \to \gamma\gamma)} = 121. \tag{3.27}$$

Thus, in order to see if the top-pion can generate the experimentally required signal strength, it suffices to compute the ratio of the partial widths to $Z\gamma$ and $\gamma\gamma$ and compare with the number in Eq. (3.27). This number turns out to be ≈ 0.02 for the top-pion.[11] Thus, we conclude that the top-pion cannot generate the observed ratio of the 4ℓ to $\gamma\gamma$ rates. Though this might seem to be a problem for models with strong top-quark dynamics in general, we point out that the 4ℓ signal involves very few events and conclusions about the viability of our model based on this observation should be postponed until higher-statistics results are available from the ATLAS and CMS collaborations.

3.3.5 Limits from the Ditau Channel

Searching for light neutral top-pions decaying to $\tau\tau$ is difficult because of the large Drell-Yan background. For scalars that are produced in part by vector boson fusion, the sensitivity can be enhanced by implementing cuts that preferentially select the VBF channel, but unfortunately this option is not available for pseudoscalars like the top-pion.

[11] We note that this is independent of $\sin\omega$, which cancels out in the ratio. $\sin\omega$ in our model is analogous to the parameter c in [177] - one that can be tuned to adjust the production cross-section to the proper value.

Looking specifically at the case where the neutral top-pion is responsible for the diphoton excess at 125 GeV ($M_{\Pi_t^0} = 125$ GeV and $\sin\omega \simeq 0.5$, corresponding to an enhancement in the $\gamma\gamma$ channel by about a factor of 2 compared to the SM Higgs prediction), then we expect a $\tau\tau$ signal rate, from the gluon fusion channel, approximately equal to that of the SM Higgs. This is about a factor of 3 below the sensitivity of the $H_{\mathrm{SM}} \to \tau\tau$ search from ATLAS [163] (4.7 fb^{-1} at 7 TeV). However, that ATLAS analysis includes events in a "Higgs plus two jet" event category, corresponding to VBF production, to improve the sensitivity to the SM Higgs, so this limit does not directly apply to the neutral pseudoscalar top-pion of our model. The papers [168, 45, 161, 44] reporting the discovery of a new scalar in the diphoton channel do analyze data from the ditau channel, but neither finds conclusive evidence that the new state decays to tau lepton pairs. In the future, perhaps a dedicated search focused on the gluon fusion production channel would be sensitive to the Π_t^0.

3.4 Charged top-pion phenomenology

Charged top-pions would be pair-produced via electroweak processes at LHC and their dominant decay channels are hadronic. Therefore a direct search for Π_t^+ would be hampered by a combination of low cross-section and high backgrounds. The main constraints on these states presently come from top quark decays.

3.4.1 Branching ratios

We plot the branching ratios of the charged top-pion as a function of $M_{\Pi_t^\pm}$ in Fig. 3.5, assuming that the mass of the neutral top-pion is fixed at 125 GeV. For top-pion masses below m_t, the dominant decays are into $\tau\nu$ and offshell t^*b; their relative rates depend on the top-pion mass and $\sin\omega$. The decay to cs has a branching ratio a little less than half that of $\tau\nu$; the rate for bc is many times smaller when $\sin\omega \gtrsim 0.5$. For masses above m_t, decays to tb overwhelmingly dominate.

If $M_{\Pi_t^+} > M_{\Pi_t^0}$ then the off-shell decay $\Pi_t^+ \to \Pi_t^0 W^{+*}$ becomes possible. As this branching ratio never exceeds 5%, it is phenomenologically unimportant for our purposes.

Since the charged top-pion seldom decays to the neutral top-pion even when kinematically allowed to do so, Fig. 3.5 also gives a good sense of the branching ratios of the charged top-pion for the case in which the top-pions are degenerate.

3.4.2 Limits from $t \to \Pi^+ b$

The ATLAS collaboration has searched for evidence of charged scalars in top quark decays using 4.6 fb^{-1} of data gathered at 7 TeV [208]. Because this was motivated as a search for the charged Higgs of the MSSM, which decays almost exclusively to $\tau\nu$ for large $\tan\beta$, their search assumed that the charged scalar would decay only to $\tau\nu$. Specifically, they set a limit on $B \equiv \mathrm{BR}(t \to H^+ b)$, assuming that $\mathrm{BR}(H^+ \to \tau\nu) = 1$. The latter assumption is built directly into their analysis in that they scale the simulated cross section for SM $t\bar{t}$ background, in which $t \to Wb$, by $(1 - B)^2$.

The conclusions of the ATLAS $t \to H^+ b$ analysis cannot be directly applied to the charged top-pion because $\mathrm{BR}(\Pi_t^+ \to \tau\nu) \neq 1$, as can be seen in Fig. 3.5. In fact, as also illustrated in the left pane of Fig. 3.6, the value of $\mathrm{BR}(\Pi_t^+ \to \tau\nu)$ ranges from a maximum of about 0.7 for a relatively light Π_t^+ and large $\sin\omega$, to close to zero for a heavier top-pion and lower $\sin\omega$ (due to the competing $t^* b$ decay).

Nevertheless, we can adapt the ATLAS $t \to H^+ b$ limits to extract information about the charged top-pion. The charged top-pion signal is the same as that for the charged Higgs

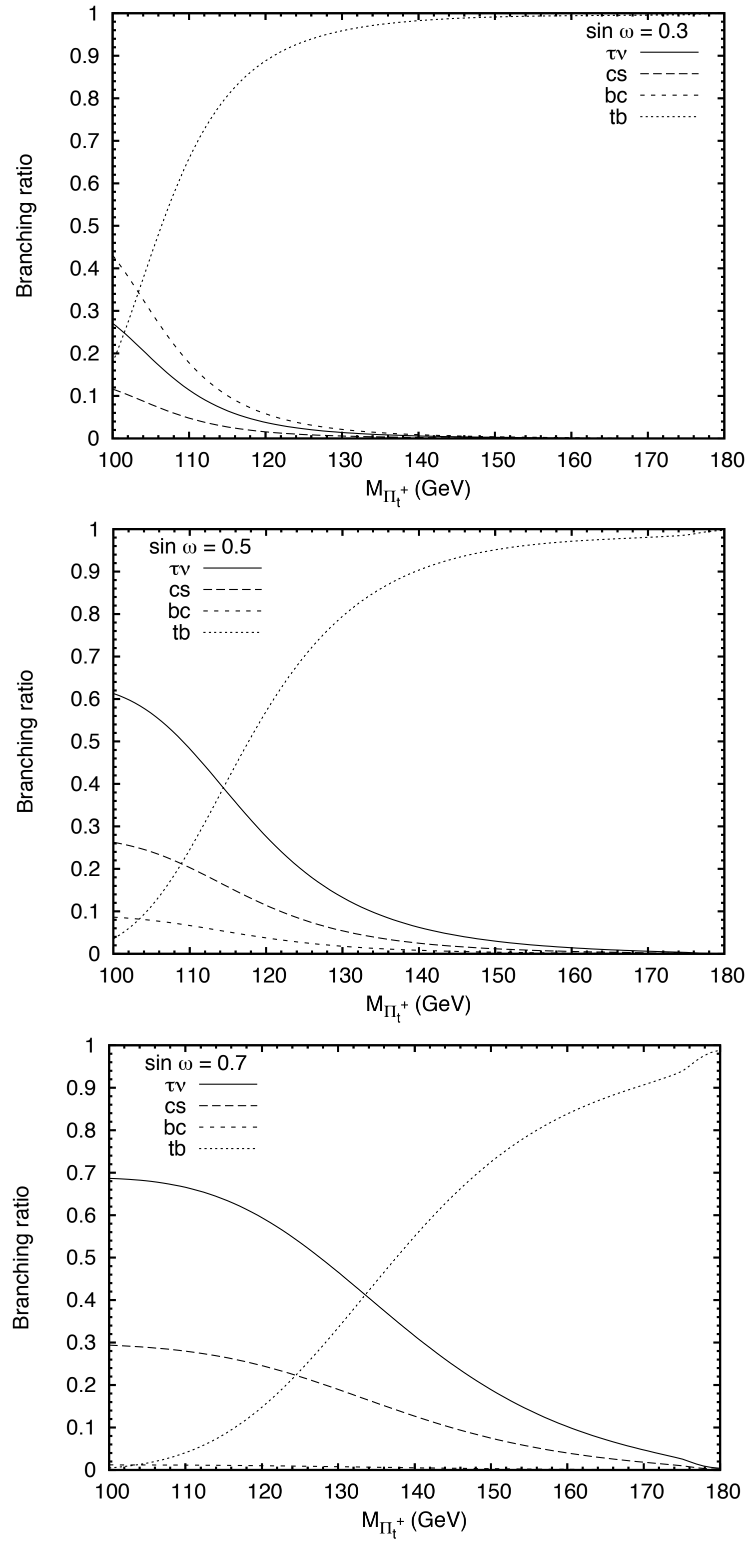

Figure 3.5: Branching ratios of the charged top-pion to the dominant final states, for $\sin\omega = 0.3$, 0.5, and 0.7 (top to bottom). We include off-shell decays to t^*b and also off-shell decays to $\Pi_t^0 W^+$ assuming $M_{\Pi_t^0} = 125$ GeV. These branching ratios were computing using a modified version of HDECAY [160].

studied in Ref. [208], provided that the parameter B is replaced by $\mathrm{BR}(t \to \Pi_t^+ b) \times \mathrm{BR}(\Pi_t^+ \to \tau\nu)$. We calculated the top quark decay branching ratio at tree level neglecting the bottom quark mass, using

$$\mathrm{BR}(t \to \Pi_t^+ b) = \frac{\cot^2\omega(1 - M_{\Pi^+}^2/m_t^2)^2}{(1 + 2M_W^2/m_t^2)(1 - M_W^2/m_t^2)^2 + \cot^2\omega(1 - M_{\Pi^+}^2/m_t^2)^2}. \tag{3.28}$$

We have calculated the Π_t^+ decay branching ratios using a modified version of `HDECAY` [160] as discussed before. Combining these branching fractions, we show contours of $\mathrm{BR}(t \to \Pi_t^+ b) \times \mathrm{BR}(\Pi_t^+ \to \tau\nu)$ in the $M_{\Pi_t^+}$ vs. $\sin\omega$ plane in the right-hand pane of Fig. 3.6.

However, the "SM-like" top-pair events to which the signal events are compared in setting a limit on exotic top decays will no longer include only $t \to Wb$ events. This sample will now potentially contain events in which a top-pion decays to bt^*, yielding $t \to \Pi^+ b \to W^+ b\bar{b}b$, where the W^+b comes from the off-shell top quark. While the kinematic features of these top decays will differ from those of SM decays, the events may be similar enough to be picked up in the SM top quark sample. To see how common these events are, we show contours of $\mathrm{BR}(t \to \Pi_t^+ b) \times \mathrm{BR}(\Pi^+ \to t^* b)$ in the plane of $M_{\Pi_t^+}$ and $\sin\omega$ in the left-hand panel of Fig. 3.7. The product of branching ratios can be significant: it lies above 0.3 for $\sin\omega < 0.45$ and $M_{\Pi_t^+} \sim 140$ GeV. In this case more than half of all $t\bar{t}$ events would contain at least one top quark decaying to $\Pi_t^\pm b$ followed by $\Pi_t^\pm \to t^* b \to W^\pm b\bar{b}$; we suspect that this could distort kinematic distributions and b-tag rates in the $t\bar{t}$ sample enough to be noticed. Similarly, for $\sin\omega = 0.5$ and $M_{\Pi_t^+} \simeq 145$ GeV, we find $\mathrm{BR}(t \to \Pi_t^+ b) \times \mathrm{BR}(\Pi^+ \to t^* b) \simeq 0.2$, leading to about 40% of $t\bar{t}$ events containing at least one top quark decaying to $\Pi_t^\pm b$ followed by $\Pi_t^\pm \to t^* b \to W^\pm b\bar{b}$.

While deliberately distinguishing these $t \to \Pi^+ b \to W^+ b\bar{b}b$ events from SM top quark

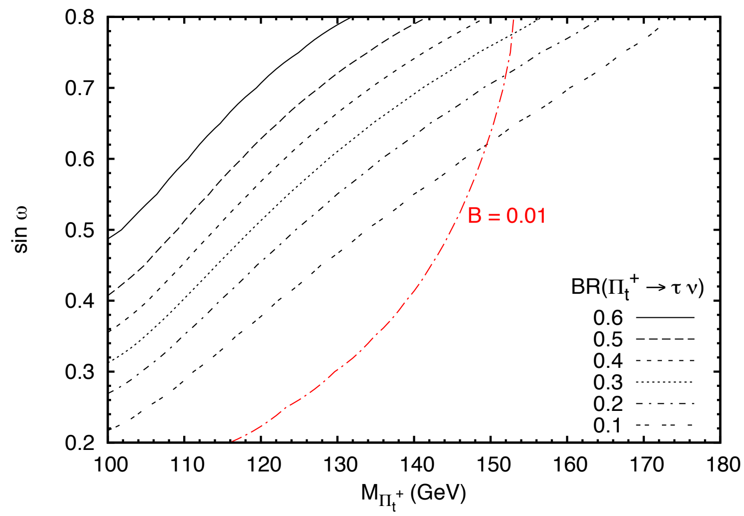

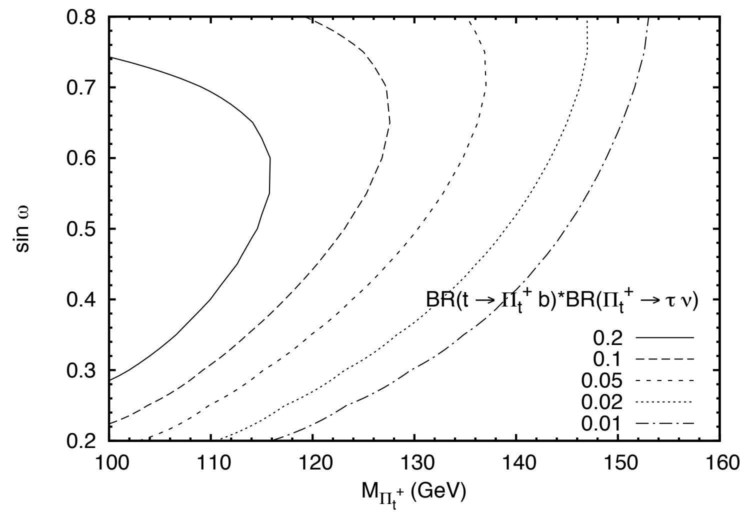

Figure 3.6: Top: Contours of $\mathrm{BR}(\Pi_t^+ \to \tau\nu)$ as a function of $M_{\Pi_t^+}$ and $\sin\omega$. Bottom: Contours of $\mathrm{BR}(t \to \Pi_t^+ b) \times \mathrm{BR}(\Pi_t^+ \to \tau\nu)$ as a function of $M_{\Pi_t^+}$ and $\sin\omega$. We interpret the ATLAS $t \to H^+ b$ search [208] to exclude $B \equiv \mathrm{BR}(t \to \Pi_t^+ b) \times \mathrm{BR}(\Pi_t^+ \to \tau\nu) > 0.01$.

decays would require a dedicated analysis, in the meantime, we can make the conservative assumption that all of these events will be included in the "SM-like" sample. When this is the case, the comparison between exotic and SM-like events gives a conservative upper limit on $\mathrm{BR}(t \to \Pi_t^+ b) \times \mathrm{BR}(\Pi_t^+ \to \tau\nu)$. When some of these events are not picked up in the SM-like sample, the true upper bound on the product of branching fractions is actually even stronger.

We are now ready to determine the constraints on our model. Reference [208] sets an upper bound on $B \equiv \mathrm{BR}(t \to H^+ b)$ (with $\mathrm{BR}(H^+ \to \tau\nu) = 1$) of $B \lesssim 0.05$ for $M_{H^+} = 90$ GeV, falling to $B \lesssim 0.01$ for $M_{H^+} = 120$–160 GeV. Therefore we can take the right-most contour in the left-hand pane of Fig. 3.7 as the rough exclusion limit on Π_t^+ from this search channel. This excludes charged top-pion masses below about 118, 140, 149, and 153 GeV for $\sin\omega = 0.2$, 0.4, 0.6, and 0.8, respectively. We have overlaid this exclusion curve on the plots in Fig. 3.6 to make it easier to see what values of $\mathrm{BR}(\Pi_t^+ \to \tau\nu)$ and $\mathrm{BR}(t \to \Pi_t^+ b) \times \mathrm{BR}(\Pi^+ \to t^* b)$ are still allowed in our model. Note, for instance, that, for $\sin\omega \lesssim 0.6$, the region of parameter space where the $B \leq 0.01$ limit falls has $\mathrm{BR}(\Pi_t^+ \to \tau\nu) < 0.1$.

Finally, examining the right-hand pane of Fig. 3.7, we see that if the new state observed in diphotons at around 125 GeV is to be interpreted as a Π_t^0 (with the event rate yielding $\sin\omega = 0.5$), then we would interpret the combination of the diphoton data from Refs. [206, 207] and ATLAS search [208] for $t \to H^+ b$ with $H^+ \to \tau\nu$ as jointly constraining the Π_t^+ to be heavier than about 145 GeV.

Therefore, the only phenomenologically viable case involves non-degenerate top-pions. As discussed in detail in Appendix B.1, however, this differs from the standard expectation in top color models and implies that new sources of isospin violation would have to be present.

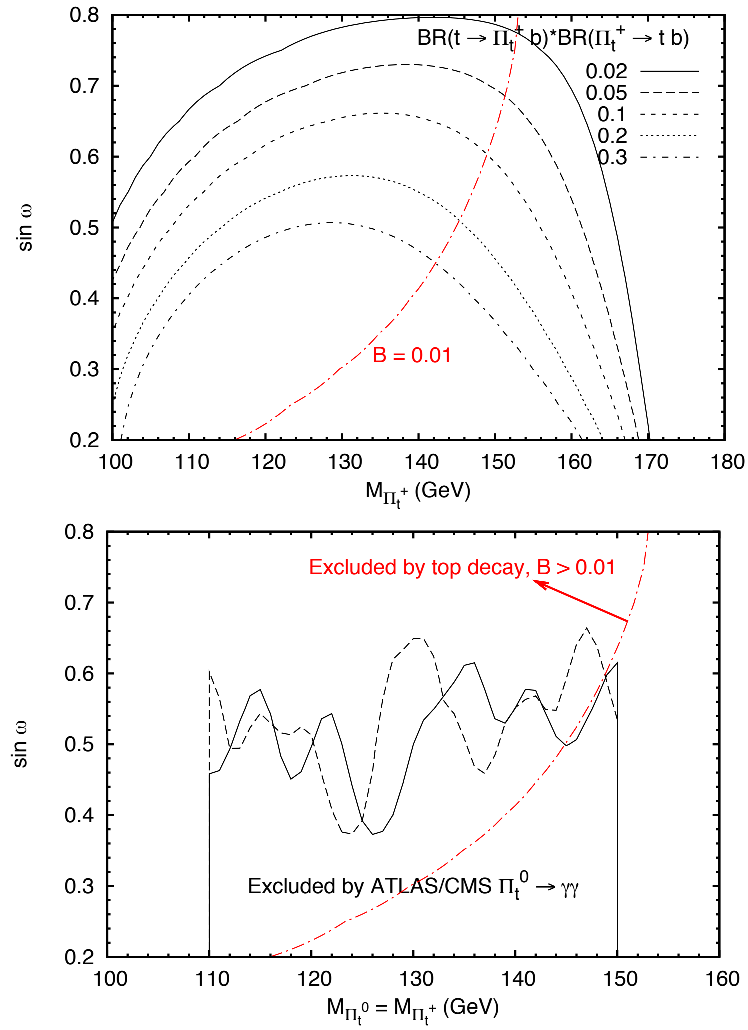

Figure 3.7: Top: Contours of $\mathrm{BR}(t \to \Pi_t^+ b) \times \mathrm{BR}(\Pi^+ \to t^* b)$ as a function of $M_{\Pi_t^+}$ and $\sin\omega$. On each plot, only the region of parameter space to the right of the red dot-dashed curve labeled "B=0.01" is still allowed by data on top-quark decays, as shown in Fig. 3.6. Bottom: comparison of the ATLAS $t \to H^+ b$ exclusion and the ATLAS (solid) and CMS (dashed) $\Pi_t^0 \to \gamma\gamma$ limits [206, 207], assuming degenerate Π_t^0 and Π_t^+.

3.5 Top-Higgs phenomenology

In addition to the top-pion states discussed above, models in which the top-quark plays a direct role in electroweak symmetry breaking contain a "top-Higgs" state. Such a state is expected to have a mass greater than about 200 GeV, and we have previously demonstrated [126] that such a top-Higgs state would produce ZZ and WW signals much *larger* than those characteristic of a SM Higgs of the same mass when decays to pairs of top-pions are kinematically forbidden. In this section we consider the constraints on the top-Higgs state assuming that the neutral top-pion is the new boson discovered at the LHC.

The couplings of the top-Higgs, along with its decay widths to the most relevant channels WW, ZZ, $t\bar{t}$, $\Pi_t^{\pm}W^{\mp}$, $\Pi_t^0 Z$, $\Pi_t^+\Pi_t^-$, and $\Pi_t^0\Pi_t^0$, are given in detail in Ref. [126]. For completeness, we reproduce the formulas for the key decay widths in Appendix B.3, along with the ratio between the LHC production cross-sections for the top-Higgs and the SM Higgs. We will first establish the current mass limits on the top-Higgs based on data from the ATLAS and CMS experiments. We then comment on the discovery prospects for the top-Higgs in the channel $H_t \to \Pi_t^0 Z$ at the 14 TeV LHC.

Reference [126] used the combined SM Higgs limits from the LHC to determine the excluded range of top-Higgs masses as a function of $\sin\omega$, for various values of the top-pion mass. In the mass range of interest, the LHC limits come entirely from the SM Higgs decays into WW and ZZ, and so are directly applicable to the top-Higgs after rescaling by the appropriate ratios of production cross section and decay branching ratios. The limits of Ref. [126] used ATLAS results with 1.0–2.3 fb^{-1} and CMS results with 1.1–1.7 fb^{-1} of integrated luminosity at 7 TeV. Here we update the limits using the more recent CMS SM Higgs search results based on 4.6–4.8 fb^{-1} at 7 TeV and also consider how the limits translate to the case where the charged and neutral top-pions are not degenerate.

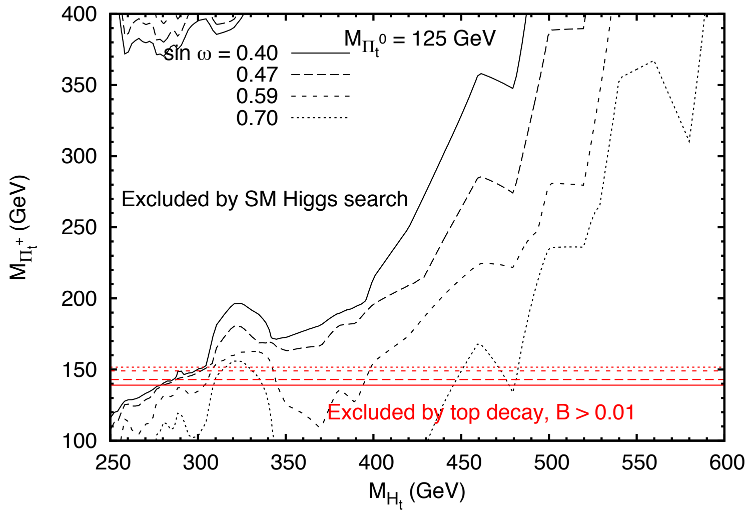

Figure 3.8: The CMS exclusion contours for M_{H_t} from searches for the SM Higgs in WW and ZZ final states [209], as a function of $M_{\Pi_t^+}$ for the special case $M_{\Pi_t^0} = 125$ GeV. We show $\sin\omega$ values of 0.40 (solid lines), 0.47 (long-dashed lines), 0.59 (short-dashed lines), and 0.70 (dotted lines), which correspond to a rate for the 125 GeV Π_t^0 in the $\gamma\gamma$ channel relative to that of the SM Higgs of $\sigma/\sigma_{\rm SM} = 3.0$, 2.0, 1.0, and 0.5, respectively. The horizontal (red) lines show our lower bound on $M_{\Pi_t^+}$ from the ATLAS $t \to H^+ b$ search [208] for the same four $\sin\omega$ values.

Fig. 3.8 shows how the top-Higgs exclusion curves behave for a variety of $\sin\omega$ values. Given that light charged top-pions are excluded by the ATLAS search [208] for $t \to H^+ b$, the top-Higgs cannot have a mass lower than about 250-300 GeV.

There is also a theoretical bound to bear in mind. For small values of $\sin\omega$, the top-Higgs couplings violate perturbativity for sufficiently high H_t masses, when the decay channels to two tops and two top-pions open up; roughly speaking this occurs when the top-Higgs width exceeds its mass. For $\sin\omega \approx 0.4$ we find this constrains the top-Higgs mass to lie below about 600 GeV, while for $\sin\omega \geq 0.5$, perturbativity considerations do not constrain the region of interest.

Many of the decay channels that are available to a heavy top-Higgs result in hadronic

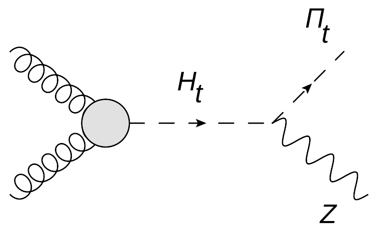

Figure 3.9: The production of a neutral top-pion and a Z from an s-channel top-Higgs.

final states with large SM backgrounds. A potential exception is $H_t \to Z\Pi_t^0 \to \ell\ell\gamma\gamma$ as shown in Fig. 3.9. Assuming the state discovered at 125 GeV is the neutral top-pion, one can then take advantage of the $H_t\Pi_t^0 Z$ coupling, and look for the top-Higgs in the process $pp \to Z\Pi_t^0 \to \ell\ell\gamma\gamma$ by using an invariant mass cut on the diphotons to cull background. We find that discovery in the allowed parameter space (see Fig. 3.8) is not possible for $\sin\omega$ values of 0.7 and above in this channel. Even for lower values of $\sin\omega$, the minimum integrated luminosity required for a 5σ discovery at the 14 TeV LHC in this mode is 100 fb^{-1} and a luminosity several times greater is required in most of the M_{H_t} vs $M_{\Pi_t^+}$ plane. Therefore, we conclude that this will not be a realistic discovery mode for the top-Higgs in the case of a light neutral top-pion. The most promising search channels for the top-Higgs therefore remain the WW and ZZ final states as used in the SM Higgs search.

3.6 Conclusions

In this chapter, we have analyzed the phenomenology of the top-pion and top-Higgs states in models with strong top dynamics, and have translated the present LHC constraints on the SM Higgs into bounds on these scalar states.

We have seen that it is possible for the observed excess in the $H_{SM} \to \gamma\gamma$ search channel to correspond to a neutral top-pion of mass $M_{\Pi_t^0} = 125$ GeV. Based on the size of the cross-section observed [168, 45, 161, 44], the corresponding value of $\sin\omega$ would be approximately 0.5. Because Π_t^0 is a pseudo scalar, however, models of strong top dynamics do not predict a visible signal in the $ZZ \to 4\ell$ channel or the WW channel, nor a diphoton signal in the vector boson fusion production channel, nor any associated production of the 125 GeV object with a W or Z. Therefore, as additional data is accumulated, we would expect the diphoton resonance to continue to grow in significance, the initial signals in the $ZZ \to 4\ell$ and WW channels to fade away, and the dijet-tagged diphoton signal to persist only at a level consistent with dijet-tagged $gg \to \Pi_t^0$ rather than dijet-tagged vector boson fusion events. Moreover, in the context of these models, we would also expect that a signal in the ditau decay channel would be present but less visible for the Π_t^0 than for the SM Higgs.

For the range of model parameters where the neutral top-pion can account for the LHC diphoton signal, searches for non-standard top-quark decays to charged scalar plus bottom quark exclude charged top-pions with masses up to about 145 GeV (as in the left-hand panel of Fig. 3.7). These searches continue to become more sensitive as the decay properties of the top-quark are measured more accurately. As a result, if the neutral top-pion has a mass of 125 GeV, it cannot be degenerate with the charged top-pion, as one would more typically expect in models of strong top dynamics. Instead, the model must contain substantial isospin violation to produce this top-pion mass splitting.

We have also updated limits on the top-Higgs. Our results show that current LHC searches for the SM Higgs in WW and ZZ exclude the existence of a top-Higgs state up to masses of order 300 GeV, with some dependence on the charged top-pion mass and $\sin\omega$ as shown in Fig. 3.8.

The implication is that current searches at the LHC strongly constrain theories with strong top-dynamics. The top triangle moose model interpolates [126] between a variety of strong top dynamics models as the value of $\sin\omega$ varies between about 0.2 and 0.8, the range studied in this chapter. In the context of strong top-dynamics, the new boson observed at the LHC is too light to be the top-Higgs [126]. Instead, the diphoton signal can be produced by a neutral top-pion of the appropriate mass and couplings, assuming that one constructs a theory including additional isospin violation, but in this case we would not expect a significant signal in the $ZZ \to 4\ell$ channel. This last stipulation is problematic since both LHC experiments report a 3σ signal in the four-lepton channel with the current data set. Moreover, if the diphoton signal corresponds to a neutral top-pion, then the theoretical context cannot be the most familiar part of the top-triangle-moose parameter space in which $0.2 \leq \sin\omega \leq 0.5$, the top-pions are degenerate, and the top-Higgs has a mass of order $2m_t$: i.e. the portion of the parameter space corresponding to classic TC2 models. Rather, the context would be the less-explored region in which $\sin\omega$ is of order 0.5 or greater, the top-pions have a substantial mass splitting, and the top-Higgs is heavier: i.e. a model in which the strong top dynamics are of the top seesaw form.

We anticipate that additional LHC data will provide further clarity about the nature of the diphoton resonance and its possible connection to strong top dynamics.

Part II

Coloron Phenomenology

Chapter 4

Distinguishing Color-Octet and Color-Singlet Resonances at the Large Hadron Collider

— This chapter is based on a work in collaboration with Anupama Atre, R.Sekhar Chivukula, and Elizabeth H. Simmons which has appeared in [6]. The contents have also appeared in the conference proceeding [5].

4.1 Introduction

We have seen in Part I how the searches for and the discovery of the Higgs boson place constraints on new physics models describing electroweak symmetry breaking via strong dynamics. Now, in Part II, let us switch gears slightly to a common feature among a larger class of new physics models: a vector resonance. In particular, we focus on the resonances that could be discovered at a hadron collider.

Hadron colliders are a rich source for the production of new resonances with strong coupling due to colored particles in the initial state. A particularly simple and powerful probe of new colored resonances is the di-jet channel where the resonance decays to two partons. Each successive hadron collider with an increase in center of mass energy and integrated luminosity has been able to probe for di-jet resonances with higher masses. Many well motivated theories of physics beyond the Standard Model (SM) predict new particles that give rise to signatures in the di-jet channel. These new particles can have different spin and color structure and a sample of such possibilities is listed below.

The color-octet vector boson arises as a result of extending the gauge group of the strong sector. The chiral structure of the couplings between quarks and the color-octet varies and the couplings can either be flavor universal or flavor non-universal. Examples of flavor universal scenarios are the axigluon [210, 211] and coloron [212, 213] where all quarks are charged under the same $SU(3)$ group. Flavor non-universal scenarios appear in the case of the topgluon where the third generation quarks are assigned to one $SU(3)$ group and the light quarks to the other [98, 100] and the axigluon where different chiralities of the same quark can be charged under different groups [214, 215, 216, 217, 218, 219] . Other examples include Kaluza-Klein (KK) gluons which are excited gluons in extra-dimensional models [220], technirhos which are composite colored vector mesons found in technicolor [152, 99, 221], models that include colored technifermions and low-scale string resonances [222].

The electrically neutral color-singlet vector boson, collectively called a Z', also appears in many beyond SM physics scenarios and can originiate from extending the electroweak $U(1)$ or $SU(2)$ gauge group. The Z' can also have flavor universal [223, 224, 225] or flavor non-universal couplings to fermions [226, 227, 228]. For reviews of Z' models, see Refs. [129, 134, 229] and the references therein. Other examples of color-singlet states probed in the di-jet channel include the spin-2 gravitons in Randall-Sundrum models [230, 231] which are KK excitations of the gravitational field [232, 233] and the electrically charged color-singlet vector boson, namely the W' [121].

Searches for new resonances in the di-jet channel have been performed at the CERN Sp̄pS [234, 235], Tevatron [236, 237, 238, 239, 240] and the Large Hadron Collider (LHC) [241, 242, 243, 244, 245, 246, 247, 248, 249]. Once a resonance has been discovered the next step is to measure the properties of the resonance. The di-jet invariant mass m_{jj} and the angular distributions of energetic jets relative to the beam axis are sensitive observables to determine the mass and spin of the resonance. In this work [6], we explore the question of determining the color structure of the resonance produced in the di-jet channel; in particular we explored whether the resonance is a color-octet or a color-singlet state.

To distinguish a color-octet and a color-singlet resonance produced in the di-jet channel we introduce a new variable called the color discriminant variable. Assuming that the new resonance decays only to quarks, this variable reflects the color structure of the resonance and is constructed from measurements which can be made in the di-jet discovery channel, namely the di-jet cross section, mass and width of the resonance. We demonstrate the utility of this variable in distinguishing color-octet and color-singlet resonances using the simple flavor universal example of a coloron and a leptophobic Z'. We also demonstrate the robustness of this method using a simplified flavor non-universal scenario[1]. We study the sensitivity of the LHC with center of mass (c.m.) energy of 14 TeV and integrated luminosities of $30, 100, 300$ and 1000 fb^{-1} to distinguish color-octet and color-singlet resonances. Motivated by current constraints on di-jet resonances and future prospects for discovery, we probe masses ranging from $2.5 - 6$ TeV with various couplings and widths.

The rest of the chapter is organized as follows. In Sec. 4.2 we describe phenomenological models for a coloron and a leptophobic Z' used as illustrative examples in this chapter. We introduce a color discriminant variable to distinguish color-octet and color-singlet resonances

[1]The general flavor non-universal scenarios are studied in Chapter 5.

in Sec. 4.3. We discuss the current constraints from collider searches and the allowed regions in parameter space in Sec. 4.4 and the uncertainties involved in measuring the color discriminant variable at the LHC in Sec. 4.5. We present our results in Sec. 4.6 and conclusions in Sec. 4.7. A discussion about uncertainties relevant to our analysis is presented in Appendix C.

4.2 General Parameterization

Color-octet and color-singlet resonances of interest to our study may be motivated in many beyond the SM physics scenarios as described in the introduction. Therefore we study a phenomenological model of color-octet and color-singlet resonances independent of the underlying theory to keep our study widely applicable. We will assume that there are no additional colored states into which the resonance can decay. If new light states are present, studying the properties of the decays of the coloron or Z' into these new particles will be instructive (see Refs. [250, 251] and references therein). The couplings of the color-octet and color-singlet resonances to SM quarks can all be the same in the simple flavor universal scenario and can all be independent in the most general flavor non-universal case. In this section, we present details about the parameterization of the interactions of color-octet and color-singlet resonances for two cases, the flavor universal scenario and an illustrative flavor non-universal scenario.

The interaction of a color-octet resonance C_μ with the SM quarks q_i has the form

$$\mathcal{L}_C = ig_s \sum_i \bar{q}_i \gamma^\mu \left(g^i_{C_L} P_L + g^i_{C_R} P_R \right) q_i C_\mu, \tag{4.1}$$

where $C_\mu = C^a_\mu t^a$ with t^a an SU(3) generator, $g^i_{C_L}$ and $g^i_{C_R}$ denote left and right chiral coupling strengths of the color-octet to the SM quarks relative to the QCD coupling g_s, the projection operators have the form $P_{L,R} = (1 \mp \gamma_5)/2$ and the quark flavors run over $i = u, d, c, s, t, b$. We will denote the color-octet resonance by C and its chiral couplings to light quarks by $g^q_{C_{L,R}}$ and to the third generation by $g^t_{C_{L,R}}$ and use the terms color-octet and coloron interchangeably.

The color-octet resonance with the interactions as in Eq. (4.1) decays primarily to two jets or a top pair and its decay width is given by

$$\begin{aligned} \Gamma_C &= \alpha_s \frac{M_C}{12}\Big[4\left(g^{q\,2}_{C_L} + g^{q\,2}_{C_R}\right) + \left(g^{t\,2}_{C_L} + g^{t\,2}_{C_R}\right) \\ &+ \left[(g^{t\,2}_{C_L} + g^{t\,2}_{C_R})(1-\mu_t) + 6 g^t_{C_L} g^t_{C_R}\mu_t\right]\sqrt{1-4\mu_t}\Big], \end{aligned} \tag{4.2}$$

where M_C and Γ_C are the mass and intrinsic width of the color-octet respectively. Decays to top quarks are modified by the kinematic factors involving $\mu_t = m_t^2/M_C^2$ with m_t the top quark mass. Strictly speaking, the bottom quark's contribution to the width is modified by factors involving $\mu_b = m_b^2/M_C^2$ but we ignore these factors since $m_b^2 << M_C^2$. For a color-octet that is heavy compared to the top quark, the expression for the total width of a color-octet in Eq. (4.2) simplifies to

$$\Gamma_C = \alpha_s \frac{M_C}{12}\left[4 g^{q\,2}_C + 2 g^{t\,2}_C\right] \tag{4.3}$$

where we have defined

$$g^{i\,2}_C \equiv g^{i\,2}_{C_L} + g^{i\,2}_{C_R} \tag{4.4}$$

for $i = q$ (light quarks u, d, c, s) and $i = t$ (quarks in the third generation t, b).

We parameterize the interaction of a color-singlet similarly to that of the color-octet. If the color-singlet has tree level couplings to SM leptons also, it can be easily distinguished from a color-octet as the octet has no decays to leptons. Hence we consider only the leptophobic variant of the color-singlet, as this can mimic a color-octet resonance in the di-jet channel. We will call such a resonance a leptophobic Z' henceforth. The interactions of a leptophobic Z' with the SM quarks are given by

$$\mathcal{L}_{Z'} = i g_w \sum_i \bar{q}_i \gamma^\mu \left(g^i_{Z'_L} P_L + g^i_{Z'_R} P_R \right) q_i Z'_\mu, \tag{4.5}$$

where $g^i_{Z'_L}$ and $g^i_{Z'_R}$ denote left and right chiral coupling strengths of the leptophobic Z' to the SM quarks relative to the weak coupling $g_w = e/\sin\theta_W$ and the quark flavors run over $i = u, d, c, s, t, b$. Again the chiral couplings of the Z' to light quarks are denoted by $g^q_{Z'_{L,R}}$ and to the third generation by $g^t_{Z'_{L,R}}$.

The leptophobic Z' with the interactions as in Eq. (4.5) decays primarily to two jets or a top pair and its decay width is given by

$$\begin{aligned} \Gamma_{Z'} &= \alpha_w \frac{M_{Z'}}{2} \Big[4 \left(g^{q\,2}_{Z'_L} + g^{q\,2}_{Z'_R} \right) + \left(g^{t\,2}_{Z'_L} + g^{t\,2}_{Z'_R} \right) \\ &+ \Big[(g^{t\,2}_{Z'_L} + g^{t\,2}_{Z'_R})(1-\mu_t) + 6 g^t_{Z'_L} g^t_{Z'_R} \mu_t \Big] \sqrt{1-4\mu_t} \Big], \end{aligned} \tag{4.6}$$

where $M_{Z'}$ and $\Gamma_{Z'}$ are the mass and intrinsic width of the leptophobic Z' respectively. Similar to the case of the color-octet, we can neglect the kinematic factors involving the mass of the top and bottom quarks when the Z' is much heavier than the SM quarks. Hence the expression for the decay width of a Z' as given in Eq. (4.6) simplifies to

$$\Gamma_{Z'} = \alpha_w \frac{M_{Z'}}{2} \left[4 {g^{q}_{Z'}}^2 + 2 {g^{t}_{Z'}}^2 \right], \tag{4.7}$$

where ${g^{i}_{Z'}}^2 \equiv {g^{i}_{Z'}}_L^2 + {g^{i}_{Z'}}_R^2$ for $i = q,\, t$. In the rest of the chapter, and also the next chapter, we will only consider color-octet and color-singlet resonances that are much heavier than the top quark.

4.2.1 Flavor Universal Scenario

In the flavor universal scenario all SM quarks have the same coupling to the color-octet resonance, *i.e.* $g^{q}_{C_{L,R}} = g^{t}_{C_{L,R}} = g_{C_{L,R}}$. The expression for the decay width of a color-octet as given in Eq. (4.3) simplifies further to

$$\Gamma_C = \frac{\alpha_s}{2} M_C g_C^2, \tag{4.8}$$

and the branching fraction for the color-octet resonance to decay to jets obeys the simple relation

$$BR(C \to jj) = 5/6, \qquad \text{where } j = u, d, c, s, b. \tag{4.9}$$

Similarly, the decay width of a Z' with flavor universal couplings to SM quarks simplifies to

$$\Gamma_{Z'} = 3 \alpha_w M_{Z'} g_{Z'}^2, \tag{4.10}$$

where $\alpha_w = g_w^2/4\pi$ and $g^{q}_{Z'_{L,R}} = g^{t}_{Z'_{L,R}} = g_{Z'_{L,R}}$. The branching fraction for a Z' to decay to jets obeys the simple relation

$$BR(Z' \to jj) = 5/6, \qquad \text{where } j = u, d, c, s, b \tag{4.11}$$

Note that although the width of the coloron is proportional to the strong coupling ($\alpha_{\rm s}(m_Z) \simeq 0.12$) and that of the leptophobic Z' is proportional to the weak coupling ($\alpha_{\rm w} \simeq 0.04$), the two resonances will have comparable widths when the couplings $g_L^2 + g_R^2$ are the same. This is due to the difference in the color factors for the two resonances.

4.2.2 An Illustrative Flavor Non-universal Scenario

The couplings of a color-octet and color-singlet resonance to SM quarks can all be independent in the most general flavor non-universal scenario. While it is desirable to study the most general case, it is computationally cumbersome and will be postponed to Chapter 5. Instead we consider an intermediate scenario where the couplings of the color-octet and the color-singlet to quarks in the third generation are different from the couplings of the quarks in the first two generations. An interesting example of such a scenario is that of a color-octet resonance (described in Refs. [214, 216, 215, 217]) that can enhance top-pair forward-backward asymmetry observed at the Tevatron [252, 253, 254, 255, 256]. For the Z', models related to strong dynamics typically feature a Z' that couples with an enhanced strength to quarks in the third family (see Ref. [129] for a review of such cases).

The couplings of a color-octet or color-singlet resonance to SM quarks in the flavor non-universal scenario we consider can be parametrized by

$$g^t_{C/Z'\,L,R} \equiv \xi g^q_{C/Z'\,L,R}\ , \tag{4.12}$$

where $t = t, b$ and $q = u, d, c, s$. The change in the total decay width of a color-octet and color-singlet in the flavor non-universal scenario compared to the width in the flavor-universal case (given by Eq. (4.8) and Eq. (4.10) respectively) is given by

$$\Gamma^{\text{non-universal}} = \Gamma^{\text{universal}} \left(\frac{4 + 2\xi^2}{6} \right). \tag{4.13}$$

The branching fraction of the color-octet and color-singlet to jets, where the jets are defined to include $j = u, d, c, s, b$ changes from

$$Br(C/Z' \to jj) = 5/6 \tag{4.14}$$

in the flavor universal case to

$$Br(C/Z' \to jj) = \frac{4 + \xi^2}{4 + 2\xi^2} \tag{4.15}$$

in the flavor non-universal case. Hence the branching fraction to jets in the flavor non-universal case decreases to 1/2 from 5/6 in the flavor universal case as ξ becomes large. This tendency towards smaller branching fraction in the flavor non-universal case tends to decrease the overall di-jet cross section for the resonance. The production rate stays the same, as it is dominated by the contribution from the first (and to a small extent from the second) generation quarks; the bottom quark with negligible parton luminosity contributes very little. However, the branching fraction reduces compared to the flavor universal scenario and hence the total di-jet cross section decreases.

Finally we note that in the narrow-width approximation the quantity ξ can be determined by a measurement of the ratio of the cross sections where the resonance decays to top quark pairs or to jets:

$$\frac{\sigma(pp \to C/Z' \to t\bar{t})}{\sigma(pp \to C/Z' \to jj)} \simeq \frac{Br(C/Z' \to t\bar{t})}{Br(C/Z' \to jj)} = \frac{\xi^2}{4+\xi^2}\,. \tag{4.16}$$

We introduce next a new variable to help distinguish color-octet and color-singlet states, described in this section, in the di-jet channel.

4.3 Color Discriminant Variable

In the previous section, we introduced generic color-octet and leptophobic color-singlet states that couple to SM quarks with differing strengths and color structures. A resonance of either type will be produced copiously at a hadron collider and will decay into two jets or top quark pairs. Decays in the top quark channel have the advantage of possible leptons in the final state and hence better reconstruction efficiencies compared to the SM QCD background. However they suffer from a smaller cross section (due to smaller branching fraction to top pairs), overall smaller efficiency due to the large number of final state particles and still a relatively large background. On the other hand the simple topology of the decay into two highly energetic central jets with a larger branching ratio and higher efficiency of jet selection makes the di-jet channel a discovery mode despite very large QCD backgrounds. Such resonances will be discovered in the di-jet channel as simple "bumps" (in the narrow width approximation) over an exponentially falling QCD di-jet background. The channel with decays to top quark pairs, while suffering from a smaller rate, is nonetheless an important one as it helps determine flavor universal from flavor non-universal scenarios as described in Sec. 4.6.2.

Once such a resonance has been discovered in the di-jet channel, it is possible to obtain a measurement of its cross section, mass and width. The question then arises about the nature of the resonance - is it a color-octet or a color-singlet resonance? An estimate of the couplings $(g_L^2 + g_R^2)$ for each resonance can be obtained from the cross section measurement [257]. This can possibly be used to eliminate some scenarios where the deduced couplings are either not motivated theoretically or excluded by other experiments. However, there will be large regions in parameter space where both color-octet and leptophobic color-singlet scenarios survive. To keep our study widely applicable we propose a model-independent approach to distinguish color-octet and color-singlet resonances that depends mainly on the kinematics of the process.

The cross section for the production and decay of a resonance in the narrow-width approximation can be written as

$$\sigma_{jj}^V \equiv \sigma(pp \xrightarrow{V} jj) \simeq \sigma(pp \to V)Br(V \to jj), \tag{4.17}$$

where V is a generic resonance, $\sigma(pp \to V)$ is the cross section for producing the resonance and $Br(V \to jj)$ is the branching fraction for the resonance to decay to jets. Using this approximation and factoring out the couplings, color factors and mass dependence explicitly we can write the cross section for a color-octet as

$$\begin{aligned} \sigma(pp \to C \to jj) &= \frac{4}{9}\alpha_s g_C^2 \frac{1}{M_C^2} \sum_q W_q(M_C) Br(C \to jj) \\ &= \frac{8}{9}\frac{\Gamma_C}{M_C^3} \sum_q W_q(M_C) Br(C \to jj), \end{aligned} \tag{4.18}$$

where the expression for the width of the flavor universal coloron in Eq. (4.8) has been used to obtain the final form of Eq. (4.18). Similarly, we can express the cross section for the leptophobic Z' as

$$
\begin{aligned}
\sigma(pp \to Z' \to jj) &= \frac{1}{3}\alpha_w g_{Z'}^2 \frac{1}{M_{Z'}^2} \sum_q W_q(M_{Z'}) Br(Z' \to jj) \\
&= \frac{1}{9}\frac{\Gamma_{Z'}}{M_{Z'}^3} \sum_q W_q(M_{Z'}) Br(Z' \to jj), \qquad (4.19)
\end{aligned}
$$

where the expression for the width of the flavor universal leptophobic Z' in Eq. (4.10) has been used to obtain the final form of Eq. (4.19). Here, $W_q(M_V)$ ($V = C$, Z') is dependent only on the parton distribution functions (PDFs), kinematics, and phase space factors and is defined by

$$
W_q(M_V) = 2\pi^2 \frac{M_V^2}{s} \int_{M_V^2/s}^{1} \frac{dx}{x} \left[f_q\left(x, \mu_F^2\right) f_{\bar{q}}\left(\frac{M_V^2}{sx}, \mu_F^2\right) + f_{\bar{q}}\left(x, \mu_F^2\right) f_q\left(\frac{M_V^2}{sx}, \mu_F^2\right) \right], \qquad (4.20)
$$

where $f_q\left(x, \mu_F^2\right)$ is the parton distribution function at the factorization scale μ_F^2. Throughout this and the next chapter, we set $\mu_F^2 = M_V^2$.

Suppose a new di-jet resonance is discovered with a particular cross section and mass; it is important to determine whether it is a coloron described by Eq. (4.18) or a Z' described by Eq. (4.19). Comparing Eqs. (4.18) and (4.19) for equal σ and equal M and noting that Σ and di-jet branching ratios are also equal in the two cases, we find the following relationship between the widths:

$$
\Gamma_{Z'}^* = 8\Gamma_C^*, \qquad (4.21)
$$

where the asterisk signifies that we are comparing bosons with equal production cross-sections (σ). This implies that if a resonance is discovered in the di-jet channel, a measurement of the width can point to the color-structure of the resonance discovered.

We get a similar expression for the flavor non-universal case by replacing the expressions for the width and the branching fraction in Eqs. (4.18) and (4.19) by those in Eqs. (4.13) and (4.15). For the flavor non-universal coloron we have

$$\begin{aligned}
\sigma(pp \to C \to jj) &= \frac{4}{9}\alpha_s g_{C_R}^2 \frac{1}{M_C^2} \sum_q W_q(M_C) Br(C \to jj) \\
&= \frac{8}{9}\frac{\Gamma_C}{M_C^3}\left(\frac{6}{4+2\xi^2}\right) \sum_q W_q(M_C)\left(\frac{4+\xi^2}{4+2\xi^2}\right), \qquad (4.22)
\end{aligned}$$

where Γ_C is the width of the coloron in the flavor non-universal case. For the flavor non-universal leptophobic Z' we have

$$\begin{aligned}
\sigma(pp \to Z' \to jj) &= \frac{1}{3}\alpha_w g_{Z'}^2 \frac{1}{M_{Z'}^2} \sum_q W_q(M_{Z'}) Br(Z' \to jj) \\
&= \frac{1}{9}\frac{\Gamma_{Z'}}{M_{Z'}^3}\left(\frac{6}{4+2\xi'^2}\right) \sum_q W_q(M_{Z'})\left(\frac{4+\xi'^2}{4+2\xi'^2}\right), \qquad (4.23)
\end{aligned}$$

where $\Gamma_{Z'}$ is the width of the leptophobic Z' in the flavor non-universal case. For a given ξ, which is determined by a measurement of the ratio of the cross sections as given in Eq. (4.16), we see that, for resonances with a mass M and yielding equal total di-jet cross sections, the relation between the width of the coloron and the leptophobic Z' in the flavor non-universal case remains the same as before:

$$\Gamma^*_{Z'} = 8\Gamma^*_C \,. \qquad (4.24)$$

We use this relation to introduce a new variable to distinguish color-octet and color-singlet resonances and parameterize it in a model-independent way.

As discussed earlier, a discovery in the di-jet channel will inspire three immediate measurements - cross section, mass and width, which in turn depend on model dependent parameters such as couplings, color-structure and mass of the resonance. Note that the cross section is proportional to the color structure, square of the couplings and M^{-2} while the width is proportional to square of the couplings and M. Denoting by σ_{jj} the cross section for producing a resonance in the di-jet channel, we define

$$D_{\text{col}} \equiv \frac{M^3}{\Gamma}\sigma_{jj}, \tag{4.25}$$

as a color discriminant variable that is dimensionless by construction. This variable depends only on the color structure of the resonance being considered for a given ξ. For example, any two points in the parameter space of a coloron will lead to the *same* D_{col} for a given ξ where as points in parameter space of a coloron and a leptophobic Z' will lead to different values of D_{col} for the same ξ. Thus one can distinguish a color-octet and a color-singlet state in a relatively model-independent fashion *i.e.* without analyzing each point in parameter space separately. Next we discuss the constraints on the parameter space and the discovery potential of color-octet and color-singlet states at the LHC.

4.4 Parameter Space in di-jet Channel

In this section we describe the region of parameter space in which using the color discriminant variable is applicable. First we discuss the current constraints on the parameter space of coloron and leptophobic Z' models. Next we discuss the discovery prospect for colorons and leptophobic Z's at the LHC with c.m. energy of 14 TeV, since the question of distinguishing the color structure of a resonance will arise only after the resonance has been discovered. The discovery and exclusion regions for the coloron and leptophobic Z' are presented in

Fig. 4.1(a) and (b), respectively, for the flavor universal scenario and in Fig. 4.1(c) and (d), respectively, for the flavor non-universal scneario.

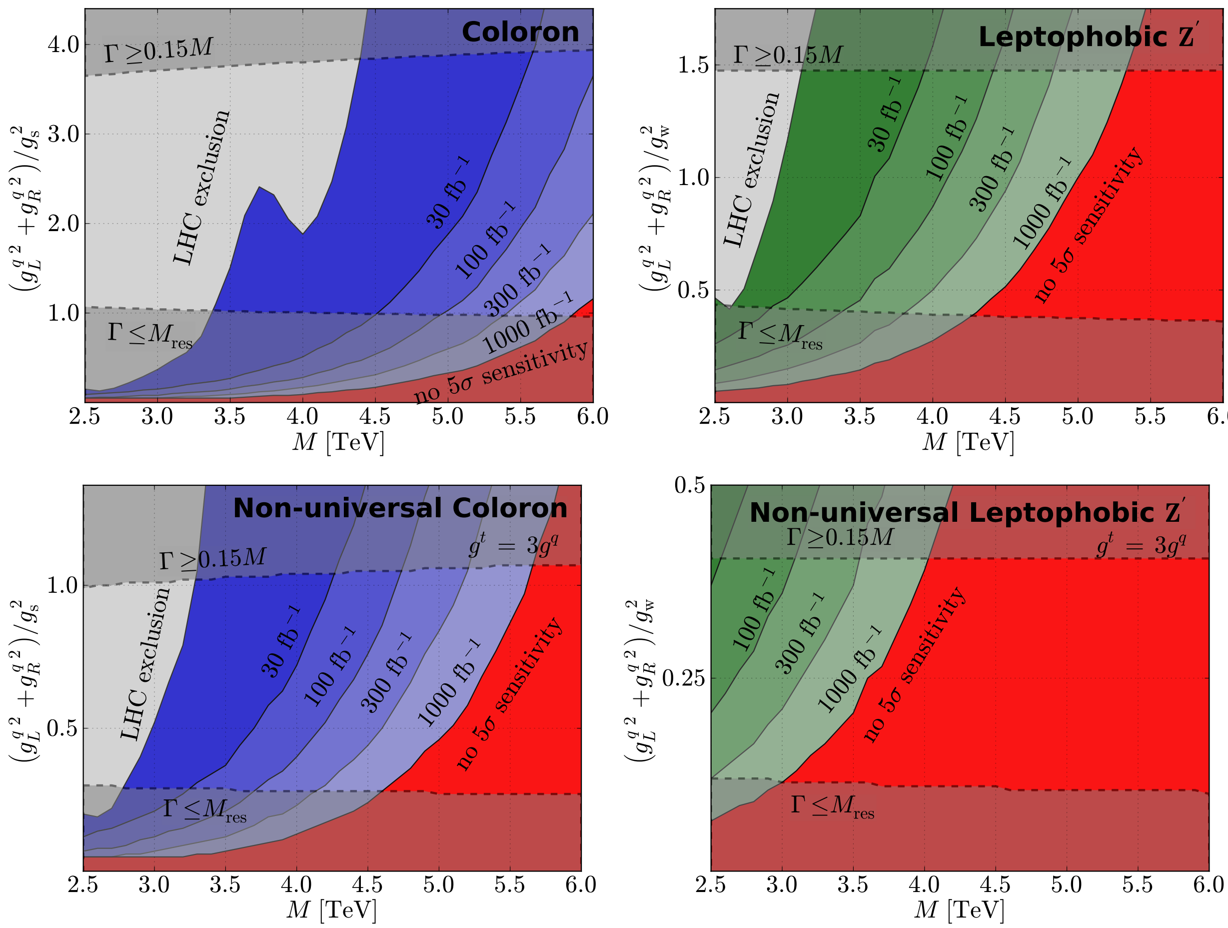

Figure 4.1: (a) Top left: 5σ discovery reach for a flavor universal coloron in the plane of the mass of the coloron (in TeV) and the square of the couplings at the LHC with $\sqrt{s} = 14$ TeV. The discovery reach is shown in varying shades of blue for different luminosities ranging from 30 fb^{-1} to 1000 fb^{-1}. The area marked "no 5σ sensitivity" corresponds to no discovery reach at 1000 fb^{-1} but may have some reach at higher luminosities. The area marked "LHC exclusion" in gray corresponds to the exclusion from 8 TeV LHC [249]. The region above the dashed line marked $\Gamma \geq 0.15M$ corresponds to the region where the narrow-width approximation used in di-jet resonance searches is not valid [258, 259, 131]. The region below the horizontal dashed line marked $\Gamma \leq M_{\rm res}$ corresponds to the region where the experimental mass resolution is larger than the intrinsic width [249]. See text for further details. (b) top right: same as (a) but for a leptophobic Z' and the discovery reach is shown in varying shades of green. (c) bottom left: same as (a) but for the flavor non-universal coloron where $g^t_{C_{L,R}} = 3g^q_{C_{L,R}}$. (d) bottom right: same as (b) but for the flavor non-universal Z' with $g^t_{Z'_{L,R}} = 3g^q_{Z'_{L,R}}$.

Searches for di-jet resonances where the width of the resonance is small compared to the mass have been carried out at the LHC by both CMS and ATLAS collaborations[2]. They have found no evidence of such resonances and set exclusion limits on the product of cross section, branching ratio and acceptance for the 8 TeV LHC run [246, 248, 249]. They also present the theoretical estimate of the product of cross section times branching fraction for various sample models, including colorons and sequential Z's. The acceptance for each model can then be estimated as a function of the mass without doing a full detector simulation. Using this estimated acceptance we translate the exclusion limits from Ref. [249] to obtain excluded regions in the plane of mass and coupling for the case of a coloron. The di-jet analysis [249] presents results only for a sequential Z' and hence we apply the acceptance for a sequential Z' to the leptophobic Z' as well. This is reasonable as the acceptance is dependent mainly on kinematics and not on the couplings and their structure at leading order. Note that in estimating the excluded regions we have used the most stringent results which come from CMS [249]. The results of this exercise are presented as gray regions labeled "LHC exclusion" in Fig. 4.1 for the coloron and leptophobic Z'. Note that a larger region of parameter space is excluded for the coloron compared to the leptophobic Z' due to the stronger coupling strength of the coloron to the SM quarks. On the other hand the excluded region for the flavor universal scenario is larger than that of the flavor non-universal scenario due to the smaller total cross section in the latter case as discussed earlier.

A resonance in the di-jet channel will be observed as a fluctuation in the exponentially falling QCD background. An estimation of the QCD di-jet background is notoriously difficult due to the reliance on leading order cross sections, uncertainties in the estimation of jet energy

[2] For a recent compilation of bounds on di-jet resonances, and their interpretation in terms of resonance couplings, see Ref. [257]. The results we present here, obtained from the experimental bounds cited, are consistent with the results of Ref. [257].

scale and other systematic uncertainties. Hence data driven methods are often employed to normalize the QCD background in a region away from the signal. In the absence of real data, a fit is performed to samples from full detector simulation to estimate the experimental sensitivity. As a full estimation of the QCD background and the sensitivity in the di-jet channel is beyond the scope (and focus) of this article, we use the results presented in Ref. [260] to estimate the discovery potential of a coloron and a leptophobic Z' in the di-jet channel at the LHC with $\sqrt{s} = 14$ TeV.

Similar to the case of current CMS studies, the authors of Ref. [260] present the minimum cross section that can be observed at the LHC with $\sqrt{s} = 14$ TeV and for luminosities up to 10 fb^{-1}. They present their discovery potential results as a product of cross section, branching ratio and acceptance for different masses of the resonance after taking into account statistical uncertainties (from background fluctuation) and systematic uncertainties. The systematic uncertainties include various sources such as jet energy scale, jet energy resolution, radiation and low mass resonance tails and luminosity. In addition they also present the theoretical estimate of the product of cross section times branching fraction for various sample models, including colorons and sequential Z's. As before, the acceptance for each model can then be estimated as a function of mass and we translate the 5σ discovery reach to regions in the plane of mass and coupling. The discovery reach from 10 fb^{-1} is then scaled appropriately to obtain the discovery reach for other values of integrated luminosities, $\mathcal{L} = 30, 100, 300$ and 1000 fb^{-1}. The regions that can be probed at the 5σ level for the case of the flavor universal and flavor non-universal coloron are presented as regions of varying shades of blue in Fig. 4.1(a) and Fig. 4.1(c) respectively for the different luminosities listed above. For the leptophobic Z', we use the acceptance for a sequential Z' as explained earlier and the discovery reach is presented in Fig. 4.1(b) and Fig. 4.1(d) as different shades of green for the flavor universal and flavor non-universal case respectively. The region shown in red and labeled "no 5σ sensitivity" in Fig. 4.1 corresponds to the case where the resonance will not be discovered at 5σ with 1000 fb^{-1}. Owing to the stronger coupling strength of the coloron to SM quarks the discovery reach for a coloron extends to larger masses while the reach for the leptophobic Z' is limited to lower masses due to the weak coupling to SM quarks. Moreover, the discovery region for the flavor non-universal scenario shrinks compared to the flavor universal scenario due to the smaller total di-jet cross section in the former case as discussed earlier.

Note that the experimental search for resonances in the di-jet channel applies in the region where the narrow-width approximation is valid. The authors of Refs. [258, 259, 131] point out that this approximation is valid only up to $\Gamma/M \leq 0.15$. The area above the top dashed line in Fig. 4.1 indicates the region where the narrow-width approximation is not valid. Similarly, the measurement of the width of a resonance is limited by the experimental mass resolution M_{res} and intrinsic widths smaller than M_{res} cannot be distinguished. The area below the bottom dashed line in Fig. 4.1 indicates the region where the intrinsic width is smaller than the experimental resolution and cannot be distinguished. The estimate of the experimental mass resolution varies with mass and has been obtained from Ref. [249]. Hence the region where our analysis is applicable is between the two dashed lines and where there is discovery potential indicated by blue (green) colored regions for a coloron (leptophobic Z').

Finally we present some details about our simulation of signal samples. The production cross section was calculated using MadGraph5 [261] and CTEQ6L1 PDFs [262] were used. The factorization and renormalization scales were set to be equal to the mass of the resonance. Next we discuss the sensitivity of the LHC to measure the color discriminant variable to distinguish color-octet and color-singlet states.

4.5 Sensitivity at the LHC

The color discriminant variable ($D_{\rm col}$) is a function of the mass (M) and intrinsic width (Γ) of the resonance as well as the cross section for producing the resonance in the di-jet channel (σ_{jj}). Hence statistical and systematic uncertainties in the measurement of the di-jet cross section, mass and intrinsic width of the resonance play a key role in the measurement of the color discriminant variable and hence in distinguishing a color-octet from a color-singlet resonance. In this section we discuss the uncertainties in the measurement of the mass, intrinsic width and the cross section for producing the resonance in the di-jet channel and their effect on the uncertainties in the measurement of $D_{\rm col}$ at the LHC with $\sqrt{s} = 14\,\text{TeV}$. Motivated by current constraints and future prospects described in Sec. 4.4 we consider resonance masses in the range $2.5 - 6$ TeV.

The uncertainty in the measurement of the di-jet cross section can be written as

$$\frac{\Delta\sigma_{jj}}{\sigma_{jj}} = \frac{1}{\sqrt{N}} \oplus \varepsilon_{\sigma\,\rm sys}\,, \tag{4.26}$$

where N is the number of signal events, $\varepsilon_{\sigma\,\rm sys}$ is the fractional systematic uncertainty and $\oplus$ indicates that the uncertainties are added in quadrature. The discovery of a resonance in the di-jet channel is a pre-requisite for measuring $D_{\rm col}$. Hence in the rest of the article N indicates the number of signal events required (above background fluctuation) to obtain a 5σ discovery and has been obtained from Ref. [260] as described in Sec. 4.4. The sources of systematic uncertainties in measuring the di-jet cross section include jet energy scale, jet energy resolution, radiation and low mass resonance tail and luminosity [36]. The effect of all these systematic uncertainties was estimated in Ref. [260] and presented as a fractional uncertainty (as a function of the mass) normalized to the di-jet cross section required to obtain 5σ discovery (above background fluctuation) at the LHC with $\sqrt{s} = 14$ TeV. The fractional uncertainty ($\varepsilon_{\sigma\,\mathrm{sys}}$) varies from 0.28 to 0.41 in the mass range of interest and is listed in Table 4.1.

The uncertainty in the measurement of the di-jet mass is given by

$$\frac{\Delta M}{M} = \frac{1}{\sqrt{N}}\left[\frac{\sigma_\Gamma}{M} \oplus \frac{M_{\mathrm{res}}}{M}\right] \oplus \left(\frac{\Delta M}{M}\right)_{\mathrm{JES}}, \tag{4.27}$$

where σ_Γ is the standard deviation corresponding to the intrinsic width of the resonance ($\Gamma \simeq 2.35\sigma_\Gamma$ assuming a Gaussian distribution), M_{res} is the experimental di-jet mass resolution and $(\Delta M/M)_{\mathrm{JES}}$ is the uncertainty in the mass measurement due to uncertainty in the jet energy scale. The various components of systematic uncertainties contributing to the uncertainty in the mass measurement depend on each experiment and detector and their estimate for different experiments and c.m. energies are listed in Table 4.1. The specific values used in our analysis are indicated by an asterisk (*).

The uncertainty in the measurement of the intrinsic width is given by

$$\frac{\Delta\Gamma}{\Gamma} = \sqrt{\frac{1}{2(N-1)}\left[1 + \left(\frac{M_{\mathrm{res}}}{\sigma_\Gamma}\right)^2\right]^2 + \left(\frac{M_{\mathrm{res}}}{\sigma_\Gamma}\right)^4\left(\frac{\Delta M_{\mathrm{res}}}{M_{\mathrm{res}}}\right)^2}, \tag{4.28}$$

where ΔM_{res} is uncertainty in the di-jet mass resolution due to uncertainty in the jet energy resolution. Again, the estimate of the various components contributing to the uncertainty in the width measurement are listed in Table 4.1 for various experiments and the values used in the analysis are indicated by an asterisk(*). See Appendix C for details on calculating the expression for uncertainty in the intrinsic width given in Eq. (4.28).

The estimation of systematic uncertainties depends on detector details and the energy of the collider and an accurate estimate of any systematic uncertainty can be done only after the machine is operational and has been calibrated. However as the LHC is yet to run at $\sqrt{s} = 14$ TeV, the energy for which we present our results, we have the choice of using the systematic uncertainties estimated using full detector simulation (but no real data) at $\sqrt{s} = 14$ TeV or of using the systematic uncertainties from real LHC data but for $\sqrt{s} = 8$ TeV. We will use the estimate for systematic uncertainties from actual LHC data where available and assume that any future LHC run will be able to reach at least the current level of uncertainties, if not better. This is a reasonable assumption as experiments tend to make improvements in their estimation of errors and efficiencies with real data, compared to original estimates from simulated data, due to improved experimental techniques. For example, the uncertainty in mass due to the uncertainty in jet energy scale at the LHC with $\sqrt{s} = 14\,\mathrm{TeV}$ was expected to be about 5% [36] while the current analyses at $8\,\mathrm{TeV}$ show that an uncertainty of 1.25% is achievable [249]. Note that we have modeled all systematic uncertainties to be Gaussian and hence added them in quadrature. We have also not included any correlation between the uncertainties. Most of the systematic uncertainties were estimated for resonance masses up to 5 TeV for the different experiments and we have extrapolated this estimate to resonance masses up to 6 TeV. To account for the possibility that the systematic uncertainties are larger than the ones we use in the analysis we also present our results for the case where all the systematic uncertainties used in evaluating D_{col} are increased by a factor of 1.5. We believe this rather conservative estimate will be able to cover reasonable fluctuations in systematic uncertainties due to higher energy, larger luminosity and other effects not included in our study.

Table 4.1: Sources of systematic uncertainty contributing to uncertainties in measurement of the cross section, mass and width of a resonance in the di-jet channel at various experiments and c.m. energies. The values used in this analysis are indicated by an asterisk.

Systematic Uncertainty	Notation	Value	Mass Range	$\sqrt{s}$	Experiment
Di-jet cross section uncertainty (fractional)	$\varepsilon_{\sigma\,\mathrm{sys}}$	$0.28 - 0.41^*$	$2.5 - 6$ TeV	14 TeV	LHC [260]
Mass resolution	$\frac{M_{\mathrm{res}}}{M}$	$0.045 - 0.035^*$	$2.5 - 6$ TeV	8 TeV	CMS [249]
		$0.045 - 0.031$	$2.5 - 6$ TeV	8 TeV	ATLAS [247]
		$0.071 - 0.062$	$2.5 - 6$ TeV	14 TeV	LHC [260]
Mass resolution uncertainty	$\frac{\Delta M_{\mathrm{res}}}{M}$	0.1^*	any	8 TeV	CMS [248]
		0.1	any	14 TeV	LHC [260]
Mass uncertainty from jet energy scale (JES)	$\left(\frac{\Delta M}{M}\right)_{\mathrm{JES}}$	0.013^*	any	8 TeV	CMS [248]
		0.028	any	8 TeV	ATLAS [247]
		0.035	any	14 TeV	LHC [260]

4.6 Results

In this section we describe the sensitivity of the LHC to distinguish a color-octet resonance from a color-singlet resonance using the color discriminant variable introduced in Sec. 4.3. We estimate the sensitivity at the LHC by evaluating D_{col} and include the uncertainties in estimating D_{col} as described in Sec. 4.5. Motivated by current constraints on di-jet resonances and future sensitivity of the LHC to discover di-jet resonances as described in Sec. 4.4, we consider the mass range of $2.5 - 6$ TeV. We will present our results for the flavor universal and the flavor non-universal case at the LHC with $\sqrt{s} = 14$ TeV for varying integrated luminosities, namely, $\mathcal{L} = 30, 100, 300$ and 1000 fb^{-1}.

4.6.1 Flavor Universal Scenario

The sensitivity of the LHC with c.m. energy of 14 TeV to distinguish color-octet and color-singlet resonances in the flavor universal scenario is shown in Fig. 4.2(a) - (d) for varying luminosities, $\mathcal{L} = 30, 100, 300$ and 1000 fb^{-1}. The sensitivity is presented in the plane of the mass of the resonance (M) in TeV and the log of the color discriminant variable (D_{col}). In each panel, there are two separate bands, corresponding to a coloron and a leptophobic Z'. For each resonance, the uncertainty in the measurement of D_{col} due to uncertainties in the measurement of the cross section, mass and width of the resonance is indicated by gray bands around the central value of D_{col} represented as a black dashed line. The outer (dark gray) band corresponds to the uncertainty in D_{col} when the width is equal to the mass resolution, *i.e.* $\Gamma = M_{\text{res}}$. A determination of the intrinsic width is not possible when $\Gamma < M_{\text{res}}$. The inner (light gray) band corresponds to the case where the width $\Gamma = 0.15M$. The narrow width approximation used in di-jet searches is not valid when $\Gamma > 0.15M$. Resonances with width $M_{\text{res}} \leq \Gamma \leq 0.15M$ will have bands that extend between the outer and inner gray bands. The blue (green) colored region indicates the region in parameter space of the coloron (leptophobic Z') that has not been excluded by current searches [249] and has the potential to be discovered at the LHC at a 5σ level as described in Sec. 4.4.

The results in Fig. 4.2 illustrate several features. First, note that the bands for coloron and leptophobic Z' are well separated vertically. This implies that the color discriminant variable is able to clearly distinguish between a color-octet and a color-singlet at the LHC after all uncertainties have been taken into account. The mass range (from $2.5-6$ TeV) can be roughly divided into three regions: the low mass region where the Z' band is green but the coloron band is grayed out; the high mass region where at least one band is grayed out,

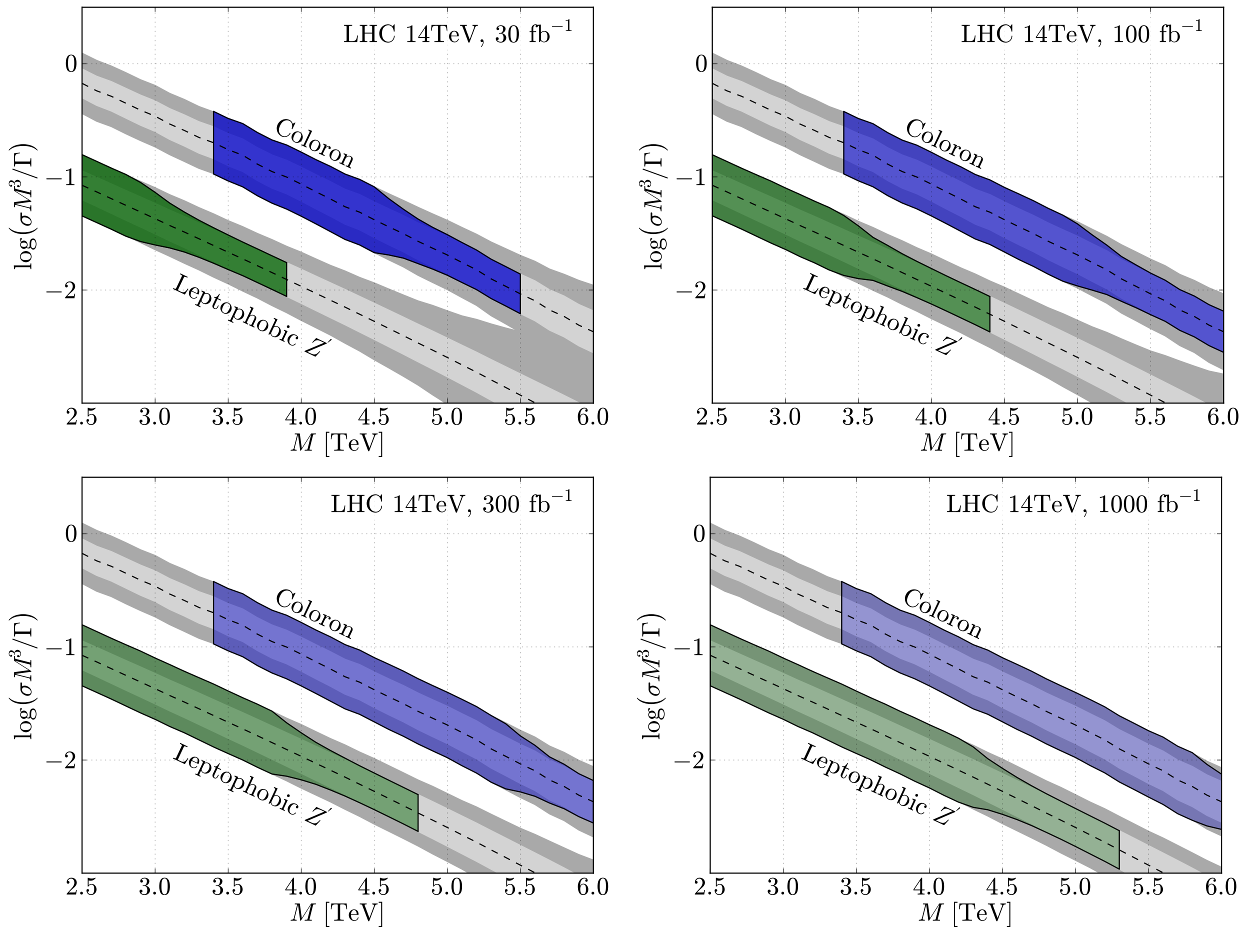

Figure 4.2: (a) Top left: Sensitivity at the LHC with $\sqrt{s} = 14$ TeV and integrated luminosity of $30\,\text{fb}^{-1}$ for distinguishing a coloron from a leptophobic Z' in the plane of the log of the color discriminant variable $\left(D_{\text{col}} = \frac{M^3}{\Gamma}\sigma_{jj}\right)$ and mass (in TeV) for the flavor universal scneario. The central value of D_{col} for each particle is shown as a black dashed line. The uncertainty in the measurement of D_{col} due to the uncertainties in the measurement of the cross section, mass and width of the resonance is indicated by gray bands. The outer (darker gray) band corresponds to the uncertainty in D_{col} when the width is equal to the experimental mass resolution *i.e.* $\Gamma = M_{\text{res}}$. The inner (lighter gray) band corresponds to the case where the width $\Gamma = 0.15M$. Resonances with width $M_{\text{res}} \leq \Gamma \leq 0.15M$ will have bands that extend between the outer and inner gray bands. The blue (green) colored region indicates the region in parameter space of the coloron (leptophobic Z') that has not been excluded by current searches [249] and has the potential to be discovered at a 5σ level at the LHC with $\sqrt{s} = 14$ TeV after statistical and systematic uncertainties are taken in to account. (b) Top right: Same as (a) but for an integrated luminosity of 100 fb^{-1}. (c) Bottom left: Same as (a) but for an integrated luminosity of 300 fb^{-1} (d) Bottom right: Same as (a) but for an integrated luminosity of 1000 fb^{-1}. Note that the colored regions in all panels correspond to the same colored regions in the mass and coupling plane used in Fig. 4.1 for different luminosities.

and an intermediate region where the coloron band is blue and the Z' band is green. The color discriminant variable can be used to distinguish colorons and leptophobic Z's in the intermediate region where both resonances are allowed, discoverable at the LHC, and have widths in the appropriate range ($M_{\text{res}} \leq \Gamma \leq 0.15M$). Note that this overlap region expands with increasing luminosity.

Our analysis is not useful in the low mass region because a coloron there is either already excluded by LHC searches or is too narrow. For example, consider a future discovery of a resonance in the di-jet channel at a mass of 3.0 TeV and 100 fb^{-1} of integrated luminosity. This could certainly correspond to a Z' lying within the green band of Fig. 4.2(b). However, from the lower left corner of Fig. 4.1(a) we also see that it could correspond to a very narrow coloron, with a width less than the detector resolution. Being unable to measure the width of such a coloron accurately, the uncertainty in the measurement of our discriminant variable D_{col} would be very large and hence we would not be able to distinguish between a coloron and a leptophobic Z'.

Now contrast this with the high mass region where the coloron has the potential to be discovered while the leptophobic Z' band is grayed out. In this case if a resonance is discovered in the di-jet channel with a mass of 5.0 TeV with 100 fb^{-1} integrated luminosity, then we would have confidence that it is a coloron and not a leptophobic Z'. A discovery in the di-jet channel (with the current analyses) requires the width to be relatively narrow ($\Gamma \leq 0.15M$), while the width of a corresponding Z' would be very broad as seen in Fig. 4.1(b). Note that there are no current experimental strategies to discover very broad resonances and it is also beyond the scope of our analysis.

The color discriminant variable is a dimensionless quantity that depends only on the color factors for a given ξ. All points in the parameter space of a coloron and leptophobic

Z' give the same value of $D^{C}_{\rm col}$ and $D^{Z'}_{\rm col}$ respectively and $D^{C}_{\rm col} \neq D^{Z'}_{\rm col}$ for a given ξ. However the results in Fig. 4.2 show a clear dependence of $D_{\rm col}$ on the mass of the resonance (M). This dependence on the mass is an artifact of the implicit dependence on mass coming from PDFs. A resonance with a large (small) mass corresponds to parton luminosity at large (small) x and hence small (large) cross section. Note that at a fixed collision energy (at the parton level) the value of $D_{\rm col}$ for a given resonance will be universal and have no mass dependence.

The uncertainties in the estimation of $D_{\rm col}$ are large for higher mass resonances compared to the ones at low mass. This is easily understood as high mass resonances have smaller cross sections and hence fewer signal events leading to large uncertainties. As the luminosity increases from 30 fb^{-1} to 1000 fb^{-1} the uncertainty at higher masses decreases due to the larger number of signal events and the width of the uncertainty bands becomes uniform. This is because systematic uncertainty will become progressively dominant when the number of events is sufficiently large that a 5σ discovery is possible.

The uncertainty in the color discriminant variable is smaller for the case of larger width (inner gray band) and is larger for the case of smaller width (outer gray band) resonances. This is because smaller width corresponds to smaller couplings and hence smaller cross section which leads to larger statistical uncertainty. In addition the uncertainty in the intrinsic width is inversely proportional to $\Gamma/M_{\rm res}$ and hence leads to larger systematic uncertainty for smaller widths. This relation between the uncertainty in the width and the mass resolution is described in Appendix C. In addition, the size of the colored band (which corresponds to the discovery reach) is smaller for larger masses. This is because the couplings corresponding to a width of $\Gamma = M_{\rm res}$ (outer region of the colored band) are small leading to a smaller cross section and hence not enough signal events for a 5σ-discovery at a given

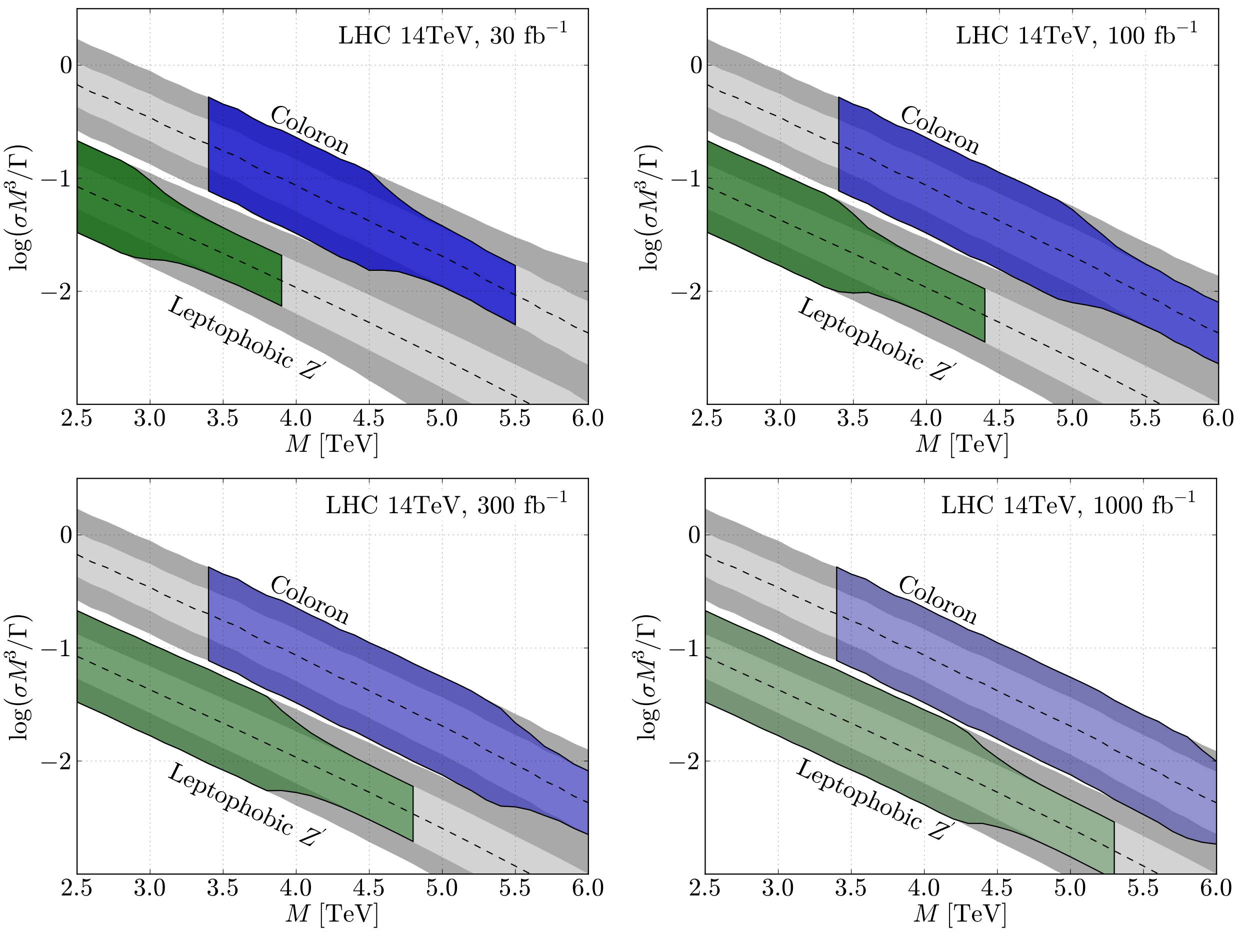

Figure 4.3: Same as Fig. 4.2, but with the systematic uncertainties in M, Γ and σ_{jj} increased by a factor of 1.5.

mass. The larger couplings which correspond to larger widths (inner region of the colored band) and larger cross sections have the potential for a 5σ discovery.

In Fig. 4.3, we display the results for the scenario where systematic uncertainties in the measurement of mass, width and cross section of the resonance in the di-jet channel listed in Sec. 4.5 were increased by a factor of 1.5. Note that our results remain robust even with this very conservative estimate of systematic uncertainties and the color-octet and color-singlet states can still be distinguished from each other.

4.6.2 Flavor Non-universal Scenario

In this section we discuss the sensitivity of the LHC with c.m. energy of 14 TeV to distinguish between color-octet and color-singlet resonances in the flavor non-universal scenario. As illustrative examples we present the results for two different flavor non-universal scenarios in Fig. 4.4 for the mass range $2.5 - 6$ TeV and for various couplings and widths. In Fig. 4.4(a) and Fig. 4.4(b) we present the results in the plane of mass of the resonance and the log of the color discriminant variable for $g^t_{L,R} = 2g^q_{L,R}$ for integrated luminosities of 300 fb^{-1} and 1000 fb^{-1} respectively. In Fig. 4.4(c) and Fig. 4.4(d) we present similar results for $g^t_{L,R} = 3g^q_{L,R}$ for integrated luminosities of 300 fb^{-1} and 1000 fb^{-1} respectively.

The results for the flavor non-universal case in Fig. 4.4 illustrate several features. As discussed in Sec. 4.3, the ratio between the widths of a color-octet and color-singlet depends only on the color factors and hence the color discriminant variable can be used to distinguish color-octet and color-singlet resonances in the flavor non-universal scenario for a given ξ. This is demonstrated by the separation between the bands for colorons and leptophobic Z's in Fig. 4.4, for the cases $\xi = 2$ and $\xi = 3$. Several features present in the flavor universal case are preserved. The reach in mass increases with increasing luminosity; the uncertainty in the

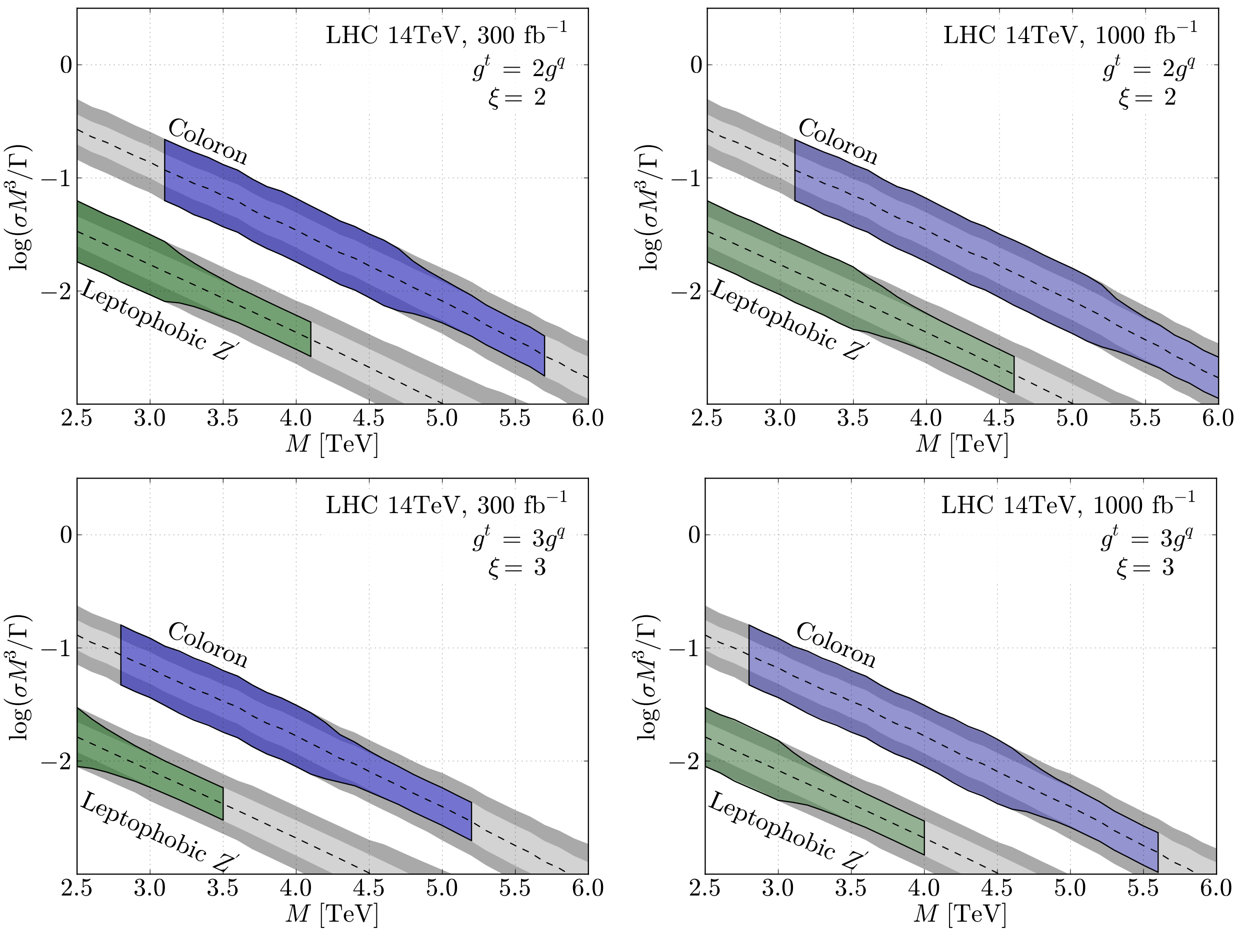

Figure 4.4: (a) Top left: same as Fig. 4.2(c), but for the flavor non-universal case with $g^t_{L,R} = 2g^q_{L,R}$. (b) Top right: same as (a) but for integrated luminosity of 1000 fb^{-1}. (c) Bottom left: same as (a) but for $g^t_{L,R} = 3g^q_{L,R}$. (d) Bottom right: same as (c) but for integrated luminosity of 1000 fb^{-1}.

estimation of D_{col} is large for larger masses and is dominated by systematic uncertainties when the number of events is large and the uncertainties for resonances with small (large) widths is large (small). There are also some new features specific to the flavor non-universal case. The reach in mass decreases with increasing ξ. As discussed in Sec. 4.4, as ξ changes the production cross section remains the same while the branching fraction to jets decreases leading to a smaller di-jet cross section and hence fewer signal events. Note that the central value of D_{col} decreases with increasing ξ due to the dependance of the di-jet cross section on ξ^2 as shown in Eqs. (4.22) and (4.23).

So far we have presented results for distinguishing a color-octet and a color-singlet state in the flavor universal case and in the flavor non-universal case for a given ξ. In Fig. 4.5 we present the sensitivity of the color discriminant variable for varying ξ at the LHC with $\sqrt{s} = 14$ TeV. In Fig. 4.5(a) and (b) we present results for $M = 3$ TeV and integrated luminosities of 300 fb^{-1} and 1000 fb^{-1} respectively while Fig. 4.5(c) and (d) are for $M =$ 4 TeV and integrated luminosities of 300 fb^{-1} and 1000 fb^{-1} respectively. As before the central values are indicated by dashed (black) lines and the reach for colorons (leptophobic Z's) are denoted by blue (green) regions. The different points marked a, b, c, d correspond to different parameter points used as examples below.

With the discovery of a resonance in the di-jet channel a measurement of the mass, width and cross section and hence of the color discriminant variable is possible. Several scenarios may be allowed for a given measured value of mass and D_{col}. For example, in Fig. 4.5(a), for $\log(D_{\text{col}}) = -1.5$ a few of the allowed possibilities include a leptophobic Z' with $\xi = 1$ and a coloron with $\xi = 3.5$ or 4.5 and are marked by the points labeled a, b, c respectively. Similar possibilities are shown for other masses and luminosities in Fig. 4.5(b) - (d) for different measured values of D_{col} and are labeled as a, b, c, d. With just the measurements from the

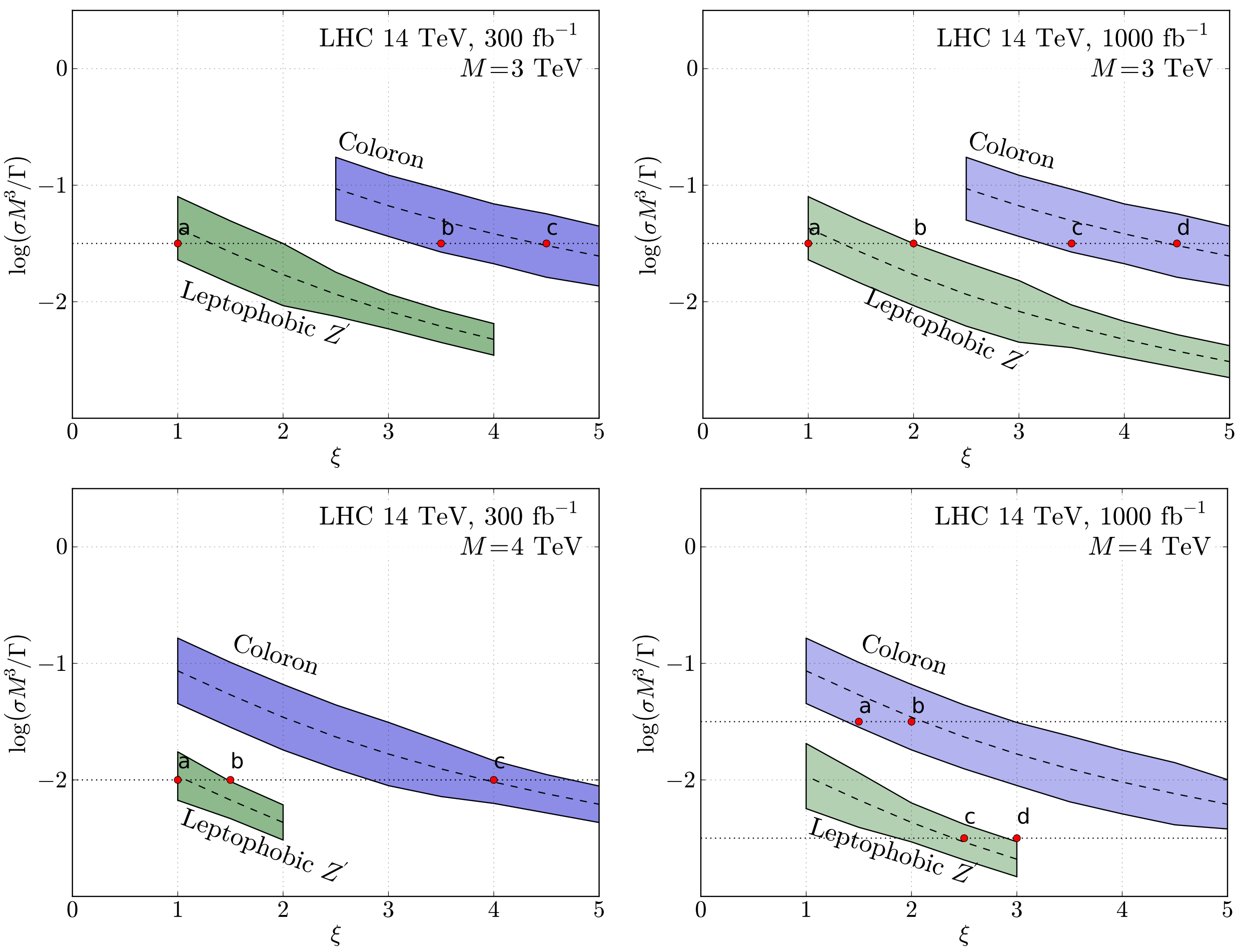

Figure 4.5: (a) Top left: Sensitivity to distinguish color-octet and color-singlet scenarios at the LHC with $\sqrt{s} = 14$ TeV and integrated luminosity of 300 fb^{-1} for a resonance of mass 3 TeV for different values of ξ. (b) Top right: same as (a) but for integrated luminosity of 1000 fb^{-1}. (c) Bottom left: same as (a) but for a resonance with mass 4 TeV. (d) Bottom right: same as (c) but for integrated luminosity of 1000 fb^{-1}. The different points marked a, b, c, d correspond to different parameter points used as examples in the text.

di-jet discovery channel it would not be possible to distinguish which of these scenarios is being realized in nature. Additional information is required, for instance, by measuring ξ from the ratio of the cross sections when the resonance decays to top pairs vs jets as given in Eq. (4.16). With these two measurements, *i.e.* $D_{\rm col}$ and ξ, one can distinguish between color-octet and color-singlet resonances and their flavor structure.

Finally, we note that distinguishing between color-octet and color-singlet resonances of various flavor structures depends on the reach of ξ as well as the precision with which ξ can be measured at the LHC. This in turn depends on the measurements of the cross section in the di-jet channel and the top pair channel and the associated uncertainties. For example, a resonance may be discovered at a given mass in the di-jet channel and a measurement of $D_{\rm col}$ may be made. However a measurement of the cross section in the top pair channel may not be possible or may have large uncertainties due to limited statistics (because of small branching to top pairs). In such a case a measurement of ξ is not possible or has very large errors and the ability to distinguish various flavor scenarios is reduced. A detailed exploration of the reach and precision with which ξ can be measured is beyond the scope and focus of this article. Instead we refer the interested reader to experimental studies of resonance searches in the top pair [263, 264, 265, 266] and di-jet channels [260] and the results of such studies can provide an estimate of ξ and the uncertainties in measuring ξ.

4.7 Summary

Di-jet resonance searches are simple but powerful model-independent probes for discovering new particles motivated in many new physics scenarios. Once a resonance has been discovered in the di-jet channel it will be very important to measure its properties. The di-jet (discovery) channel can provide information about the mass and spin of the resonance as well as constrain the coupling strength. It does not provide information about the chiral structure; that can be obtained by including information from the channel where the resonance is produced in association with a SM electroweak gauge boson. The next question that remains to be resolved is the color structure of the new resonance; in particular, whether it is a color-octet or color-singlet resonance.

In the work on which this chapter is based, we proposed a new variable called the color discriminant variable ($D_{\rm col}$) to distinguish color-octet from color-singlet resonances. This variable is relatively model-independent and is sensitive to the color and flavor structure. In order to make our study as widely applicable as possible, we studied phenomenological models of color-octet and color-singlet resonances without being tied down to a specific theory. As illustrative examples we studied colorons and leptophobic Z's in the flavor universal case as well as an illustrative flavor non-universal scenario. We analyzed the current constraints on the parameter space and the discovery potential of coloron and leptophobic Z' models at the future LHC. We sampled a wide range of masses, couplings and values of ξ, which parameterizes the relative coupling strength of the third generation and first generation SM quarks to the new resonance.

We studied the sensitivity to distinguish color-octet and color-singlet resonances in the flavor universal as well as flavor non-universal scenarios and presented our results for the LHC with c.m. energy of 14 TeV for varying luminosities, $\mathcal{L} = 30,\ 100,\ 300$ and 1000 fb^{-1}, after including all uncertainties. We found that our method has a wide reach in mass and couplings as well as ξ. A measurement of $D_{\rm col}$ alone can distinguish between color-octet and color-singlet states for a given flavor scenario. However to distinguish between different flavor scenarios we will need additional information which comes from a measurement of ξ.

Together, D_{col} and ξ can help distinguish a color-octet from a color-singlet state as well as establish the nature of the couplings in the flavor sector. We find that the LHC will be able to provide information about the color and flavor structure of a new di-jet resonance for a wide range of couplings and masses and hence point us in the direction of the underlying theoretical structure.

Chapter 5

Distinguishing Flavor Non-universal Colorons from Z' Bosons with Heavy Flavor Measurements

— *This chapter is based on a work in collaboration with R. Sekhar Chivukula and Elizabeth H. Simmons which has appeared in [7].*

5.1 Introduction

In the previous chapter, we have established the possibility of distinguishing whether a vector resonance is either a leptophobic color-singlet or a color-octet, using a variable available with the discovery of the resonance: the "color discriminant variable", D_{col}. The variable is constructed from the dijet cross-section for the resonance (σ_{jj}), its mass (M), and its total decay width (Γ), observables that will be available from the dijet channel measurements of the resonance:

$$D_{\mathrm{col}} \equiv \frac{M^3}{\Gamma}\sigma_{jj}, \tag{5.1}$$

For a narrow-width resonance, the color discriminant variable is independent of the resonance's overall coupling strength. We also illustrated applications of the color discriminant variable technique for two simple cases. The first was a flavor universal model with identical couplings to all quarks — see Sec. 4.2.1. In the second, the overall strength of couplings to quarks in the third generation was allowed to be different from those in the first two (couplings to top and bottom were kept equal) — see Sec. 4.2.2. Combining D_{col} with information about the $t\bar{t}$ cross-section[1] for the resonance ($pp \to V \to t\bar{t}$) still enabled us to distinguish C from Z' in the second case. While these two scenarios clearly illustrate the application of the method, they did not encompass the features of a typical Z', whose up- and down-type couplings are usually also different from one another.

In this work [7] we demonstrate the application of the D_{col} method to more general scenarios where couplings to quarks within the same generation (e.g., up vs. down, left-handed vs right-handed) are different, while still allowing couplings to quarks in the third generation to be different from those in the first two. This general scenario corresponds to more realistic models, especially those featuring a Z', as in the case where the gauge group responsible for the existence of the resonance does not commute with the gauge groups of the Standard Model. We discuss how one could incorporate information from heavy resonance decays to of a top pair ($t\bar{t}$) and a bottom pair ($b\bar{b}$) in order to determine what type of resonance has been discovered.

The rest of the chapter is organized as follows. We lay out the phenomenological parameters we use, as well as key assumptions imposed on them, in section 5.2. Then, we discuss the detailed application to flavor-nonuniversal scenarios in section 5.3. The parameter space to which our method is applicable is then presented in section 5.4. After reprising, in section 5.5, the estimation of uncertainties for the LHC at $\sqrt{s} = 14\,\mathrm{TeV}$ from [6], we present our

[1] Studies of the sensitivity of a resonance decaying to $t\bar{t}$ at the $\sqrt{s} = 14\,\mathrm{Tev}$ LHC include [267, 268, 269, 270, 271].

results in section 5.6 and discuss them in section 5.7. Model-independent plots for various combinations of resonance couplings and masses are presented in Appendix D to illustrate how well each relevant observable must be measured to distinguish between the coloron and the Z'.

5.2 General Parameterization and Assumptions

In this section, we introduce the assumptions about properties regarding chiral and generation structures that are used in this chapter. The phenomenological parameterizations of the coloron and leptophobic Z' couplings are the same as what have been used in Chapter 4.

Couplings between the vector boson and the left- and right-handed forms of the up- and down-type fermions are not necessarily equal in general. It is true that a color octet resonance, originating from interactions described by a gauge group commuting with $SU(2)_L$ of the standard model, will have the same couplings to the left-handed up- and down-type quarks. The same is not generally the case for a Z' boson. Moreover, the couplings of either a coloron or Z' to right-handed up- and down-type quarks may differ.

Couplings between the vector boson and the left- and right-handed forms of the up- and down-type fermions are not necessarily equal in general. It is true that a color octet resonance, originating from interactions described by a gauge group commuting with $SU(2)_L$ of the standard model, will have the same couplings to the left-handed up- and down-type quarks. The same is not generally the case for a Z' boson. Moreover, the couplings of either a coloron or Z' to right-handed up- and down-type quarks may differ.

In addition, the couplings can generally be different among the three generations of quarks. The observed suppressions of flavor-changing neutral currents disfavor a TeV-scaled resonance with non-universal couplings to the first two generations[2]. So we will limit our interests throughout this article to scenarios where couplings for the first two generations are the same. The third generation is special. In models where top quark plays a unique role, the couplings to quarks in the third generation are often assumed to be different from those for the light quark generations.

Therefore, under this assumption, a coloron has 6 free parameters describing its couplings to quarks:

$$\begin{aligned} &g^{u,c}_{C_L} = g^{d,s}_{C_L} \qquad &\text{and} \qquad &g^{u,c}_{C_R},\, g^{d,s}_{C_R} \\ &g^{t}_{C_L} = g^{b}_{C_L} \qquad &\text{and} \qquad &g^{t}_{C_R},\, g^{b}_{C_R}\,, \end{aligned} \tag{5.2}$$

while a leptophobic Z' has 8:

$$\begin{aligned} &g^{u,c}_{Z'_L},\, g^{d,s}_{Z'_L} \qquad &\text{and} \qquad &g^{u,c}_{Z'_R},\, g^{d,s}_{Z'_R} \\ &g^{t}_{Z'_L},\, g^{b}_{Z'_L} \qquad &\text{and} \qquad &g^{t}_{Z'_R},\, g^{b}_{Z'_R}\,. \end{aligned} \tag{5.3}$$

The dependence on these parameters does not fully manifest itself in measurements available after a discovery; *i.e.*, width and dijet cross section. After all, those observables are not sensitive to chiral structures of the coupling, as the left- and right-handed couplings enter symmetrically. So we denote

$$g^{q2} \equiv g^{q2}_L + g^{q2}_R \tag{5.4}$$

[2]See, for example, Table 4 of Ref. [272].

and notice that the four relevant parameters for our analysis of colorons are

$$g_C^{u\,2} = g_C^{c\,2}, \quad g_C^{d\,2} = g_C^{s\,2}, \quad g_C^{t\,2}, \quad g_C^{b\,2} \tag{5.5}$$

and, similarly, there are four

$$g_{Z'}^{u\,2} = g_{Z'}^{c\,2}, \quad g_{Z'}^{d\,2} = g_{Z'}^{s\,2}, \quad g_{Z'}^{t\,2}, \quad g_{Z'}^{b\,2} \tag{5.6}$$

for a leptophobic Z'.

The dijet cross section ($\sigma(pp \to V \to jj)$) plays an important role in evaluating the color discriminant variable. In this analysis, we make a distinction between quarks from the first two "light" generations and those from the third. So we will classify what is referred to as "dijet" resonance accordingly. Not only does this simplify the analysis, as we shall see later on, but measurements of the cross sections to the $t\bar{t}$ and $b\bar{b}$ final states (respectively, $\sigma(pp \to V \to t\bar{t})$ and $\sigma(pp \to V \to b\bar{b})$) will provide distinct information allowing the identification of the color structure of the resonance. Throughout the article, quarks that constitute a jet j are those from the first two generations[3]; namely,

$$j = u,\, d,\, c,\, s. \tag{5.7}$$

With these definitions, we now demonstrate how to construct a color discriminant variable.

[3]Notice that the definition of jets is different from that in Chapter 4.

5.3 Defining Color Discriminant Variables in Flavor Non-universal Models

In this section, we extend the definition of the color discriminant variable, introduced in Section 4.3 of the previous chapter, to general scenarios of a resonance with flavor non-universal couplings.

Recall the simple flavor universal scenario from Sec. 4.3. Since the overall coupling strength can be factored out as a ratio of observables (Γ_V/M_V) as shown in (4.18) and (4.19), the color discriminant variable is defined as

$$D_{\rm col}^{C} = \frac{M_C^3}{\Gamma_C}\sigma_{jj}^{C} = \frac{8}{9}\left[\sum_q W_q(M_C)Br(C \to jj)\right] \tag{5.8}$$

$$D_{\rm col}^{Z'} = \frac{M_{Z'}^3}{\Gamma_{Z'}}\sigma_{jj}^{Z'} = \frac{1}{9}\left[\sum_q W_q(M_{Z'})Br(Z' \to jj)\right] \tag{5.9}$$

for the coloron and Z', respectively. Here we have used the $W_q(M)$ function defined in Eq.4.20. In a flavor non-universal scenario, one cannot always factor out the dependence of couplings appearing in a production cross section in this manner. Branching fractions of the decay final states are also not necessarily the same for two resonances. In the following sections, we will demonstrate that even when this is the case, the color discriminant variable method remains valuable.

In a flavor non-universal scenario, we will follow the parameterization and assumptions introduced in section 5.2. The production cross section and decay width for the coloron are

$$\begin{aligned}
\sigma(pp \to C) &= \frac{4}{9}\frac{\alpha_s}{M_C^2}\left[g_C^{u\,2}\left(W_u + W_c\right) + g_C^{d\,2}\left(W_d + W_s\right) + g_C^{b\,2}W_b\right] \\
&= \frac{4}{9}\frac{\alpha_s}{M_C^2}\left(g_C^{u\,2} + g_C^{d\,2}\right)\left[\frac{g_C^{u\,2}}{g_C^{u\,2} + g_C^{d\,2}}\left(W_u + W_c\right)\right. \\
&\qquad \left. + \left(1 - \frac{g_C^{u\,2}}{g_C^{u\,2} + g_C^{d\,2}}\right)\left(W_d + W_s\right) + \frac{g_C^{b\,2}}{g_C^{u\,2} + g_C^{d\,2}}W_b\right], \qquad (5.10) \\
\Gamma_C &= \frac{\alpha_s}{12}M_C\left[2g_C^{u\,2} + 2g_C^{d\,2} + g_C^{t\,2} + g_C^{b\,2}\right] \\
&= \frac{\alpha_s}{12}M_C\left(g_C^{u\,2} + g_C^{d\,2}\right)\left[2 + \frac{g_C^{t\,2}}{g_C^{u\,2} + g_C^{d\,2}} + \frac{g_C^{b\,2}}{g_C^{u\,2} + g_C^{d\,2}}\right], \qquad (5.11)
\end{aligned}$$

where they have been written using parametrization that allows some of them to, as we shall see, correspond to observables. The expressions for leptophobic Z' are similar

$$\begin{aligned}
\sigma(pp \to Z') &= \frac{1}{3}\frac{\alpha_w}{M_{Z'}^2}\left(g_{Z'}^{u\,2} + g_{Z'}^{d\,2}\right)\left[\frac{g_{Z'}^{u\,2}}{g_{Z'}^{u\,2} + g_{Z'}^{d\,2}}\left(W_u + W_c\right)\right. \\
&\qquad \left. + \left(1 - \frac{g_{Z'}^{u\,2}}{g_{Z'}^{u\,2} + g_{Z'}^{d\,2}}\right)\left(W_d + W_s\right) + \frac{g_{Z'}^{b\,2}}{g_{Z'}^{u\,2} + g_{Z'}^{d\,2}}W_b\right], \qquad (5.12) \\
\Gamma_{Z'} &= \frac{\alpha_w}{2}M_{Z'}\left(g_{Z'}^{u\,2} + g_{Z'}^{d\,2}\right)\left[2 + \frac{g_{Z'}^{t\,2}}{g_{Z'}^{u\,2} + g_{Z'}^{d\,2}} + \frac{g_{Z'}^{b\,2}}{g_{Z'}^{u\,2} + g_{Z'}^{d\,2}}\right]. \qquad (5.13)
\end{aligned}$$

The color discriminant variables are, for the coloron,

$$\begin{aligned}
D_{\text{col}}^C &= \frac{16}{3}\left(W_u + W_c\right)\left[\frac{g_C^{u\,2}}{g_C^{u\,2} + g_C^{d\,2}} + \left(1 - \frac{g_C^{u\,2}}{g_C^{u\,2} + g_C^{d\,2}}\right)\left(\frac{W_d + W_s}{W_u + W_c}\right)\right. \\
&\qquad \left. + \frac{g_C^{b\,2}}{g_C^{u\,2} + g_C^{d\,2}}\left(\frac{W_b}{W_u + W_c}\right)\right] \times \left\{\frac{2}{\left(2 + \frac{g_C^{t\,2}}{g_C^{u\,2}+g_C^{d\,2}} + \frac{g_C^{b\,2}}{g_C^{u\,2}+g_C^{d\,2}}\right)^2}\right\} \qquad (5.14)
\end{aligned}$$

and for the Z',

$$
\begin{aligned}
D_{\text{col}}^{Z'} &= \frac{2}{3}\left(W_u+W_c\right)\left[\frac{g_{Z'}^{u\,2}}{g_{Z'}^{u\,2}+g_{Z'}^{d\,2}}+\left(1-\frac{g_{Z'}^{u\,2}}{g_{Z'}^{u\,2}+g_{Z'}^{d\,2}}\right)\left(\frac{W_d+W_s}{W_u+W_c}\right)\right. \\
&\left.+\frac{g_{Z'}^{b\,2}}{g_{Z'}^{u\,2}+g_{Z'}^{d\,2}}\left(\frac{W_b}{W_u+W_c}\right)\right]\times\left\{\frac{2}{\left(2+\frac{g_{Z'}^{t\,2}}{g_{Z'}^{u\,2}+g_{Z'}^{d\,2}}+\frac{g_{Z'}^{b\,2}}{g_{Z'}^{u\,2}+g_{Z'}^{d\,2}}\right)^2}\right\}
\end{aligned}
\tag{5.15}
$$

where parts related to resonance production are grouped within the square brackets, while those related to decay are grouped within curly braces. Notice that the appearance of the factor 2 in the decay part of the expressions is due to our assumption that the first two generations couple identically to the vector resonance.

The relative strength with which the vector boson couples to the $u-$ and $d-$type quarks of the light SM generations, $g_u^2/\left(g_u^2+g_d^2\right)$, which we will call the "up ratio" for brevity, is not accessible by experiments available in the dijet channel. However, equivalent information for quarks in the third generation can be measured by comparing the dijet and heavy flavor cross sections:

$$
\frac{g_t^2}{g_u^2+g_d^2}=2\frac{\sigma(pp\to t\bar{t})}{\sigma(pp\to jj)} \qquad \text{"top ratio"} \tag{5.16}
$$

and

$$
\frac{g_b^2}{g_u^2+g_d^2}=2\frac{\sigma(pp\to b\bar{b})}{\sigma(pp\to jj)}\,. \qquad \text{"bottom ratio"} \tag{5.17}
$$

Supplementary measurements of these ratios of cross sections will help pinpoint the structure of couplings of the resonance.

While our expressions (5.14 5.15) for D_{col} appear to have a complicated dependence on multiple parameters involving different quark flavors, recalling that the coloron and Z' are being produced by collisions of quarks lying inside protons simplifies matters considerably. First, the contribution of b-quarks to the production part of D_{col} [square brackets within (5.14) and (5.15)] is suppressed significantly by their relative scarcity in the protons, as reflected by the range of the ratios of the parton density functions $\frac{W_d+W_s}{W_u+W_c}$ and $\frac{W_b}{W_u+W_c}$. We plot the values of these functions in Fig. 5.1 for mass range of $2.5-6$ TeV at a pp collider with center-of-mass energy 14 TeV. Here and throughout the chapter, the CT09MCS from the CTEQ Collaboration is used[4] as the parton distribution function set [273]. In that figure, we allow the factorization scale to vary by a factor of 2 from the mass of the resonance. The effect of this variation has been illustrated as the width of each band in the plot. From the plot we conclude that unless the resonance has a considerably stronger coupling to the b than to quarks in first two generations, the precise strength of the couplings to third-generation quarks becomes relevant to D_{col} only through the decay part of the expressions (5.14) and (5.15), the part in curly braces.

Second, we see that the experimentally inaccessible parameter that we call the up ratio appears unlikely to leave us confused as to whether a new dijet resonance is a coloron or a leptophobic Z'. From Fig. 5.1 we see that the ratio $(W_d + W_s)\,/\,(W_u + W_c)$ is fairly flat over the range of masses considered — varying between 0.5 and 0.09 as the mass goes from 2.5 TeV to 6 TeV. The dependence of D_{col} on the up ratio is suppressed by a factor of $1-(W_d + W_s)\,/\,(W_u + W_c)$. So the only situation where confusion might arise is if a coloron had a very small up-ratio and an otherwise similar Z' had an up ratio near the maximum

[4]The more recent CT09MCS Parton Distribution Function yields results consistent with the CTEQ6L1 set used in the work on which Chapter 4 is based.

value of one. This is understood as follows. Consider two resonances having the same top and bottom ratios. A coloron with negligible up ratio will have

$$D_{\text{col}}^{C} \propto 16\left[\frac{{g_C^u}^2}{{g_C^u}^2+{g_C^d}^2}+\left(1-\frac{{g_C^u}^2}{{g_C^u}^2+{g_C^d}^2}\right)\left(\frac{W_d+W_s}{W_u+W_c}\right)\right] \to 16\left[\frac{W_d+W_s}{W_u+W_c}\right] \tag{5.18}$$

while a Z' with the up ratio close to 1 will have

$$D_{\text{col}}^{Z'} \propto 2\left[\frac{{g_{Z'}^u}^2}{{g_{Z'}^u}^2+{g_{Z'}^d}^2}+\left(1-\frac{{g_{Z'}^u}^2}{{g_{Z'}^u}^2+{g_{Z'}^d}^2}\right)\left(\frac{W_d+W_s}{W_u+W_c}\right)\right] \to 2\,. \tag{5.19}$$

We see that in this particular setting, the values of D_{col}^{C} and $D_{\text{col}}^{Z'}$ will be closer to each other at higher masses. We will illustrate this further in Section 5.6.

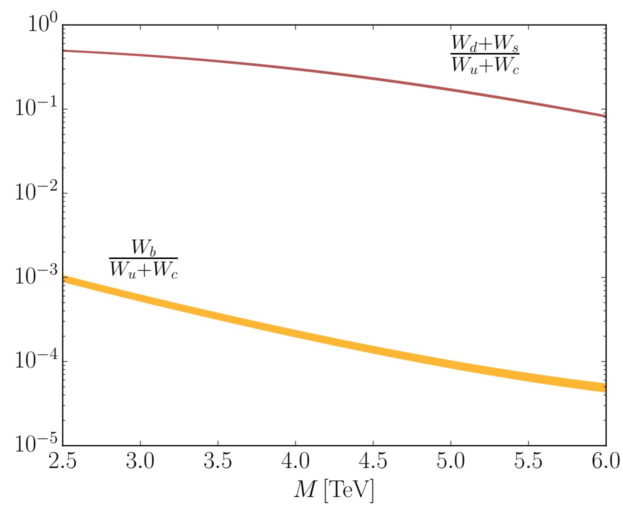

Figure 5.1: Ratios of parton density functions as a function of the mass of the produced vector resonance. This figures shows two such ratios: the relative contribution of parton density functions, defined in Eq. (4.20), for the down-type quarks of the first two generations $\left(\frac{W_d+W_s}{W_u+W_c}\right)$ (top curve, in brown) and for bottom quarks $\left(\frac{W_b}{W_u+W_c}\right)$ (bottom curve, in orange) relative to the up-type quarks for the first two generations. The values have been calculated using CT09MCS parton distribution functions with factorization scale varied by a factor of 2 away from the mass of the resonance in the range $2.5-6.0$ TeV. The results of this variation are illustrated as a band for each function. Note that the upper curve depends only weakly on the resonance mass and that the lower curve's values are always $\sim \mathcal{O}(10^{-3})$ or less over the entire mass range.

5.3.1 General prescription for using D_{col} in flavor-nonuniversal scenarios

Now that we know the parameters that affect the determination of D_{col}, the general prescription of the analysis goes as follows. After a resonance has been discovered, one uses the measurements of three observables; dijet cross section, mass, and total decay width to evaluate D_{col}. This particular value of D_{col} could correspond to various configurations of flavor-nonuniversal couplings denoted by three coupling ratios; namely, the up ratio, top ratio, and bottom ratio. The up ratio cannot be experimentally measured, but the top ratio and bottom ratio are accessible by measuring the $t\bar{t}$ and $b\bar{b}$ cross sections. In many circumstances, these two cross section measurements together with D_{col} suffice to identify the color structure of a resonance of given mass and dijet cross section. The illustration of this method and its limitation are presented in Section 5.6.

First, however, we must determine the region of parameter space where the coloron discriminant variable is relevant: the region where one can discover the resonance and measure M, Γ and σ_{jj} precisely. This is the topic of the next section.

5.4 Accessible Dijet Resonances at the 14 TeV LHC

A resonance discovered in a dijet channel but not in dilepton channel could be either a coloron or a leptophobic Z'. The color discriminant variable allows one to distinguish between the two particles in a model-independent manner; i.e., without having to analyze each set of couplings separately. In this section, we describe the region of parameter space to which this method is applicable[5]. In this region the resonance has not already been excluded by

[5]A detailed discussion was presented in [6].

the current searches, is within the reach of future searches, and has a total width that is measurable and consistent with the designation "narrow".

One may deduce the current exclusion limits on resonances in the dijet channel using the limits on the production cross section times branching ratio ($\sigma \times Br(jj)$) from the (null) searches for narrow-width resonances carried out by the ATLAS and CMS collaborations [246, 248, 249] at $\sqrt{s} = 8\,\text{TeV}$. We use the most stringent constraint, which comes from CMS [249]. As the exclusion limit is provided in the form of $\sigma \times Br(jj) \times (\text{Acceptance})$, we estimate the acceptance of the detector for each value of the resonance mass by comparing, within the same theoretical model, $\sigma \times Br(jj)$ that we calculated vs. $\sigma \times Br(jj) \times$ (Acceptance) provided by CMS. The acceptance is a characteristic of properties of the detector and kinematics, the latter being the same for coloron and Z' to the leading order; thus we use throughout our analysis the acceptance obtained from a comparison within a sequential Z' model. The excluded region of parameter space is displayed in gray in Figs. 5.4 and 5.3.

Sensitivity to a dijet resonance in future LHC experiments with $\sqrt{s} = 14\,\text{TeV}$ depends on the knowledge of QCD backgrounds, the measurements of dijet mass distributions, and statistical and systematic uncertainties. CMS [260] has estimated the limits on $\sigma \times Br(jj) \times (\text{Acceptance})$ that will be required in order to attain a 5σ discovery at CMS with integrated luminosities up to $10\,\text{fb}^{-1}$, including both statistical and systematic uncertainties. We obtain the acceptance for CMS at $\sqrt{s} = 14\,\text{TeV}$ in the same manner as described in the previous paragraph. The sensitivity for the dijet discovery from $10\,\text{fb}^{-1}$ is then scaled to the integrated luminosities $\mathcal{L} = 30,\ 100,\ 300,\ 1000\,\text{fb}^{-1}$ considered in our studies (assuming that the systematic uncertainty scales with the squared root of integrated luminosity). The predicted discovery reaches for these luminosities are shown in varying shades of blues for coloron and greens for Z' in Figs. 5.4 and 5.3. Sensitivity to a dijet resonance in future LHC experiments with $\sqrt{s} = 14\,\mathrm{TeV}$ depends on the knowledge of QCD backgrounds, the measurements of dijet mass distributions, and statistical and systematic uncertainties.

Sensitivity to a dijet resonance in future LHC experiments with $\sqrt{s} = 14\,\mathrm{TeV}$ depends on the knowledge of QCD backgrounds, the measurements of dijet mass distributions, and statistical and systematic uncertainties. Ref. [260] presents estimates of the limits on $\sigma \times Br(jj) \times$ (Acceptance) that will be required in order to attain a 5σ discovery at CMS with integrated luminosities up to $10\,\mathrm{fb}^{-1}$ with statistical uncertainty alone as well as with statistical and systematic uncertainties combined. We obtain the acceptance for CMS at $\sqrt{s} = 14\,\mathrm{TeV}$ in the same manner as described in the previous paragraph. The sensitivity from $10\,\mathrm{fb}^{-1}$ is then scaled to the integrated luminosities $\mathcal{L} = 30$, 100, 300, $1000\,\mathrm{fb}^{-1}$ considered in our studies. The predicted discovery reaches for these luminosities are shown in varying shades of blue for coloron and green for Z' in Figs. 5.4 and 5.3.

The total decay width also constrains the absolute values of the coupling constants. On the one hand, experimental searches are designed for narrow-width dijet resonances; hence their exclusion limits are not applicable when the resonance is too broad, which translates to about $\Gamma/M = 0.15$ as the upper limit [258, 259, 131]. On the other hand, the appearance of (intrinsic) total decay width in the expression for the color discriminant variable requires that the width be accurately measurable; width values smaller than the experimental dijet mass resolution, M_{res}, cannot be distinguished. The region of parameter space that meets both constraints and is relevant to our analysis is shown in Figs. 5.4 and 5.3 as the region between the two dashed horizontal curves labeled $\Gamma \geq 0.15M$ and $\Gamma \leq M_{\mathrm{res}}$. Regions where the width is too broad or too narrow are shown with a cloudy overlay to indicate that they are not accessible via our analysis.

In Figs. 5.4 and 5.3, we also show the contours in the region of parameter space along which the uncertainties in measuring D_{col} are 20% and 50% at the LHC with $\sqrt{s} = 14\,\text{TeV}$ for the integrated luminosity of $1000\,\text{fb}^{-1}$. We will estimate uncertainties for relevant observables in the accessible region in the next section.

5.5 Systematic Uncertainties at the $14\,\text{TeV}$ LHC

Statistical and systematic uncertainties on dijet cross section, mass, and intrinsic width of the resonance will play a key role in determining how well D_{col} can discriminate between models at the LHC with $\sqrt{s} = 14\,\text{TeV}$. The actual values of the systematic uncertainties at the LHC with $\sqrt{s} = 14\,\text{TeV}$ will be obtained only after the experiment has begun. In this section, we discuss the estimates of the uncertainties that we use in our calculations.

The effect of systematic uncertainties in the jet energy scale, jet energy resolution, radiation and low mass resonance tail and luminosity on the dijet cross section at the 14 TeV LHC was estimated in Ref. [260]. It is presented there as a fractional uncertainty (as a function of the mass) normalized to the dijet cross section required to obtain a 5σ discovery above background fluctuations. The dijet mass resolution, the uncertainty of the dijet mass resolution, and the uncertainty of the mass itself (due to uncertainty in the jet energy scale), also affect the determination of both the mass and intrinsic width. Table 4.1 in Chapter 4 lists these estimated uncertainties for $\sqrt{s} = 14$ TeV together with the values from the actual CMS and ATLAS experiments at $\sqrt{s} = 8$ TeV. Here, we use the estimate for systematic uncertainties from actual LHC data where available and assume that any future LHC run will be able to reach at least that level of precision. The values we use are marked in Table 4.1 with asterisks.

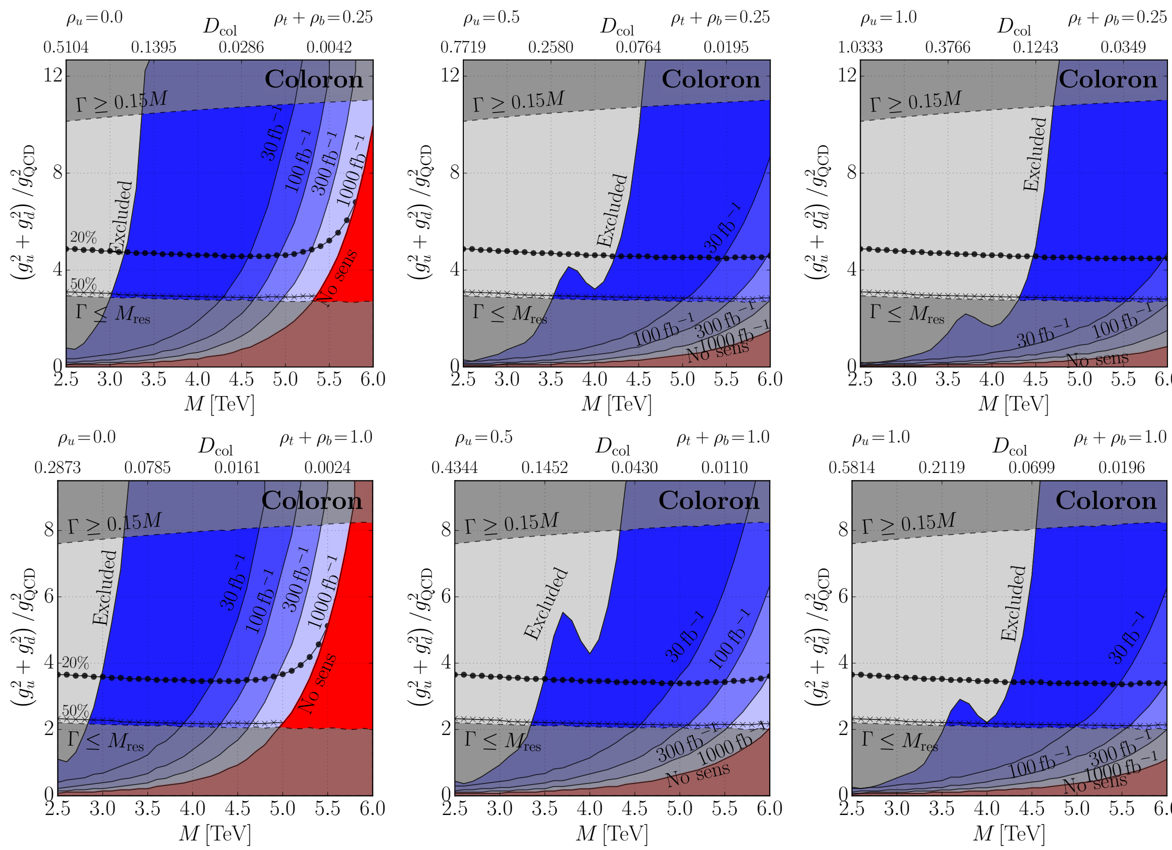

Figure 5.2: Region of parameter space (scaled coupling strength $(g_u^2 + g_d^2)/g_{\rm QCD}^2$ vs. coloron mass M) where the color discriminant variable analysis applies at the LHC with $\sqrt{s} = 14\,$TeV. The configurations of coupling ratios vary as follows: $\rho_u \equiv g_u^2/(g_u^2 + g_d^2)$ increasing from 0 to 1 (from left to right panels), and $\rho_t + \rho_b \equiv (g_t^2 + g_b^2)/(g_u^2 + g_d^2)$ increasing from 0.25 to 4 (from top to bottom panels). The 5σ discovery reach, with statistical and systematic uncertainties included, is shown in varying shades of blue for different luminosities ranging from 30 fb^{-1} to 1000 fb^{-1}. The red area marked "no 5σ sensitivity" lies beyond the discovery reach at 1000 fb^{-1}. The gray area on the left of each plot marked "excluded" has been excluded by the 8 TeV LHC [249]. In the region above the dashed line marked $\Gamma \geq 0.15M$, the narrow-width approximation used in dijet resonance searches is not valid [258, 259, 131]. In the region below the horizontal dashed line marked $\Gamma \leq M_{\rm res}$, the experimental mass resolution is larger than the intrinsic width [249], so that one cannot determine $D_{\rm col}$. The contours marked 20% and 50% indicate the region above which the uncertainty in measuring $D_{\rm col}$, as estimated in Sec. 5.5, is smaller than 20% and 50%, respectively. *Continued next page.*

Figure 5.2 (cont'd)

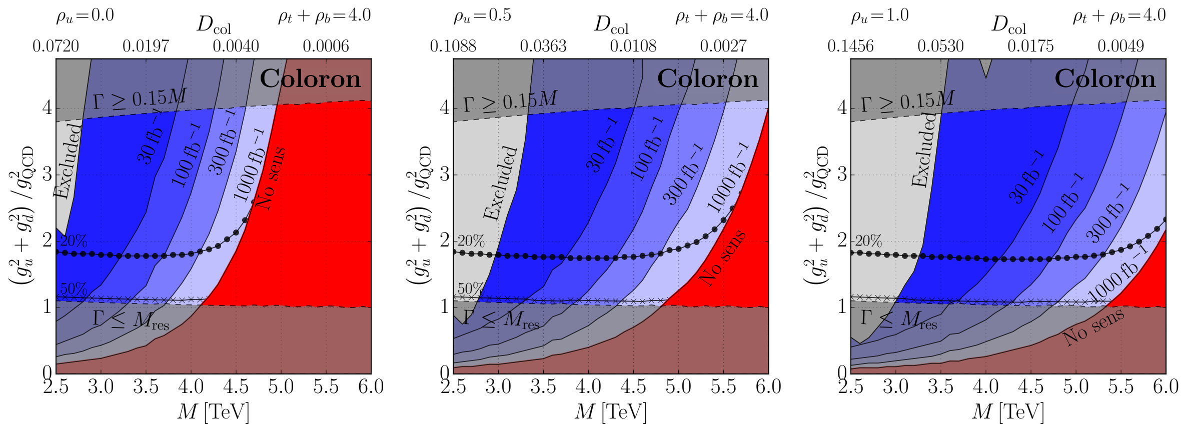

5.6 Applying the Color Discriminant Variable to Flavor-non-universal Models at the LHC

In this section we illustrate how the color discriminant variable $D_{\rm col}$ (as described in Section 5.3) may be used to distinguish whether a newly discovered dijet resonance is a coloron or a leptophobic Z' even if it is flavor non-universal. As previously mentioned, we will focus on resonances having masses within $2.5 - 6\,\mathrm{TeV}$ at the $\sqrt{s} = 14\,\mathrm{TeV}$ LHC with integrated luminosities up to $1000\,\mathrm{fb}^{-1}$. The values of $D_{\rm col}$ as well as other observables have been evaluated using the uncertainties estimated in Section 5.5 and the region of parameter space to which this analysis is applicable was identified in Section 5.4.

5.6.1 Demonstration that C and Z' lie in different regions of coupling ratio space

As we have seen, the value of $D_{\rm col}$ at a fixed mass and dijet cross section may correspond to a variety of combinations of values of the three ratios of couplings, the up ratio $(\frac{g_u^2}{g_u^2+g_d^2})$, the top ratio $(\frac{g_t^2}{g_u^2+g_d^2})$, and the bottom ratio $(\frac{g_b^2}{g_u^2+g_d^2})$. The last two are directly determined

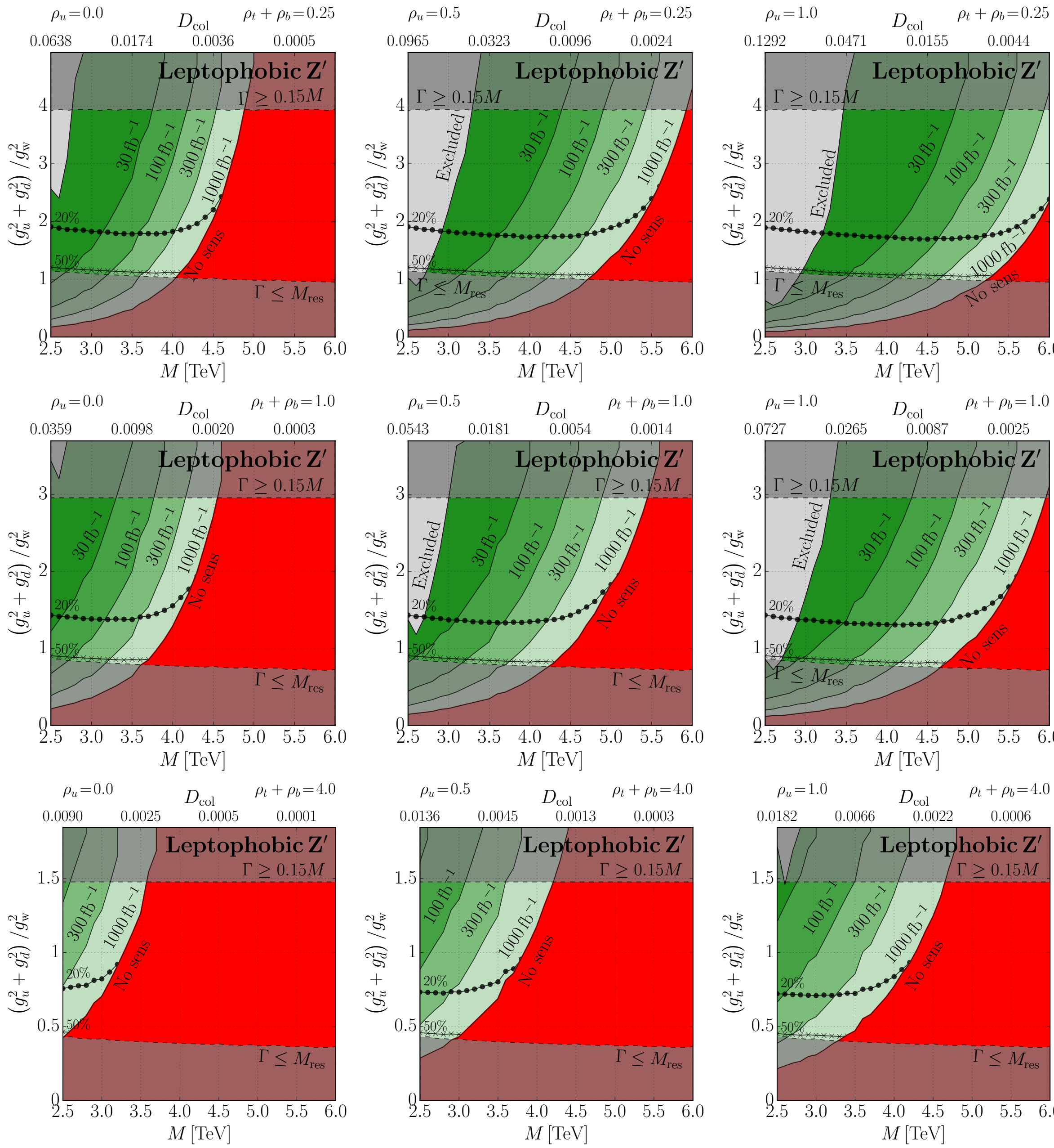

Figure 5.3: Same as Fig. 5.4 but for a flavor-nonuniversal Z'. Notice that while a leptophobic Z' having relatively large couplings to quarks in the third generation is still within the reach of the future LHC, its total width would typically be too large to be included in analyses for narrow resonances.

from the measurements of $\sigma_{t\bar{t}}$ and $\sigma_{b\bar{b}}$ while D_{col} is relatively insensitive to the first ratio, as mentioned in Section 5.3. The question is, therefore, whether measuring the mass, width, dijet cross-section, $\sigma_{t\bar{t}}$ and $\sigma_{b\bar{b}}$ can definitively identify the color charge of a newly discovered resonance. We find that it can. We will illustrate this finding for resonances of mass 3 TeV and 4 TeV, as we have seen in Fig. 5.4 and 5.3 that most colorons with lower masses are excluded by the current experiments and most Z' bosons with higher masses are not within reach of the future LHC run at $1000\,\text{fb}^{-1}$.

In Fig. 5.4, we show the region of parameter space of the three coupling ratios (using the observables $\frac{\sigma_{t\bar{t}}}{\sigma_{jj}}$ and $\frac{\sigma_{b\bar{b}}}{\sigma_{jj}}$ in place of the top and bottom ratios, respectively) in which coloron or Z' models (each displayed as a point) with the same mass lead to a certain range of dijet cross-section and D_{col}. We choose the range for the dijet cross-section to be within 1 standard deviation from the value that allows a 5σ discovery at luminosity $1000\,\text{fb}^{-1}$. We selected range of D_{col} to be within 50% from $D_{\text{col}} = 3 \times 10^{-3}$ for this illustration as it permits the required measurements to be made for either a coloron or Z' as discussed in Section 5.4. Points in the accessible area of parameter space are highlighted in blue if the discoverable resonance is a C and in green if it is a Z'. These points lie in the blue regions of Fig. 5.4 for colorons or the green regions of Fig. 5.3 for Z'.

We now explore the features that Fig. 5.4 exhibits. The 3-dimensional plots in the left panel show that models of C and leptophobic Z' which correspond to measurable observables appear in different region of $\frac{\sigma_{t\bar{t}}}{\sigma_{jj}}$ vs $\frac{\sigma_{b\bar{b}}}{\sigma_{jj}}$ vs $\frac{g_u^2}{g_u^2+g_d^2}$ three-dimensional parameter space. The symmetry between the $\frac{\sigma_{t\bar{t}}}{\sigma_{jj}}$ and $\frac{\sigma_{b\bar{b}}}{\sigma_{jj}}$ axes illustrates the rarity of having a heavy resonance produced via $b\bar{b}$ annihilation - the only process in which b quarks could contribute to D_{col} without a corresponding contribution from t quarks. In addition, we see that while the up ratio is experimentally inaccessible, the top view figures displayed in the right panels show

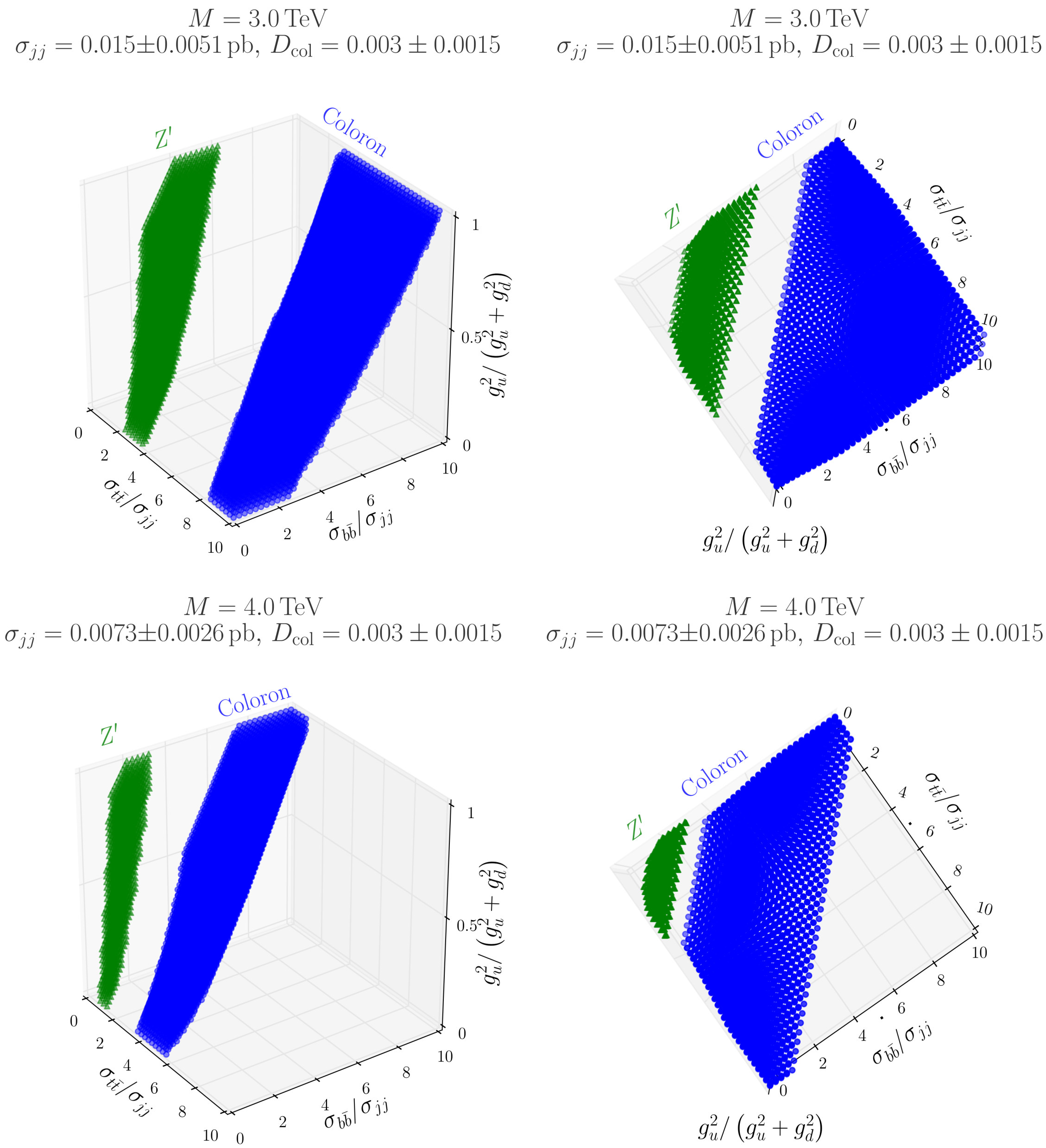

Figure 5.4: Illustration that the proposed measurements suffice to identify the color structure of a new dijet resonance. These plots show regions of the 3-d parameter space $g_u^2/(g_u^2+g_d^2)$ vs. $\sigma_{t\bar{t}}/\sigma_{jj}$ vs. $\sigma_{b\bar{b}}/\sigma_{jj}$, at fixed values of mass (3 TeV on the top panels and 4 TeV on the bottom panels) where dijet cross section and D_{col} fall within a certain range. The cross section is within about 35% the value required for a 5σ discovery at the LHC with $\sqrt{s} = 14\,\mathrm{TeV}$ at $\mathcal{L} = 1000\,\mathrm{fb}^{-1}$. The range of 50% from $D_{\mathrm{col}} = 3\times10^{-3}$ is chosen for illustration. Points in parameter space that are accessible to the LHC are circles highlighted in blue for C and triangles highlighted in green for Z'. Each plot on the left panel is shown again, as viewed from above, on the right. The two views make clear that colorons and Z' bosons lie in distinguishably separate regions of parameter space; in particular, our ability to measure the ratio $g_u^2/(g_u^2+g_d^2)$ will not prevent us from determining the color structure of a new vector resonance at the 14 TeV LHC.

that this does not typically lead to confusion between a coloron and a Z', just as we have argued in Sec. 5.3. That is, even having projected the 3D data of all up ratio values onto the bottom-ratio vs. top-ratio plane, the blue coloron and green Z' points still lie in distinct regions.

5.6.2 Using heavy flavor measurements to tell C from Z'

Fig. 5.4 not only shows that the coloron and Z' lie in different regions of parameter space, but also implies that measurements of the top and bottom decays of the new resonance will almost always enable us to determine its color structure.

Let us assume that a new resonance has been found and that its mass, dijet cross-section, and D_{col} have been measured. For illustration, take the values of these observables to be those used in Fig. 5.4 (for the same LHC energy, luminosity and estimated uncertainties). Because there is a gap between the Z' and C regions of that figure when the up ratio is 0, and because the boundaries of the regions are angled rather than vertical, we can see that a Z' with the minimum up ratio value of 0 would not be mistaken for a coloron. On the other hand, a Z' with the maximum up ratio (equal to 1) lies as close as possible to the coloron region of parameter space. So we will want to compare a Z' with an up ratio of 1 (one that does not couple to d or s quarks) to a coloron with varying values of the up ratio.

This very comparison is presented in Fig. 5.5, which is plotted in the top-ratio vs bottom-ratio plane. The up ratio for the Z' is fixed to be 1; the up ratio for the C is varied from 0 (left panels) to 1 (right panels). We see that as the up ratio for the coloron increases from its minimum to maximum values, the blue coloron region of parameter space moves out from the origin, away from the green Z' region of parameter space. Correspondingly, if we were to decrease the up ratio of the Z' boson, the green Z' region would shift closer to the origin, away from the blue coloron region. In general, the coloron and Z' regions do not overlap.

Given the shape and orientation of the regions corresponding to color-singlet and color-octet resonances in the plots, measuring both the top ratio and bottom ratio would clearly allow us to distinguish the new resonance's color structure. Moreover, we see that if either the top ratio or bottom ratio were measured to be sufficiently large, we would know that the resonance must be a coloron (because the Z' region is already at its maximum distance from the origin). For example, a measurement of $\sigma_{t\bar{t}}/\sigma_{jj} \gtrapprox 6$ for a 3 TeV resonance or $\sigma_{t\bar{t}}/\sigma_{jj} \gtrapprox 3$ for a 4 TeV resonance, for the values of σ_{jj} used in Fig. 5.5, would identify it as a color-octet.

We note that there could still be a rare situation where our inability to measure the up ratio would prevent us from determining the color structure of a new resonance. The regions of parameter space corresponding to the extreme cases of a coloron with only down-type light quark couplings and a Z' with only up-type light quark couplings could potentially overlap. As mentioned in Sec. 5.3, this is more likely to happen for heavier resonances due to decreasing values of parton distribution functions for down-type light quarks at higher resonance masses. For example, given our estimations of uncertainties, such an overlap could occur for a 4 TeV resonance as illustrated in the lower left panel of Fig. 5.5.

The determination of the color structure of a resonance generally requires measurements of both $\sigma_{t\bar{t}}$ and $\sigma_{b\bar{b}}$. As with the dijet cross sections, systematic uncertainties for these measurements will be obtained after the experiment (at 14 TeV) has started[6]. While the estimation of these uncertainties lies beyond the scope of this article, our result should illustrate that measuring the $t\bar{t}$ and $b\bar{b}$ cross sections to an uncertainty of $\mathcal{O}(1)$ still provides

[6] Systematic uncertainties on the total SM background yields from recent $t\bar{t}$ resonance searches at $\sqrt{s} = 7, 8$ TeV [274, 275] are $\sim \mathcal{O}(20\%)$. Estimates for the total systematic uncertainty for $t\bar{t}$ final state at $\sqrt{s} = 14$ TeV can be extracted, for example, from a study for the fully hadronic channel presented in reference [276], which is $\sim \mathcal{O}(40 - 50\,\%)$. The $b\bar{b}$ resonance at $\sqrt{s} = 8$ TeV search has been carried out by CMS [277], while the estimate for systematic uncertainties at $\sqrt{s} = 14$ TeV is currently not available.

significant information. For the purpose of comparing models and estimating the required uncertainties, additional plots illustrating models of coloron and leptophobic Z' that lead to the same value of $D_{\rm col}$, without uncertainties being taken into account, are presented in Appendix D.

The determination of the color structure of a resonance requires generally requires precise measurements of both $\sigma_{t\bar{t}}$ and $\sigma_{b\bar{b}}$. As with the dijet cross sections, systematic uncertainties for these measurements will be obtained after the experiment has started. While the estimation of these uncertainties lies beyond the scope of this article, our results in this section should illustrate the precision required for distinguishing among color structures. For the purpose of comparing models and estimating the required uncertainties, additional plots illustrating models of coloron and leptophobic Z' that lead to the same value of $D_{\rm col}$, without uncertainties being taken into account, are presented in the Appendix D.

5.7 Discussion

The simple topology and large production rate for a dijet final state not only allows a Beyond the Standard Model vector boson to be observed via dijet resonance searches, it also allows the determination of crucial properties of the new resonance. The measurements are particularly useful in distinguishing between a color-octet vector resonance (C) and a color-singlet one that couples only to colored particles (leptophobic Z'). In this article, we showed that the method for distinguishing between the two types of resonances in a model-independent manner using the color discriminant variable introduced in Ref. [6], can be extended to more general and realistic scenarios of flavor non-universal couplings in a wide range of models.

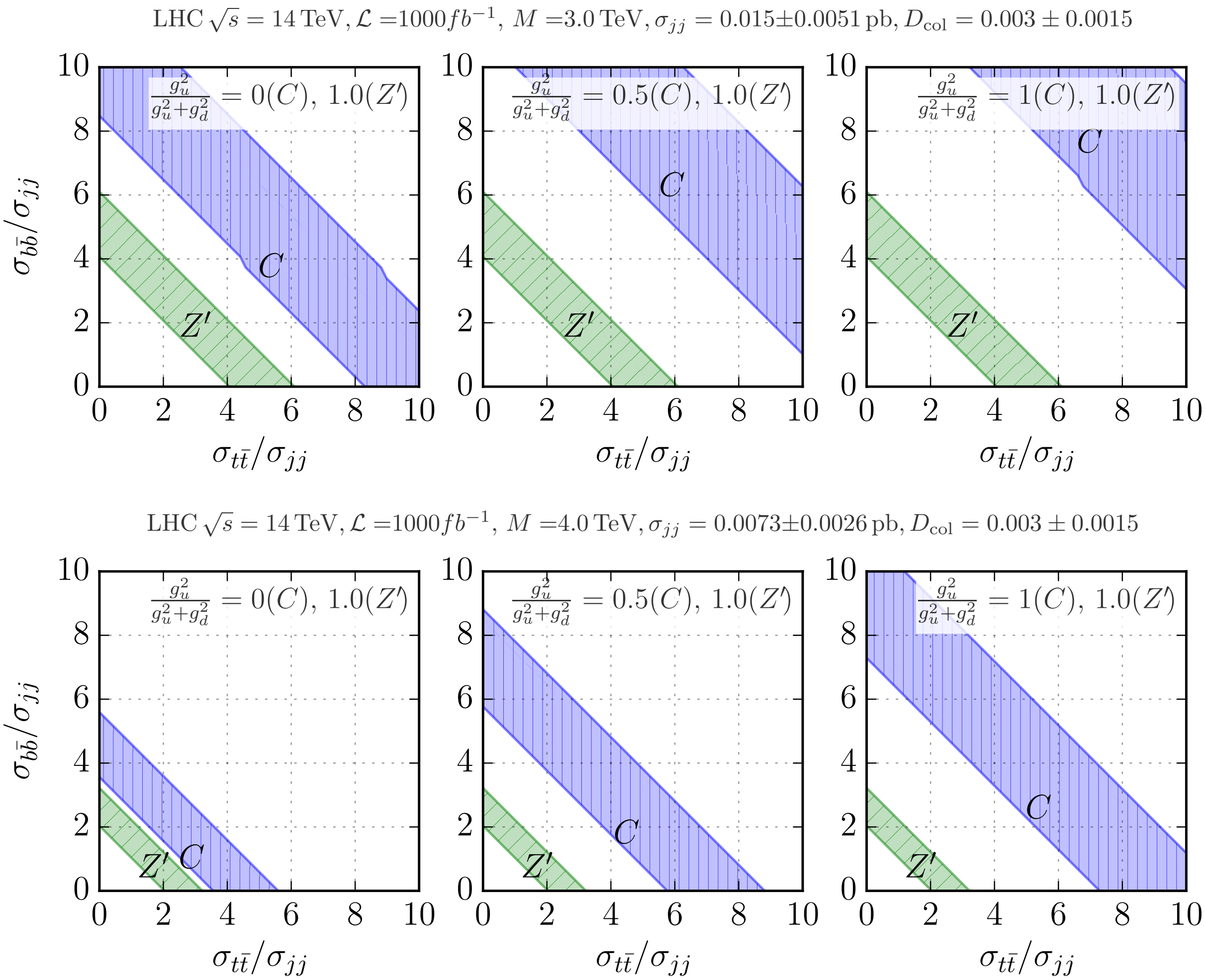

Figure 5.5: Further illustration that measuring $\sigma_{t\bar{t}}$ and $\sigma_{b\bar{b}}$ will show whether a resonance of a given mass, dijet cross-section, and D_{col} is a coloron or Z'. We display regions of parameter space that correspond to a dijet cross section within 1σ uncertainty of the value required for a discovery at the LHC with $\sqrt{s} = 14\,\mathrm{TeV}$ at $\mathcal{L} = 1000\,\mathrm{fb}^{-1}$ (the same values used in Fig.5.4), and that also have the illustrative color discriminant variable within a range of 50% around value of $D_{\mathrm{col}} = 3 \times 10^{-3}$, for resonances with masses 3 TeV (top panel) and 4 TeV (bottom panel). Coloron and Z' models that are within reach are displayed in a vertically-hatched blue region and a diagonally-hatched green region, respectively. Note that in nearly all of the displayed areas, the colorons and Z' bosons lie in different regions of parameter space. However, at the bottom left panel for a 4 TeV resonance, there is a small overlapping region that could correspond either to a C coupling only to down-type light quarks or to a Z' coupling only to up-type light quarks.

The color discriminant variable, $D_{\rm col}$, is constructed from measurements available directly after the discovery of the resonance via the dijet channel; namely, its mass, its total decay width, and its dijet cross section. Assuming the new resonance couples identically to quarks of the first two generations, $D_{\rm col}$ depends on three model-specific ratios of coupling constants: the up ratio ($\frac{g_u^2}{g_u^2+g_d^2}$), the top ratio ($\frac{g_t^2}{g_u^2+g_d^2}$), and the bottom ratio ($\frac{g_b^2}{g_u^2+g_d^2}$). We showed that the method is generally not dependent on knowing the up ratio, a quantity which is not presently accessible to experiment. Since $D_{\rm col}$ is insensitive to chiral structure, discriminating between color-singlet and color-octet resonances with flavor non-universal couplings requires only measurements of the $t\bar{t}$ and $b\bar{b}$ resonance cross sections. Our results are illustrated in Figs. 5.4 and 5.5, with further scenarios explored in the Appendix D.

Our analysis assumed that the coloron and Z' have only negligible couplings to any non-Standard Model fermions that may exist. It is straightforward to consider an extension to models where the resonance does couple to new fermions. While the coloron always has only visible decay channels (as it couples to colored particles), the Z' could have non-negligible decay branching fraction into non-Standard Model invisible particles. In that case, the leptophobic Z' and the coloron would be even easier to distinguish from one another by the color discriminant variable. Simply put, the Z''s invisible decays would increase its total width, which appears in the denominator of the expression for its color discriminant variable[7]. This means the value of the Z''s color discriminant variable, which is already smaller than that of the coloron by a factor of 8, would be further reduced due to the appearance of non-negligible invisible decays. Therefore, a leptophobic Z' with invisible decays will correspond to a region in the $\frac{g_u^2}{g_u^2+g_d^2}$ vs. $\frac{\sigma_{t\bar{t}}}{\sigma_{jj}}$ vs. $\frac{\sigma_{b\bar{b}}}{\sigma_{jj}}$ parameter space (such as those presented in Fig. 5.4) that lies even further away from the region occupied by colorons.

[7] *Cf.* the curly braces of Eq. (5.15).

To summarize: we have generalized the color discriminant variable for use in determining the color structure of new bosons that may have flavor non-universal couplings to quarks. We focused on resonances having masses $2.5 - 6.0\,\mathrm{TeV}$ for the LHC with center-of-mass energy $\sqrt{s} = 14\,\mathrm{TeV}$ and integrated luminosities up to 1000, fb^{-1}. After having taken relevant uncertainties and exclusion limits from current experiment and sensitivity for future experiments into account, we find that the future runs of the LHC can reliably determine the color structure of a resonance decaying to the dijet final state.

Chapter 6

Probing Color Octet Couplings at the Large Hadron Collider

— This chapter is based on a work in collaboration with Anupama Atre, R.Sekhar Chivukula, Elizabeth H. Simmons, and Jiang-Hao Yu which has appeared in [4]. Part of its content have also appeared in the conference proceeding [5].

6.1 Introduction

In addition to the color structure of a new vector resonance, the way the resonance couples to different chiralities of the known fermions will provide a helpful insight as to the origin of the particle. At a hadron collider, as the initial states are composed of colored particles, the LHC will generally produce a resonance coupled to these colored particles at a large rate. This makes the LHC an ideal machine for exploring new colored resonances associated with new strong dynamics. This chapter is based on the work [4] studying the chiral structure of the couplings of a color-octet vector resonance collectively referred to as a coloron.

The high production rate of a colored resonance (due to strong coupling) and the simple topology of the final state (decay into two jets) makes the search for di-jet resonances one of the early signatures that are studied at hadron colliders. Once a new colored resonance is discovered, measuring its properties will be the next important task. The di-jet invariant mass m_{jj} and the angular distributions of energetic jets relative to the beam axis are sensitive observables to determine the properties, such as mass and spin of the resonance. As I have shown in Chapters 4 and 5, basic observables available with a dijet resonance discovery can help distinguish a coloron from a leptophobic Z'. The basic observables are the mass, width, cross section to dijet final states, and cross sections to heavy flavors state of $t\bar{t}$ and $b\bar{b}$. Although one can use these observables to constrain the coupling strength of the colored resonance to the Standard Model (SM) quarks, they are not sufficient to determine the chiral structure of the couplings. All these observables receive equal contributions from left- and right-handed chirality quarks.

Some additional information about the chiral couplings can potentially be gleaned from the measurement of the forward-backward asymmetry of the top-antitop pair ($A^{t\bar{t}}_{FB}$). Such a measurement has been made at the Tevatron. According to the Standard Model, QCD is the interaction responsible for observing more top quarks moving along the direction of the proton beam than along the anti-proton beam. In QCD, the gluons couple equally to left- and right-handed quarks. So the non-zero $A^{t\bar{t}}_{FB}$ could then predicted via next-to-leading order corrections. The observations in 2011 at the Tevatron [254, 255] were of $\mathcal{O}(20\%)$, which were larger than the predictions of $\mathcal{O}(5\%)$, available at the time this work was completed in 2012[1], by the Standard Model [280, 281]. Motivated by these results, various models with specific chiral structures of the color-octet particle that give rise to a large asymmetry have been proposed (see, for example, [216, 218]). Unlike the Tevatron, which uses proton-antiproton initial state, the initial proton-proton initial state of the LHC is symmetric. The

[1]In November 2014, a next-to-next-to-leading-order (NNLO) calculation combining all known Standard Model corrections was completed by the authors of Ref. [278]. They found the asymmetry predicted by the Standard Model to be $9.5 \pm 0.7\%$ which is in agreement with the most recent measurement by the DØ collaboration [279] of $10.6 \pm 3\%$.

forward backward asymmetry of the top-antitop pair is diluted at that machine compared to the large asymmetry at the Tevatron [282, 283].

We proposed a new channel for studying coloron couplings at the LHC: the associated production of a W or Z gauge boson with the coloron. The chiral couplings of the weak gauge bosons to the fermions in the associated production channel provides additional information about the chiral structure of the new strong dynamics. Combining the associated production channel with the di-jet channel makes it possible to extract the chiral couplings of the colored resonance because the cross-sections of each channel have a different dependence on the coloron's couplings to fermions. The functional form of the dependence of these measurements on the chiral couplings in the di-jet channel is $g_L^2 + g_R^2$; in the Wjj channel it is g_L^2 and in the Zjj channel it is $ag_L^2 + bg_R^2$. A cartoon illustration of these three measurements along with the di-jet measurement is shown in Fig. 6.1. Notice that while combining the different channels will narrow the allowed range of couplings, there remains an ambiguity in extracting the sign of the couplings. This method of using the associated production of a weak gauge boson to illuminate the properties of a new resonance was studied earlier in the context of the measurement of Z' couplings [140, 136].

In this work [4] we studied the sensitivity of the LHC with center of mass (c.m.) energy of 14 TeV to probe the chiral structure of the couplings for colored resonances with 10 fb^{-1} and 100 fb^{-1} integrated luminosity by the method proposed above. We studied colored resonances with masses in the range 2.5 TeV to 4.5 TeV and various couplings and widths; this mass range runs from the lightest colorons still allowed by LHC dijet searches to the heaviest colorons to which the LHC is likely to be sensitive.

The rest of the chapter is organized as follows. In Sec.6.2, we present a simple parameterization for the colored resonances and our notation. In Sec.6.3, we discuss the signal and

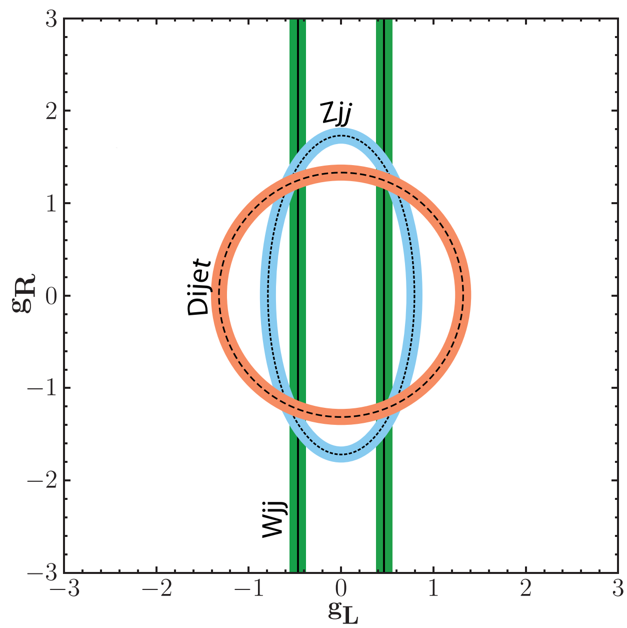

Figure 6.1: A cartoon illustration of the form of prospective constraints on chiral couplings from the di-jet channel (dashed black circle with red band), the channel with associated production of a W boson (solid black parallel lines with green band) and the channel with associated production of a Z boson (dotted black ellipse with blue band). Combining the constraints from different channels will narrow the range of allowed couplings.

associated backgrounds, the Monte Carlo simulation details in Sec.6.3.1 and the channels with charged and neutral gauge bosons in Sec. 6.3.2 and Sec.6.3.3 respectively. We present a discussion of our results in Sec.6.4 and conclusions in Sec.6.5.

6.2 General Parameterization

The color-octet resonance of interest to our study may be motivated in many BSM scenarios as noted in the introduction. Hence we explore a phenomenological model of color-octet resonances independent of the underlying theory. The interaction of the color-octet resonance C^μ with the SM quarks q_i has the form

$$\mathcal{L} = ig_s\bar{q}_i C^\mu \gamma_\mu \left(g_V^i + g_A^i \gamma_5\right) q_i = ig_s \bar{q}_i C^\mu \gamma_\mu \left(g_L^i P_L + g_R^i P_R\right) q_i, \tag{6.1}$$

where $C_\mu = C_\mu^a t^a$ with t^a an SU(3) generator, g_V^i and g_A^i (or g_L^i and g_R^i) denote vector and axial (or left and right) coupling strengths relative to the QCD coupling g_s, the projection operators have the form $P_{L,R} = (1 \mp \gamma_5)/2$ and the quark flavors run over $i = u, c, d, s, b, t$. For simplicity, we will denote the color-octet resonance by C and its chiral couplings to light quarks by $g_{L,R}^q$ and to the third generation by $g_{L,R}^t$.

The various couplings $g_{L,R}^{q,t}$ can all be independent in the most general non-universal case and can all be the same in simple flavor universal scenarios. A study of the former case would be desirable but it is computationally cumbersome and the latter case, while simple, does not include some interesting scenarios. Furthermore the authors of Ref. [259] found that the flavor universal case is excluded at 99.5% by a global fit to top pair data for color-octet masses less than 3 TeV. An interesting (yet manageable and general) example is that of a color-octet resonance that can enhance top-pair forward-backward asymmetry in models allowing non-universal couplings when [215, 284, 217]

$$g_A^q g_A^t < 0. \tag{6.2}$$

Motivated by the $A_{FB}^{t\bar{t}}$ measurement at the Tevatron we choose the following non-universal couplings as in Ref. [215] as an example.

$$g_V^t = g_V^q \qquad \text{and} \qquad g_A^t = -g_A^q, \tag{6.3}$$

or in terms of $g_L - g_R$,

$$g_L^t = g_R^q, \qquad \text{and} \qquad g_R^t = g_L^q. \tag{6.4}$$

This example is sufficient to demonstrate the utility of the method of measuring couplings described in this article. This choice of couplings also allows us to easily compare the reach of our study with that of Ref. [215] which is consistent with the $A_{FB}^{t\bar{t}}$ measurement. A more general study involving fully independent couplings is beyond the scope of this study and will be addressed in a future publication.

The color-octet resonance with the interactions as in Eq. (6.1) decays primarily to two jets or a top pair and its decay width is given by

$$\begin{aligned}\Gamma_C &= \alpha_s \frac{m_C}{12}\Big[4\left({g_L^q}^2 + {g_R^q}^2\right) + \left({g_L^t}^2 + {g_R^t}^2\right) \\ &+ \Big[({g_L^t}^2 + {g_R^t}^2)(1-\mu_t) + 6 g_L^t g_R^t \mu_t\Big]\sqrt{1-4\mu_t}\Big],\end{aligned} \tag{6.5}$$

where the terms in the first line come from decays to light quarks and to the bottom quark, while the terms in the second line come from decays to top quarks. Decays to top quarks are modified by the kinematic factors involving $\mu_t = m_{top}^2/m_C^2$ with m_{top} and m_C the top quark and color-octet mass respectively. Strictly speaking, the bottom quark's contribution to the width is modified by factors involving μ_b but we ignore these factors since $m_b^2 << m_C^2$. For an octet that is heavy compared to the top quark and whose couplings are of the form given in Eq. (6.4) the expression for the decay width simplifies to

$$\Gamma_C = \frac{\alpha_s}{2} m_C \left(g_L^2 + g_R^2\right) = \alpha_s m_C \left(g_V^2 + g_A^2\right). \tag{6.6}$$

In this simplified version, the branching fraction for the color-octet resonance to decay to any single quark flavor obeys the simple relation

$$BR(C \to q_i \bar{q}_i) = 1/6, \qquad \text{where } i = u, d, c, s, t, b. \tag{6.7}$$

6.3 Collider Phenomenology

In this section we study the collider phenomenology of color-octet states produced in association with a W or Z gauge boson and discuss the signal and associated backgrounds. We present the the Monte Carlo simulation details in Sec.6.3.1, and in Sec.6.3.2 and Sec.6.3.3 we study the modes of associated production with a W and a Z boson, respectively.

The color-octet states (C) are produced and decay to two jets via the process

$$pp \xrightarrow{C} j\ j. \tag{6.8}$$

They can also be produced in association with a weak gauge boson via the processes

$$pp \xrightarrow{C} j\ j\ W^{\pm}, \tag{6.9}$$

$$pp \xrightarrow{C} j\ j\ Z, \tag{6.10}$$

where $j = u, d, s, c, b$. We will refer to the processes in Eq. (6.9) and Eq. (6.10) as the CW and CZ channels, respectively. Representative diagrams of interest for the associated production modes, which include s and t channel diagrams with the emission of the gauge bosons in either the initial or final state, are shown in Fig. 6.2. The final state channels that we study are

$$pp \rightarrow \ell^{\pm} \not{E}_T\ 2j, \quad \ell^{+}\ell^{-}\ 2j, \tag{6.11}$$

coming from $W^{\pm}(\rightarrow \ell^{\pm}\nu)$ or $Z(\rightarrow \ell^{+}\ell^{-})$, respectively and $\ell = e, \mu$. Although the inclusion of the τ lepton in the final state could increase signal statistics, for simplicity we ignore this experimentally more challenging channel.

The relevant backgrounds to the signal processes in Eq. (6.11) are

- $W+$ jets, $Z+$ jets with W, Z leptonic decays;
- top pair production with fully leptonic, semi-leptonic and hadronic decays (where some final state particles may be missed or mis-identified);
- single top production leading to a $W^{\pm}b\ q$ final state;
- $W^{+}W^{-}, W^{\pm}Z$ and ZZ with all possible decay combinations leading to the final state in Eq. (6.11);

Next, we present some details about the Monte Carlo simulation.

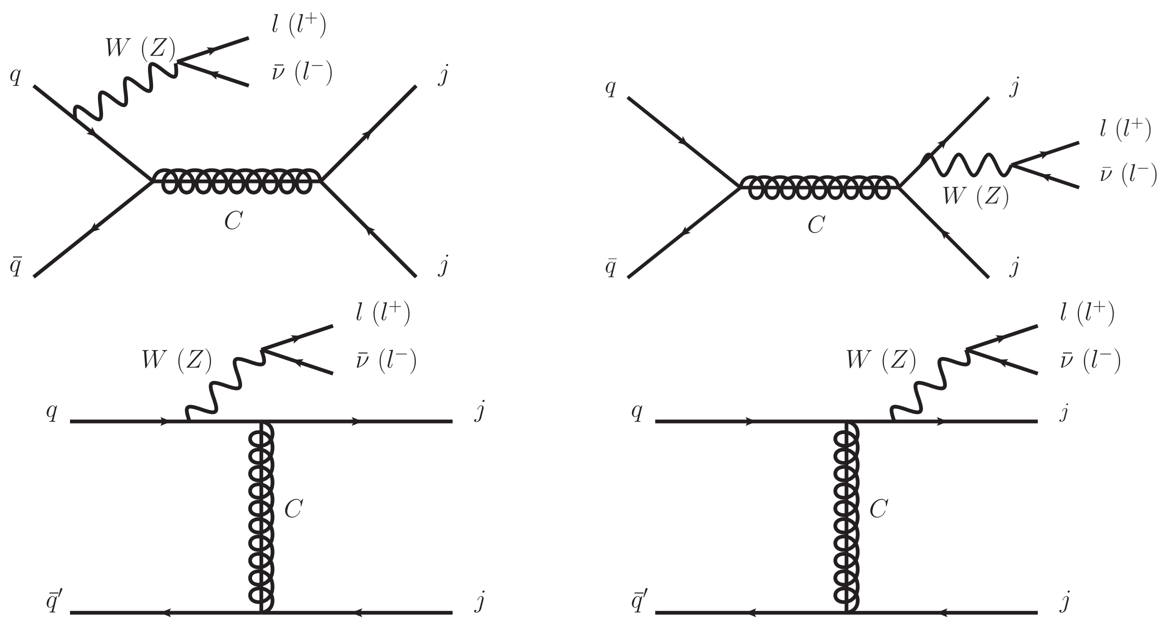

Figure 6.2: Representative Feynman diagrams for associated production of a W, Z gauge boson with a color-octet resonance, C. Both s and t channel diagrams along with initial or final state radiation of the associated gauge boson are shown. We assume that the weak gauge boson decays leptonically.

6.3.1 Monte Carlo Simulation

We have performed a detailed simulation of both the signal and all the relevant backgrounds using Madgraph/Madevent [285] for event generation at the partonic level, PYTHIA [286] for parton showering with initial and final state radiation as well as hadronization and PGS [287] for detector simulation. All the detector simulation parameters were set to default values that correspond to the LHC Detector in Madgraph/Madevent. The CTEQ6L1 Parton Distribution Functions (PDFs) [262] were used for both signal and background samples. For the signal processes we set the factorization and renormalization scales to be $\mu_F = \mu_R = m_C$. For the background processes the renormalization and factorization scales are set to $\mu_F = \mu_R = Q$ where $Q^2 = \sum(m_i^2 + p_T^{j_i 2})$.

We simulate signal samples with color-octet masses, $m_C = 2.5$ to 4.5 (4.0) TeV for the

CW (CZ) channel. For each mass, we do an exhaustive sampling of couplings $g^q_{L,R}, g^t_{L,R}$, where the couplings $g^t_{L,R}$ follow the relation in Eq. (6.4). This exhaustive sampling of couplings gives us color-octets with varying widths, $\Gamma_C/m_C \sim 0.025 - 0.50$. While we use the entire sample in estimating the reach of the signal, we will only present details about the samples with $\Gamma_C/m_C = 0.05, 0.10, 0.20, 0.30$ for simplicity and clarity of presentation. We show the parton-level cross sections for a few different color-octet masses and widths at the LHC with $\sqrt{s} = 14$ TeV in Table 6.1 for illustration. Also shown, for comparison, are the sizes of the standard model backgrounds at parton level.

Table 6.1: Representative cross sections at parton level in fb for the CW and CZ signal modes and backgrounds at the LHC with $\sqrt{s} = 14$ TeV. The signal is shown for $m_C = 2.5$ to 4.5 TeV and for a few sample coupling values that correspond to $\Gamma_C/m_C = 0.05,\ 0.10,\ 0.20$ and 0.30. For the backgrounds a requirement that $p_T^{j1} > 250\,\text{GeV}$ and $p_T^{j2} > 200\,\text{GeV}$ was applied in all cases, except for $t\bar{t}$ where $p_T^{j1} > 150\,\text{GeV}$ and $p_T^{j2} > 100\,\text{GeV}$ was applied.

m_C (TeV)	Γ/m_C	Signal - CW			Signal - CZ		
		g_L^q	g_R^q	σ (fb)	g_L^q	g_R^q	σ (fb)
2.5	0.05	-0.42	0.82	8.4	-0.82	-0.42	3.5
3.0	0.10	0.59	1.2	7.5	-1.09	-0.71	3.0
3.5	0.20	0.71	1.7	6.4	-1.49	1.08	3.5
4.0	0.30	1.2	1.8	8.2	-1.92	-1.17	3.8
4.5	0.30	-1.2	1.9	7.8	-	-	-

Background	σ (fb)
$(W \to \ell\nu) + 2$ jets	9500
$t\bar{t}$ semi leptonic	4200
$(Z \to \ell\ell) + 2$ jets	1000
single top ($t \to \ell^{\pm}\nu b$)	160
Total	15000

The backgrounds for the process of interest are listed in Sec.6.3. We generate all the backgrounds with the requirement that $p_T^{j1} > 250\,\text{GeV}$ and $p_T^{j2} > 200\,\text{GeV}$ (at the parton level) except top-pair production where we used $p_T^{j1} > 150\,\text{GeV}$ and $p_T^{j2} > 100\,\text{GeV}$. We verified that requiring large cuts on the p_T of the leading jets at the parton level does not distort the distributions in the region of interest to us (higher p_T regions) or affect the background efficiencies.

For the CW channel the leading background is $W+$ jets with leptonic decays of the W. There is also a sizable contribution to the background from top pair production with semi-leptonic decays. Other decay modes of top pair such as the fully leptonic mode where one lepton is lost and the hadronic mode where there is a fake lepton turn out to be negligible after the acceptance and optimized cuts are applied. The single top background as well as those from $Z+$ jets where one lepton is lost turn out to be relevant at the sub-leading level. The background from all the diboson channels turns out to be insignificant after the acceptance and optimized cuts are applied. For the CZ channel the only relevant background is $Z+$ jets with leptonic decays of Z. The other backgrounds such as top pair with fully leptonic decays and diboson channels turn out to be insignificant after the acceptance and optimized cuts are included. While we analyzed all the backgrounds, we only list the cross sections for the leading and sub-leading backgrounds in Table 6.1 for illustration.

We summarize below the minimum cuts imposed (after detector simulation) in reconstructing the physics objects for our analysis.

$$\begin{aligned}
&p_T^j > 40 \text{ GeV}, \quad |\eta_j| < 2.5, \quad \Delta R(jj) > 0.4, \quad \# \text{ jets} \geq 2, \\
&p_T^\ell > 25 \text{ GeV}, \quad |\eta_\ell| < 2.5, \quad \Delta R(j\ell) > 0.4, \quad \Delta R(\ell\ell) > 0.2, \\
&\not{E}_T > 25 \text{ GeV}, \quad \# \text{ isolated leptons} = 1(2) \text{ for } CW(CZ) \text{ channel}, \\
&m_Z - 20 \text{ GeV} < m_{\ell\ell} < m_Z + 20 \text{ GeV}.
\end{aligned} \tag{6.12}$$

Note that the $\not{E}_T$ cut is only for the CW channel and the $\Delta R(\ell\ell)$ and $m_{\ell\ell}$ cuts are only for the CZ channel. All other cuts are applied for both channels.

6.3.2 Charged Current Channel with W-Decays to Leptons

In this section we study the case where the color-octet is produced in association with a W boson and investigate the prospects of this channel at the LHC with $\sqrt{s} = 14$ TeV. The color-octet decays to two jets and the W boson decays leptonically $W \to \ell\nu$ ($\ell = e, \mu$) giving us a final state $jj\ell\not{E}_T$. We probe color-octet masses from 2.5 to 4.5 TeV for a wide range of couplings $g^q_{L,R}, g^t_{L,R}$ and decay widths (Γ_C) and describe the analysis in detail below.

Each event is required to contain at least two jets and exactly one lepton isolated from other leptons and jets, the criteria for which are listed in Eq. (6.12). There are also additional minimum requirements on the transverse momentum and rapidity of the jets, leptons and missing energy listed in Eq. (6.12). We will refer to these requirements as acceptance cuts. As jets from the decay of a heavy resonance are highly energetic, we identify the two jets with the highest p_T as the jets from the decay of the color-octet. In Fig. 6.3(a) and (b) we show the transverse momentum distributions for these jets normalized to unit area for a color-octet with mass $m_C = 3$ TeV and two different widths $\Gamma_C/m_C = 0.05$ and 0.20. It is clear from the distributions that the p_T of the jets is a good discriminant to separate signal from the background. The signal distributions are very broad and the background distributions are sharply peaked at lower transverse momentum. In addition, since associated production would be studied after the existence and mass of the color-octet have been established by dijet studies, we can use transverse momentum cuts that are optimized based on the mass of the color-octet state.

The efficiencies of the acceptance cuts and the optimized transverse momentum cuts for various signal and background samples (optimized to give 3σ significance) are shown in Table 6.2 and 6.3 for different mass values of the color-octet at 14 TeV c.m. energy. The couplings and widths for the mass points shown are the same as in Table 6.1. We can achieve very good separation of signal from background by just using these simple p_T cuts as seen from Table 6.2 and 6.3. We find that the commonly used kinematic variable H_T, which is the sum of the transverse momenta of final state particles, is dominated by the two hardest jets and there is no significant gain in efficiency by further optimizing on this variable. Similarly, we have investigated the possibility of using the reconstruction of the mass peak as another useful discriminant; as discussed in Sec.6.4, we found that its likely utility is limited.

Finally we mention some details about the signal simulation sample. We study different color-octet masses from 2.5 TeV to 4.5 TeV. While we show only a few points for illustration in Table 6.2 and 6.3, we sample a wide range of couplings $g^q_{L,R}, g^t_{L,R}$ and decay widths (Γ_C) ranging from very narrow widths $\sim 2.5\%$ to upwards of 40% for each mass point. We estimate the significance for each point in parameter space by $s/\sqrt{b}$, where s (b) are the number of signal (background) events. The results of this analysis are presented in Sec.6.4.

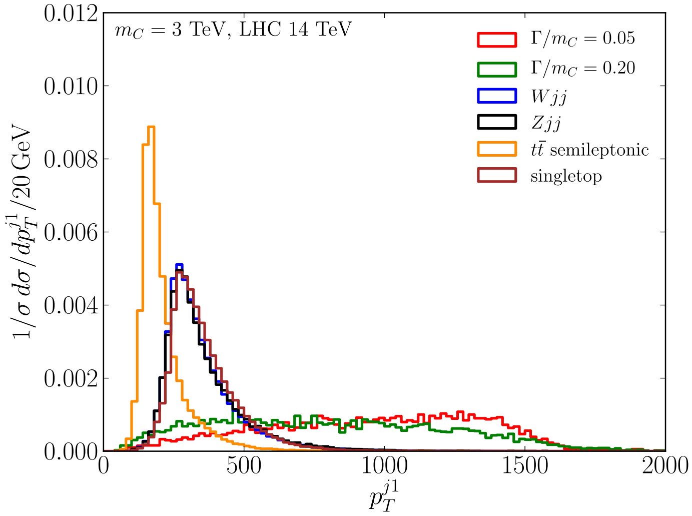

(a)

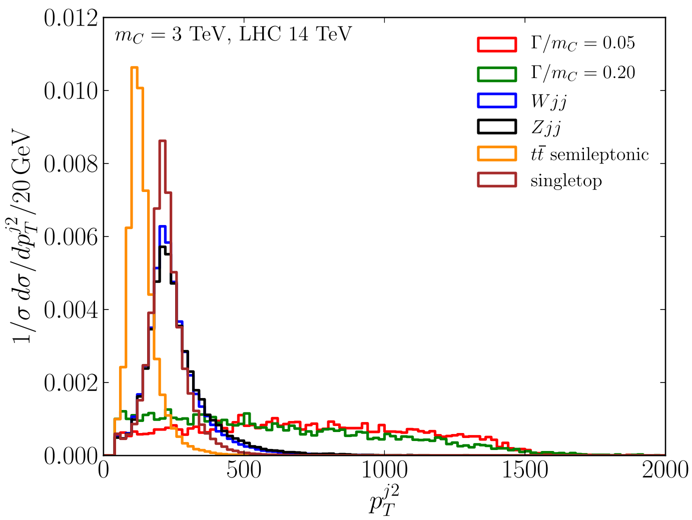

(b)

Figure 6.3: (a) Top: transverse momentum of the hardest jet ($p_T^{j_1}$) for a color-octet with mass $m_C = 3$ TeV and two different widths $\Gamma_C/m_C = 0.05$ and 0.20. (b) Bottom: same as (a) but for the second hardest jet ($p_T^{j_2}$). The relatively broad and flat transverse momentum distributions of the signal events contrast with the distributions for the backgrounds, which all peak sharply at lower transverse momenta.

Table 6.2: Selection efficiencies (in percent) for signal (ϵ_{m_C}) and background (ϵ_{BG}) samples for the case of the CW channel with leptonic decays of W into electrons and muons. The couplings and widths for the mass points shown are the same as those in Table 6.1.

Efficiencies (in %)				
Cuts for $m_C = 2.5$ TeV	Acceptance cuts see Eq. (6.12)	$p_T^{j_1} > 825$ GeV	$p_T^{j_2} > 775$ GeV	Overall
$\epsilon_{2.5}$	54	53	63	18
ϵ_{Wjj}	54	1.3	36	0.25
$\epsilon_{t\bar{t}}$	58	8.9×10^{-2}	6.1	3.1×10^{-3}
ϵ_{Zjj}	13	1.5	49	9.2×10^{-2}
ϵ_{t}	56	5.0×10^{-1}	6.1	1.7×10^{-2}
Cuts for $m_C = 3.0$ TeV	Acceptance cuts see Eq. (6.12)	$p_T^{j_1} > 1000$ GeV	$p_T^{j_2} > 950$ GeV	Overall
$\epsilon_{3.0}$	54	41	60	13
ϵ_{Wjj}	54	4.6×10^{-1}	35	8.8×10^{-2}
$\epsilon_{t\bar{t}}$	58	1.9×10^{-2}	7.5	7.9×10^{-4}
ϵ_{Zjj}	13	5.5×10^{-1}	48	3.3×10^{-2}
ϵ_{t}	56	1.1×10^{-1}	4.1	2.5×10^{-3}
Cuts for $m_C = 3.5$ TeV	Acceptance cuts see Eq. (6.12)	$p_T^{j_1} > 1100$ GeV	$p_T^{j_2} > 1050$ GeV	Overall
$\epsilon_{3.5}$	51	30	62	9.8
ϵ_{Wjj}	54	2.7×10^{-1}	35	5.2×10^{-2}
$\epsilon_{t\bar{t}}$	58	9.0×10^{-3}	1.9	9.5×10^{-5}
ϵ_{Zjj}	13	3.3×10^{-1}	48	2.0×10^{-2}
ϵ_{t}	56	5.0×10^{-2}	4.5	1.3×10^{-3}

6.3.3 Neutral Current Channel with Z-Decays to Charged Leptons

In this section we study the case where the color-octet is produced in association with a Z boson and investigate the prospects of this channel at the LHC with $\sqrt{s} = 14$ TeV. The color-octet decays to two jets and the Z boson decays leptonically $Z \to \ell\ell$ ($\ell = e, \mu$) giving

Table 6.3: Same as Table 6.2, but for $m_c = 4.0$ and $4.5\,\text{TeV}$.

Efficiencies (in %)				
Cuts for $m_C = 4.0$ TeV	Acceptance cuts see Eq. (6.12)	$p_T^{j1} > 1200$ GeV	$p_T^{j2} > 1150$ GeV	Overall
$\epsilon_{4.0}$	49	21	61	6.5
ϵ_{Wjj}	54	1.6×10^{-1}	34	3.0×10^{-2}
$\epsilon_{t\bar{t}}$	58	6.8×10^{-3}	0	0
ϵ_{Zjj}	13	2.1×10^{-1}	42	1.1×10^{-2}
ϵ_{t}	56	2.4×10^{-2}	1.8	2.5×10^{-4}
Cuts for $m_C = 4.5$ TeV	Acceptance cuts see Eq. (6.12)	$p_T^{j1} > 1350$ GeV	$p_T^{j2} > 1300$ GeV	Overall
$\epsilon_{4.5}$	50	16	59	4.5
ϵ_{Wjj}	54	8.0×10^{-2}	31	1.4×10^{-2}
$\epsilon_{t\bar{t}}$	58	7.1×10^{-4}	0	0
ϵ_{Zjj}	13	9.0×10^{-2}	35	4.0×10^{-3}
ϵ_{t}	56	5.4×10^{-3}	8.3	2.5×10^{-4}

us a final state $jj\ell\ell$. All the details of the signal simulation are the same as in Sec.6.3.2, except that we sample color-octet masses from 2.5 TeV to 4.0 TeV as there is no sensitivity in this channel for higher mass resonances.

The event is required to contain at least two jets and exactly two leptons isolated from other leptons and jets in the event, the criteria for which are listed in Eq. (6.12). We require that the two isolated leptons reconstruct a Z boson with the condition that $m_Z - 20\text{ GeV} < m_{\ell\ell} < m_Z + 20\text{ GeV}$. There are also additional minimum requirements on the transverse momentum and rapidity of the jets and leptons listed in Eq. (6.12). We will refer to these combined requirements as acceptance cuts. The p_T of the two hardest jets is a good discriminant to separate signal from the background as in the case of the CW channel. The efficiencies of the acceptance cuts and the optimized transverse momentum cuts for various signal and background samples (that give 3σ significance) are shown in Table 6.4 for different mass values of the color-octet at 14 TeV c.m. energy. The couplings and widths for the mass points shown are the same as those in Table 6.1. Again, we sample a much broader range of couplings and widths and show only a few points for illustration.

Table 6.4: Selection efficiencies (in percent) for signal (ϵ_{m_C}) and background (ϵ_{BG}) samples for the case of the CZ channel with leptonic decays of Z into electron and muon pairs. The couplings and widths for the mass points shown are the same as those in Table 6.1.

Efficiencies (in %)				
Cuts for $m_C = 2.5$ TeV	Acceptance cuts see Eq. (6.12)	$p_T^{j1} > 850$ GeV	$p_T^{j2} > 800$ GeV	Overall
$\epsilon_{2.5}$	34	47	68	11
ϵ_{Zjj}	42	8.4×10^{-1}	43	1.5×10^{-1}
Cuts for $m_C = 3.0$ TeV	Acceptance cuts see Eq. (6.12)	$p_T^{j1} > 975$ GeV	$p_T^{j2} > 925$ GeV	Overall
$\epsilon_{3.0}$	34	38	69	8.9
ϵ_{Zjj}	42	3.9×10^{-1}	45	7.3×10^{-2}
Cuts for $m_C = 3.5$ TeV	Acceptance cuts see Eq. (6.12)	$p_T^{j1} > 1050$ GeV	$p_T^{j2} > 1000$ GeV	Overall
$\epsilon_{3.5}$	33	27	70	6.2
ϵ_{Zjj}	42	2.5×10^{-1}	44	4.6×10^{-2}
Cuts for $m_C = 4.0$ TeV	Acceptance cuts see Eq. (6.12)	$p_T^{j1} > 1200$ GeV	$p_T^{j2} > 1150$ GeV	Overall
$\epsilon_{4.0}$	34	17	74	4.4
ϵ_{Zjj}	42	1.1×10^{-1}	49	2.2×10^{-2}

It is evident from Table 6.4 that we can achieve very good separation of signal from background for the CZ channel as well by using just simple p_T cuts as in the case of CW channel. Again, we investigated the possible improvements one could make by using the invariant mass of the color-octet resonance as a discriminant. The situation for the case of the associated production of the Z boson with leptonic decays is slightly better, as full information for reconstructing the final state is readily available from the reconstructed leptons. However, as detailed in Sec.6.4, we determined that it would not add appreciably to the present analysis. Next, we discuss the results of our analysis and the sensitivity at the LHC.

6.4 Sensitivity at the LHC

In this section we will describe the sensitivity of the associated production channel at the LHC, the current constraints from direct searches and future sensitivity at the LHC to provide a broad view of the reach of the LHC in determining the chiral structure of the couplings of a color-octet resonance. We have simulated signal and background events for two different scenarios at the LHC with $\sqrt{s} = 14$ TeV: an early run with an integrated luminosity of 10 fb^{-1} and a longer run with 100 fb^{-1} integrated luminosity. We estimate the number of signal and background events after optimizing the transverse momentum cuts as described in Sec.6.3.2 and 6.3.3 and the statistical significance is calculated as $s/\sqrt{b}$ where s (b) is the number of signal (background) events.

We present the results of our analysis for the LHC in Figs. (6.4-6.8) in the plane of the couplings g_L^q, g_R^q for different masses, m_C, of the color-octet. The sensitivity for the channel with associated production of a $W(Z)$ gauge boson is presented in the upper (lower) panels of Figs. (6.4-6.6), while the left (right) panels are for integrated luminosity of 10 (100) fb^{-1}. In Figs. 6.7(a) and (b) we show the sensitivity for a 4.5 TeV color-octet resonance for 10 fb^{-1} and 100 fb^{-1} respectively in the CW channel. The CZ channel has no sensitivity at this mass and we do not show that channel in Fig. 6.7. The different colored bands represent varying significance of signal observation from 2σ to greater than 5σ. The black

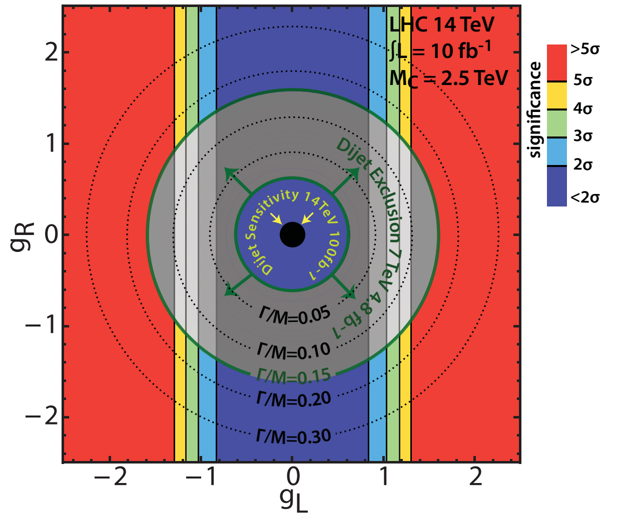

(a)

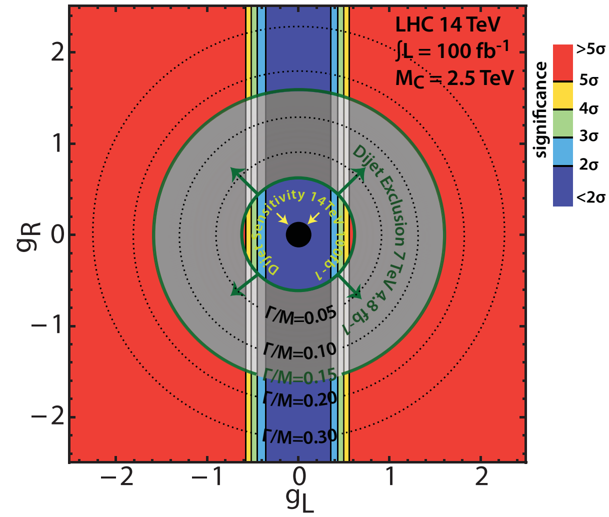

(b)

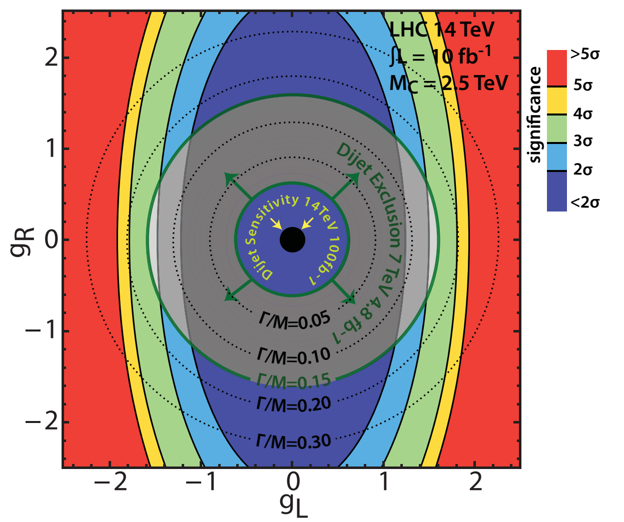

(c)

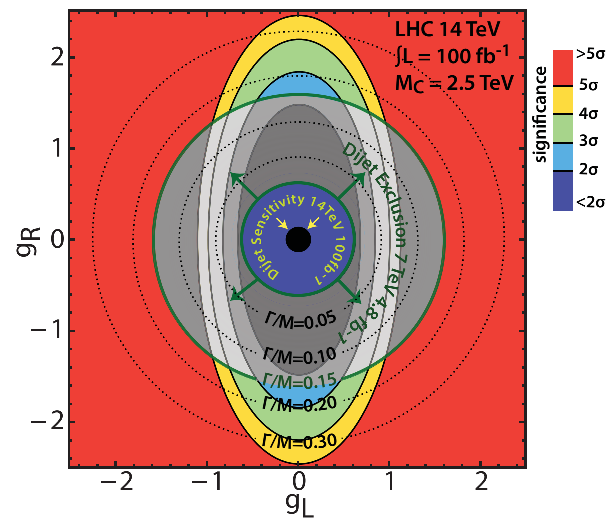

(d)

Figure 6.4: (a) Top left: sensitivity plot for a color-octet of mass $m_C = 2.5$ TeV produced in association with a W gauge boson, in the plane of the couplings g_L^q, g_R^q at the LHC with 10 fb^{-1} of data and $\sqrt{s} = 14$ TeV; (b) top right: same as (a) but for 100 fb^{-1} of data; (c) bottom left: same as (a) but for a color-octet produced in association with a Z boson; (d) bottom right: same as (c) but for 100 fb^{-1} of data. The various color bands show the regions with varying significance from 2σ to $> 5\sigma$. The inner solid green circle is the limit from current direct searches for narrow dijet resonances at the LHC [244, 241, 243, 242, 245]. The outer green circle corresponds to a contour with $\Gamma_C/m_C = 0.15$. The region between the two circles represented as a faded gray region is excluded for narrow resonances while the region beyond the outer green circle is allowed for broad resonances. The small black region in the center lies beyond the projected dijet sensitivity at the LHC with 100 fb^{-1} of data [260]. The black dotted contours indicate the combinations of couplings that give rise to varying widths $\Gamma_C/m_C = 0.05,\ 0.10,\ 0.20$ and 0.30.

dotted curves are contours of constant widths and we show the curves for several values of $\Gamma_C/m_C = 0.05,\ 0.10,\ 0.20$ and 0.30. The small black region in the center lies outside the projected dijet sensitivity (i.e. couplings within the black region result in a dijet production rate too small to be observed) at the LHC with 100 fb^{-1} of data [260].

The Tevatron [240] and the LHC [244, 241, 243, 242, 245] have looked for resonances in the dijet spectra, and the most stringent constraints come from the LHC as expected. This data places stronger constraints on low mass resonances and there is essentially no constraint on color-octets with masses above 3.5 TeV. The inner green solid circle is the limit from the current non-observation of narrow resonances in the dijet channel at the LHC [244, 241, 243, 242, 245] and the region outside this inner green circle can potentially be excluded. However there is a caveat here. The analyses of the LHC dijet searches make the assumption of a resonance with a narrow width of order 10% - 15%. The authors of Ref. [258, 259, 131] argue that in the case where the resonance is not narrow ($\Gamma_C/m_C > 15\%$) the constraints from dijet data can be relaxed. We mark the contour of $\Gamma_C/m_C = 0.15$ by the outer solid green circle. The area between the two green circles which is shown as a faded gray region (where the narrow-width approximation is valid) is excluded. The region beyond the outer green circle which corresponds to resonances with broader widths is possibly allowed. For example, in Fig. 6.4(a) the dijet constraint would be valid for narrow resonances (up to the outer green circle labeled $\Gamma_C/m_C = 0.15$) and would not be applicable to the regions outside this curve. As the LHC accumulates more data, the simple dijet analyses would remain sensitive only to the region inside the $\Gamma_C/m_C = 0.15$ curve. Of course a different analysis of dijet data without the narrow width assumption could ultimately be sensitive to the whole region. The region corresponding to broad resonances (beyond the outer green circle marked $\Gamma_c/m_C = 0.15$) has large couplings and hence will be largely accessible at the

LHC.

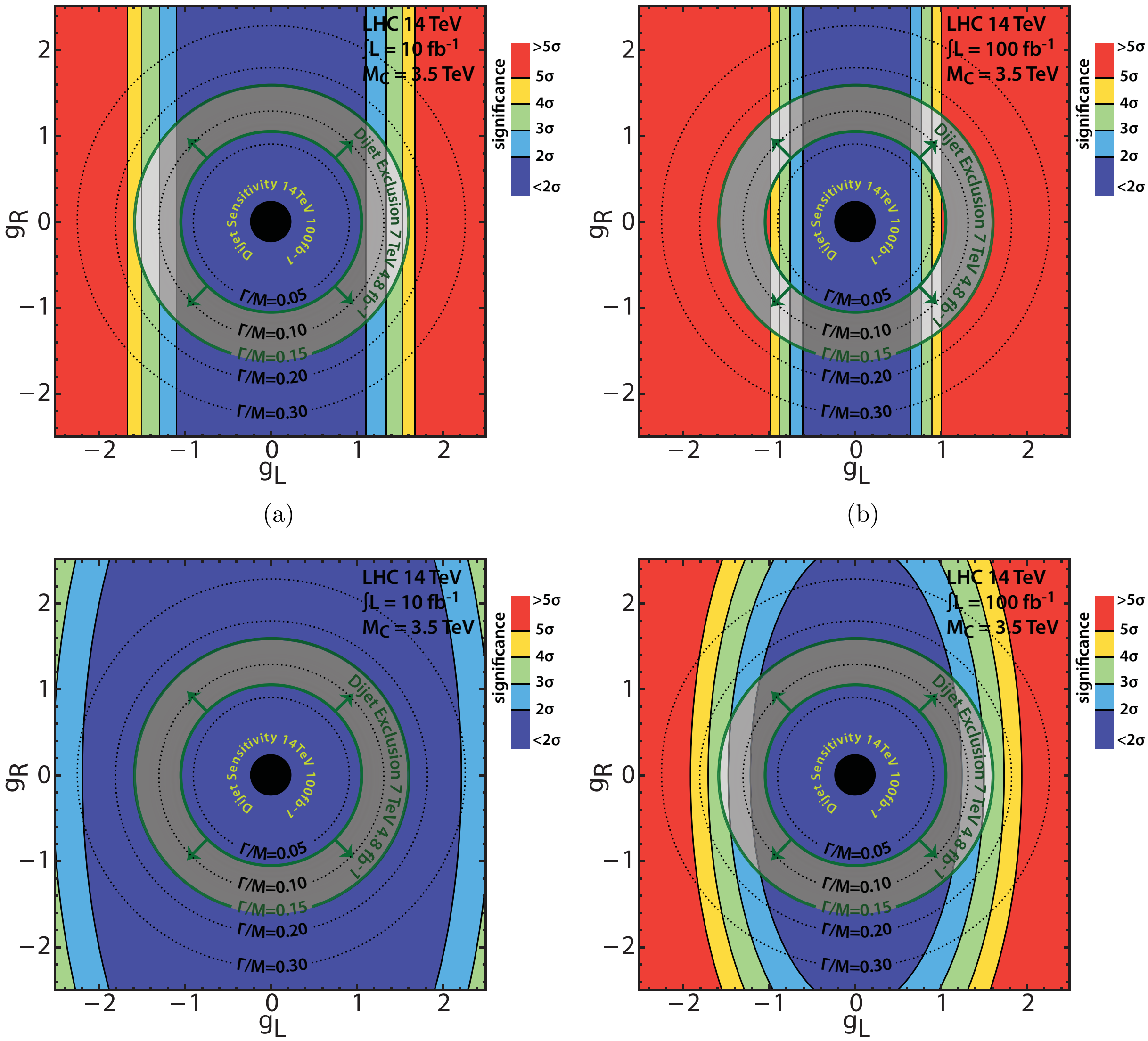

Figure 6.5: Same as Fig. 6.4 but for $m_C = 3.5$ TeV.

The results in Figs. (6.4-6.8) illustrate several features. Firstly, in the channel with associated production of a W boson, there is no sensitivity in the region near $g_L^q = 0$ due to the left-handed couplings of the W boson, and the sensitivity improves as we move away from the $g_L^q = 0$ axis. The channel with the associated production of a Z boson on the other hand is sensitive to both left and right-handed couplings and sensitivity in the region close

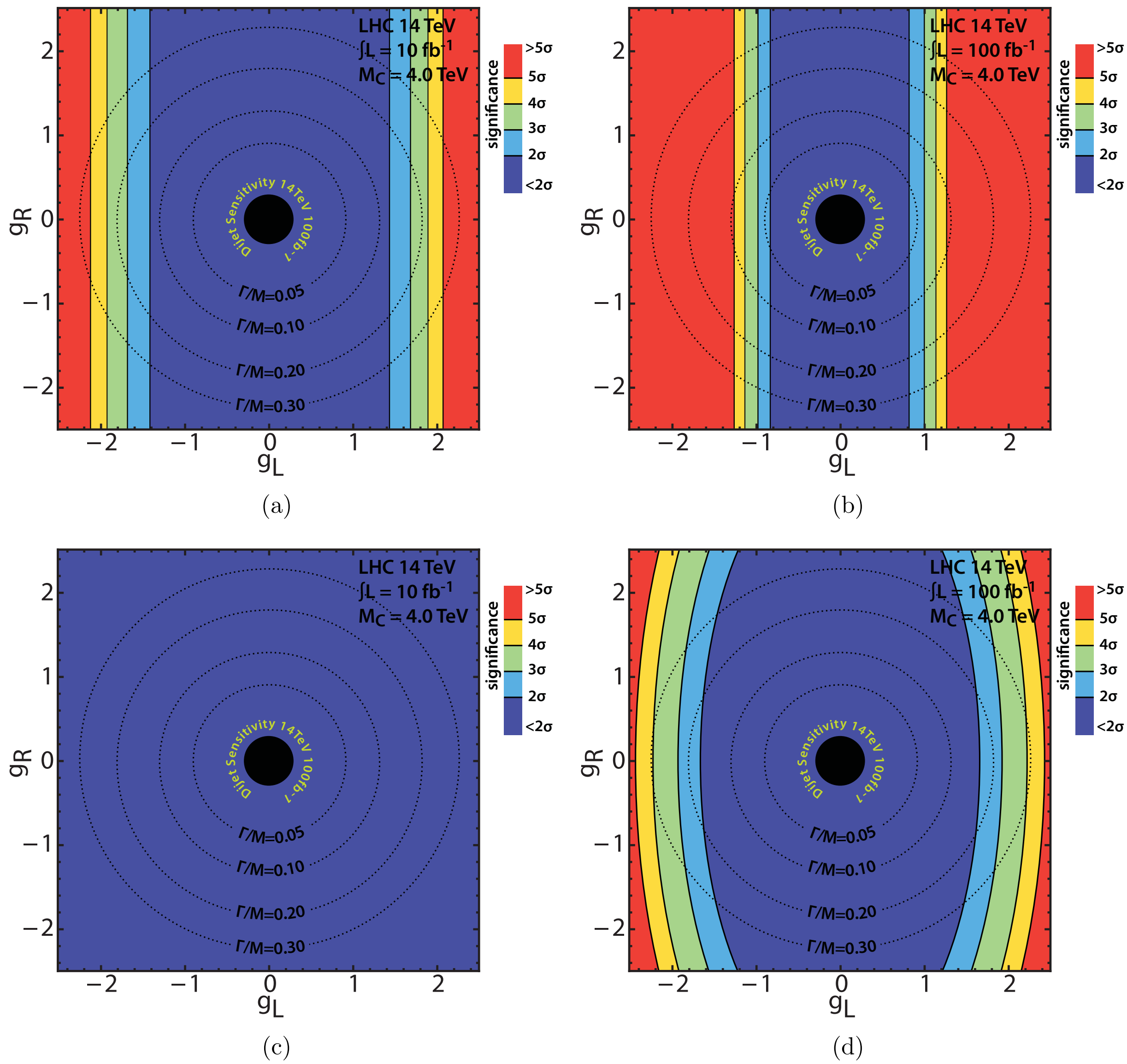

Figure 6.6: Same as Fig. 6.4 but for $m_C = 4$ TeV.

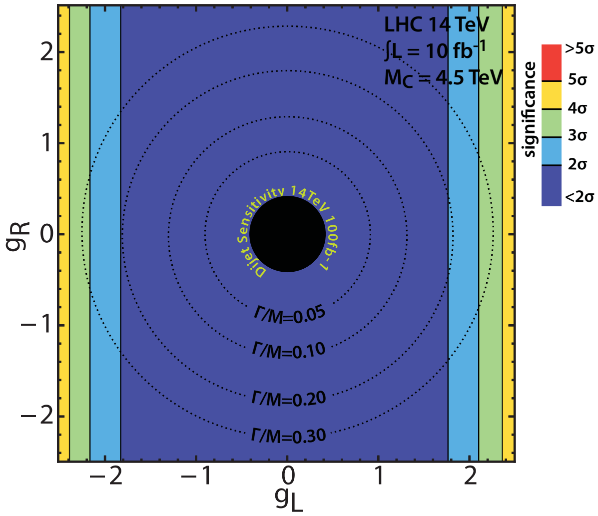

(a)

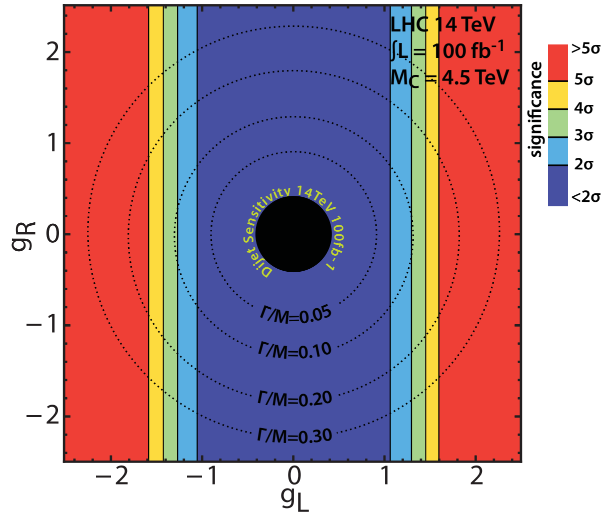

(b)

Figure 6.7: (a) Left: same as Fig. 6.4(a) but for $m_C = 4.5$ TeV; (b) right: same as (a) but for 100 fb^{-1} of data. The figures for the corresponding CZ channels are not presented as there is not sufficient sensitivity at this mass.

to $g_L^q = 0$ is non-zero. The smaller production cross section for this channel along with the small leptonic branching fractions for Z decays limit the gain in sensitivity. Nonetheless this channel provides an additional measurement and hence useful information in untangling the couplings.

We present the results for both 10 fb^{-1} and 100 fb^{-1} of data, and as expected, the longer run with more data has better sensitivity and can probe masses up to 4.5 (4.0) TeV in the channel with associated production of a $W(Z)$ gauge boson. We also show the projected limit of sensitivity in the dijet channel for the LHC with 100 fb^{-1} data as the small black circle in the center with small couplings. This can be improved even further, essentially allowing one to get closer to near zero couplings by the following observation. The theoretical analysis that produced the projected sensitivity [260] selects for a rather narrow region in pseudo-rapidity of the jets leading to a small acceptance. The analyses of actual LHC data for the 7 TeV dijet spectrum at the LHC [244, 241, 243, 242, 245] include larger regions of pseudo-rapidity giving rise to an acceptance larger than the one in Ref. [260]. It is safe to assume that the final acceptance will be at least equal to or even better than the current one and the small black region in the center could shrink even further.

Finally, the dijet reach is much better than that of associated production channel at the LHC, essentially probing near zero couplings. If the LHC were to discover a resonance with such small couplings, one would have to find other novel ways of understanding the chiral structure of couplings as the associated production channel does not have sensitivity in those regions of parameter space.

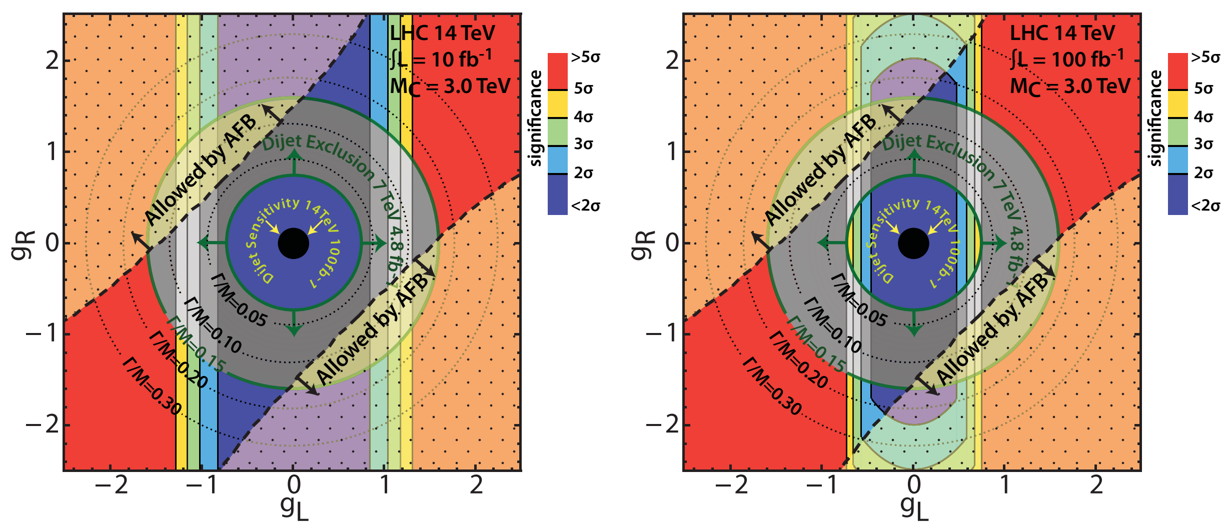

(a) (b)

Figure 6.8: (a) Left: same as Fig. 6.4(a) but for $m_C = 3$ TeV. Here we have combined the sensitivity in the associated production channel from both W and Z bosons. The couplings allowed by the current measurement of $A_{FB}^{t\bar{t}}$ at the Tevatron [288, 289] as interpreted in Ref. [217] are shown by the translucent yellow dotted region; (b) right: same as (a) but for 100 fb^{-1} of data;

Separately, we note that the Tevatron has made a measurement of the top-pair forward-backward asymmetry ($A_{FB}^{t\bar{t}}$) [288, 289]. The authors of Ref. [217] have translated this measurement into constraints on the couplings of color-octet resonances. We show this additional constraint for the case of a color-octet with mass $m_C = 3$ TeV in Figs. 6.8(a) and

(b) for 10 fb^{-1} and 100 fb^{-1} respectively. The region consistent with the $A_{FB}^{t\bar{t}}$ measurement is shown in translucent yellow with small dots. Note that for clarity of presentation we have combined the sensitivity from CW and CZ channels in Figs. 6.8(a) and (b). There are studies [259] that do global fits of data from top pair production including cross section, angular measurement, indirect searches and electroweak constraints under certain assumptions. The interested reader can combine our analysis with that of Ref. [259] to see how those other constraints (and assumptions) will affect the reach of the LHC for color-octet resonances.

Next, we discuss some possible means for achieving further improvements to the sensitivity. The reconstruction of the mass peak can be a useful discriminant to separate signal from background provided the mass of the resonance is known from prior measurements. The signal for our process comes from both s and t-channel diagrams as shown in Fig. 6.2. In the case where the s-channel contribution dominates and the associated W gauge boson is from the initial state, it is straightforward to form the invariant mass of the resonance $m_C = m(j_1, j_2)$ for the signal and backgrounds. As the jets from the decay of the color-octet are very energetic, there is hard radiation from the jets and we found that using the three hardest jets reconstructs the invariant mass better and so it is better to use $m_C = m(j_1, j_2, j_3)$ for the signal and backgrounds. In the case where the associated W gauge boson is produced in the final state with $W \to \ell\nu$ decay, we do not have full information to reconstruct the event. Since we cannot determine which of the two configurations the final state W comes from, one can make the conservative choice of using the transverse mass:

$$m_T^2 = \left(\sqrt{p_T^{W2} + m_W^2} + p_T^{j1} + p_T^{j2} + p_T^{j3}\right)^2 - \left(\vec{p}_T^{\,W} + \vec{p}_T^{\,j1} + \vec{p}_T^{\,j2} + \vec{p}_T^{\,j3}\right)^2 .$$

Our initial investigation found that selecting events based on a transverse mass cut yielded only modest improvement. Even reconstructing events with a leptonically decaying W using the W rest mass approximation did not help much. However further study may be warranted.

The situation for the case of the associated production of a Z boson with leptonic decays is slightly better as full information for reconstructing the final state is readily available. In the case where the s-channel contribution dominates, the invariant mass of the resonance can be reconstructed from $m_C = m(j_1, j_2, j_3)$ (initial state Z) or $m_C = m(j_1, j_2, j_3, Z)$ (final state Z). Since we cannot determine which of the two configurations the Z boson comes from, we pick the one closest to the resonance mass and call it m_C^{rec}. In Fig. 6.9 we show the reconstructed invariant mass (m_C^{rec}) for a 3 TeV color-octet resonance with width $\Gamma_C/m_C = 0.05$ and 0.30. The distribution for m_C^{rec} is normalized to unit area. While it is easy to distinguish the mass peak for the case of a very narrow resonance, it becomes increasingly harder to do so for broader resonances. Furthermore it will be hard to determine the mass of a broad resonance even in the dijet channel. Since we sample a wide range of couplings which lead to varying widths from 2.5% to greater than 40% of the mass, using the invariant mass as a discriminant is not useful for the entire range. Also, in the case where the t-channel contribution is not negligible the resonance peak is diluted and the utility of the invariant mass as a discriminant is further reduced. In view of these observations we do not use the invariant mass as a discriminant to separate signal from backgrounds for either the CW or CZ channel but mention it here for completeness as a possible improvement one could make for the appropriate cases (narrow width resonances).

The analysis reported here gives only an estimate of the LHC reach and we discuss some considerations about uncertainties and systematic effects. Our predictions for the signal and background are at the leading order (LO) and no k-factors have been taken into account. Varying the scales by a factor of two around the central value results in a variation of the

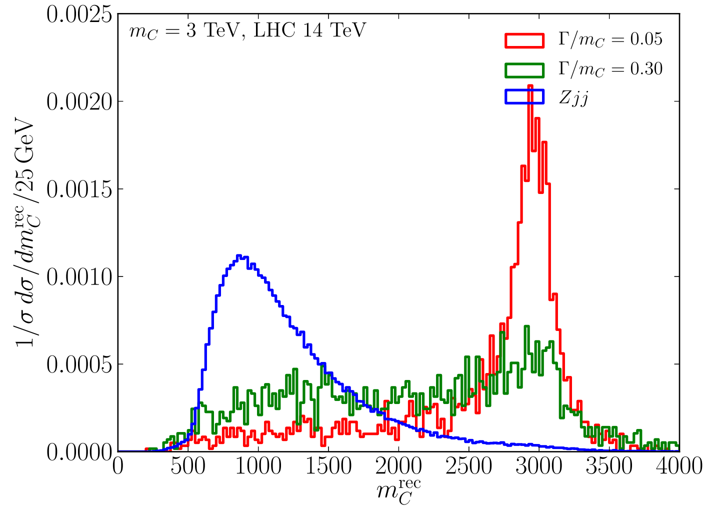

Figure 6.9: Reconstructed invariant mass (m_C^{rec}) for a 3 TeV color-octet resonance with width $\Gamma_C/m_C = 0.05$ and 0.30 after acceptance cuts.

signal cross sections of order $15 - 30\%$ and can be used as an estimate of the uncertainty of the leading order (LO) cross sections. For the backgrounds one can use the k-factors where available or they can be normalized to data in regions outside the signal. Multijet events, which are abundant at the LHC, can fake the signal for the CW channel if jets are misreconstructed as leptons and if jet transverse energies are poorly measured, leading to a presence of missing energy in the events. As explained in Ref. [290] these effects will be small with optimized experimental methods. Also high luminosity measurements have to contend with the issue of pile up effects which become important for the longer run. Estimating these effects are beyond the scope of this work and we only mention them as possible sources of uncertainties that will need to be accounted for in an experimental analysis.

6.5 Summary

The LHC has been running successfully and opening up new frontiers at the TeV scale. Among the many new possibilities for discovery at the LHC are color-octet resonances that are motivated in many BSM theories. These new colored particles will be produced copiously at a hadron collider and show up as resonance mass peaks in the dijet spectrum. Once these particles are discovered it is of paramount importance to measure the properties such as mass, spin and coupling structure to pinpoint the underlying theory. While some information (such as mass and spin) can be obtained from the discovery mode, other information vital to probing the theory such as chiral couplings cannot be obtained from that measurement.

In this chapter we proposed a new channel, namely the associated production of a W or Z gauge boson with a color-octet resonance to provide information about the chiral structure. We combined the information from the dijet (discovery) mode with the associated production to uncover the chiral structure of the couplings of color-octet resonances to SM quarks. In order to make our study as widely applicable as possible, we have performed a phenomenological analysis of color-octets without being tied down to a specific theory. We sampled a wide range of masses, couplings and decay widths of color-octets and optimized the kinematic cuts to enhance the signal over the SM backgrounds. With this optimized analysis, we determined the sensitivity for the couplings and masses at the LHC and presented the results in the couplings plane for each mass after taking into account existing constraints. For one sample case of $m_C = 3$ TeV we also show the effect of being consistent with the $A_{FB}^{t\bar{t}}$ measurement at the Tevatron.

We studied two scenarios at the LHC with c.m. energy of 14 TeV, one with the early data of 10 fb^{-1} integrated luminosity and the other with the longer run accumulating 100

fb^{-1} of data. As expected the early run is sensitive to lower masses and larger couplings but the reach dramatically improves both in terms of mass and couplings for the longer run. In particular the early run can probe masses up to 4.5 TeV but with relatively large couplings compared to the strong QCD coupling while the longer run explores a much larger region in couplings. We find encouraging results that the LHC will be able to provide information about the chiral structure for a wide range of couplings and masses and hence point us in the direction of the underlying theoretical structure.

Chapter 7

Conclusion

The Standard Model is a well-established theory that has shortcomings in both phenomenological and theoretical aspects. The origin of mass, an aspect that is treated as an input of the Standard Model, could be addressed by new physics theories featuring dynamical breaking of the electroweak symmetry under the influence of new strong dynamics. The region of energy in which the physics responsible for electroweak symmetry breaking lies is also within the coverage of the LHC. Given that the collider still has at least a decade of experiments in its schedule, we are certainly within one of the most exciting eras of modern particle physics.

This thesis accounts for two questions one generally asks during this data-rich era: what do the current LHC data tell us about potential extensions of the Standard Model and what can we do if, in the near-future experiments, a signal from new physics is found? In particular, my collaborators and I studied how data from the Higgs searches and discovery constraint models with strong dynamics in Part I. Then we studied ways to characterize a vector resonance, a common predictions among most new physics models in Part II.

In Part I, we saw in Chapter 2 that even the first set of LHC data in 2011, before the discovery of the Higgs-like boson, has already put challenges to a large number of technicolor and topcolor-assisted technicolor models that include colored technifermions. These theories predicted enhanced rates of the di-tau and di-photon final states in the Standard Model Higgs searches, which were highly constrained by the data.

The fate of models featuring strong top-dynamics were studied in Chapter 3. We used an effective model focusing on phenomenological aspects of models with strong top-dynamics to analyze general phenomena of the models. The data in 2012, available with the discovery of the Higgs-like particle, also highly constrained a large class of strong top-dynamics models.

As a matter of fact, the data on Higgs searches from the first run at the LHC put great challenges not only on models featuring strong dynamics, but also on most new physics models that account for electroweak symmetry breaking. With the precisions of measurements achieved so far [17], the data indicate that the discovered particle with mass of 126 GeV is consistent with properties predicted by the Standard Model. The absence of other states similar to the Higgs boson also put tight constraints on models inspired by the lack of "naturalness" of the Standard Model. In the scenario that the discovered particle is actually *the* Higgs boson, a requirement of a mechanism (be it the Standard Model or new physics) preventing the unitarity issue at a TeV scale could be considered satisfied. In this scenario, new physics is no longer "guaranteed" at a TeV scale. Nevertheless, new physics could still show up as small deviations from the Standard Model predictions. Therefore, high precision measurements of the Higgs properties will be one of the first priorities of the next run of the LHC and the next collider. Still, there are other aspects of motivations for new physics and the chance of having a trace of such new physics showing up at the LHC is everything but negligible.

In Part II, we studied how one could characterize a common prediction of various new physics models, a new vector boson. We focused on direct searches in the dijet final state which provides large rates and simple topology: the final state a large class of new physics models might show up.

We saw in Chapter 4 and 5 that a color-octet vector boson could be distinguished from a color-singlet leptophobic one, which has similar decay channels, using simple measurements available with its discovery in a dijet final state. We found that our method for discriminating the color structure is applicable to a vector boson that could show up during both early and long-term runs at the 14 TeV LHC.

We also saw in Chapter 6 that the future LHC runs could also help probe the chiral structure of a new vector boson, allowing us to study its origin. We introduced a method utilizing associate productions of a color-octet vector boson with the Standard Model's weak bosons to determine the chiral couplings. From a phenomenological point of view, a vast region of non-excluded parameter space is still within reach of the LHC. There are still less well-explored areas of well-motivated ideas.

With the LHC, the ATLAS and CMS collaborations have pushed particle physics past an important milestone with the discovery of the particle whose properties consistent with the Higgs boson of the Standard Model. They have also shaped the directions of developments towards new physics, or even a new collider, as they observed no deviations from other Standard Model's predictions. Within a short period of time, the LHC has already put great challenges on models describing new physics at a TeV scale — a great benefit of doing physics in the era with abundant inputs from experiments. We can expect that the future runs of the LHC, with higher luminosity and higher center of mass energy, will help identify the behavior of the Higgs and the mechanism electroweak symmetry breaking.

APPENDICES

Appendix A

The Standard Model

In this appendix, I provide a partial review of the gauge theory for electroweak interactions and mass generations in the Standard Model.

A.1 Gauge Theory for Electroweak Interaction

A charged current weak interaction involving left-handed leptons and hadrons at energy scales of beta decay processes $\sim \mathcal{O}(\mathrm{MeV})$ is well-described by a theory pioneered by Fermi [291] (later generalized by Feynman–Gell-Mann [292] and Sudarshan–Marshak [293]). The prototypical Hamiltonian describing this class of theory, involving an interaction that changes a flavor of fermions, is

$$H = \frac{G_F}{\sqrt{2}} \int \mathrm{d}^3 x J^\mu(x) J^\dagger_\mu(x) \tag{A.1}$$

where $G_F = 1.16637 \times 10^{-5}\mathrm{GeV}^{-2}$ is a Fermi's constant and

$$J^\mu = \sum_{\text{leptons}} \bar{l}\gamma^\mu P_L \nu_l + \sum_{\text{hadrons}} \bar{p}\gamma^\mu (c_V + c_A\gamma^5) n \tag{A.2}$$

with $P_L = \frac{1-\gamma^5}{2}$ defined as the left-handed projection operator, and $c_{V,A}$ are constants $\mathcal{O}(1)$. The coupling dimension $(\mathrm{mass})^{-2}$ of (A.1) implies this is an effective theory and is non-renormalizable. This means above a certain energy scale of a few hundred GeVs, the scattering cross section increases with energy such that unitarity is violated; rendering the theory non-predictive. In other words, one cannot always express formulae in terms of experimentally-measured variables that remain finite and do not depend on the high-energy limit of the theory. The behavior at high energy for processes involving four fermions can be soften by regarding this theory as a low-energy limit of a theory having an electrically-charged intermediate vector bosons $W^{\pm}$, with mass $M_W \sim 80\,\mathrm{GeV}$, as a mediator of the interaction. This is equivalent to writing the Hamiltonian as $H \sim \int \mathrm{d}^3x J^{\mu}(x) W^{-}(x) + h.c.$. Still, this does not eliminate the problem with unitarity as the cross section involving the newly-introduced particle such as $e^{+}e^{-} \rightarrow W^{+}W^{-}$ grows as $(\text{energy})^2$. This can also be viewed from the point that a momentum propagator for a massive vector field with four momenta k_{μ} does not have a "safe" high-energy behavior; *i.e.*,

$$D_{\mu\nu}(k) = -i\frac{\left(g_{\mu\nu} - k_{\mu}k_{\nu}/M_W^2\right)}{k^2 - M_W^2} \xrightarrow[k \to \infty]{} \mathcal{O}(1) \tag{A.3}$$

rather falling with $\sim \frac{1}{k^2}$, in the way the proton propagator does in QED. This can be seen as a result of the presence of the $k^{\mu}k^{\nu}$ term. In addition, with only two charged vector bosons, the charged current is not conserved. This can be illustrated with one set of $l\,, \nu_l$ by inspecting that the time evolution of Q^{-}, $Q^{-} \sim \int \mathrm{d}^3x \nu_l^{\dagger}(1-\gamma^5) l$ is not zero and is proportional to a charge corresponding to a neutral current; *i.e.*,

$$\dot{Q}^{-} \sim [Q^{-}, H] = \int \mathrm{d}^3x \left(l^{\dagger}(1-\gamma^5) l + \nu_l^{\dagger}(1-\gamma^5)\nu_l \right) W^{-}\,. \tag{A.4}$$

Neutral current weak interaction, which involves fermions with both left- and right-handed chiralities, can also be described by a Hamiltonian similar to (A.1) with an electrically-neutral massive vector boson Z, with $M_Z \sim 90\,\mathrm{GeV}$, at high-energy limit. This kind of interaction has a distinctive experimental feature that processes involving changes of a fermion's flavor is highly suppressed. Similarly to the immediate charged vector boson, the theory including neutral vector boson also has issues with high-energy limit. The prescription of the theory for weak interaction which does not have issue at high energy is hinted by the symmetry structure of the fermion contents.

The inclusion of neutral current, together with various experimental evidence, indicate that under charged weak interactions, left-handed fermions are treated equally; *i.e.,* as a doublet of $l - \nu_l$ while the right-handed charged lepton appears as a singlet (as it does not participate in the interaction). Observed phenomena so far provided no strong evidence of the right-handed (Dirac) neutrinos, hence they have been excluded from the current picture. This structure under weak interaction is written as

$$\begin{pmatrix} \nu_e \\ \\ e^- \end{pmatrix}_L , \quad \begin{pmatrix} \nu_\mu \\ \\ \mu^- \end{pmatrix}_L , \quad \begin{pmatrix} \nu_\tau \\ \\ \tau^- \end{pmatrix}_L , \quad e^-_R , \quad \mu^-_R , \quad \tau^-_R . \tag{A.5}$$

Quarks also share similar structure except that all flavors have their right-handed partners involved in weak interaction processes:

$$\begin{pmatrix} u \\ \\ d' \end{pmatrix}_L , \quad \begin{pmatrix} c \\ \\ s' \end{pmatrix}_L , \quad \begin{pmatrix} t \\ \\ b' \end{pmatrix}_L , \quad u_R , \quad d'_R , \quad c_R , \quad s'_R , \quad t_R , \quad b'_R , \tag{A.6}$$

where the prime indicate there is a difference between mass and "gauge" eigenstates, which can be safely omitted for the current discussion. It turns out that the prescription that could explain the interaction of this nature while avoiding issues aforementioned is a gauge theory which treats the $W^\pm$ and Z as gauge fields. In this picture, the "neutral charge" appearing in (A.4) is a consequence of the closure property of the $SU(2)$ gauge group; namely, $[T^+, T^-] = T^3$, where $T^a = \tau^a/2$ and $T^\pm = T^1 \pm iT^2$ with τ^a being the Pauli matrices, the generators of the Lie algebra of $SU(2)$. However, a gauge group $SU(2)$ alone does not provide a complete picture for weak interaction.

The picture of a gauge field explaining weak interaction having $W^\pm$ and Z as mediators inevitably has to include photons as the $W^\pm$ are charged under electromagnetic interaction. In other words, the explanation of weak interaction as a gauge theory automatically demands a unification of electromagnetic and weak interactions. The minimum gauge group having 4 gauge bosons which correctly explains the observed phenomena turns out to be a product group $SU(2) \times U(1)$ [13, 14, 15]. The $U(1)$, hence its gauge field, in $SU(2) \times U(1)$ does not correspond directly to electromagnetism. This is because its charge *cannot* be the electromagnetic charge Q — Q has a preferred direction in the weak isospin space, distinguishing between the two members of the left-handed doublets. In other words, Q is not a constant of motion as it does not commute with the $SU(2)$ generators. The quanta of gauge field W^3 coupled to T^3 cannot be treated as a photon for similar reason[1] - photon does not couple to T^3. The quantum number corresponding to an operator commuting with the $SU(2)$ generators is called, historically, a weak hypercharge Y; hence the $U(1)$ group being designated $U(1)_Y$. As the $SU(2)$ part also affects only fermions with left-handed chirality, it is common to denote the gauge group for electroweak interaction as $SU(2)_L \times U(1)_Y$. The connection between the gauge boson of $U(1)_Y$, called the B^μ, and photon A^μ, hence the form of the $U(1)_Y$ operator, can be identified using the known form of electromagnetic interaction.

The form of $U(1)_Y$ charge is deduced from the form of electric charge for the left-handed particles. The charge corresponding to the right-handed fermions automatically commutes

[1]This is also the reason one cannot describe weak interaction using just an $SU(2)$ gauge group.

with the T^a of $SU(2)_L$. The argument applies on both lepton and quark families where the former is chosen for illustration. Denoting the lepton doublet as

$$L_l = \begin{pmatrix} \nu_l \\ \\ l^- \end{pmatrix} , \tag{A.7}$$

the corresponding electric charge,

$$Q_{\text{Left}} = T_3 - \frac{1}{2} \int \mathrm{d}^3 x L_l^\dagger L_l \tag{A.8}$$

has its second part commuting with T^a's of the $SU(2)_L$. This leads to the form of the Y; namely, $Y \propto Q - T_3$ is an invariant, reflecting the feature of generators of Abelian symmetry which has arbitrary normalization. We use a *convention*

$$Y = Q - T_3 \,. \tag{A.9}$$

With this convention quantum numbers of particles content of the $SU(2)_L \times U(1)_Y$ are listed in table A.1. This leads to the expression of electromagnetic current

$$J_{\text{em}}^{(l)\mu} = \bar{l}\gamma^\mu Q l = Q \bar{L}_l \gamma^\mu \left(\frac{1}{2} - T_3 \right) L_l + \bar{l}_R \gamma^\mu Q l_R \tag{A.10}$$

for leptons as well as for other fermions to be written using currents corresponding to $SU(2)_L \times U(1)_Y$,

$$J_{\text{em}}^\mu = J_3^\mu + J_Y^\mu \,, \tag{A.11}$$

where

$$J_a^\mu = \bar{L}_f \gamma^\mu T^a L_f \,, \tag{A.12}$$

and

$$J_Y^\mu = \bar{L}_f \gamma^\mu Y_f L_f + \bar{f}_R \gamma^\mu Y_f f_R \tag{A.13}$$

Knowing the form of the $U(1)_Y$ charge, interactions between currents and the fields to be regarded as gauge fields allows us to write down the form of gauge theory for electroweak interaction.

Table A.1: Hypercharge assignments for fermions.

fermions	T	T_3	Q	Y
ν_e, ν_μ, ν_τ	1/2	1/2	0	-1/2
e_L, μ_L, τ_L	1/2	-1/2	-1	-1/2
e_R, μ_R, τ_R	0	0	-1	-1
u_L, c_L, t_L	1/2	1/2	2/3	1/6
d'_L, s'_L, b'_L	1/2	-1/2	-1/3	1/6
u_R, c_R, t_R	0	0	2/3	2/3
d'_R, s'_R, b'_R	0	0	-1/3	-1/3

The connection between the gauge fields for $SU(2)_L \times U(1)_Y$, W_μ^a and B_μ and the physical gauge fields $W_\mu^\pm$, Z_μ, and A_μ can be obtained by demanding that the electrically neutral part of the gauge interaction term eventually be expressed using the physical fields Z_μ and A_μ

$$g J_a^\mu W_\mu^a + g' J_Y^\mu B_\mu \supset g_Z J_Z^\mu Z_\mu + e J_{\rm em}^\mu A_\mu \,, \tag{A.14}$$

where g, g', g_Z, e denote appropriate couplings to different fields and J_Z^μ is to be determined.

This means Z and A are linear combinations of W^3 and B; hence the "rotation"

$$Z_\mu = -B_\mu \sin\theta_W + W_\mu^3 \cos\theta_W \tag{A.15}$$

$$A_\mu = B_\mu \cos\theta_W + W_\mu^3 \sin\theta_W \,, \tag{A.16}$$

where θ is known as weak mixing angle or Weinberg angle[2]. Observe that only Z can interact with T^3. This leads, by inspecting the left-handed side of (A.14) which contains the term $T^3(gW^3 - g'B)$, to

$$\sin\theta_W = \frac{g'}{\sqrt{g^2 + g'^2}}\,, \qquad \cos\theta_W = \frac{g}{\sqrt{g^2 + g'^2}}\,, \tag{A.17}$$

once a proper normalization has been included. This agrees with the requirement that photon couples to electromagnetic current J_{em} with strength e. This in turn demands that both g and g' are not smaller than e; *i.e.*,

$$e = g\sin\theta_W = g'\cos\theta_W \,. \tag{A.18}$$

At this stage, we have the interaction term for the $SU(2)_L \times U(1)_Y$ interaction expressed in terms of the physical fields at low-energy,

$$\begin{aligned} gJ_a^\mu W_\mu^a + g' J_Y^\mu B_\mu &= \frac{g}{\sqrt{2}}(J^{+\mu}W_\mu^+ + J^{-\mu}W_\mu^-) \\ &\quad + \frac{g}{\cos\theta_W}(J^{3\mu} - \sin^2\theta_W J_{\text{em}}^\mu) Z_\mu + eJ_{\text{em}}^\mu A_\mu \end{aligned} \tag{A.19}$$

where $W_\mu^\pm = (W_\mu^1 \mp iW_\mu^2)/\sqrt{2}$, which determines $g_Z = \frac{g}{\cos\theta_W}$ hence J_μ^Z introduced in

[2]The mixing was introduced by Glashow [13].

(A.14).

To formally introduce a gauge theory where its gauge fields eventually have interactions presented in (A.19), one introduces a covariant derivative

$$D_\mu = \partial_\mu - igT^a W_\mu^a - ig' Y B_\mu \,, \tag{A.20}$$

as well as the field strength

$$F_{\mu\nu}^a = \partial_\mu W_\nu^a - \partial_\nu W_\mu^a + g\varepsilon_{abc} W_\mu^b W_\nu^c \,, \qquad B_{\mu\nu} = \partial_\mu B_\nu - \partial_\nu B_\mu \,. \tag{A.21}$$

Then the gauge theory for electroweak interaction has the form

$$\begin{aligned} \mathcal{L} \;=\; & \sum_l i\bar{L}_l^i \gamma^\mu D_\mu L_l^i + \sum_l i\bar{l}_R^i \gamma^\mu D_\mu l_R^i \\ & + \sum_i i\bar{L}_q^i \gamma^\mu D_\mu L_q^i + \sum_i i\bar{u}_R^i \gamma^\mu D_\mu u_R^i + \sum_i i\bar{d}_R^i \gamma^\mu D_\mu d_R^i \\ & - \frac{1}{4} F_{\mu\nu}^a F^{\mu\nu a} - \frac{1}{4} B_{\mu\nu} B^{\mu\nu} \,, \end{aligned} \tag{A.22}$$

where the superscript $i = 1, 2, 3$ denotes the fermion generations.

The gauge theory for electroweak interaction having interactions shown in (A.22) alone does not provide a consistent theory explaining observed phenomena for an obvious fact: it cannot describe massive gauge fields, which are required as weak interaction is short-ranged. Observe that left-handed and right-handed fermions do not appear in a symmetric manner in the Lagrangian. This means that they have to be massless; otherwise the gauge symmetry is violated. We will come back to the issue of fermion masses later. For now, we consider the requirements for a theory with a massive gauge field, which are well-illustrated in the case of an Abelian theory, QED.

The masslessness of photon in QED is a result of the location of a pole in its *full* propagator. Starting from the free propagator $D_0^{\mu\nu} = \left(g^{\mu\nu}k^2 - k^\mu k^\nu\right)/k^2$, one constructs the full propagator by collecting a set of 1-particle-irreducible diagrams (whose cut on one internal line will not result in two diagrams where each has two external photon lines) to all orders,

$$\begin{aligned} iD^{\mu\nu} &= iD_0^{\mu\nu} + iD_0^{\mu\alpha}\left(i\Pi_{\alpha\beta}\right)iD_0^{\beta\nu} + iD_0^{\mu\alpha}\left(i\Pi_{\alpha\beta}\right)iD_0^{\beta\gamma}\left(i\Pi_{\gamma\delta}\right)iD_0^{\delta\nu} + \ldots \\ &= i\frac{D_0^{\mu\nu}}{1+\Pi(q^2)} \end{aligned} \tag{A.23}$$

Here $\Pi^{\mu\nu}$ is a vacuum polarization tenser defined from electromagnetic current $J(x)$

$$i\Pi^{\mu\nu}(k^2) = e^2\int \mathrm{d}^4x \mathrm{e}^{ikx}\langle 0|TJ^\mu(x)J^\nu(0)|0\rangle \equiv i(g^{\mu\nu}k^2 - k^\mu k^\nu)\Pi(k^2)\,, \tag{A.24}$$

which is conserved $k_\mu\Pi^{\mu\nu}(k) = 0$ (*i.e.*, it has only transverse polarizations), reflecting that photon interacts with a conserved current. The exact propagator (A.23) implies that photon have mass μ^2 if $\Pi(k^2)$ had a pole at $k^2 = 0$ with $\Pi(k^2) \to \mu^2/k^2$. This pole could arise if there were a massless particle in an intermediate state of the diagram, which is not possible in QED as all the contributions to $\Pi(k^2)$ are from one-photon-irreducible diagrams (hence no one-photon intermediate state by construction). Gauge invariance does not prohibit such a pole, though. In order to obtain that, one expects an addition of a massless particle, say π, having coupling to the gauge field (conserved current) that allows a transition $A - \pi$. This transition naturally has a coupling $ieFk^\mu$, where k^μ is the photon's momentum and F is a constant. The process $A - \pi - A$ is allowed to be included in the one-photon-irreducible diagrams and eventually contributes to the polarization tensor via the $k^\mu k^\nu$ term as $-ie^2F^2k^\mu k^\nu/k^2$ (where $1/k^2$ comes from the propagator of the massless π). Thus, noting that gauge invariance forces the presence of the $g^{\mu\nu}$ term, we arrive at the singular part of the vacuum polarization tensor

$$i\Pi^{\mu\nu}(k^2) \xrightarrow[k\to 0]{} i(g^{\mu\nu}k^2 - k^\mu k^\nu)e^2F^2/k^2 \tag{A.25}$$

So the full propagator is

$$iD^{\mu\nu}(k) \xrightarrow[k\to 0]{} i\frac{D_0^{\mu\nu}(k)}{1+e^2F^2/k^2}\,, \tag{A.26}$$

which could lead to a gauge boson that still couples to a conserved current while being massive. Notice that the propagator retains safe high-energy behavior; *i.e.*, $D^{\mu\nu}(k) \to \mathcal{O}\left(\frac{1}{k^2}\right)$ as $k \to \infty$.

It was the mechanism of spontaneous breaking of local symmetry, developed by Brout, Englert, Higgs, Guralnik, Hagen, Kibble, and Anderson [27, 28, 29, 30, 31], that provides a way to incorporate mass of the gauge fields while preserving gauge symmetry in the Lagrangian; hence maintaining safe behavior at high energy. There, the additional massless particle π is the Nambu-Goldstone boson of a hidden global symmetry, which eventually shows up as an extra unphysical degree of freedom that can be "gauged away". We provide a review of how the mechanism works in the next section.

A.2 Hidden Symmetry and the "Brout–Englert–Higgs–Guralnik–Hagen–Kibble–Anderson Mechanism"

Electroweak symmetry does not manifest at low energy as we know that masses of the gauge fields corresponding to the group $SU(2) \times U(1)$ are not degenerate: photon is massless while the rest have masses of $\mathcal{O}(100\,\mathrm{GeV})$. The symmetry describing the interactions has to be hidden by some means, leaving only the $U(1)$ for electromagnetism apparent. The mechanism of spontaneous breaking, or hiding, of a local symmetry provides a way to incorporate massive gauge bosons into a theory without spoiling the much needed ingredient, a gauge symmetry. It is a result of works pioneered by various physicists including Nambu, Goldstone, Brout, Englert, Guralnik, Hagen, Higgs, Kibble, and Anderson. For brevity, we refer to this mechanism as the BEH mechanism. The mechanism illustrates the interplay between a spontaneous breaking of global symmetry and the gauge theory for electroweak interaction; *i.e.*, how gauge bosons become massive due to interactions with the so-called would-be Nambu-Goldstone bosons of the hidden global symmetry. In this section, we review its foundations and its applications to electroweak symmetry.

A.2.1 Spontaneous hidden of a global symmetry

One aspect of the foundations of the BEH mechanism is the spontaneous hidden, or broken, of a global continuous symmetry. This happens when the symmetry respected by the Lagrangian does not manifest in the ground state of the system, the vacuum. In other words, generators T^a ($a = 1, \ldots, \dim(G)$) corresponding to the symmetry group G of the system can be partitioned to two parts $T^a = (X^r, Y^h)$ where X^r are called broken generators, $e^{i\varepsilon^r X^r}|0\rangle \neq |0\rangle$, and $e^{i\varepsilon^h Y^h}|0\rangle = |0\rangle$. If $e^{i\varepsilon^h Y^h}$ forms a group H, we say that the symmetry is broken down from G to H, where the orientation of H in G is arbitrary. In this case, $h = 1, \ldots, \dim(H)$ and $i = 1, \ldots, \dim(G) - \dim(H)$. Now since $X^i|0\rangle \neq 0$, there are $\dim(G) - \dim(H)$ states $|\pi^r(p)\rangle$ that are connected to the vacuum via *conserved* currents $J^{\mu r}(x)$ constructed from broken generators. Their non-zero matrix elements can be parametrized as

$$\langle 0|J^{\mu r}(x)|\pi^s(p)\rangle = ip^\mu F^{rs} e^{-ip\cdot x}\,, \qquad r,\, s = 1, \ldots, \dim(G) - \dim(H) \tag{A.27}$$

where F^{rs} is the element of a constant matrix which can be diagonalized $F^{rs} = \delta_{rs}F$. Since the current $J^{\mu r}$ is conserved; *i.e.*, $\partial_\mu J^{\mu r} = 0$,

$$0 = \langle 0|\partial_\mu J^{\mu r}(x)|\pi^s(p)\rangle = -p^2 F\delta_{rs} e^{-ip\cdot x}. \tag{A.28}$$

This implies $m_\pi^{s2} = p^2 = 0$; namely there are $\dim(G) - \dim(H)$ massless states, one for each broken generator X^r that does not annihilate the vacuum. These massless states are referred to as Nambu-Goldstone bosons. Apparently, they have not shown up in observed physical spectrum either. It is the BEH mechanism that explains the absence of these Nambu-Goldstone bosons, at the benefits of having massive gauge fields, when the symmetry that is hidden is a local gauge symmetry.

A.2.2 The BEH mechanism

The idea of BEH mechanism is as follows. The Lagrangian describing the theory of interest can be partitioned into two parts: one preserving a gauge symmetry (the corresponding gauge group is called here W) and the other having a global symmetry group G large enough to contain that gauge group, while being spontaneously broken down to a subgroup H. Then, conserved currents and the gauge fields are allowed to interact in a gauge invariant manner (*i.e.*, via the "$gJ^\mu A_\mu$" term where g is the gauge coupling). This results in what is usually referred to as "gauging the global symmetry". From the conserved currents $J_W^{\mu a}$ constructed from generators belonging to the gauge group W, there will be linear combinations of those that do not annihilate the vacuum; *i.e.*, those corresponding to broken generators. These gauge currents will allow transitions between a vacuum and the states $|\pi^r(p)\rangle$ with the following amplitude

$$\langle 0|J_W^{\mu a}(x)|\pi^s(p)\rangle = ip^\mu F^{as} e^{-ip\cdot x}\,. \tag{A.29}$$

This leads to an interaction between the gauge fields, called here $A^{\mu a}$ and the states $|\pi^r\rangle$ with coupling $ig_a p^\mu F^{ar}$ where g_a represents gauge couplings (no summation over a). These particular states $|\pi^r\rangle$ will contribute to the transition $A^a - \pi^r - A^b$ in the vacuum polarization tensor $\Pi^{ab}_{\mu\nu}(k)$ of the gauge fields via the "$k^\mu k^\nu$" terms as

$$\sum_r g_a g_b F^{ar} F^{br} k^\mu k^\nu / k^2 \tag{A.30}$$

(summation over r, the various $|\pi^r\rangle$ states, only). Since the tensor $\Pi^{ab}_{\mu\nu}$ is gauge invariant by construction, it has to have the following asymptotic $k \to 0$ form

$$i\Pi^{ab}_{\mu\nu}(k) \xrightarrow[k\to 0]{} i(g_{\mu\nu}k^2 - k^\mu k^\nu)\sum_r g_a g_b F^{ar} F^{br}/k^2\,. \tag{A.31}$$

In a manner similar to what we saw in the previous section on the propagator of a photon, this vacuum polarization leads a full propagator whose residue is interpret as mass:

$$m_{ab}^2 = \sum_r g_a g_b F^{ar} F^{br} \,. \tag{A.32}$$

In other words, due to gauge symmetry, the states that would have been the Nambu-Goldstone bosons in the physical states were "eaten" so that the gauge fields become massive. The gauge fields have the longitudinal degree of freedom at the expense of the would-be Nambu-Goldstone bosons. Next, we consider a specific application of the mechanism in the electroweak sector of the standard model.

A.2.3 BEH mechanism and electroweak interaction

The gauge group $SU(2)_L \times U(1)_Y$ describing electroweak interaction is relevant at high energy while only the $U(1)_{\text{em}}$ of QED manifests at low energy compared to the weak scale of $\mathcal{O}(100\,\text{GeV})$. So the group G of the global symmetry breaking part of the Lagrangian has to be at least as large as $SU(2) \times U(1)$. The choice of G will actually determine the structure of the symmetry breaking. We will consider the minimal case of $G = SU(2) \times U(1)$. Then, all the gauge bosons of $SU(2)_L \times U(1)_Y$ couples to 4 generators T^a of G, while only 3 of those do not annihilate a vacuum. This means there will be 4 conserved currents $J_W^{\mu a} = (J_1^\mu, J_2^\mu, J_3^\mu, J_Y^\mu)$ connecting between the 3 Nambu-Goldstone bosons and a vacuum with amplitudes

$$\langle 0 | J_W^{\mu a}(x) | \pi^s(p) \rangle = i p^\mu F^{as} e^{-ip\cdot x} \quad a = 1, 2, 3, Y, \; s = 1, 2, 3 \tag{A.33}$$

and a constraint, whose form of the current determined by (A.11), indicating that electric charge is conserved; *i.e.*, $\left(J_3^\nu + J_Y^\mu\right)|0\rangle = 0$. This means

$$\langle 0|J_Y^\mu(x)|\pi^3(p)\rangle = -\langle 0|J_3^\mu(x)|\pi^3(p)\rangle\,. \tag{A.34}$$

Thus, singular parts (as $p^2 \to 0$) of the vacuum polarization tensors become

$$\Pi^{ab}(p^2) = \frac{g^2F^2\delta^{ab}}{p^2}\,, \quad \Pi^{YY}(p^2) = \frac{g'^2F^2}{p^2}\,, \quad \Pi^{aY}(p^2) = -\frac{gg'F^2\delta^{a3}}{p^2}\,, \tag{A.35}$$

which, after being incorporated to full propagators, lead to a mass matrix, with rows and columns constructed from $W_1^\mu, W_2^\mu, W_3^\mu, B^\mu$:

$$M^2 = F^2\begin{pmatrix} g^2 & & & \\ & g^2 & & \\ & & g^2 & -gg' \\ & & -gg' & g'^2 \end{pmatrix}. \tag{A.36}$$

The 2×2 lower-right block can be diagonalized to $\mathrm{diag}[(g^2+g'^2)F^2, 0]$ using exactly the same states Z_μ and A_μ defined in (A.17). So masses of the gauge fields are

$$M_W^2 = g^2F^2\,, \qquad M_Z^2 = (g^2+g'^2)F^2\,, \qquad M_A = 0\,, \tag{A.37}$$

with a constraint

$$\frac{M_W^2}{M_Z^2\cos^2\theta_W} = 1\,. \tag{A.38}$$

This also indicates that $F \sim \mathcal{O}(M_W,\, M_Z)$. In short, masses of the gauge fields are the result of their interactions with the Nambu-Goldstone bosons of the hidden global symmetry.

It is important to emphasize that in the BEH mechanism, there is no specific requirement the structure of an object that lead to spontaneous hidden of a symmetry by developing its vacuum expectation value under a certain circumstance. Apart from the requirement that it has to be a Lorentz scalar, the object could be either an elementary scalar such as the complex scalar "Higgs" doublet in the standard model, or a composite scalar showing up as result of a fermion condensate $\langle 0|\bar{\Psi}\Psi|0\rangle$. The Standard Model utilizes the elementary scalar as the agent of electroweak symmetry breaking. Strong dynamics models implement the condensate. In this appendix, we focus on the BEH mechanism in the Standard Model.

A.2.4 The "standard" BEH mechanism in the standard model

In the standard model, the field whose non-zero vacuum expectation value breaks electroweak symmetry is a fundamental scalar. The choice of a representation of the scalar field under the electroweak gauge group $SU(2)_L \times U(1)_Y$ is arbitrary. Only experiments can tell which one is preferred. The minimal model introduced by Weinberg [14] uses a fundamental scalar doublet of $SU(2)$ and lead to predictions in good agreement with experiments. A complex doublet H that causes a symmetry breaking has self-interaction structure determined by the potential terms of

$$\mathcal{L}_H = \partial_\mu H^\dagger \partial^\mu H - \mu^2 H^\dagger H - \lambda (H^\dagger H)^2\,. \tag{A.39}$$

The assumption that the symmetry breaks; *i.e.*, the condition $\mu^2 < 0$, implies that the vacuum corresponds to one of equivalent configurations of non-zero $\langle 0|H|0\rangle$ that satisfies

$$v^2 \equiv \langle 0|H^\dagger H|0\rangle = -\frac{\mu^2}{\lambda}\,. \tag{A.40}$$

The particular vacuum that leads to the pattern $SU(2)_L \times U(1)_Y \to U(1)_{\text{em}}$ is

$$Q\langle 0|H|0\rangle = \left(T^3 + Y\right)\langle 0|H|0\rangle = 0\,. \tag{A.41}$$

In the standard convention usually employed, the doublet satisfying this condition is

$$H = \begin{pmatrix} h^+ \\ \\ h^0 \end{pmatrix}, \qquad \text{with} \qquad \langle 0|H|0\rangle = \begin{pmatrix} 0 \\ \\ \frac{v}{\sqrt{2}} \end{pmatrix} \tag{A.42}$$

where its form of vacuum expectation value is reachable from any other vacua by an $SU(2)$ transformation. When electroweak gauge interaction is introduced (which, in this case, is equivalent to gauging the aforementioned global symmetry) the kinetic term of (A.39) contains

$$\mathcal{L}_H \supset \left|D_\mu H\right|^2 = \left|\left(\partial_\mu - igT^a W^a_\mu - ig'YB_\mu\right)H\right|^2\,. \tag{A.43}$$

Couplings between the gauge fields and the H doublet explains the masses of the gauge fields, when H develops a vacuum expectation value, at the expense of the unphysical degrees of freedom of H. The disappearance of the unphysical degrees of freedom is apparent when they are parameterized as

$$H = e^{iT^a\pi^a/v} \begin{pmatrix} 0 \\ \\ \frac{v+h}{\sqrt{2}} \end{pmatrix} , \tag{A.44}$$

which can be removed by a transformation allowed by the gauge freedom. With the definition of the gauge fields in (A.17), the kinetic term (A.43) contains

$$\mathcal{L}_H \supset \left[\frac{1}{4}g^2v^2\right] W^{\mu+}W_{\mu-}\left(1+\frac{h}{v}\right)^2 + \frac{1}{2}\left[\frac{1}{4}\left(g^2+g'^2\right)v^2\right] Z^{\mu+}Z_\mu \left(1+\frac{h}{v}\right)^2 , \tag{A.45}$$

explaining the massiveness of the gauge fields as well as their interactions with the scalar field h. The vacuum expectation value v can be identified with the constant F in (A.37) as $v = 2F$. Quantities in the brackets are interpret as masses of the gauge fields. Notice that there is no gauge choice that removes all the four degrees of freedom of H. The field h thus remains in the physical spectrum.

An elementary scalar particle is a feature of the BEH mechanism when the gauge symmetry is broken by a scalar field. This is the Higgs boson. As indicated in (A.45), it has cubic and quartic interactions with the gauge fields (as hhV and $hhVV$) with coupling strengths proportional to their masses. Its mass and self-interaction is described by the potential term in (A.39), under the same gauge choice that leads to (A.45), as

$$\mathcal{L}_H \supset -\frac{1}{2}m_h^2h^2 - \frac{gm_h^2}{2M_W}h^3 - \frac{g^2m_h^2}{8M_W^2}h^4 , \tag{A.46}$$

where we have replaced $\lambda = g^2m_h^2/(2M_W^2)$. In other words, Higgs self-coupling, hence the potential driving the electroweak symmetry breaking, is predicted as a function of the Higgs mass.

A.2.5 Fermion masses in the standard model

Fermions have masses. However, the Standard Model is a chiral theory. This means that masses of the fermions cannot be explained via a typical Dirac mass form of $m_f(\bar{f}_L f_R + \bar{f}_R f_L)$ as only the left-handed (chirality) fermions carry the weak isospin charge. Unlike the gauge bosons, fermions do not automatically become massive under the BEH mechanism when the gauge group and the representation of the Higgs have been chosen. Their masses have to be explained from phenomenological requirements via appropriate interactions with the Higgs fields.

Fermion masses in the Standard Model are a result of interactions with the Higgs field or its complex conjugate

$$\widetilde{H} = i\sigma_2 H^* \,, \tag{A.47}$$

where σ_2 is the Pauli matrix. Denoting different generations with a superscript i, j, the interactions are written in the (electroweak) gauge eigenstate as

$$- y_u^{ij} Q_L^i \widetilde{H} u_R^j - y_d^{ij} Q_L^i H d_R^j - y_e^{ij} L_L^i H e_R^j + \text{h.c.} \,. \tag{A.48}$$

The coupling matrix $f^{ij}_{u/d/e}$, the Yukawa couplings, are not necessarily diagonal and have to be determined from experiments. The mixing between generations in the gauge eigenstates can be removed here via a transformation to the mass eigenstate by unitary matrix $U^{(u/d)L/R}$ leaving the Lagrangian in the flavor-diagonal form. This in turns means that the charged currents have flavor-changing nature, quantified conventionally by $V_{CKM} \equiv U^{u}L(U^{d}L)^\dagger$ where V_{CKM} is known as the Cabibbo-Kobayashi-Maskawa matrix. Once the Higgs develops a non-zero vacuum expectation value $\sim v$, the fermions will have mass $m_f \sim yv$.

Appendix B

Strong Top Dynamics

B.1 TC2 in the NJL Approximation

In this appendix, we calculate the top-Higgs and top-pion spectrum in topcolor assisted technicolor (TC2) models [100], using the Nambu–Jona-Lasinio (NJL) [76] approximation for the topcolor dynamics. On phenomenological grounds [104], we expect the "cutoff" Λ of the NJL topcolor theory (which is of order the mass of the gauge-bosons of the topcolor model, *i.e.* the top-gluon and Z') to be much higher than the technicolor scale Λ_{TC}, which is of order 1 TeV. We can therefore construct the low-energy theory which we use to compute the scalar spectrum in two stages.

First, as described in the next section, we integrate out the strong topcolor-induced four-fermion operators using the Nambu–Jona-Lasinio approximation, and construct an effective theory involving a composite top-Higgs field coupled to the third-generation quarks and the technifermions. This effective theory will be valid at energies below the topcolor cutoff and above the scale at which the technicolor interactions become strong. Next, as described in the third section, we match to an effective technicolor chiral Lagrangian valid at low energies. In the fourth section we use this effective Lagrangian to compute the scalar spectrum of the theory. Custodial isospin violation is necessarily present in the theory so as to explain the top-bottom mass difference. In the fifth section we consider what constraints the limits on the custodial isospin violating parameter ΔT place on the parameters of the model, and what these restrictions imply for the scalar mass spectrum. In the last section, we consider the mass splitting between the charged- and neutral-top-pions.

B.1.1 TC2 Dynamics

In the NJL approximation,[1] the interactions of interest in this model include

$$\frac{g_t^2}{\Lambda^2}(\bar{\psi}_{L0}t_{R2})(\bar{t}_{R2}\psi_{L0}) + \frac{\eta g_t^2}{\Lambda^2}\left[(\bar{\psi}_{L0}t_{R2})(\bar{U}_R Q_L) + h.c.\right] \tag{B.1}$$

where the first four-fermion operator is the traditional topcolor interaction responsible for top-quark condensation and the second, arising from ETC interactions [82, 81], couples the top-quark to the weak-doublet and singlet technifermions [79, 80] Q_L and U_R. Here g_t and Λ represent the top-color coupling and cutoff, respectively. We expect the second operator to arise from ETC interactions at a scale larger than Λ, and for convenience we characterize the strength of these interactions (relative to topcolor) through the small dimensionless parameter η. All weak, color, and technicolor indices implicit in Eq. (B.1) are summed.

For strong g_t, we expect that the topcolor interactions will give rise to a bound electroweak scalar state with the quantum numbers of the standard model Higgs boson. In the NJL approximation, this may be seen directly. The interactions Eq. (B.1) may be recast as

$$\frac{g_t^2}{\Lambda^2}\left[\bar{\psi}_{L0}t_{R2} + \eta\bar{Q}_L U_R\right]\left[\bar{t}_{R2}\psi_{L0} + \eta\bar{U}_R Q_L\right] - \frac{\eta^2 g_t^2}{\Lambda^2}(\bar{Q}_L U_R)(\bar{U}_R Q_L)\ , \tag{B.2}$$

which, following [96], may be rewritten in terms of an auxiliary electroweak doublet scalar

[1] The NJL approximation [76, 96, 294] involves two parts. First we approximate the effects of exchange of heavy top-color gauge bosons by four-fermion contact interactions and include only those parts of the interaction responsible for coupling left- and right-handed fermion currents. Second, as discussed below, we analyze the effect of these interactions in the "fermion bubble" approximation. Here, and in the following, we also neglect additional TC2 interactions involving the right-handed bottom quark.

field Φ (with $SU(2) \times U(1)$ quantum numbers $2_{-1/2}$)

$$- \Lambda^2 \Phi^\dagger \Phi - g_t \left[(\bar{\psi}_{L0} t_{R2} + \eta \bar{Q}_L U_R) \Phi + h.c. \right] - \frac{\eta^2 g_t^2}{\Lambda^2} (\bar{Q}_L U_R)(\bar{U}_R Q_L) \ . \tag{B.3}$$

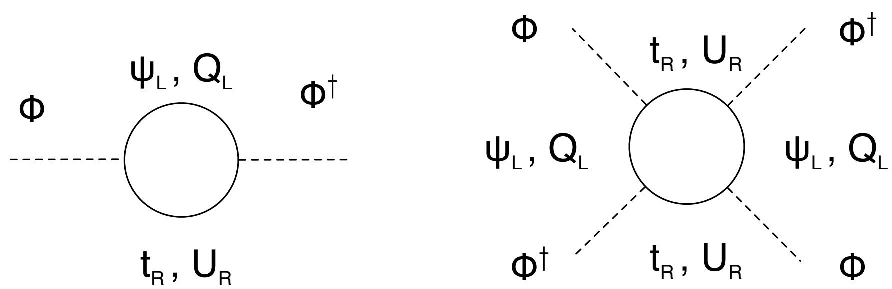

Figure B.1: Diagrammatic representation of "fermion bubble" approximation yielding the kinetic energy and mass (left) and self-couplings (right) of the composite Φ field. The two-point function is resumed to generate the kinetic energy term for the composite scalar field.

In the "fermion bubble" approximation [76, 96, 294] illustrated in Fig. B.1, and close to the critical point for chiral symmetry breaking, the auxiliary field Φ becomes a light propagating composite state. To leading order in the number of fermions (colors for quarks or technicolors for technifermions), the effects of the strong topcolor interactions at a scale $\mu \ll \Lambda$ may be summarized by the effective Lagrangian

$$\begin{aligned} \mathcal{L}_{tc} &= D_\mu \Phi D^\mu \Phi - \tilde{m}_\Phi^2 \Phi^\dagger \Phi - \tilde{g}_t (\bar{\psi}_{L0} t_{R2} \Phi + h.c.) - \frac{\tilde{\lambda}}{2} (\Phi^\dagger \Phi)^2 \\ &\quad - \eta \tilde{g}_t (\bar{Q}_L U_R \Phi + h.c.) - \frac{\eta^2 g_t^2}{\Lambda^2} (\bar{Q}_L U_R)(\bar{U}_R Q_L) \end{aligned} \tag{B.4}$$

with the couplings

$$\tilde{g}_t^2(\mu) = \frac{(4\pi)^2}{(N_C + \eta^2 N_{TC}) \ln(\Lambda^2/\mu^2)}, \tag{B.5}$$

$$\tilde{\lambda}(\mu) = 2 \frac{(4\pi)^2}{(N_C + \eta^2 N_{TC}) \ln(\Lambda^2/\mu^2)}. \tag{B.6}$$

Here, in order to have a conventional kinetic energy term, we have rescaled the field Φ by

$$Z_\Phi^{1/2} = \left(\frac{g_t^2}{(4\pi)^2} (N_C + \eta^2 N_{TC}) \ln \frac{\Lambda^2}{\mu^2} \right)^{1/2} . \tag{B.7}$$

The mass parameter for the composite field Φ is given by,

$$\tilde{m}_\Phi^2 = Z_\Phi^{-1} \left[\Lambda^2 - \frac{2g_t^2}{(4\pi)^2} (N_C + \eta^2 N_{TC})(\Lambda^2 - \mu^2) \right] . \tag{B.8}$$

The composite Higgs is light, and the effective theory valid, when $\mu \ll \Lambda$ and g_t is close to the critical coupling g_t^* for topcolor chiral symmetry given by

$$\frac{2g_t^{*2}}{(4\pi)^2} (N_C + \eta^2 N_{TC}) = 1 . \tag{B.9}$$

For convenience, we conclude this section with a brief discussion of the $\eta \to 0$ limit. As we will see, η will be rather small and many of the parametric estimates that follow will derive from this limit. If we define f as the expectation value of Φ through

$$\langle \Phi \rangle = \begin{pmatrix} \frac{f}{\sqrt{2}} \\ \\ 0 \end{pmatrix} , \tag{B.10}$$

we see from Eqs. (B.4) and (B.5) that

$$m_t^2 = \frac{\tilde{g}_t^2(m_t) f^2}{2} = \frac{(4\pi)^2 f^2}{2N_C \ln(\Lambda^2/m_t^2)} , \tag{B.11}$$

where we choose $\mu = m_t$ as appropriate in evaluating the top-quark mass. This expression is usually rewritten as

$$f^2 = \frac{2N_C m_t^2}{(4\pi)^2} \log\left(\frac{\Lambda^2}{m_t^2}\right) \ , \tag{B.12}$$

and reproduces the Pagels-Stokar relation [295] appropriate in this limit [76, 96, 294]. Note that, in the effective Lagrangian of Eq. (B.4), the top quark receives mass only through its coupling to the composite Higgs. Therefore, to the extent that η is small, this relation continues to be true even after including the effects of technicolor.

B.1.2 Technicolor

Next, we consider matching[2] the Lagrangian in Eq. (B.4) to the chiral Lagrangian valid at scales below the scale of technicolor chiral symmetry breaking, Λ_{TC}. In what follows, we will use the Naive Dimensional Analysis (NDA) [296, 297, 180] estimate $\Lambda_{TC} \simeq 4\pi F$, where F is the technicolor pion decay constant (the analog of $f_\pi \approx 93$ MeV in QCD). To keep track of the chiral symmetry properties of the technifermion – scalar coupling in $\mathcal{L}_{tc}$ we introduce the 2×2 matrix

$$\mathcal{M} = \eta \tilde{g}_t \ (\Phi \ 0) \ , \tag{B.13}$$

which serves as a spurion "transforming" as $\mathcal{M} \rightarrow L\mathcal{M}R^\dagger$ under the $SU(2)_L \times SU(2)_R$ chiral symmetries of the technifermions. The coupling of the technifermions to the field Φ, then, is similar to the mass term in QCD, and hence we expect the effective Lagrangian

$$\mathcal{L}_{TC}^{(2)} = \frac{F^2}{4} \mathrm{tr}[D_\mu \Sigma^\dagger D^\mu \Sigma] + 4\pi F^3 \left(\frac{c_1}{2}\right) \mathrm{tr}[\mathcal{M}^\dagger \Sigma + \Sigma^\dagger \mathcal{M}] \ , \tag{B.14}$$

[2] In principle, if $\Lambda/\Lambda_{TC} \gg 1$, we should also include the scaling of the operators in Eq. (B.4) due to the technicolor interactions. In practice, all of the relevant corrections can be absorbed into a redefinition of η – and hence will be neglected in what follows.

where c_1 is an unknown chiral coefficient related to the magnitude of the technifermion condensate which, in QCD, is approximately 2.[3] Here Σ is the $SU(2)_L \times SU(2)_R/SU(2)_V$ nonlinear sigma model field associated with electroweak symmetry breaking, and is to be associated with $\Sigma_{01}\Sigma_{12}$ in the triangle Moose model described in Sec. 3.2 above.

The second term in Eq. (B.14) arises from the ETC coupling of the top quark and is of particular interest since it couples the top-color and technicolor chiral symmetries – and hence will give rise to the top-pion masses. To analyze this term, it is convenient to rewrite Σ in terms of a two-component complex unimodular vector ξ

$$\Sigma = \begin{pmatrix} \xi & -i\sigma_2 \xi^* \end{pmatrix} = \begin{pmatrix} \xi & \tilde{\xi} \end{pmatrix} , \tag{B.16}$$

where

$$\xi\xi^\dagger + \tilde{\xi}\tilde{\xi}^\dagger = \mathcal{I}_{2\times 2}, \quad \xi^\dagger\xi = \tilde{\xi}^\dagger\tilde{\xi} = 1, \quad \xi^\dagger\tilde{\xi} = \tilde{\xi}^\dagger\xi = 0 \ . \tag{B.17}$$

By the usual convention, ξ has the following vacuum expectation value

$$\langle \xi \rangle = \begin{pmatrix} 1 \\ 0 \end{pmatrix} , \tag{B.18}$$

in unitary gauge. With this convention the combined $\Phi - \xi$ potential is a special case of a two-Higgs potential (with $F\xi$ playing the role of a second "Higgs"), and the second term in

[3] More properly, the corresponding term in the QCD chiral Lagrangian gives

$$m_\pi^2 = 4\pi f_\pi c_1 (m_u + m_d) \approx (135\,\mathrm{MeV})^2 \cdot \left(\frac{m_u + m_d}{8\,\mathrm{MeV}}\right) \cdot \left(\frac{c_1}{2}\right) \ . \tag{B.15}$$

.

Eq. (B.14) becomes

$$F m_{Mix}^2 [\Phi^\dagger \xi + h.c.] \ , \tag{B.19}$$

with mass-squared

$$m_{Mix}^2(\Lambda_{TC}) = 4\pi F^2 \left(\frac{c_1}{2}\right) \eta \tilde{g}_t(\Lambda_{TC}) \ , \tag{B.20}$$

renormalized at scale $\Lambda_{TC} = 4\pi F$.

At scales $\mu < \Lambda_{TC}$, the parameters $\tilde{\lambda}(\mu)$, $m_{Mix}^2(\mu)$, and $\tilde{m}_\Phi^2$ continue to renormalize through the top-quark loop diagrams illustrated in Fig. (B.1), *i.e.* the formulas in Eqs. (B.5), (B.6), and (B.8) continue to apply with $\eta \to 0$. The complete effective Lagrangian at scale μ is

$$\begin{aligned} \mathcal{L}_{TC2}^{(2)}(\mu) \;\; = \;\; & \frac{F^2}{4}\mathrm{tr}[D_\mu \Sigma^\dagger D^\mu \Sigma] + D_\mu \Phi D^\mu \Phi - \tilde{m}_\Phi^2(\mu) \Phi^\dagger \Phi + F m_{Mix}^2(\mu) [\Phi^\dagger \xi + h.c.] \\ & - \tilde{g}_t(\mu)(\bar{\psi}_{L0} t_{R2} \Phi + h.c.) - \frac{\tilde{\lambda}(\mu)}{2}(\Phi^\dagger \Phi)^2 \end{aligned} \tag{B.21}$$

In what follows we will need the values of these parameters evaluated at low energies, $\mu \simeq m_t$. We will find that $\eta \ll 1$; hence, in the derivations below we will apply Eqs. (B.5), (B.6), and (B.8) in the $\eta \to 0$ limit.

B.1.3 Minimizing the Potential and the Scalar Spectrum

We are interested in identifying the region of parameter space where topcolor and technicolor jointly yield electroweak symmetry breaking, *i.e.* Φ has the vacuum expectation value shown in Eqs. (B.10) and (B.18), with[4]

$$f = v\sin\omega\ , \qquad F = v\cos\omega\ , \tag{B.22}$$

and where $v \approx 246\,\mathrm{GeV}$ is the usual weak scale. We will assume that all of the low-energy mass parameters (the masses of all the scalars in the spectrum and the top-quark) have the same order of magnitude, and we adopt $\mu \simeq m_t$ implicitly in what follows.

The $\Phi - \xi$ potential may be written

$$\begin{aligned} V(\Phi,\xi) &= \frac{\tilde{\lambda}}{2}(\Phi^\dagger\Phi)^2 + \tilde{m}^2_\Phi \Phi^\dagger\Phi - F m^2_{Mix}[\Phi^\dagger\xi + h.c.] \\ &= \frac{\tilde{\lambda}}{2}\left(\Phi^\dagger\Phi - \frac{f^2_{tc}}{2}\right)^2 - F m^2_{Mix}[\Phi^\dagger\xi + h.c.] + const. \end{aligned} \tag{B.23}$$

where, $f_{tc} = -2\tilde{m}^2_\Phi/\tilde{\lambda}$. Requiring the minimum of the potential to occur at (B.22), we see that

$$\left.\frac{\partial V}{\partial f}\right|_{\langle\Phi\rangle,\langle\xi\rangle} = 0 \Rightarrow \frac{\tilde{\lambda}}{2} f(f^2 - f^2_{tc}) - \sqrt{2} m^2_{Mix} F = 0 \tag{B.24}$$

Using Eq. (B.24) to eliminate f^2_{tc} in favor of f^2 and m^2_{Mix}, the potential can be rewritten as

$$\begin{aligned} V(\Phi,\xi) &= \frac{\tilde{\lambda}}{2}\left(\Phi^\dagger\Phi - \frac{f^2}{2} + \frac{\sqrt{2}m^2_{Mix}F}{\tilde{\lambda}f}\right)^2 - F m^2_{Mix}[\Phi^\dagger\xi + h.c.] + const. \\ &= \frac{\tilde{\lambda}}{2}\left(\Phi^\dagger\Phi - \frac{f^2}{2}\right)^2 + \frac{\sqrt{2}m^2_{Mix}F}{f}\left|\Phi - \frac{f}{\sqrt{2}}\xi\right|^2 + const.\ , \end{aligned} \tag{B.25}$$

[4] Note that the value of F here differs from that in the Top Triangle Moose model, Eq. (3.4) since there electroweak symmetry breaking occurs collectively through the symmetry breaking encoded through *both* Σ_{01} and Σ_{12}.

which is precisely the form found in [125].

From this we find

$$M_{\Pi}^2 = \sqrt{2} m_{Mix}^2 \frac{v^2}{Ff} \ , \tag{B.26}$$

and, using Eqs. (B.11) and (B.20),

$$M_{\Pi}^2 = 8\pi v m_t \cdot \left(\frac{c_1}{2}\right) \cdot \eta \cdot \frac{\cos\omega}{\sin^2\omega} \ . \tag{B.27}$$

Note that this leading contribution to the top-pion masses yields *degenerate* charged- and neutral-top-pions. The same potential also yields the top-higgs mass M_{H_t},

$$M_{H_t}^2 \ = \ \tilde{\lambda} f^2 + \frac{\sqrt{2} m_{Mix}^2 F}{f} = 4m_t^2 + M_{\Pi}^2 \cos^2\omega \ , \tag{B.28}$$

where the form of the relation between M_{H_t}, M_{Π}, and $\cos\omega$ is fixed from the form of the potential [125], and the relation between $\tilde{\lambda}$ and m_t is fixed in the NJL approximation [96].

Note that the TC2 theory in the NJL limit is specified primarily by four parameters: g_t, Λ, η, and F. Physical quantities will only depend on these four parameters, up to coefficients in the chiral Lagrangian (such as c_1) of order 1. Using Eqs. (B.12), (B.22), and (B.27), we will trade the parameters g_t, Λ, η, and F for m_t, v, $\sin\omega$, and M_{Π}.

B.1.4 Constraints from ΔT

The physics giving rise to the top-quark mass violates custodial isospin, causing deviations in the low-energy parameter $\Delta\rho = \alpha\Delta T$. Consider the Lagrangian shown in Eq. (B.4). The Yukawa interaction between the composite Higgs Φ and the top-quark gives rise to the usual top-quark mass dependent contribution – just as in the standard model. The last two terms

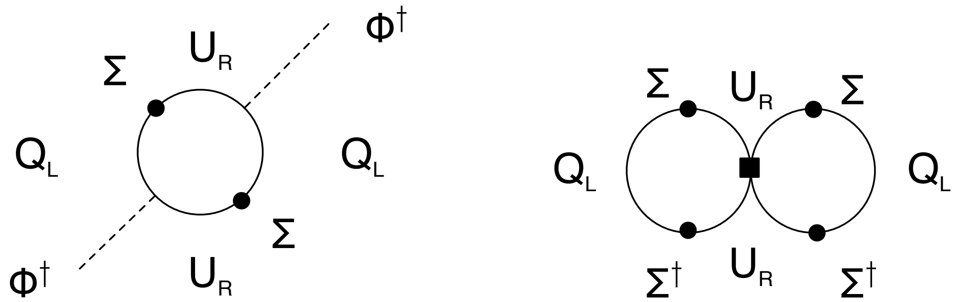

Figure B.2: Diagrams corresponding to the two leading contributions to $\alpha\Delta T$ in the TC2 model. The diagram on the left gives rise to the operator shown in Eq. (B.29). The diagram on the right arises from the four-technifermion operator shown in Eq. (B.32). The small black circles in these diagrams represent the dynamical technifermion mass arising from technicolor chiral symmetry breaking, as parameterized by the field Σ in the chiral Lagrangian of Eq. (B.14).

in this Lagrangian, the Yukawa interaction between the technifermions and the composite Higgs and the four-technifermion operator, give rise to new contributions which we consider below.

Consider first the technifermion Yukawa coupling. This operator violates custodial isospin by one unit, $\Delta I = 1$, and therefore the leading contribution to $\alpha\Delta T$ arises through *two* insertions of this operator as shown in left-hand panel of Fig. B.2. This diagram yields an operator of the form

$$\frac{c_T}{(4\pi)^2}\mathrm{tr}[\mathcal{M}^\dagger(D^\mu\Sigma)\mathcal{M}^\dagger(D_\mu\Sigma)] \ , \tag{B.29}$$

where, consistent with NDA [296, 297, 180], the constant c_T is expected to be of order 1. Computing the effect of this operator on the W and Z masses, we find

$$\alpha|\Delta T| = \frac{2|c_T|\eta^2 m_t^2}{(4\pi v)^2} \ , \tag{B.30}$$

or, alternatively, rewriting the dependence on η in terms of M_Π^2, we find

$$\alpha|\Delta T| = \frac{|c_T|}{2} \cdot \left(\frac{2}{|c_1|}\right)^2 \cdot \frac{1}{\cos^2\omega}\left(\frac{M_\Pi \sin\omega}{4\pi v}\right)^4 \; . \tag{B.31}$$

If we require $|\Delta T| \lesssim 0.5$, we find from Eq. (B.30) that $\eta \lesssim 0.6$. The equivalent constraint, in terms of M_Π, from Eq. (B.31) is shown as the red solid line in Fig. B.3. This is a rather weak upper bound, phenomenologically speaking. Theoretically, it is still an interesting bound because it derives directly from the Yukawa coupling operator in the low-energy chiral expansion that also gives rise to M_Π withough any dependence on the details of technicolor dynamics at high energies.

On the other hand, since the ETC interaction between the top quark and technifermions in Eq. (B.1) couples to both the left-handed current $\bar\psi_{L0}\gamma^\mu Q_L$ and right-handed current $\bar t_{R2}\gamma^\mu U_R$, it is natural to expect that there are ETC gauge bosons that couple to U_R with the same strength. The exchange of such an ETC boson will give rise to the $\Delta I = 2$ operator,

$$\frac{\eta g_t^2}{\Lambda^2}(\bar U_R\gamma^\mu U_R)(\bar U_R\gamma_\mu U_R) \; , \tag{B.32}$$

which can contribute directly to ΔT. In particular, the diagram on the right of Fig. B.2 yields the operator

$$c_{T'} \cdot \frac{\eta g_t^2}{\Lambda^2} \cdot F^4 \left(\mathrm{Tr}\left[\Sigma^\dagger D_\mu \Sigma \begin{pmatrix} 1 & 0 \\ 0 & 0 \end{pmatrix} \right] \right)^2 \; , \tag{B.33}$$

where $c_{T'}$ is an unknown chiral coefficient of order 1.[5] The correction to $|\Delta T|$ is

$$\alpha|\Delta T| = \frac{4|c_{T'}|}{v^2} \cdot \frac{\eta g_t^2 F^4}{\Lambda^2} \ . \tag{B.34}$$

To evaluate this expression, we use Eq. (B.27) to rephrase η in terms of M_Π, apply Eq. (B.22) to eliminate F, and approximate g_t^2 by g_t^{*2} as in Eq. (B.9) [neglecting the term of order η^2]:

$$\alpha|\Delta T| = \frac{4\pi}{N_C} \cdot |c_{T'}| \cdot \left(\frac{2}{|c_1|}\right) \cdot \sin^2\omega \cos^3\omega \cdot \frac{vM_\Pi^2}{m_t\Lambda^2} \ . \tag{B.35}$$

This constraint is represented by the blue long-dashed line in Fig. B.3.

Figure B.3 summarizes the approximate constraints on the $\sin\omega - M_\Pi$ plane that arise from limits on $\alpha|\Delta T|$ as discussed above. The pink-shaded regions are excluded; the area above the solid red line is excluded due to the impact of the technifermion Yukawa coupling and the area to the left of the blue long-dashed line is excluded by the effects of ETC gauge boson exchange. In the left-hand pane, a few dotted curves for different values of η are shown to indicate how that dimensionless parameter varies with $\sin\omega$ and M_Π; in the right-hand pane, a few nearly-horizontal purple contours corresponding to several values of the top-Higgs mass are shown.

B.1.5 Top-Pion Mass Splitting

Finally, we consider the mass splitting between the charged and neutral top-pions. The leading contribution comes from the same diagram that produces the operator in Eq. (B.29). In particular, in addition to the derivative operator discussed above, these diagrams give rise

[5] In fact, it is exactly equal to 1 in the vacuum insertion approximation.

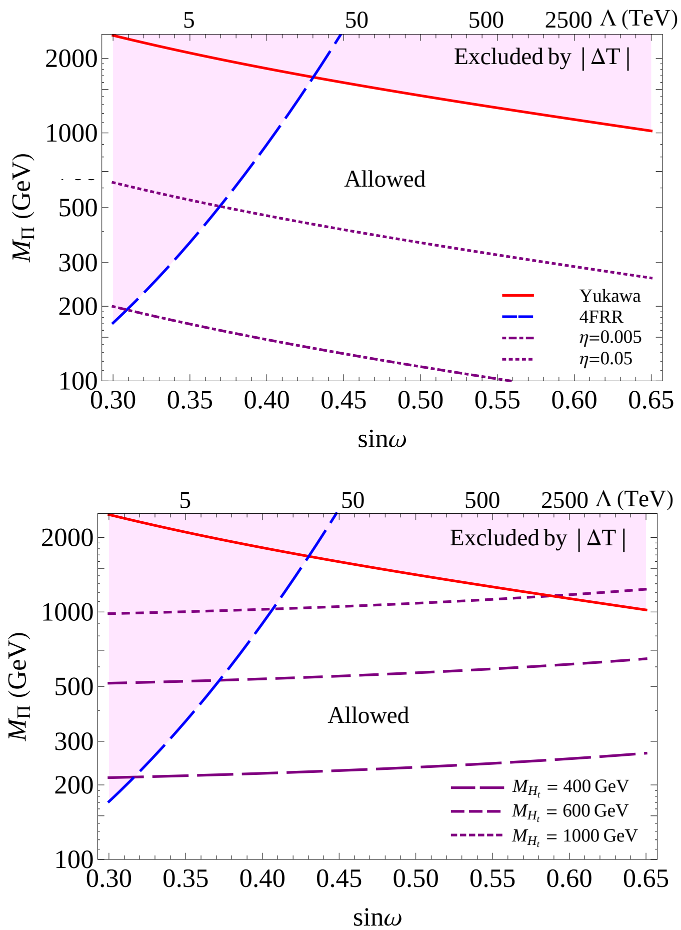

Figure B.3: Top: Approximate constraints on M_Π and $\sin\omega$ in the TC2 model in the NJL approximation coming from bounds on $\alpha|\Delta T|$. The constraints shown arise from taking $|\Delta T| < 0.5$ and assuming that $c_1/2 = c_T = c_{T'} = 1$; the shaded pink region is excluded. The red solid line shows the bound arising from the operator in Eq. (B.31) (red line); the blue long-dashed line shows the bound from Eq. (B.34) (blue dashed line). The dotted purple curves on the top pane depict contours of constant η from Eq.(B.4); the dashed purple curves in the bottom pane are contours of constant top-Higgs mass from Eq. (B.28).

to the operators

$$\tilde{\lambda}_4 F^2 \Phi^\dagger \xi \xi^\dagger \Phi + \tilde{\lambda}_{5'} F^2 \left(\Phi^\dagger \xi \Phi^\dagger \xi + \xi^\dagger \Phi \xi^\dagger \Phi \right) \tag{B.36}$$

where, using NDA, the parameters λ_i are

$$\tilde{\lambda}_i = c_i (\eta \tilde{g}_t)^2 \ , \tag{B.37}$$

and the c_i are parameters of order 1. Comparing the operators in Eq. (B.36) with those in the two-Higgs doublet model (ξ transforms precisely as a Higgs, but with fixed magnitude) we see that these terms each give rise to mass splittings of order

$$\Delta M_\Pi^2 = M_{\Pi^+}^2 - M_{\Pi^0}^2 \propto \tilde{\lambda}_i v^2 \ . \tag{B.38}$$

From the relations derived previously, we find

$$\Delta M_\Pi^2 \propto c_i \left(\frac{2}{c_1}\right)^2 \cdot \frac{M_\Pi^4}{32\pi^2 v^2} \cdot \frac{\sin^2\omega}{\cos^2\omega} \ , \tag{B.39}$$

and therefore, ignoring factors of order one

$$\frac{\Delta M_\Pi}{M_\Pi} \propto \left(\frac{M_\Pi}{6.2\,\mathrm{TeV}}\right)^2 \cdot \frac{\sin^2\omega}{\cos^2\omega} \ . \tag{B.40}$$

From this we see that, for the allowed range of M_Π, the mass-splitting between the charged top-pion and the neutral top-pion is typically very small, and always less than O(10%). For M_{Π_t} of order 200 GeV, the mass splitting is of order 100 MeV.

Based on this analysis, it is clear that the classic TC2 dynamics do not lead to large splittings between the top and neutral top-pions. A model with a large splitting must contain additional isospin violation, beyond the minimum required to generate the top quark's mass.

B.2 Alternative Fermion Couplings and Constraints from $b \to s\gamma$

The couplings of the top-pion and top-Higgs to fermions are model dependent. In this appendix we discuss the relation between the assumptions about the flavor structure that are used in chapter 3 and the simpler form of the fermion couplings used in [119].

The form for the light fermion masses given in [119] is

$$\mathcal{L} \;=\; M_D \left[\epsilon_L \bar{\psi}_{L0} \Sigma_{01} \psi_{R1} + \bar{\psi}_{R1} \psi_{L1} + \bar{\psi}_{L1} \Sigma_{12} \begin{pmatrix} \epsilon_{uR} & 0 \\ 0 & \epsilon_{dR} \end{pmatrix} \begin{pmatrix} u_{R2} \\ d_{R2} \end{pmatrix} \right]. \tag{B.41}$$

We have denoted the Dirac mass that sets the scale of the heavy fermion masses as M_D. Here, ϵ_L is a parameter that describes the degree of delocalization of the left handed fermions and is assumed to be universal for the light quark generations and the leptons. All the flavor violation for the light fermions is then encoded in the last term; the delocalization parameters for the right handed fermions, ϵ_{fR}, which can be adjusted to realize the masses and mixings of the up and down type fermions. The mass of the top quark arises from similar terms with a unique left-handed delocalization parameter ϵ_{tL} and also from a unique Lagrangian term reflecting the coupling of the top-Higgs to the top quark:

$$\mathcal{L}_{top} = -\lambda_t \bar{\psi}_{L0}\, \Phi\, t_R + h.c. \tag{B.42}$$

If this simple picture for the fermion masses is correct, then top-color provides mass only to the top-quark while the three-site/technicolor sector provides mass to both the top-quark and all lighter-quarks. In this case, insofar as the third-generation quarks are concerned, the

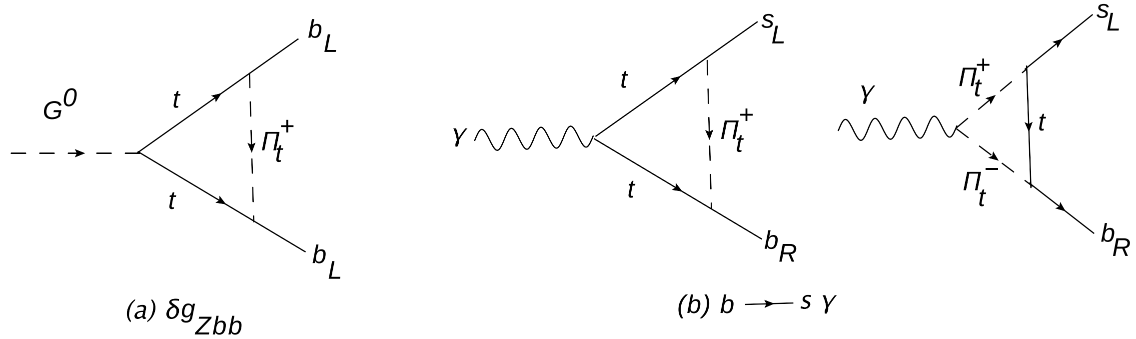

Figure B.4: Loop corrections to δg_{Zbb} and $b \to s\gamma$ arising from exchange of charged top-pions.

pattern of top-pion couplings is the same as the pattern of charged-Higgs couplings in "type-II" two-Higgs-doublet models [158] – with the top-Higgs playing the role of the Higgs-doublet coupling to top-quark and the technicolor-sector playing the role of the Higgs-doublet giving mass to the bottom.

$$\begin{aligned}
\mathcal{L}_{yukawa} &= (2\sqrt{2}G_F)^{1/2} \sum_{i,j} \bar{u}_i(\cot\omega\, m_{ui} V_{ij} P_L + \tan\omega\, V_{ij} m_{dj} P_R) d_j \Pi^+ + h.c. \\
&\supset (2\sqrt{2}G_F)^{1/2} \left[m_t V_{tb} \cot\omega\, \bar{t}_R b_L + m_t V_{ts} \cot\omega\, \bar{t}_R s_L + m_b V_{tb} \tan\omega\, \bar{t}_L b_R\right] \Pi^+ \\
&\quad + h.c. \qquad \text{(B.43)}
\end{aligned}$$

These couplings imply significant corrections from charged top-pion exchange to the processes $Z \to \bar{b}b$ and $b \to s\gamma$, as illustrated in Fig. B.4. The correction to the process $Z \to \bar{b}b$ comes predominantly from the first term in Eq. (B.43) – and is characteristic of top color theories [203]. As explained in [125], the top-color corrections to $Z \to \bar{b}b$ can be compensated for by an adjustment of the top-quark delocalization parameter ϵ_{tL}.

The potential corrections to $b \to s\gamma$, however, are more problematic. These arise from vertices involving both the second interaction in Eq. (B.43) [which is necessary since the process involves the strange-quark] and either the first or third one. These contributions are

Table B.1: Lower bound on $M_{\Pi_t^+}$ from $b \to s\gamma$ assuming the fermion couplings in Eq. (B.43).

$\sin\omega$	0.16	0.19	0.23	0.26	0.30	0.34	0.40	0.46
$M_{\Pi_t^+}(GeV)$	754	685	617	551	500	440	396	363

$\sin\omega$	0.53	0.60	0.70	0.83	0.96
$M_{\Pi_t^+}(GeV)$	332	311	289	270	254

particularly severe[6] in the case of small $\sin\omega$. Translating the bounds in two-Higgs models to the case at hand [298], we find that the couplings of Eq.(B.43) imply the stringent lower bounds on the charged top-pion shown in Table B.1. Charged top-pion masses of this order, and hence neutral pion and top-Higgs masses which are expected to be of the same order, would be very difficult to observe at the LHC. As discussed in the text, this constraint does not apply if left-handed mixing is purely in the up-quark sector.

B.3 Formulas for the top-Higgs decay widths

The couplings of the top-Higgs, along with its decay widths to the relevant channels WW, ZZ, $t\bar{t}$, $\Pi_t^{\pm}W^{\mp}$, $\Pi_t^0 Z$, $\Pi_t^+\Pi_t^-$, and $\Pi_t^0\Pi_t^0$, were given in Ref. [126]. For completeness, we reproduce the key formulas below.

For the limit-setting in Sec. 3.5, we compute the top-Higgs production cross section with the aid of the 7 TeV LHC SM Higgs cross sections in the gluon fusion and VBF modes from

[6] The role of β in type-II two-Higgs-doublet models is played here by ω. In two-Higgs models one often considers $\tan\beta \simeq m_t/m_b \gg 1$ – while here, we are mostly interested in $\tan\omega = f/F \lesssim 1$.

Ref. [204, 299]. To the extent that the narrow-width approximation is valid, we can write

$$\begin{aligned} \frac{\sigma(pp \to H_t \to WW)}{\sigma(pp \to H_{\rm SM} \to WW)} &= \frac{\left[\sigma_{gg}(pp \to H_t) + \sigma_{\rm VBF}(pp \to H_t)\right] {\rm BR}(H_t \to WW)}{\left[\sigma_{gg}(pp \to H_{\rm SM}) + \sigma_{\rm VBF}(pp \to H_{\rm SM})\right] {\rm BR}(H_{\rm SM} \to WW)} \\ &\simeq \frac{\frac{1}{\sin^2\omega}\sigma_{gg}(pp \to H_{\rm SM}) + \sin^2\omega\, \sigma_{\rm VBF}(pp \to H_{\rm SM})}{\sigma_{gg}(pp \to H_{\rm SM}) + \sigma_{\rm VBF}(pp \to H_{\rm SM})} \\ &\quad \times \frac{{\rm BR}(H_t \to WW)}{{\rm BR}(H_{\rm SM} \to WW)}, \end{aligned} \tag{B.44}$$

and analogously for the ZZ final state [note that ${\rm BR}(H_t \to ZZ)/{\rm BR}(H_{\rm SM} \to ZZ) = {\rm BR}(H_t \to WW)/{\rm BR}(H_{\rm SM} \to WW)$]. The approximation in the second line is exact insofar as (i) the QCD corrections to Higgs production are the same for the top-Higgs and the SM Higgs and (ii) the efficiencies of the inclusive LHC Higgs searches are the same for events arising from gluon fusion and VBF.

For decays to a top-pion and a gauge boson,

$$\begin{aligned} \Gamma(H_t \to \Pi_t^{\pm} W^{\mp}) &= \frac{\cos^2\omega}{8\pi v^2} M_{H_t}^3 \beta_W^3, \\ \Gamma(H_t \to \Pi_t^0 Z) &= \frac{\cos^2\omega}{16\pi v^2} M_{H_t}^3 \beta_Z^3, \end{aligned} \tag{B.45}$$

where

$$\beta_V^2 \equiv \left[1 - \frac{(M_{\Pi_t} + M_V)^2}{M_{H_t}^2}\right]\left[1 - \frac{(M_{\Pi_t} - M_V)^2}{M_{H_t}^2}\right]. \tag{B.46}$$

For decays to two top-pions,

$$\begin{aligned} \Gamma(H_t \to \Pi_t^+ \Pi_t^-) &= \frac{\lambda_{H\Pi^+\Pi^-}^2}{16\pi M_{H_t}} \sqrt{1 - \frac{4M_{\Pi_t^+}^2}{M_{H_t}^2}}, \\ \Gamma(H_t \to \Pi_t^0 \Pi_t^0) &= \frac{\lambda_{H\Pi^0\Pi^0}^2}{32\pi M_{H_t}} \sqrt{1 - \frac{4M_{\Pi_t^0}^2}{M_{H_t}^2}}, \end{aligned} \tag{B.47}$$

where

$$
\begin{aligned}
\lambda_{H\Pi^+\Pi^-} &= \frac{1}{v\sin\omega}\left[M_{H_t}^2\cos^2\omega - M_{\Pi_t^+}^2 + 2M_{\Pi_t^+}^2\sin^2\omega\right], \\
\lambda_{H\Pi^0\Pi^0} &= \frac{1}{v\sin\omega}\left[M_{H_t}^2\cos^2\omega - M_{\Pi_t^+}^2 + 2M_{\Pi_t^0}^2\sin^2\omega\right].
\end{aligned} \tag{B.48}
$$

For decays to top-quark pairs,

$$
\Gamma(H_t \to t\bar{t}) = \frac{3m_t^2}{8\pi v^2\sin^2\omega} M_{H_t}\left(1 - \frac{4m_t^2}{M_{H_t}^2}\right)^{3/2} . \tag{B.49}
$$

By comparison, the width to gauge-bosons is suppressed by $\sin^2\omega$:

$$
\begin{aligned}
\Gamma(H_t \to W^+W^-) &= \frac{M_{H_t}^3\sin^2\omega}{16\pi v^2}\sqrt{1-x_W}\left[1 - x_W + \frac{3}{4}x_W^2\right], \\
\Gamma(H_t \to ZZ) &= \frac{M_{H_t}^3\sin^2\omega}{32\pi v^2}\sqrt{1-x_Z}\left[1 - x_Z + \frac{3}{4}x_Z^2\right],
\end{aligned} \tag{B.50}
$$

where $x_V = 4M_V^2/M_{H_t}^2$.

Appendix C

Uncertainty of Intrinsic Width Measurement

The uncertainty in the intrinsic width of the resonance plays a key role in the estimation of the uncertainties in D_{col}, the variable we propose to distinguish a color-octet and a color-singlet state. In this section we extract the uncertainty of the intrinsic width from a measurement of the total width and a knowledge of the systematic uncertainties in measuring that width. The systematic uncertainties relevant to width measurement are the di-jet mass resolution and the uncertainty in the di-jet mass resolution; we model them to have a Gaussian distribution and ignore correlations between them.

The standard deviation of the observed invariant mass distribution (σ_T) is related to the standard deviation of the intrinsic width ($\sigma_\Gamma \simeq \Gamma/2.35$ assuming a Gaussian distribution) and that of the detector mass resolution (M_{res}) by

$$\sigma_\Gamma = \sqrt{\sigma_T^2 - M_{\mathrm{res}}^2}\,. \tag{C.1}$$

This implies that

$$(\Delta\sigma_\Gamma)^2 = \left(\frac{\sigma_T \Delta\sigma_T}{\sqrt{\sigma_T^2 - M_{\mathrm{res}}^2}}\right)^2 + \left(\frac{M_{\mathrm{res}}\Delta M_{\mathrm{res}}}{\sqrt{\sigma_T^2 - M_{\mathrm{res}}^2}}\right)^2\,, \tag{C.2}$$

or

$$\left(\frac{\Delta\sigma_\Gamma}{\sigma_\Gamma}\right)^2 = \left(1+\frac{M_{\rm res}^2}{\sigma_\Gamma^2}\right)^2\left(\frac{\Delta\sigma_T}{\sigma_T}\right)^2 + \left(\frac{M_{\rm res}^2}{\sigma_\Gamma^2}\right)^2\left(\frac{\Delta M_{\rm res}}{M_{\rm res}}\right)^2 , \tag{C.3}$$

where Eq. (C.1) was used to obtain Eq. (C.3).

For N observed signal events, where N is sufficiently large, the uncertainty of the observed width $\Delta\sigma_T$ is given by $\sigma_T/\sqrt{2(N-1)}$ [300]. So Eq. (C.3) leads to

$$\frac{\Delta\sigma_\Gamma}{\sigma_\Gamma} = \sqrt{\left[1+\left(\frac{M_{\rm res}}{\sigma_\Gamma}\right)^2\right]^2\frac{1}{2(N-1)} + \left(\frac{M_{\rm res}}{\sigma_\Gamma}\right)^4\left(\frac{\Delta M_{\rm res}}{M_{\rm res}}\right)^2}, \tag{C.4}$$

where $\Delta\sigma_\Gamma/\sigma_\Gamma = \Delta\Gamma/\Gamma$. Note that for large N, the above expression simplifies to

$$\frac{\Delta\Gamma}{\Gamma} = \left(\frac{M_{\rm res}}{\sigma_\Gamma}\right)^2\left(\frac{\Delta M_{\rm res}}{M_{\rm res}}\right) = \left(\frac{M_{\rm res}}{\Gamma/2.35}\right)^2\left(\frac{\Delta M_{\rm res}}{M_{\rm res}}\right) . \tag{C.5}$$

This expression shows that the uncertainty in the intrinsic width is inversely proportional to $\Gamma/M_{\rm res}$ which implies that the uncertainty in the intrinsic width is small (large) when the intrinsic width is large (small).

Appendix D

Curves with Constant D_{col}

In this section we present the relationship between the values of color discriminant variable and the input parameters of the models; namely, $\frac{g_u^2}{g_u^2+g_d^2}$, $\frac{\sigma_{t\bar{t}}}{\sigma_{jj}}$, and $\frac{\sigma_{b\bar{b}}}{\sigma_{jj}}$, without taking uncertainties into account. This provides a set of "benchmarks" illustrating how a set of curves for fixed D_{col} shifts with changing up ratio and mass, and how well each relevant observable must be measured to distinguish colorons from Z' bosons.

In each subplot of Fig. D.1 and D.2, we show models of colorons and leptophobic Z''s leading to the same (here, exact) value of D_{col}. Curves corresponding to three illustrative values of the experimentally inaccessible up-ratio $\frac{g_u^2}{g_u^2+g_d^2}$ are displayed; we used the minimum (0) and maximum (1) values of the ratio, along with an intermediate value (0.5). The sets of plots for resonances of masses 3.0 TeV and 3.5 TeV are shown in Fig. D.1 (top and bottom panels, respectively), while similar plots for 4.0 TeV and 4.5 TeV are shown in Fig. D.2.

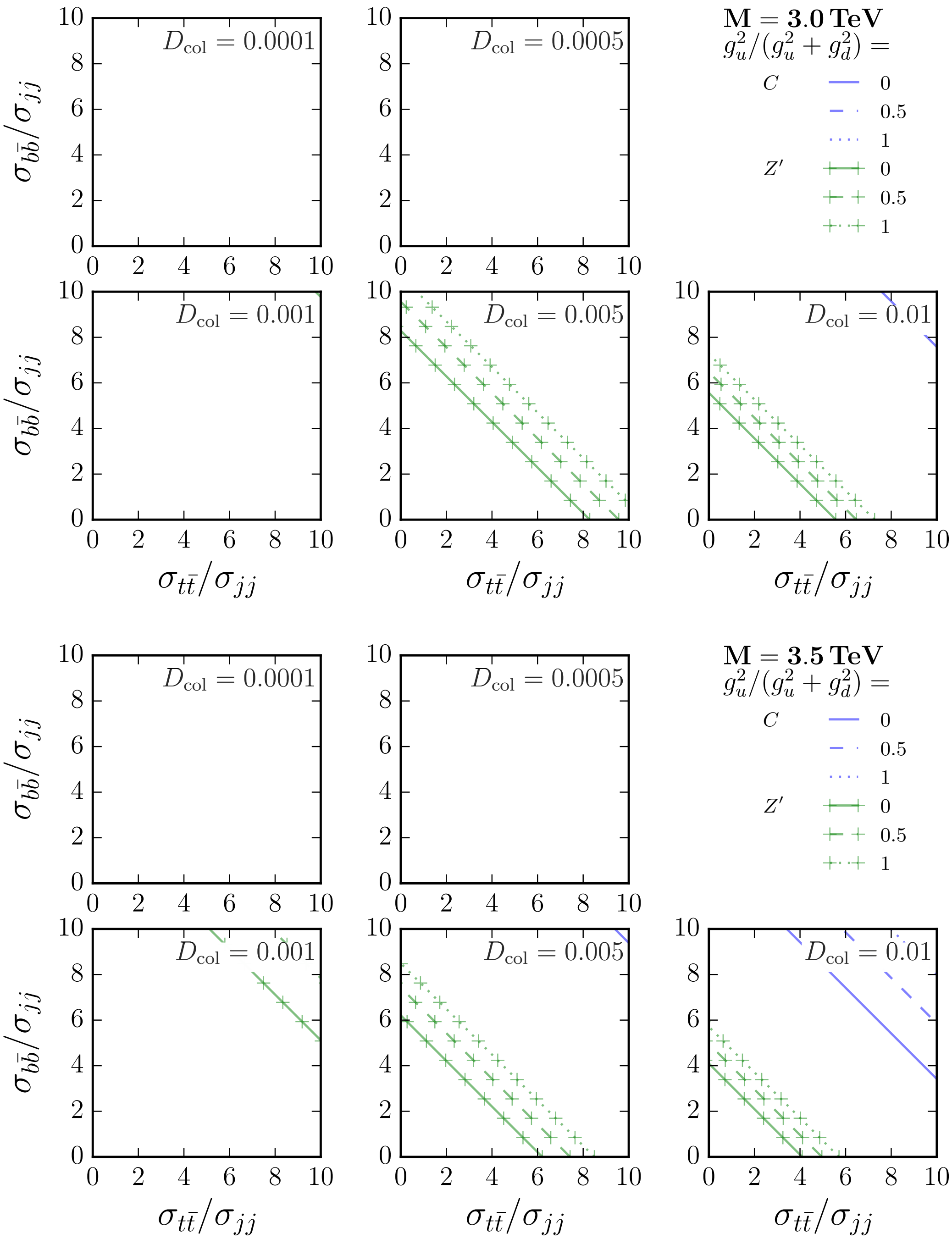

Figure D.1: The region of parameter space for the colorons (in blue) and Z' bosons (in green) that is consistent with measurements of the ratios $\sigma_{t\bar{t}}$ and $\sigma_{b\bar{b}}$, the mass, cross section, and $D_{\rm col}$ at the LHC with $\sqrt{s} = 14\,\text{TeV}$. The value of $D_{\rm col}$ in a given plot is listed at upper right. The three blue (green) lines in a given plot correspond to colorons (Z' bosons) with three different values of the experimentally inaccessible coupling ratio (the $g_u^2/(g_u^2+g_d^2)$). These plots illustrate the measurement precision in $\sigma_{t\bar{t}}$ and $\sigma_{b\bar{b}}$ that is required to distinguish between the coloron and the leptophobic Z'. The set of plots for resonances with a mass of 3.0 TeV (3.5 TeV) is in the top (bottom) panel.

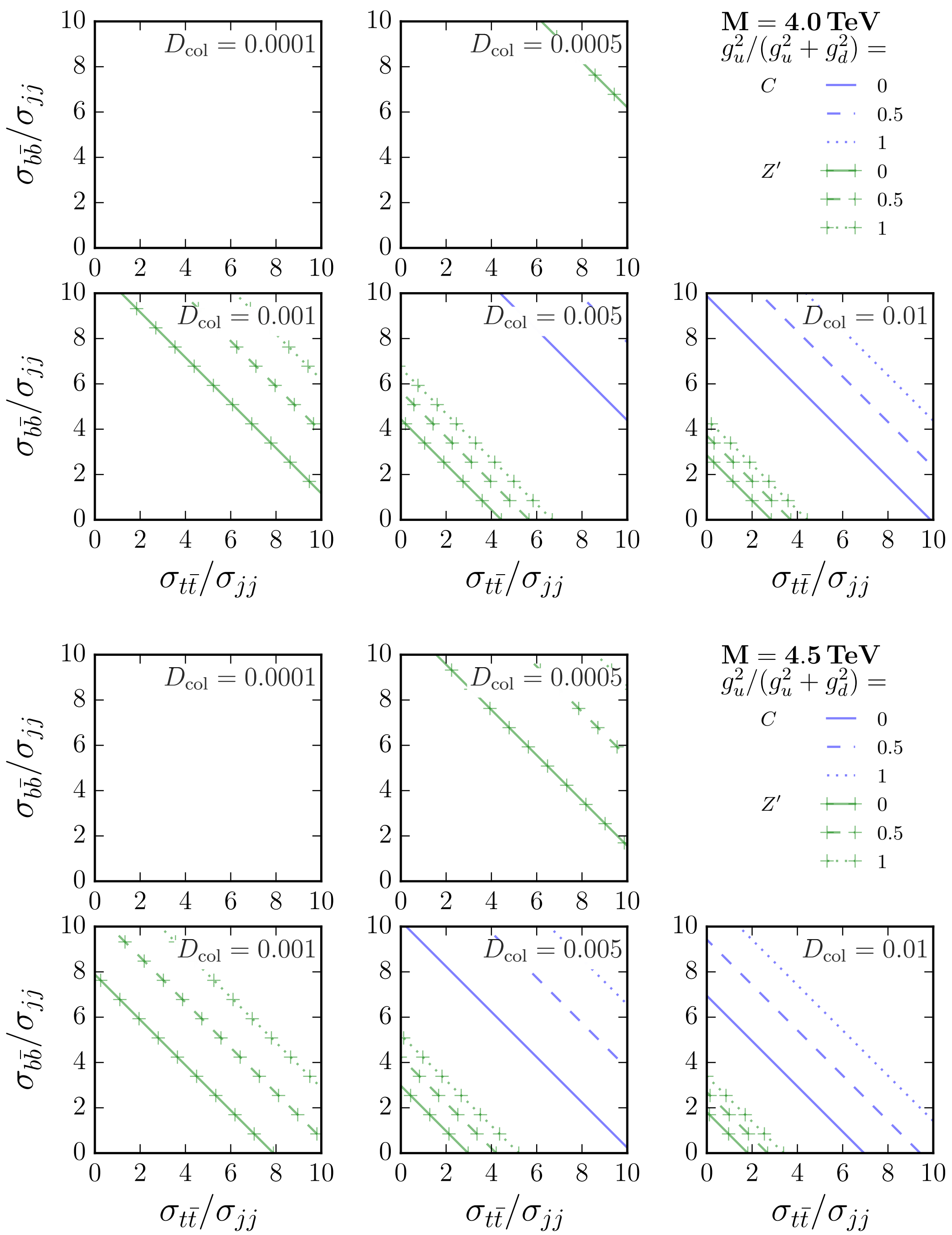

Figure D.2: Same as Fig. D.1, but for 4.0 TeV (top panel) and 4.5 TeV (bottom panel) resonances.

BIBLIOGRAPHY

BIBLIOGRAPHY

[1] R. S. Chivukula, P. Ittisamai, E. H. Simmons, and J. Ren, *Technipion Limits from LHC Higgs Searches*, Phys.Rev. **D84** (2011) 115025, `arXiv:1110.3688 [hep-ph]`. *Erratum: ibid.* **D85** (2012) 119903.

[2] R. S. Chivukula, P. Ittisamai, J. Ren, and E. H. Simmons, *Technicolor in the LHC Era*, `arXiv:1202.1505 [hep-ph]`.

[3] R. S. Chivukula, P. Ittisamai, E. H. Simmons, B. Coleppa, H. E. Logan, et al., *Discovering Strong Top Dynamics at the LHC*, Phys.Rev. **D86** (2012) 095017, `arXiv:1207.0450 [hep-ph]`.

[4] A. Atre, R. S. Chivukula, P. Ittisamai, E. H. Simmons, and J.-H. Yu, *Probing Color Octet Couplings at the Large Hadron Collider*, Phys.Rev. **D86** (2012) 054003, `arXiv:1206.1661 [hep-ph]`.

[5] E. H. Simmons, A. Atre, R. S. Chivukula, P. Ittisamai, N. Vignaroli, et al., *Coloron Models and LHC Phenomenology*, `arXiv:1304.0255 [hep-ph]`.

[6] A. Atre, R. S. Chivukula, P. Ittisamai, and E. H. Simmons, *Distinguishing Color-Octet and Color-Singlet Resonances at the Large Hadron Collider*, Phys.Rev. **D88** (2013) 055021, `arXiv:1306.4715 [hep-ph]`.

[7] R. S. Chivukula, P. Ittisamai, and E. H. Simmons, *Distinguishing Flavor Non-universal Colorons from Z' Bosons at the LHC*, `arXiv:1406.2003 [hep-ph]`.

[8] R. Feynman, *A Relativistic cutoff for classical electrodynamics*, Phys.Rev. **74** (1948) 939–946.

[9] J. S. Schwinger, *On Quantum electrodynamics and the magnetic moment of the electron*, Phys.Rev. **73** (1948) 416–417.

[10] J. Schwinger, *On Radiative Corrections to Electron Scattering*, Phys.Rev. **75** (1949) 898–899.

[11] S.-I. Tomonaga and J. Oppenheimer, *On Infinite Field Reactions in Quantum Field Theory*, Phys.Rev. **74** (1948) 224–225.

[12] F. Dyson, *The Radiation theories of Tomonaga, Schwinger, and Feynman*, Phys.Rev. **75** (1949) 486–502.

[13] S. Glashow, *Partial Symmetries of Weak Interactions*, Nucl.Phys. **22** (1961) 579–588.

[14] S. Weinberg, *A Model of Leptons*, Phys.Rev.Lett. **19** (1967) 1264–1266.

[15] A. Salam, *Weak and Electromagnetic Interactions*, Conf.Proc. **C680519** (1968) 367–377.

[16] G. 't Hooft and M. Veltman, *Regularization and Renormalization of Gauge Fields*, Nucl.Phys. **B44** (1972) 189–213.

[17] Particle Data Group Collaboration, K. Olive et al., *Review of Particle Physics*, Chin.Phys. **C38** (2014) 090001.

[18] C.-N. Yang and R. L. Mills, *Conservation of Isotopic Spin and Isotopic Gauge Invariance*, Phys.Rev. **96** (1954) 191–195.

[19] H. Fritzsch, M. Gell-Mann, and H. Leutwyler, *Advantages of the Color Octet Gluon Picture*, Phys.Lett. **B47** (1973) 365–368.

[20] O. Greenberg, *Spin and Unitary Spin Independence in a Paraquark Model of Baryons and Mesons*, Phys.Rev.Lett. **13** (1964) 598–602.

[21] D. J. Gross and F. Wilczek, *Ultraviolet Behavior of Nonabelian Gauge Theories*, Phys.Rev.Lett. **30** (1973) 1343–1346.

[22] H. D. Politzer, *Reliable Perturbative Results for Strong Interactions?*, Phys.Rev.Lett. **30** (1973) 1346–1349.

[23] S. R. Coleman and E. J. Weinberg, *Radiative Corrections as the Origin of Spontaneous Symmetry Breaking*, Phys.Rev. **D7** (1973) 1888–1910.

[24] Y. Nambu, *Axial vector current conservation in weak interactions*, Phys.Rev.Lett. **4** (1960) 380–382.

[25] J. Goldstone, *Field Theories with Superconductor Solutions*, Nuovo Cim. **19** (1961) 154–164.

[26] J. Goldstone, A. Salam, and S. Weinberg, *Broken Symmetries*, Phys.Rev. **127** (1962) 965–970.

[27] F. Englert and R. Brout, *Broken Symmetry and the Mass of Gauge Vector Mesons*, Phys.Rev.Lett. **13** (1964) 321–323.

[28] P. W. Higgs, *Broken Symmetries and the Masses of Gauge Bosons*, Phys.Rev.Lett. **13** (1964) 508–509.

[29] P. W. Higgs, *Broken symmetries, massless particles and gauge fields*, Phys.Lett. **12** (1964) 132–133.

[30] G. Guralnik, C. Hagen, and T. Kibble, *Global Conservation Laws and Massless Particles*, Phys.Rev.Lett. **13** (1964) 585–587.

[31] P. W. Anderson, *Plasmons, Gauge Invariance, and Mass*, Phys.Rev. **130** (1963) 439–442.

[32] D. Ross and M. Veltman, *Neutral Currents and the Higgs Mechanism*, Nucl.Phys. **B95** (1975) 135.

[33] ATLAS Collaboration, *ATLAS: Detector and physics performance technical design report. Volume 1*, Tech. Rep. CERN-LHCC-99-14, CERN, 1999. `http://alice.cern.ch/format/showfull?sysnb=0317330`.

[34] ATLAS Collaboration, *ATLAS: Detector and physics performance technical design report. Volume 2*, Tech. Rep. CERN-LHCC-99-15, CERN, 1999.

[35] CMS Collaboration, G. Bayatian et al., *CMS physics: Technical design report*, Tech. Rep. CERN-LHCC-2006-001, CERN, 2006. `http://cdsweb.cern.ch/record/922757`.

[36] CMS Collaboration, G. Bayatian et al., *CMS technical design report, volume II: Physics performance*, J.Phys. **G34** (2007) 995–1579.

[37] UA2 Collaboration, M. Banner et al., *Observation of Single Isolated Electrons of High Transverse Momentum in Events with Missing Transverse Energy at the CERN anti-p p Collider*, Phys.Lett. **B122** (1983) 476–485.

[38] UA2 Collaboration, P. Bagnaia et al., *Evidence for Z0 —> e+ e- at the CERN anti-p p Collider*, Phys.Lett. **B129** (1983) 130–140.

[39] UA1 Collaboration, G. Arnison et al., *Further Evidence for Charged Intermediate Vector Bosons at the SPS Collider*, Phys.Lett. **B129** (1983) 273–282.

[40] CDF Collaboration, F. Abe et al., *Observation of top quark production in $\bar{p}p$ collisions*, Phys.Rev.Lett. **74** (1995) 2626–2631, `arXiv:hep-ex/9503002 [hep-ex]`.

[41] D0 Collaboration, S. Abachi et al., *Observation of the top quark*, Phys.Rev.Lett. **74** (1995) 2632–2637, `arXiv:hep-ex/9503003 [hep-ex]`.

[42] DONUT Collaboration, K. Kodama et al., *Observation of tau neutrino interactions*, Phys.Lett. **B504** (2001) 218–224, `arXiv:hep-ex/0012035 [hep-ex]`.

[43] ALEPH Collaboration, DELPHI Collaboration, L3 Collaboration, OPAL Collaboration, SLD Collaboration, LEP Electroweak Working Group, SLD Electroweak Group, SLD Heavy Flavour Group Collaboration, S. Schael et al., *Precision electroweak measurements on the Z resonance*, Phys.Rept. **427** (2006) 257–454, `arXiv:hep-ex/0509008 [hep-ex]`.

[44] ATLAS Collaboration, G. Aad et al., *Observation of a new particle in the search for the Standard Model Higgs boson with the ATLAS detector at the LHC*, Phys.Lett. **B716** (2012) 1–29, `arXiv:1207.7214 [hep-ex]`.

[45] CMS Collaboration, S. Chatrchyan et al., *Observation of a new boson at a mass of 125 GeV with the CMS experiment at the LHC*, Phys.Lett. **B716** (2012) 30–61, `arXiv:1207.7235 [hep-ex]`.

[46] ATLAS Collaboration, G. Aad et al., *Measurements of Higgs boson production and couplings in diboson final states with the ATLAS detector at the LHC*, Phys.Lett. **B726** (2013) 88–119, `arXiv:1307.1427 [hep-ex]`.

[47] ATLAS Collaboration, G. Aad et al., *Measurement of Higgs boson production in the diphoton decay channel in pp collisions at center-of-mass energies of 7 and 8 TeV with the ATLAS detector*, `arXiv:1408.7084 [hep-ex]`.

[48] ATLAS Collaboration, G. Aad et al., *Measurements of fiducial and differential cross sections for Higgs boson production in the diphoton decay channel at $\sqrt{s} = 8$ TeV with ATLAS*, JHEP **1409** (2014) 112, `arXiv:1407.4222 [hep-ex]`.

[49] CMS Collaboration, V. Khachatryan et al., *Observation of the diphoton decay of the Higgs boson and measurement of its properties*, Eur.Phys.J. **C74** (2014) no. 10, 3076, `arXiv:1407.0558 [hep-ex]`.

[50] CMS Collaboration, S. Chatrchyan et al., *Evidence for the direct decay of the 125 GeV Higgs boson to fermions*, Nature Phys. **10** (2014) , arXiv:1401.6527 [hep-ex].

[51] CMS Collaboration, S. Chatrchyan et al., *Evidence for the 125 GeV Higgs boson decaying to a pair of τ leptons*, JHEP **1405** (2014) 104, arXiv:1401.5041 [hep-ex].

[52] CMS Collaboration, S. Chatrchyan et al., *Measurement of the properties of a Higgs boson in the four-lepton final state*, Phys.Rev. **D89** (2014) 092007, arXiv:1312.5353 [hep-ex].

[53] CMS Collaboration, S. Chatrchyan et al., *Measurement of Higgs boson production and properties in the WW decay channel with leptonic final states*, JHEP **1401** (2014) 096, arXiv:1312.1129 [hep-ex].

[54] B. Pontecorvo, *Mesonium and anti-mesonium*, Sov.Phys.JETP **6** (1957) 429.

[55] B. Pontecorvo, *Inverse beta processes and nonconservation of lepton charge*, Sov.Phys.JETP **7** (1958) 172–173.

[56] S. Bilenky, *The History of neutrino oscillations*, Phys.Scripta **T121** (2005) 17–22, arXiv:hep-ph/0410090 [hep-ph].

[57] WMAP Collaboration, D. Spergel et al., *First year Wilkinson Microwave Anisotropy Probe (WMAP) observations: Determination of cosmological parameters*, Astrophys.J.Suppl. **148** (2003) 175–194, arXiv:astro-ph/0302209 [astro-ph].

[58] G. Bertone, D. Hooper, and J. Silk, *Particle dark matter: Evidence, candidates and constraints*, Phys.Rept. **405** (2005) 279–390, arXiv:hep-ph/0404175 [hep-ph].

[59] WMAP Collaboration, D. Spergel et al., *Wilkinson Microwave Anisotropy Probe (WMAP) three year results: implications for cosmology*, Astrophys.J.Suppl. **170** (2007) 377, arXiv:astro-ph/0603449 [astro-ph].

[60] WMAP Collaboration, E. Komatsu et al., *Seven-Year Wilkinson Microwave Anisotropy Probe (WMAP) Observations: Cosmological Interpretation*, Astrophys.J.Suppl. **192** (2011) 18, arXiv:1001.4538 [astro-ph.CO].

[61] Planck Collaboration, P. Ade et al., *Planck 2013 results. XVI. Cosmological parameters*, Astron.Astrophys. (2014) , arXiv:1303.5076 [astro-ph.CO].

[62] G. F. Giudice, *Naturally Speaking: The Naturalness Criterion and Physics at the LHC*, `arXiv:0801.2562 [hep-ph]`.

[63] W. A. Bardeen, *On naturalness in the standard model*, tech. rep., Fermilab, 1995. `http://cds.cern.ch/record/295811`.

[64] K. G. Wilson, *Renormalization group and critical phenomena. 2. Phase space cell analysis of critical behavior*, Phys.Rev. **B4** (1971) 3184–3205.

[65] G. Altarelli, *The Higgs: so simple yet so unnatural*, EPJ Web Conf. **71** (2014) 00005.

[66] B. W. Lee, C. Quigg, and H. Thacker, *Weak Interactions at Very High-Energies: The Role of the Higgs Boson Mass*, Phys.Rev. **D16** (1977) 1519.

[67] H. Georgi and S. Glashow, *Unity of All Elementary Particle Forces*, Phys.Rev.Lett. **32** (1974) 438–441.

[68] P. Langacker and M.-x. Luo, *Implications of precision electroweak experiments for M_t, ρ_0, $\sin^2\theta_W$ and grand unification*, Phys.Rev. **D44** (1991) 817–822.

[69] U. Amaldi, W. de Boer, and H. Furstenau, *Comparison of grand unified theories with electroweak and strong coupling constants measured at LEP*, Phys.Lett. **B260** (1991) 447–455.

[70] H. E. Haber and G. L. Kane, *The Search for Supersymmetry: Probing Physics Beyond the Standard Model*, Phys.Rept. **117** (1985) 75–263.

[71] H. P. Nilles, *Supersymmetry, Supergravity and Particle Physics*, Phys.Rept. **110** (1984) 1–162.

[72] S. Gubser, I. R. Klebanov, and A. M. Polyakov, *Gauge theory correlators from noncritical string theory*, Phys.Lett. **B428** (1998) 105–114, `arXiv:hep-th/9802109 [hep-th]`.

[73] J. M. Maldacena, *The Large N limit of superconformal field theories and supergravity*, Int.J.Theor.Phys. **38** (1999) 1113–1133, `arXiv:hep-th/9711200 [hep-th]`.

[74] J. Bardeen, L. Cooper, and J. Schrieffer, *Theory of superconductivity*, Phys.Rev. **108** (1957) 1175–1204.

[75] J. Bardeen, L. Cooper, and J. Schrieffer, *Microscopic theory of superconductivity*, Phys.Rev. **106** (1957) 162.

[76] Y. Nambu and G. Jona-Lasinio, *Dynamical Model of Elementary Particles Based on an Analogy with Superconductivity. I.*, Phys.Rev. **122** (1961) 345–358.

[77] Y. Nambu and G. Jona-Lasinio, *Dynamical Model Of Elementary Particles Based On An Analogy With Superconductivity. II*, Phys.Rev. **124** (1961) 246–254.

[78] S. Weinberg, *Implications of Dynamical Symmetry Breaking*, Phys.Rev. **D13** (1976) 974–996.

[79] S. Weinberg, *Implications of Dynamical Symmetry Breaking: An Addendum*, Phys.Rev. **D19** (1979) 1277–1280.

[80] L. Susskind, *Dynamics of Spontaneous Symmetry Breaking in the Weinberg-Salam Theory*, Phys.Rev. **D20** (1979) 2619–2625.

[81] S. Dimopoulos and L. Susskind, *Mass Without Scalars*, Nucl.Phys. **B155** (1979) 237–252.

[82] E. Eichten and K. D. Lane, *Dynamical Breaking of Weak Interaction Symmetries*, Phys.Lett. **B90** (1980) 125–130.

[83] P. Sikivie, L. Susskind, M. B. Voloshin, and V. I. Zakharov, *Isospin Breaking in Technicolor Models*, Nucl.Phys. **B173** (1980) 189.

[84] B. Holdom, *Raising the Sideways Scale*, Phys.Rev. **D24** (1981) 1441.

[85] B. Holdom, *Techniodor*, Phys.Lett. **B150** (1985) 301.

[86] K. Yamawaki, M. Bando, and K.-i. Matumoto, *Scale Invariant Technicolor Model and a Technidilaton*, Phys.Rev.Lett. **56** (1986) 1335.

[87] T. W. Appelquist, D. Karabali, and L. Wijewardhana, *Chiral Hierarchies and the Flavor Changing Neutral Current Problem in Technicolor*, Phys.Rev.Lett. **57** (1986) 957.

[88] T. Appelquist and L. Wijewardhana, *Chiral Hierarchies and Chiral Perturbations in Technicolor*, Phys.Rev. **D35** (1987) 774.

[89] T. Appelquist and L. Wijewardhana, *Chiral Hierarchies from Slowly Running Couplings in Technicolor Theories*, Phys.Rev. **D36** (1987) 568.

[90] R. S. Chivukula, *An Introduction to dynamical electroweak symmetry breaking*, `arXiv:hep-ph/9701322 [hep-ph]`.

[91] R. S. Chivukula, *Weak Isospin Violation in 'Walking' Technicolor*, Phys.Rev.Lett. **61** (1988) 2657.

[92] V. Miransky, M. Tanabashi, and K. Yamawaki, *Dynamical Electroweak Symmetry Breaking with Large Anomalous Dimension and t Quark Condensate*, Phys.Lett. **B221** (1989) 177.

[93] V. Miransky, M. Tanabashi, and K. Yamawaki, *Is the t Quark Responsible for the Mass of W and Z Bosons?*, Mod.Phys.Lett. **A4** (1989) 1043.

[94] Y. Nambu, *bootstrap Symmetry Breaking In Electroweak Unification*, Tech. Rep. EFI-89-08, Chicago U., EFI, 1989.

[95] W. Marciano, *heavy Top Quark Mass Predictions*, Phys.Rev.Lett. **62** (1989) 2793–2796.

[96] W. A. Bardeen, C. T. Hill, and M. Lindner, *Minimal Dynamical Symmetry Breaking of the Standard Model*, Phys.Rev. **D41** (1990) 1647.

[97] G. Cvetic, *Top quark condensation*, Rev.Mod.Phys. **71** (1999) 513–574, `arXiv:hep-ph/9702381 [hep-ph]`.

[98] C. T. Hill, *Topcolor: Top quark condensation in a gauge extension of the standard model*, Phys.Lett. **B266** (1991) 419–424.

[99] C. T. Hill and E. H. Simmons, *Strong dynamics and electroweak symmetry breaking*, Phys.Rept. **381** (2003) 235–402, `arXiv:hep-ph/0203079 [hep-ph]`.

[100] C. T. Hill, *Topcolor assisted technicolor*, Phys.Lett. **B345** (1995) 483–489, `arXiv:hep-ph/9411426 [hep-ph]`.

[101] K. D. Lane and E. Eichten, *Natural topcolor assisted technicolor*, Phys.Lett. **B352** (1995) 382–387, `arXiv:hep-ph/9503433 [hep-ph]`.

[102] K. D. Lane, *Symmetry breaking and generational mixing in topcolor assisted technicolor*, Phys.Rev. **D54** (1996) 2204–2212, `arXiv:hep-ph/9602221 [hep-ph]`.

[103] M. B. Popovic and E. H. Simmons, *A Heavy top quark from flavor universal colorons*, Phys.Rev. **D58** (1998) 095007, `arXiv:hep-ph/9806287 [hep-ph]`.

[104] F. Braam, M. Flossdorf, R. S. Chivukula, S. Di Chiara, and E. H. Simmons, *Hypercharge-Universal Topcolor*, Phys.Rev. **D77** (2008) 055005, `arXiv:0711.1127 [hep-ph]`.

[105] B. A. Dobrescu and C. T. Hill, *Electroweak symmetry breaking via top condensation seesaw*, Phys.Rev.Lett. **81** (1998) 2634–2637, `arXiv:hep-ph/9712319 [hep-ph]`.

[106] R. S. Chivukula, B. A. Dobrescu, H. Georgi, and C. T. Hill, *Top quark seesaw theory of electroweak symmetry breaking*, Phys.Rev. **D59** (1999) 075003, `arXiv:hep-ph/9809470 [hep-ph]`.

[107] H.-J. He, C. T. Hill, and T. M. Tait, *Top quark seesaw, vacuum structure and electroweak precision constraints*, Phys.Rev. **D65** (2002) 055006, `arXiv:hep-ph/0108041 [hep-ph]`.

[108] R. S. Chivukula, D. A. Dicus, and H.-J. He, *Unitarity of compactified five-dimensional Yang-Mills theory*, Phys.Lett. **B525** (2002) 175–182, `arXiv:hep-ph/0111016 [hep-ph]`.

[109] R. S. Chivukula and H.-J. He, *Unitarity of deconstructed five-dimensional Yang-Mills theory*, Phys.Lett. **B532** (2002) 121–128, `arXiv:hep-ph/0201164 [hep-ph]`.

[110] R. S. Chivukula, D. A. Dicus, H.-J. He, and S. Nandi, *Unitarity of the higher dimensional standard model*, Phys.Lett. **B562** (2003) 109–117, `arXiv:hep-ph/0302263 [hep-ph]`.

[111] C. Csaki, C. Grojean, H. Murayama, L. Pilo, and J. Terning, *Gauge theories on an interval: Unitarity without a Higgs*, Phys.Rev. **D69** (2004) 055006, `arXiv:hep-ph/0305237 [hep-ph]`.

[112] C. Csaki and D. Curtin, *A Flavor Protection for Warped Higgsless Models*, Phys.Rev. **D80** (2009) 015027, `arXiv:0904.2137 [hep-ph]`.

[113] G. Cacciapaglia, C. Csaki, G. Marandella, and J. Terning, *A New custodian for a realistic Higgsless model*, Phys.Rev. **D75** (2007) 015003, `arXiv:hep-ph/0607146 [hep-ph]`.

[114] G. Cacciapaglia, C. Csaki, C. Grojean, and J. Terning, *Curing the Ills of Higgsless models: The S parameter and unitarity*, Phys.Rev. **D71** (2005) 035015, `arXiv:hep-ph/0409126 [hep-ph]`.

[115] G. Cacciapaglia, C. Csaki, C. Grojean, and J. Terning, *Oblique corrections from Higgsless models in warped space*, Phys.Rev. **D70** (2004) 075014, `arXiv:hep-ph/0401160 [hep-ph]`.

[116] C. Csaki, C. Grojean, L. Pilo, and J. Terning, *Towards a realistic model of Higgsless electroweak symmetry breaking*, Phys.Rev.Lett. **92** (2004) 101802, `arXiv:hep-ph/0308038 [hep-ph]`.

[117] O. Aharony, S. S. Gubser, J. M. Maldacena, H. Ooguri, and Y. Oz, *Large N field theories, string theory and gravity*, Phys.Rept. **323** (2000) 183–386, `arXiv:hep-th/9905111 [hep-th]`.

[118] R. S. Chivukula, B. Coleppa, S. Di Chiara, E. H. Simmons, H.-J. He, et al., *A Three Site Higgsless Model*, Phys.Rev. **D74** (2006) 075011, `arXiv:hep-ph/0607124 [hep-ph]`.

[119] R. Sekhar Chivukula, N. D. Christensen, B. Coleppa, and E. H. Simmons, *The Top Triangle Moose: Combining Higgsless and Topcolor Mechanisms for Mass Generation*, Phys.Rev. **D80** (2009) 035011, `arXiv:0906.5567 [hep-ph]`.

[120] ATLAS Collaboration, G. Aad et al., *Measurement of the Higgs boson mass from the* $H \to \gamma\gamma$ *and* $H \to ZZ^* \to 4\ell$ *channels with the ATLAS detector using 25* fb^{-1} *of pp collision data*, Phys.Rev. **D90** (2014) 052004, `arXiv:1406.3827 [hep-ex]`.

[121] E. Eichten, I. Hinchliffe, K. D. Lane, and C. Quigg, *Super Collider Physics*, Rev.Mod.Phys. **56** (1984) 579–707.

[122] E. Eichten, I. Hinchliffe, K. Lane, and C. Quigg, *Signatures for Technicolor*, Phys.Rev. **D34** (1986) 1547.

[123] R. S. Chivukula, R. Rosenfeld, E. H. Simmons, and J. Terning, *Strongly coupled electroweak symmetry breaking: Implication of models*, `arXiv:hep-ph/9503202 [hep-ph]`.

[124] A. Belyaev, A. Blum, R. S. Chivukula, and E. H. Simmons, *The Meaning of Higgs: tau+ tau- and gamma gamma at the Tevatron and the LHC*, Phys.Rev. **D72** (2005) 055022, `arXiv:hep-ph/0506086 [hep-ph]`.

[125] R. S. Chivukula, E. H. Simmons, B. Coleppa, H. E. Logan, and A. Martin, *Top-Higgs and Top-pion phenomenology in the Top Triangle Moose model*, Phys.Rev. **D83** (2011) 055013, `arXiv:1101.6023 [hep-ph]`.

[126] R. S. Chivukula, E. H. Simmons, B. Coleppa, H. E. Logan, and A. Martin, *LHC Limits on the Top-Higgs in Models with Strong Top-Quark Dynamics*, Phys.Rev. **D84** (2011) 095022, `arXiv:1108.4000 [hep-ph]`.

[127] CDF Collaboration, T. Aaltonen et al., *Search for charged Higgs bosons in decays of top quarks in p anti-p collisions at s**(1/2) = 1.96 TeV*, Phys.Rev.Lett. **103** (2009) 101803, `arXiv:0907.1269 [hep-ex]`.

[128] D0 Collaboration, V. Abazov et al., *Search for charged Higgs bosons in top quark decays*, Phys.Lett. **B682** (2009) 278–286, `arXiv:0908.1811 [hep-ex]`.

[129] P. Langacker, *The Physics of Heavy Z' Gauge Bosons*, Rev.Mod.Phys. **81** (2009) 1199–1228, `arXiv:0801.1345 [hep-ph]`.

[130] P. Langacker, R. W. Robinett, and J. L. Rosner, *New Heavy Gauge Bosons in p p and p anti-p Collisions*, Phys.Rev. **D30** (1984) 1470.

[131] R. M. Harris and K. Kousouris, *Searches for Dijet Resonances at Hadron Colliders*, Int.J.Mod.Phys. **A26** (2011) 5005–5055, `arXiv:1110.5302 [hep-ex]`.

[132] LHC/LC Study Group Collaboration, G. Weiglein et al., *Physics interplay of the LHC and the ILC*, Phys.Rept. **426** (2006) 47–358, `arXiv:hep-ph/0410364 [hep-ph]`.

[133] F. Yu, *Di-jet resonances at future hadron colliders: A Snowmass whitepaper*, `arXiv:1308.1077 [hep-ph]`.

[134] A. Leike, *The Phenomenology of extra neutral gauge bosons*, Phys.Rept. **317** (1999) 143–250, `arXiv:hep-ph/9805494 [hep-ph]`.

[135] J. D. Anderson, M. H. Austern, and R. N. Cahn, *Measurement of Z-prime couplings at future hadron colliders through decays to tau leptons*, Phys.Rev. **D46** (1992) 290–302.

[136] F. del Aguila, M. Cvetic, and P. Langacker, *Determination of Z-prime gauge couplings to quarks and leptons at future hadron colliders*, Phys.Rev. **D48** (1993) 969–973, `arXiv:hep-ph/9303299 [hep-ph]`.

[137] M. Cvetic and S. Godfrey, *Discovery and identification of extra gauge bosons*, `arXiv:hep-ph/9504216 [hep-ph]`.

[138] M. Dittmar, A.-S. Nicollerat, and A. Djouadi, *Z-prime studies at the LHC: An Update*, Phys.Lett. **B583** (2004) 111–120, `arXiv:hep-ph/0307020 [hep-ph]`.

[139] F. Petriello and S. Quackenbush, *Measuring Z' couplings at the CERN LHC*, Phys.Rev. **D77** (2008) 115004, `arXiv:0801.4389 [hep-ph]`.

[140] M. Cvetic and P. Langacker, *V-prime Z and V-prime W production as tests of heavy gauge boson couplings at future hadron colliders*, Phys.Rev. **D46** (1992) 4943, `arXiv:hep-ph/9207216 [hep-ph]`.

[141] ATLAS Collaboration, G. Aad et al., *Search for the Standard Model Higgs boson in the two photon decay channel with the ATLAS detector at the LHC*, Phys.Lett. **B705** (2011) 452–470, `arXiv:1108.5895 [hep-ex]`.

[142] CMS Collaboration, CMS Collaboration, *Search for a Higgs boson decaying into two photons in the CMS detector*, Tech. Rep. CMS-PAS-HIG-11-021, CERN, 2011. `http://cds.cern.ch/record/1376642`.

[143] ATLAS Collaboration, ATLAS Collaboration, *Update of the Combination of Higgs Boson Searches in pp Collisions at sqrt(s) = 7 TeV with the ATLAS Experiment at the LHC*, Tech. Rep. ATLAS-CONF-2011-135, CERN, 2011. `http://cds.cern.ch/record/1383838`.

[144] ATLAS Collaboration, ATLAS Collaboration, *Search for neutral MSSM Higgs bosons decaying to tau+tau- pairs in proton-proton collisions at sqrt(s) = 7 TeV with the ATLAS detector*, Tech. Rep. ATLAS-CONF-2011-132, CERN, 2011. `http://cds.cern.ch/record/1383835`.

[145] CMS Collaboration, CMS Collaboration, *Search for Neutral Higgs Bosons Decaying to Tau Pairs in pp Collisions at sqrts=7 TeV*, Tech. Rep. CMS-PAS-HIG-11-020, CERN, 2011. `http://cds.cern.ch/record/1378096`.

[146] A. Manohar and L. Randall, *Searching for neutral pseudoGoldstone bosons in Z0 decays*, Phys.Lett. **B246** (1990) 537–540.

[147] L. Randall and E. H. Simmons, *Signatures of neutral pseudoGoldstone bosons from technicolor*, Nucl.Phys. **B380** (1992) 3–21.

[148] G. Rupak and E. H. Simmons, *Limits on pseudoscalar bosons from rare Z decays at LEP*, Phys.Lett. **B362** (1995) 155–163, arXiv:hep-ph/9507438 [hep-ph].

[149] V. Lubicz and P. Santorelli, *Production of neutral pseudoGoldstone bosons at LEP-2 and NLC in multiscale walking technicolor models*, Nucl.Phys. **B460** (1996) 3–36, arXiv:hep-ph/9505336 [hep-ph].

[150] R. Casalbuoni, A. Deandrea, S. De Curtis, D. Dominici, R. Gatto, et al., *Detecting and studying the lightest pseudoGoldstone boson at future pp, e^+e^- and $\mu^+\mu^-$ colliders*, Nucl.Phys. **B555** (1999) 3–52, arXiv:hep-ph/9809523 [hep-ph].

[151] K. R. Lynch and E. H. Simmons, *Composite scalars at CERN LEP: Constraining technicolor theories*, Phys.Rev. **D64** (2001) 035008, arXiv:hep-ph/0012256 [hep-ph].

[152] E. Farhi and L. Susskind, *Technicolor*, Phys.Rept. **74** (1981) 277.

[153] K. D. Lane and M. Ramana, *Walking technicolor signatures at hadron colliders*, Phys.Rev. **D44** (1991) 2678–2700.

[154] K. D. Lane, *Technihadron production and decay in low scale technicolor*, Phys.Rev. **D60** (1999) 075007, arXiv:hep-ph/9903369 [hep-ph].

[155] S. Dimopoulos, S. Raby, and G. L. Kane, *Experimental Predictions from Technicolor Theories*, Nucl.Phys. **B182** (1981) 77–103.

[156] J. R. Ellis, M. K. Gaillard, D. V. Nanopoulos, and P. Sikivie, *Can One Tell Technicolor from a Hole in the Ground?*, Nucl.Phys. **B182** (1981) 529–545.

[157] B. Holdom, *A Phenomenological Lagrangian for Hypercolor*, Phys.Rev. **D24** (1981) 157.

[158] J. F. Gunion, H. E. Haber, G. L. Kane, and S. Dawson, *The Higgs Hunter's Guide*, Front.Phys. **80** (2000) 1–448.

[159] LHC Higgs Cross Section Working Group Collaboration, S. Dittmaier et al., *Handbook of LHC Higgs Cross Sections: 1. Inclusive Observables*, arXiv:1101.0593 [hep-ph].

[160] A. Djouadi, J. Kalinowski, and M. Spira, *HDECAY: A Program for Higgs boson decays in the standard model and its supersymmetric extension*, Comput.Phys.Commun. **108** (1998) 56–74, `arXiv:hep-ph/9704448 [hep-ph]`.

[161] ATLAS Collaboration, ATLAS Collaboration, *An update to the combined search for the Standard Model Higgs boson with the ATLAS detector at the LHC using up to 4.9 fb1 of pp collision data at s = 7 TeV*, Tech. Rep. ATLAS-CONF-2012-019, CERN, 2012. `http://cds.cern.ch/record/1430033`.

[162] ATLAS Collaboration, ATLAS Collaboration, *Search for the Standard Model Higgs boson in the decay mode H -> tau+ tau- -> ll + 4 neutrinos in Association with jets in Proton-Proton Collisions at sqrt(s) =7 TeV with the ATLAS detector*, Tech. Rep. ATLAS-CONF-2011-133, CERN, 2011. `http://cds.cern.ch/record/1383836`.

[163] ATLAS Collaboration, ATLAS Collaboration, *Search for the Standard Model Higgs boson in the $H \to \tau^+\tau^-$ decay mode with 4.7 fb^{-1} of ATLAS data at 7 TeV*, Tech. Rep. ATLAS-CONF-2012-014, CERN, 2012. `http://cds.cern.ch/record/1429662`.

[164] A. Azatov, R. Contino, and J. Galloway, *Model-Independent Bounds on a Light Higgs*, JHEP **1204** (2012) 127, `arXiv:1202.3415 [hep-ph]`.

[165] F. Sannino and K. Tuominen, *Orientifold theory dynamics and symmetry breaking*, Phys.Rev. **D71** (2005) 051901, `arXiv:hep-ph/0405209 [hep-ph]`.

[166] R. Foadi, M. T. Frandsen, T. A. Ryttov, and F. Sannino, *Minimal Walking Technicolor: Set Up for Collider Physics*, Phys.Rev. **D76** (2007) 055005, `arXiv:0706.1696 [hep-ph]`.

[167] A. Belyaev, R. Foadi, M. T. Frandsen, M. Jarvinen, F. Sannino, et al., *Technicolor Walks at the LHC*, Phys.Rev. **D79** (2009) 035006, `arXiv:0809.0793 [hep-ph]`.

[168] CMS Collaboration, S. Chatrchyan et al., *Search for the standard model Higgs boson decaying into two photons in pp collisions at $\sqrt{s} = 7$ TeV*, Phys.Lett. **B710** (2012) 403–425, `arXiv:1202.1487 [hep-ex]`.

[169] W. Bernreuther, P. Gonzalez, and M. Wiebusch, *Pseudoscalar Higgs Bosons at the LHC: Production and Decays into Electroweak Gauge Bosons Revisited*, Eur.Phys.J. **C69** (2010) 31–43, `arXiv:1003.5585 [hep-ph]`.

[170] G. Burdman, C. E. Haluch, and R. D. Matheus, *Is the LHC Observing the Pseudo-scalar State of a Two-Higgs Doublet Model ?*, Phys.Rev. **D85** (2012) 095016, `arXiv:1112.3961 [hep-ph]`.

[171] B. Holdom, *A pseudoscalar at the LHC: technicolor vs a fourth family*, Phys.Lett. **B709** (2012) 381–384, `arXiv:1201.0185 [hep-ph]`.

[172] E. Cervero and J.-M. Gerard, *Minimal violation of flavour and custodial symmetries in a vectophobic Two-Higgs-Doublet-Model*, Phys.Lett. **B712** (2012) 255–260, `arXiv:1202.1973 [hep-ph]`.

[173] M. T. Frandsen and F. Sannino, *Discovering a Light Scalar or Pseudoscalar at The Large Hadron Collider*, `arXiv:1203.3988 [hep-ph]`.

[174] J. Moffat, *Has A 125 GeV Pseudoscalar Resonance Been Observed at the LHC?*, `arXiv:1204.4702 [hep-ph]`.

[175] A. Barroso, P. Ferreira, R. Santos, and J. P. Silva, *Probing the scalar-pseudoscalar mixing in the 125 GeV Higgs particle with current data*, Phys.Rev. **D86** (2012) 015022, `arXiv:1205.4247 [hep-ph]`.

[176] I. Low, J. Lykken, and G. Shaughnessy, *Have We Observed the Higgs (Imposter)?*, Phys.Rev. **D86** (2012) 093012, `arXiv:1207.1093 [hep-ph]`.

[177] B. Coleppa, K. Kumar, and H. E. Logan, *Can the 126 GeV boson be a pseudoscalar?*, Phys.Rev. **D86** (2012) 075022, `arXiv:1208.2692 [hep-ph]`.

[178] C. T. Hill, S. Pokorski, and J. Wang, *Gauge invariant effective Lagrangian for Kaluza-Klein modes*, Phys.Rev. **D64** (2001) 105005, `arXiv:hep-th/0104035 [hep-th]`.

[179] N. Arkani-Hamed, A. G. Cohen, and H. Georgi, *(De)constructing dimensions*, Phys.Rev.Lett. **86** (2001) 4757–4761, `arXiv:hep-th/0104005 [hep-th]`.

[180] H. Georgi, *A Tool Kit for Builders of Composite Models*, Nucl.Phys. **B266** (1986) 274.

[181] R. Casalbuoni, S. De Curtis, D. Dominici, and R. Gatto, *Effective Weak Interaction Theory with Possible New Vector Resonance from a Strong Higgs Sector*, Phys.Lett. **B155** (1985) 95.

[182] R. Casalbuoni, A. Deandrea, S. De Curtis, D. Dominici, R. Gatto, et al., *Degenerate BESS model: The Possibility of a low-energy strong electroweak sector*, Phys.Rev. **D53** (1996) 5201–5221, `arXiv:hep-ph/9510431 [hep-ph]`.

[183] R. S. Chivukula, E. H. Simmons, H.-J. He, M. Kurachi, and M. Tanabashi, *Multi-gauge-boson vertices and chiral Lagrangian parameters in Higgsless models with ideal fermion delocalization*, Phys.Rev. **D72** (2005) 075012, `arXiv:hep-ph/0508147 [hep-ph]`.

[184] R. S. Chivukula, E. H. Simmons, H.-J. He, M. Kurachi, and M. Tanabashi, *Ideal fermion delocalization in Higgsless models*, Phys.Rev. **D72** (2005) 015008, `arXiv:hep-ph/0504114 [hep-ph]`.

[185] R. S. Chivukula, E. H. Simmons, H.-J. He, M. Kurachi, and M. Tanabashi, *Deconstructed Higgsless models with one-site delocalization*, Phys.Rev. **D71** (2005) 115001, `arXiv:hep-ph/0502162 [hep-ph]`.

[186] M. Kurachi, R. S. Chivukula, E. H. Simmons, H.-J. He, and M. Tanabashi, *Oblique corrections in deconstructed Higgsless models*, `arXiv:hep-ph/0409134 [hep-ph]`.

[187] R. S. Chivukula, E. H. Simmons, H.-J. He, M. Kurachi, and M. Tanabashi, *Universal non-oblique corrections in Higgsless models and beyond*, Phys.Lett. **B603** (2004) 210–218, `arXiv:hep-ph/0408262 [hep-ph]`.

[188] R. S. Chivukula, E. H. Simmons, H.-J. He, M. Kurachi, and M. Tanabashi, *The Structure of corrections to electroweak interactions in Higgsless models*, Phys.Rev. **D70** (2004) 075008, `arXiv:hep-ph/0406077 [hep-ph]`.

[189] K. Lane and A. Martin, *An Effective Lagrangian for Low-Scale Technicolor*, Phys.Rev. **D80** (2009) 115001, `arXiv:0907.3737 [hep-ph]`.

[190] R. Foadi, S. Gopalakrishna, and C. Schmidt, *Higgsless electroweak symmetry breaking from theory space*, JHEP **0403** (2004) 042, `arXiv:hep-ph/0312324 [hep-ph]`.

[191] R. Foadi, S. Gopalakrishna, and C. Schmidt, *Effects of fermion localization in Higgsless theories and electroweak constraints*, Phys.Lett. **B606** (2005) 157–163, `arXiv:hep-ph/0409266 [hep-ph]`.

[192] R. Foadi and C. Schmidt, *An Effective Higgsless theory: Satisfying electroweak constraints and a heavy top quark*, Phys.Rev. **D73** (2006) 075011, `arXiv:hep-ph/0509071 [hep-ph]`.

[193] M. Bando, T. Kugo, and K. Yamawaki, *Nonlinear Realization and Hidden Local Symmetries*, Phys.Rept. **164** (1988) 217–314.

[194] M. Bando, T. Kugo, and K. Yamawaki, *On the Vector Mesons as Dynamical Gauge Bosons of Hidden Local Symmetries*, Nucl.Phys. **B259** (1985) 493.

[195] M. Bando, T. Kugo, and K. Yamawaki, *Composite Gauge Bosons and 'Low-energy Theorems' of Hidden Local Symmetries*, Prog.Theor.Phys. **73** (1985) 1541.

[196] M. Bando, T. Kugo, S. Uehara, K. Yamawaki, and T. Yanagida, *Is rho Meson a Dynamical Gauge Boson of Hidden Local Symmetry?*, Phys.Rev.Lett. **54** (1985) 1215.

[197] M. Bando, T. Fujiwara, and K. Yamawaki, *Generalized Hidden Local Symmetry and the A1 Meson*, Prog.Theor.Phys. **79** (1988) 1140.

[198] M. E. Peskin and T. Takeuchi, *Estimation of oblique electroweak corrections*, Phys.Rev. **D46** (1992) 381–409.

[199] D. Kominis, *Flavor changing neutral current constraints in topcolor assisted technicolor*, Phys.Lett. **B358** (1995) 312–317, `arXiv:hep-ph/9506305 [hep-ph]`.

[200] G. Buchalla, G. Burdman, C. Hill, and D. Kominis, *GIM violation and new dynamics of the third generation*, Phys.Rev. **D53** (1996) 5185–5200, `arXiv:hep-ph/9510376 [hep-ph]`.

[201] H.-J. He and C. Yuan, *New Method for Detecting Charged Scalars at Colliders*, Phys.Rev.Lett. **83** (1999) 28–31, `arXiv:hep-ph/9810367 [hep-ph]`.

[202] G. Burdman, *Scalars from top condensation models at hadron colliders*, Phys.Rev.Lett. **83** (1999) 2888–2891, `arXiv:hep-ph/9905347 [hep-ph]`.

[203] G. Burdman and D. Kominis, *Model independent constraints on topcolor from R(b)*, Phys.Lett. **B403** (1997) 101–107, `arXiv:hep-ph/9702265 [hep-ph]`.

[204] LHC Higgs Cross Section Working Group (summer 2011), *SM Higgs production cross sections at $\sqrt{s} = 7$ TeV (update in CERN Report 3)*, tech. rep., CERN, 2011. `https://twiki.cern.ch/twiki/bin/view/LHCPhysics/CERNYellowReportPageAt7TeV`.

[205] M. Spira, A. Djouadi, D. Graudenz, and P. Zerwas, *Higgs boson production at the LHC*, Nucl.Phys. **B453** (1995) 17–82, `arXiv:hep-ph/9504378 [hep-ph]`.

[206] ATLAS Collaboration, G. Aad et al., *Search for the Standard Model Higgs boson in the diphoton decay channel with 4.9 fb^{-1} of pp collisions at $\sqrt{s} = 7$ TeV with ATLAS*, Phys.Rev.Lett. **108** (2012) 111803, `arXiv:1202.1414 [hep-ex]`.

[207] CMS Collaboration, S. Chatrchyan et al., *Search for anomalous production of highly boosted Z bosons decaying to dimuons in pp collisions at $\sqrt{s} = 7$ TeV*, Phys.Lett. **B722** (2013) 28–47, `arXiv:1210.0867 [hep-ex]`.

[208] ATLAS Collaboration, G. Aad et al., *Search for charged Higgs bosons decaying via $H^+ \to \tau\nu$ in top quark pair events using pp collision data at $\sqrt{s} = 7$ TeV with the ATLAS detector*, JHEP **1206** (2012) 039, `arXiv:1204.2760 [hep-ex]`.

[209] CMS Collaboration, S. Chatrchyan et al., *Combined results of searches for the standard model Higgs boson in pp collisions at $\sqrt{s} = 7$ TeV*, Phys.Lett. **B710** (2012) 26–48, `arXiv:1202.1488 [hep-ex]`.

[210] P. H. Frampton and S. L. Glashow, *Chiral Color: An Alternative to the Standard Model*, Phys.Lett. **B190** (1987) 157.

[211] P. H. Frampton and S. L. Glashow, *Unifiable Chiral Color With Natural Gim Mechanism*, Phys.Rev.Lett. **58** (1987) 2168.

[212] R. Chivukula, A. G. Cohen, and E. H. Simmons, *New strong interactions at the Tevatron?*, Phys.Lett. **B380** (1996) 92–98, `arXiv:hep-ph/9603311 [hep-ph]`.

[213] E. H. Simmons, *Coloron phenomenology*, Phys.Rev. **D55** (1997) 1678–1683, `arXiv:hep-ph/9608269 [hep-ph]`.

[214] O. Antunano, J. H. Kuhn, and G. Rodrigo, *Top quarks, axigluons and charge asymmetries at hadron colliders*, Phys.Rev. **D77** (2008) 014003, `arXiv:0709.1652 [hep-ph]`.

[215] P. Ferrario and G. Rodrigo, *Constraining heavy colored resonances from top-antitop quark events*, Phys.Rev. **D80** (2009) 051701, `arXiv:0906.5541 [hep-ph]`.

[216] P. H. Frampton, J. Shu, and K. Wang, *Axigluon as Possible Explanation for p anti-p —> t anti-t Forward-Backward Asymmetry*, Phys.Lett. **B683** (2010) 294–297, `arXiv:0911.2955 [hep-ph]`.

[217] G. Rodrigo and P. Ferrario, *Charge asymmetry: A Theory appraisal*, Nuovo Cim. **C033** (2010) no. 4, 221–228, `arXiv:1007.4328 [hep-ph]`.

[218] R. S. Chivukula, E. H. Simmons, and C.-P. Yuan, *Axigluons cannot explain the observed top quark forward-backward asymmetry*, Phys.Rev. **D82** (2010) 094009, `arXiv:1007.0260 [hep-ph]`.

[219] G. Marques Tavares and M. Schmaltz, *Explaining the t-tbar asymmetry with a light axigluon*, Phys.Rev. **D84** (2011) 054008, arXiv:1107.0978 [hep-ph].

[220] D. Dicus, C. McMullen, and S. Nandi, *Collider implications of Kaluza-Klein excitations of the gluons*, Phys.Rev. **D65** (2002) 076007, arXiv:hep-ph/0012259 [hep-ph].

[221] K. Lane and S. Mrenna, *The Collider phenomenology of technihadrons in the technicolor straw man model*, Phys.Rev. **D67** (2003) 115011, arXiv:hep-ph/0210299 [hep-ph].

[222] I. Antoniadis, *A Possible new dimension at a few TeV*, Phys.Lett. **B246** (1990) 377–384.

[223] G. Senjanovic and R. N. Mohapatra, *Exact Left-Right Symmetry and Spontaneous Violation of Parity*, Phys.Rev. **D12** (1975) 1502.

[224] H. Georgi, E. E. Jenkins, and E. H. Simmons, *Ununifying the Standard Model*, Phys.Rev.Lett. **62** (1989) 2789.

[225] H. Georgi, E. E. Jenkins, and E. H. Simmons, *The Ununified Standard Model*, Nucl.Phys. **B331** (1990) 541.

[226] D. J. Muller and S. Nandi, *Top flavor: A Separate SU(2) for the third family*, Phys.Lett. **B383** (1996) 345–350, arXiv:hep-ph/9602390 [hep-ph].

[227] E. Malkawi, T. M. Tait, and C. Yuan, *A Model of strong flavor dynamics for the top quark*, Phys.Lett. **B385** (1996) 304–310, arXiv:hep-ph/9603349 [hep-ph].

[228] R. Chivukula, E. H. Simmons, and J. Terning, *A Heavy top quark and the Z b anti-b vertex in noncommuting extended technicolor*, Phys.Lett. **B331** (1994) 383–389, arXiv:hep-ph/9404209 [hep-ph].

[229] J. L. Hewett and T. G. Rizzo, *Low-Energy Phenomenology of Superstring Inspired E(6) Models*, Phys.Rept. **183** (1989) 193.

[230] L. Randall and R. Sundrum, *A Large mass hierarchy from a small extra dimension*, Phys.Rev.Lett. **83** (1999) 3370–3373, arXiv:hep-ph/9905221 [hep-ph].

[231] L. Randall and R. Sundrum, *An Alternative to compactification*, Phys.Rev.Lett. **83** (1999) 4690–4693, arXiv:hep-th/9906064 [hep-th].

[232] H. Davoudiasl, J. Hewett, and T. Rizzo, *Phenomenology of the Randall-Sundrum Gauge Hierarchy Model*, Phys.Rev.Lett. **84** (2000) 2080, arXiv:hep-ph/9909255 [hep-ph].

[233] J. Bijnens, P. Eerola, M. Maul, A. Mansson, and T. Sjostrand, *QCD signatures of narrow graviton resonances in hadron colliders*, Phys.Lett. **B503** (2001) 341–348, arXiv:hep-ph/0101316 [hep-ph].

[234] UA1 Collaboration, G. Arnison et al., *Measurement of the Inclusive Jet Cross-Section at the CERN p anti-p Collider*, Phys.Lett. **B172** (1986) 461.

[235] UA2 Collaboration, J. Alitti et al., *A Search for new intermediate vector mesons and excited quarks decaying to two jets at the CERN $\bar{p}p$ collider*, Nucl.Phys. **B400** (1993) 3–24.

[236] CDF Collaboration, F. Abe et al., *The Two jet invariant mass distribution at $\sqrt{s} = 1.8$ TeV*, Phys.Rev. **D41** (1990) 1722–1725.

[237] CDF Collaboration, F. Abe et al., *Search for new particles decaying to dijets in $p\bar{p}$ collisions at $\sqrt{s} = 1.8$ TeV*, Phys.Rev.Lett. **74** (1995) 3538–3543, arXiv:hep-ex/9501001 [hep-ex].

[238] CDF Collaboration, F. Abe et al., *Search for new particles decaying to dijets at CDF*, Phys.Rev. **D55** (1997) 5263–5268, arXiv:hep-ex/9702004 [hep-ex].

[239] D0 Collaboration, V. Abazov et al., *Search for new particles in the two jet decay channel with the D0 detector*, Phys.Rev. **D69** (2004) 111101, arXiv:hep-ex/0308033 [hep-ex].

[240] CDF Collaboration, T. Aaltonen et al., *Search for new particles decaying into dijets in proton-antiproton collisions at s**(1/2) = 1.96-TeV*, Phys.Rev. **D79** (2009) 112002, arXiv:0812.4036 [hep-ex].

[241] ATLAS Collaboration, G. Aad et al., *Search for New Particles in Two-Jet Final States in 7 TeV Proton-Proton Collisions with the ATLAS Detector at the LHC*, Phys.Rev.Lett. **105** (2010) 161801, arXiv:1008.2461 [hep-ex].

[242] CMS Collaboration, V. Khachatryan et al., *Search for Dijet Resonances in 7 TeV pp Collisions at CMS*, Phys.Rev.Lett. **105** (2010) 211801, arXiv:1010.0203 [hep-ex].

[243] CMS Collaboration, S. Chatrchyan et al., *Search for Resonances in the Dijet Mass Spectrum from 7 TeV pp Collisions at CMS*, Phys.Lett. **B704** (2011) 123–142, arXiv:1107.4771 [hep-ex].

[244] ATLAS Collaboration, G. Aad et al., *Search for New Physics in the Dijet Mass Distribution using 1 fb^{-1} of pp Collision Data at $\sqrt{s} = 7$ TeV collected by the ATLAS Detector*, Phys.Lett. **B708** (2012) 37–54, arXiv:1108.6311 [hep-ex].

[245] ATLAS Collaboration, ATLAS Collaboration, *Search for New Physics in Dijet Mass and Angular Distributions using 4.8/fb of pp Collisions at sqrt(s) = 7 TeV collected by the ATLAS Detector*, Tech. Rep. ATLAS-CONF-2012-038, CERN, 2012. http://cds.cern.ch/record/1432206.

[246] ATLAS Collaboration, G. Aad et al., *ATLAS search for new phenomena in dijet mass and angular distributions using pp collisions at $\sqrt{s} = 7$ TeV*, JHEP **1301** (2013) 029, arXiv:1210.1718 [hep-ex].

[247] ATLAS Collaboration, ATLAS Collaboration, *Search for New Phenomena in the Dijet Mass Distribution updated using* $13.0\, fb^{-1}$ *of pp Collisions at sqrts = 8 TeV collected by the ATLAS Detector*, Tech. Rep. ATLAS-CONF-2012-148, CERN, 2012. http://cds.cern.ch/record/1493487.

[248] CMS Collaboration, S. Chatrchyan et al., *Search for narrow resonances using the dijet mass spectrum in pp collisions at $\sqrt{s}$=8TeV*, Phys.Rev. **D87** (2013) no. 11, 114015, arXiv:1302.4794 [hep-ex].

[249] CMS Collaboration, CMS Collaboration, *Search for Narrow Resonances using the Dijet Mass Spectrum with 19.6fb-1 of pp Collisions at sqrts=8 TeV*, Tech. Rep. CMS-PAS-EXO-12-059, CERN, 2013. http://cds.cern.ch/record/1519066.

[250] B. A. Dobrescu, K. Kong, and R. Mahbubani, *Massive color-octet bosons and pairs of resonances at hadron colliders*, Phys.Lett. **B670** (2008) 119–123, arXiv:0709.2378 [hep-ph].

[251] R. S. Chivukula, E. H. Simmons, and N. Vignaroli, *Same-Sign Dileptons from Colored Scalars in the Flavorful Top-Coloron Model*, Phys.Rev. **D88** (2013) 034006, arXiv:1306.2248 [hep-ph].

[252] D0 Collaboration, V. Abazov et al., *First measurement of the forward-backward charge asymmetry in top quark pair production*, Phys.Rev.Lett. **100** (2008) 142002, arXiv:0712.0851 [hep-ex].

[253] CDF Collaboration, T. Aaltonen et al., *Forward-Backward Asymmetry in Top Quark Production in $p\bar{p}$ Collisions at sqrts = 1.96 TeV*, Phys.Rev.Lett. **101** (2008) 202001, `arXiv:0806.2472 [hep-ex]`.

[254] D0 Collaboration, V. M. Abazov et al., *Forward-backward asymmetry in top quark-antiquark production*, Phys.Rev. **D84** (2011) 112005, `arXiv:1107.4995 [hep-ex]`.

[255] CDF Collaboration, T. Aaltonen et al., *Evidence for a Mass Dependent Forward-Backward Asymmetry in Top Quark Pair Production*, Phys.Rev. **D83** (2011) 112003, `arXiv:1101.0034 [hep-ex]`.

[256] CDF Collaboration, CDF Collaboration, *Study of the Top Quark Production Asymmetry and Its Mass and Rapidity Dependence in the Full Run II Tevatron Dataset*, Tech. Rep. CDF-Note-10807, Fermilab, 2012. `http://www-cdf.fnal.gov/physics/new/top/2012/LepJet_AFB_Winter2012/CDF10807.pdf`.

[257] B. A. Dobrescu and F. Yu, *Coupling-mass mapping of dijet peak searches*, Phys.Rev. **D88** (2013) no. 3, 035021, `arXiv:1306.2629 [hep-ph]`.

[258] Y. Bai, J. L. Hewett, J. Kaplan, and T. G. Rizzo, *LHC Predictions from a Tevatron Anomaly in the Top Quark Forward-Backward Asymmetry*, JHEP **1103** (2011) 003, `arXiv:1101.5203 [hep-ph]`.

[259] U. Haisch and S. Westhoff, *Massive Color-Octet Bosons: Bounds on Effects in Top-Quark Pair Production*, JHEP **1108** (2011) 088, `arXiv:1106.0529 [hep-ph]`.

[260] K. Gumus, N. Akchurin, S. Esen, and R. M. Harris, *CMS Sensitivity to Dijet Resonances*, Tech. Rep. CMS-NOTE-2006-070, CERN, 2006. `http://cds.cern.ch/record/962025`.

[261] J. Alwall, M. Herquet, F. Maltoni, O. Mattelaer, and T. Stelzer, *MadGraph 5 : Going Beyond*, JHEP **1106** (2011) 128, `arXiv:1106.0522 [hep-ph]`.

[262] J. Pumplin, D. Stump, J. Huston, H. Lai, P. M. Nadolsky, et al., *New generation of parton distributions with uncertainties from global QCD analysis*, JHEP **0207** (2002) 012, `arXiv:hep-ph/0201195 [hep-ph]`.

[263] ATLAS Collaboration, ATLAS Collaboration, *Reconstruction of High Mass $t\bar{t}$ Resonances in the Lepton+Jets Channel*, Tech. Rep. ATL-PHYS-PUB-2009-081, CERN, 2009. `http://cds.cern.ch/record/1177410`.

[264] CMS Collaboration, CMS Collaboration, *Search for narrow resonances in top-pair production close to threshold in the semileptonic muon channel at sqrt(s) = 10 TeV*, Tech. Rep. CMS-PAS-TOP-09-009, CERN, 2009. `http://cds.cern.ch/record/1194523`.

[265] CMS Collaboration, CMS Collaboration, *Search for heavy narrow t-tbar resonances in muon-plus-jets final states with the CMS detector*, Tech. Rep. CMS-PAS-EXO-09-008, CERN, 2009. `http://cds.cern.ch/record/1194498`.

[266] ATLAS Collaboration, ATLAS Collaboration, *New ATLAS event generator tunes to 2010 data*, Tech. Rep. ATL-PHYS-PUB-2011-008, CERN, 2011. `http://cds.cern.ch/record/1345343`.

[267] ATLAS Collaboration, *Studies of Sensitivity to New Dilepton and Ditop Resonances with an Upgraded ATLAS Detector at a High-Luminosity LHC*, Tech. Rep. ATL-PHYS-PUB-2013-003, CERN, 2013. `http://cdsweb.cern.ch/record/1516108`.

[268] ATLAS Collaboration, ATLAS Collaboration, *Physics at a High-Luminosity LHC with ATLAS*, `arXiv:1307.7292 [hep-ex]`.

[269] CMS Collaboration, CMS Collaboration, *Projected Performance of an Upgraded CMS Detector at the LHC and HL-LHC: Contribution to the Snowmass Process*, `arXiv:1307.7135`.

[270] Top Quark Working Group Collaboration, K. Agashe et al., *Working Group Report: Top Quark*, `arXiv:1311.2028 [hep-ph]`.

[271] I. Iashvili, S. Jain, A. Kharchilava, and H. B. Prosper, *Discovery potential for heavy tt resonances in dilepton+jets final states in pp collisions at ps= 14 TeV*, `arXiv:1309.7684 [hep-ex]`.

[272] UTfit Collaboration, M. Bona et al., *Model-independent constraints on $\Delta F = 2$ operators and the scale of new physics*, JHEP **0803** (2008) 049, `arXiv:0707.0636 [hep-ph]`.

[273] H.-L. Lai, J. Huston, S. Mrenna, P. Nadolsky, D. Stump, et al., *Parton Distributions for Event Generators*, JHEP **1004** (2010) 035, `arXiv:0910.4183 [hep-ph]`.

[274] ATLAS Collaboration, *A search for $t\bar{t}$ resonances in the lepton plus jets final state with ATLAS using 14 fb^1 of pp collisions at $\sqrt{s} = 8$ TeV*, Tech. Rep. ATLAS-CONF-2013-052, CERN, 2013. `http://cds.cern.ch/record/1547568`.

[275] CMS Collaboration, S. Chatrchyan et al., *Search for Z ' resonances decaying to* $t\bar{t}$ *in dilepton+jets final states in pp collisions at* $\sqrt{s} = 7$ *TeV*, Phys.Rev. **D87** (2013) 072002, arXiv:1211.3338 [hep-ex].

[276] K. Agashe, O. Antipin, M. Backovic, A. Effron, A. Emerman, et al., *Warped Extra Dimensional Benchmarks for Snowmass 2013*, arXiv:1309.7847 [hep-ph].

[277] CMS Collaboration, CMS Collaboration, *Search for Heavy Resonances Decaying into bb and bg Final States in pp Collisions at sqrt(s) = 8 TeV*, Tech. Rep. CMS-PAS-EXO-12-023, CERN, 2012. http://cds.cern.ch/record/1542405.

[278] M. Czakon, P. Fiedler, and A. Mitov, *Resolving the Tevatron top quark forward-backward asymmetry puzzle*, arXiv:1411.3007 [hep-ph].

[279] D0 Collaboration, V. M. Abazov et al., *Measurement of the forward-backward asymmetry in top quark-antiquark production in ppbar collisions using the lepton+jets channel*, Phys.Rev. **D90** (2014) no. 7, 072011, arXiv:1405.0421 [hep-ex].

[280] V. Ahrens, A. Ferroglia, M. Neubert, B. D. Pecjak, and L. L. Yang, *The top-pair forward-backward asymmetry beyond NLO*, Phys.Rev. **D84** (2011) 074004, arXiv:1106.6051 [hep-ph].

[281] W. Hollik and D. Pagani, *The electroweak contribution to the top quark forward-backward asymmetry at the Tevatron*, Phys.Rev. **D84** (2011) 093003, arXiv:1107.2606 [hep-ph].

[282] CMS Collaboration, S. Chatrchyan et al., *Measurement of the charge asymmetry in top-quark pair production in proton-proton collisions at* $\sqrt{s} = 7$ *TeV*, Phys.Lett. **B709** (2012) 28–49, arXiv:1112.5100 [hep-ex].

[283] ATLAS Collaboration, G. Aad et al., *Measurement of the charge asymmetry in top quark pair production in pp collisions at* $\sqrt{s} = 7$ *TeV using the ATLAS detector*, Eur.Phys.J. **C72** (2012) 2039, arXiv:1203.4211 [hep-ex].

[284] P. Ferrario and G. Rodrigo, *Massive color-octet bosons and the charge asymmetries of top quarks at hadron colliders*, Phys.Rev. **D78** (2008) 094018, arXiv:0809.3354 [hep-ph].

[285] J. Alwall, P. Demin, S. de Visscher, R. Frederix, M. Herquet, et al., *MadGraph/MadEvent v4: The New Web Generation*, JHEP **0709** (2007) 028, arXiv:0706.2334 [hep-ph].

[286] T. Sjostrand, S. Mrenna, and P. Z. Skands, *PYTHIA 6.4 Physics and Manual*, JHEP **0605** (2006) 026, `arXiv:hep-ph/0603175 [hep-ph]`.

[287] J. Conway et al., *PGS 4 Pretty Good Simulation of high energy collisions*, http://www.physics.ucdavis.edu/ conway/research/software/pgs/pgs4-general.htm, June, 2012.

[288] CDF Collaboration, *Measurement of the Inclusive Forward-Backward Asymmetry and its Rapidity Dependence $A_{fb}(|\Delta y|)$ of tt Production in 5.3/fb of Tevatron Data*, Tech. Rep. Conf. Note 10224, Fermilab, 2010. `http://www-cdf.fnal.gov/physics/new/top/2010/tprop/Afb/cdfnote_10224_public_v02_for_10185_ttbarAfbDeltay.pdf`.

[289] D0 Collaboration, *Measurement of the forward-backward production asymmetry of t and tbar quarks in ppbar to ttbar events*, Tech. Rep. D0-Note 6062-CONF, Fermilab, 2010. `http://www-d0.fnal.gov/Run2Physics/WWW/results/prelim/TOP/T90/T90.pdf`.

[290] A. Atre, G. Azuelos, M. Carena, T. Han, E. Ozcan, et al., *Model-Independent Searches for New Quarks at the LHC*, JHEP **1108** (2011) 080, `arXiv:1102.1987 [hep-ph]`.

[291] E. Fermi, *An attempt of a theory of beta radiation. 1.*, Z.Phys. **88** (1934) 161–177.

[292] R. Feynman and M. Gell-Mann, *Theory of Fermi interaction*, Phys.Rev. **109** (1958) 193–198.

[293] E. Sudarshan and R. Marshak, *Chirality invariance and the universal Fermi interaction*, Phys.Rev. **109** (1958) 1860–1860.

[294] R. S. Chivukula and H. Georgi, *Large N and vacuum alignment in topcolor models*, Phys.Rev. **D58** (1998) 075004, `arXiv:hep-ph/9805478 [hep-ph]`.

[295] H. Pagels and S. Stokar, *The Pion Decay Constant, Electromagnetic Form-Factor and Quark Electromagnetic Selfenergy in QCD*, Phys.Rev. **D20** (1979) 2947.

[296] S. Weinberg, *Phenomenological Lagrangians*, Physica **A96** (1979) 327.

[297] A. Manohar and H. Georgi, *Chiral Quarks and the Nonrelativistic Quark Model*, Nucl.Phys. **B234** (1984) 189.

[298] O. Deschamps, S. Descotes-Genon, S. Monteil, V. Niess, S. T'Jampens, et al., *The Two Higgs Doublet of Type II facing flavour physics data*, Phys.Rev. **D82** (2010) 073012, `arXiv:0907.5135 [hep-ph]`.

[299] LHC Higgs Cross Section Working Group Collaboration, S. Heinemeyer et al., *Handbook of LHC Higgs Cross Sections: 3. Higgs Properties*, `arXiv:1307.1347 [hep-ph]`.

[300] Particle Data Group Collaboration, J. Beringer et al., *Review of Particle Physics (RPP)*, Phys.Rev. **D86** (2012) 010001.